Understanding the impact of order-disorder phenomena on the optical properties of photoactive semiconducting materials

Dissertation

Zur Erlangung des akademischen Grades
eines Doktors der Naturwissenschaften (Dr. rer. nat.)
Im Promotionsprogramm
Fotophysik synthetischer und biologischer multichromophorer Systeme
der Bayreuther Graduiertenschule für Mathematik und Naturwissenschaften

vorgelegt von
Fabian Panzer

Geboren in Marktredwitz, Deutschland

Bayreuth, 2016

Die vorliegende Arbeit wurde innerhalb von zwei Jahren und 7 Monaten in der Zeit von November 2013 bis Mai 2016 am Lehrstuhl für Experimentalphysik II und dem Lehrstuhl für Funktionsmaterialien der Universität Bayreuth unter der Betreuung von Prof. Dr. Anna Köhler und Prof. Dr. Ralf Moos angefertigt.

Vollständiger Abdruck der von der Bayreuther Graduiertenschule für Mathematik und Naturwissenschaften (BayNAT) genehmigten Dissertation zur Erlangung des akademischen Grades Doktor der Naturwissenschaften (Dr. rer. Nat).

Amtierender Direktor der Graduiertenschule: Prof. Dr. Stephan Kümmel

Dissertation eingereicht am: 02.06.2016
Tag des wissenschaftlichen Kolloquiums: 14.09.2016

Prüfungsausschuss:

Prof. Dr. Anna Köhler	(Erstgutachter)
Prof. Dr. Mukundan Thelakkat	(Zweitgutachter)
Prof. Dr. Stephan Kümmel	(Vorsitzender)
Prof. Dr. Markus Lippitz	

(Drittgutachter: Prof. Dr. Uli Lemmer, Karlsruher Institut für Technologie)

Table of Contents

1. Summary

Until today, organic semiconductors as well as hybrid organic-inorganic perovskites have emerged as promising classes of semiconductors. This is obvious, for instance from the significantly increase in efficiencies within the last years in optoelectronic devices such as solar cells or light emitting diodes based on these two classes. Improved device efficiencies were realised mainly due to increased efforts in the field of device engineering. However it is also clear that for further improvement of devices, a fundamental understanding on the nature and dynamics of excited states within the semiconductor material is essential. Irrespective of whether organic- or hybrid organic-inorganic perovskite semiconductors are considered, a major factor controlling device performance is the morphology of the semiconductor, since the morphology of the material is correlated in a sensitive way with its electric properties.

So in the case of organic semiconductors the questions arise how the relative alignment of individual constituents or chromophores of conjugated polymers impact on the electronic structure, how major changes in structure, such as order-disorder transitions, occur and how they can be influenced. In contrast to organic semiconductors, i.e. conjugated polymers, oligomers or small molecules, hybrid organic-inorganic perovskites have a crystalline nature. Therefor the correlation between morphology and electronic structure transforms into the aim to understand how structural changes of the perovskite unit cell impact on corresponding electronic structure. On the one hand it is known that the structure of the unit cell of hybrid perovskites can undergo minor and also major changes dependent on temperature. On the other hand, a deep understanding on the origin of these temperature dependent changes has not yet established. Therefore relevant questions in that context are concerned with: what contributes to the spectral shift of the optical spectra of perovskites? How does the nature of the excited states evolve as a function of temperature and is it possible to gain control on the morphological state of the perovskite and even manipulate the latter?

This thesis contributes to the tasks and questions raised above and is thus concerned with the issue how changes in morphology modify the electronic structure and electronic interactions among chromophores and constituents of organic- and hybrid organic-inorganic semiconductors.

Chapters 4.2 – 4.6 focus on organic semiconductors. Chapter 4.2 first reveals the nature of temperature induced order-disorder transitions in the conjugated polymer P3HT to be a first order rather than a second order transition. This study is conducted by temperature dependent emission and absorption measurements of different batches of P3HT with different molecular weight and polydispersity. Both last-mentioned material properties are also identified to impact on the order-disorder transition, where the molecular weight is correlated with the critical temperature for the transition and the polydispersity impacts on how distinct the transition takes place.

Chapter 4.3 then shows how temperature dependent ordering processes of P3HT can be understood and interpreted by applying detailed spectroscopic analysis on temperature dependent emission and absorption spectra. It assigns the temperature dependent phases to main-chain and side-chain order. With that, two distinct aggregate species that differ in their side-chain order could be identified by optical spectroscopy at low temperatures.

In Chapter 4.4 the spectroscopic analysis tools developed in chapters 4.2 and 4.3 were applied to temperature dependent steady-state as well as transient absorption measurements of the conjugated polymer MEHPPV. The latter also shows an order-disorder transition which was induced by decreasing the temperature. Analysing the spectra at low temperatures revealed an ultrafast energy transfer between disordered and highly planar chain segments. It further shows that in the case of MEHPPV, disordered and highly planar chain segments must be in a close proximity.

After that, Chapter 4.5 deals with a detailed investigation of the excited state dynamics within the aggregated phase of MEHPPV. Applying transient absorption spectroscopy and coherent ultrafast electronic 2D spec1troscopy, exciton relaxation and energy transfer dynamics also in the aggregated phase are analysed.

Chapter 4.6 gives an overview on the results of temperature induced order-disorder transitions of various materials that were investigated in the Köhler group within the last years. As these transition occurs not only in polymers, but also in oligomers and even in small molecules, Chapter 4.6 puts these transitions into a more general context and shines light on how aggregate formation takes place and in which different ways the measured emission and absorption spectra can be analysed.

Chapter 4.7 - 4.9 focus on the hybrid organic-inorganic perovskite $CH_3NH_3PbI_3$. Chapter 4.7 deals with the analysis of the temperature and excitation fluence dependent emission properties of $CH_3NH_3PbI_3$ between 300 – 5 K. With that it was possible to identify a temperature independent critical excitation density for amplified spontaneous emission. A second aspect of Chapter 4.7 is concerned with the effect of local heating of the perovskite at low temperatures. Here I present the discovery on the possibility to deliberately induce structural phase changes by appropriate laser excitation which are then kinetically frozen out and finally trapped at low temperatures. As the different phases also have different band gap energies, corresponding emission of the phase takes place at distinct wavelengths. Additionally this process is found to be reversible and highly reproducible which paves the way to, in principle, exploit this phenomenon for an all optical memory device.

Beside the distinct change of the optical spectra when undergoing the tetragonal - orthorhombic phase transition, hybrid organic-inorganic perovskites additionally exhibit a temperature dependent continuous spectral shift. Chapter 4.8 works out the origin of this shift where it shows that the significant temperature dependent lattice expansion of hybrid perovskites is the dominant underlying process. Analysis on temperature dependent absorption and emission spectra in the framework of Urbach theory, further allow to distinguish between static and dynamic disorder in the material. This in turn gains knowledge on how the morphological state of this class of semiconductor is linked to its electronic structure.

In regard to commercialisation of perovskite solar cells, a crucial aspect is to have control on the structural stability during the processing. Chapter 4.9 describes a proof of principle work where perovskite layers with high crystallinity could be successfully processed using the aerosol deposition method. As the latter is a dry process where the source material (powder) is prepared independently from the deposition step, it decouples the material synthesis and layer formation, which is unique compared to all other processing methods for organic-inorganic perovskites.

An extended summary of the individual chapters is given in section 3 “Overview of the Thesis”.

Zusammenfassung

Bis heute haben organische Halbleiter als auch hybrid organisch-anorganische Perowskite sich als vielversprechende Halbleiterklasse hervorgetan. Zum Beispiel wird dies offensichtlich durch den signifikanten Anstieg der Effizienten innerhalb der letzten Jahre von opto-elektronischem Bauteilen wie Solarzellen oder LEDs, welche auf diesen beiden Materialklassen basieren. Verbesserte Bauteileffizienzen wurden hauptsächlich durch gesteigerte Bemühungen im Feld des Device-engineerings realisiert. Jedoch ist es auch klar, dass für weitere Verbesserungen von Bauteilen ein fundamentales Verständnis über die Natur und die Dynamik der angeregten Zustände innerhalb des Halbleitermaterials essentiell ist. Ungeachtet ob organische oder organisch-anorganische perowskitische Halbleiter betrachtet werden, ist ein wesentlicher Faktor welcher die Bauteileffizienz kontrolliert die Morphologie des Halbleiters, da die Morphologie des Materials sensitiv mit seinen elektrischen Eigenschaften gekoppelt ist.

Im Falle von organischen Halbleitern stellen sich daher die Fragen wie sich die relative Anordnung der einzelnen Konstituenten oder Chromophore von konjugierten Polymeren auf deren elektronischen Struktur auswirken, wie wesentliche Änderungen in der Struktur wie beispielsweise Ordnungs-Unordnungs-Übergänge stattfinden und wie sie beeinflusst werden können. Im Gegensatz zu organischen Halbleitern, d.h. konjugierten Polymeren, Oligomere oder kleine Moleküle, besitzen hybride organische-anorganische Perowskite eine kristalline Natur. Daher geht hier der Zusammenhang zwischen Morphologie und elektronischer Struktur über in das Bestreben zu Verstehen wie sich strukturelle Änderungen der Perowskit Einheitszelle auf die entsprechende elektronische Struktur auswirken.

Auf der einen Seite ist bekannt, dass die Struktur der Einheitszelle des hybrid-Perowskiten geringfügige als auch bedeutende Änderungen in Abhängigkeit der Temperatur erfahren kann. Auf der anderen Seite, hat sich bisher ein tiefgehendes Verständnis über den Ursprung dieser temperaturabhängigen Änderungen noch nicht herausgebildet. Daher beschäftigen sich relevante Fragestellungen in diesem Zusammenhang mit: Was trägt zu den spektralen Verschiebungen in den optischen Spektren von Perowskiten bei? Wie entwickelt sich die Natur der angeregten Zustände

als Funktion der Temperatur und ist es möglich, Kontrolle über die morphologischen Zustände des Perowskiten zu erhalten und diese sogar zu manipulieren?

Diese Arbeit trägt zu den oben aufgeworfenen Aufgaben- und Fragestellungen bei und beschäftigt sich somit mit dem Aspekt, wie Änderungen in der Morphologie die elektronische Struktur und elektronische Interaktionen zwischen Konstituenten von organischen- und hybriden organisch-anorganischen Halbleitern modifizieren.

Kapitel 4.2 – 4.6 fokussieren sich auf organische Halbleiter. Kapitel 4.2 zeigt zunächst auf, dass die Natur temperaturinduzierter Ordnungs-Unordnungs-Übergänge des konjugierten Polymers P3HT vielmehr ein Prozess erster Ordnung anstelle zweiter Ordnung ist. Diese Untersuchung wurde durchgeführt mithilfe von temperatur-abhängigen Emissions- und Absorptionsmessungen an verschiedenen Chargen von P3HT, mit unterschiedlichen Molekulargewichten und Polydispersitäten. Beide letztgenannten Materialeigenschaften konnten identifiziert werden sich auf den Ordnungs-Unordnungs-Übergang auszuwirken, wobei das Molekulargewicht mit der kritischen Temperatur des Übergangs korreliert ist und die Polydispersität beeinflusst, wie deutlich der Übergang stattfindet.

Kapitel 4.3 zeigt dann wie temperaturabhängige Ordnungsprozesse von P3HT durch die Anwendung detaillierter spektroskopischer Analysen der temperaturabhängigen Emissions- und Absorptionsspektren verstanden werden können. Es weist die temperaturabhängigen Phasen der Ordnung der Haupt- und Seitenketten zu. Dadurch konnten durch optische Spektroskopie bei tiefen Temperaturen zwei individuelle Spezies von Aggregaten identifiziert werden, welche sich in der Ordnung ihrer Seitenketten unterscheiden

In Kapitel 4.4 wurden die in den Kapiteln 4.2 und 4.3 entwickelten spektroskopischen Analyse-Tool auf temperaturabhängige steady-state als auch transiente Absorptionsmessungen des konjugierten Polymers MEHPPV angewendet. Dieses zeigt auch einen Ordnungs-Unordnungs-Übergang, welche durch Temperaturerniedrigung induziert wurde. Analysen an den Spektren bei tiefen Temperaturen konnten einen ultraschnellen Energietransfer zwischen den ungeordneten und hoch planaren Kettensegmenten deutlich machen. Es zeigt weiterhin dass sich im Falle von MEHPPV, ungeordnete und hoch planare Kettensegmente in unmittelbarer Nähe zueinander befinden müssen.

Danach beschäftigt sich Kapitel 4.5 mit einer detaillierten Untersuchung der Dynamiken der angeregten Zustände innerhalb der aggregierten Phase von MEHPPV. Durch Anwendung transienter Absorptionsspektroskopie und kohärenter ultraschneller elektronischer 2D-Spektroskopie, werden Relaxationsprozesse von Exzitonen und Energietransferdynamiken auch in der aggregierten Phase untersucht.

Kapitel 4.6. gibt einen Überblick über die Ergebnisse der temperaturinduzierten Ordnungs-Unordnungs-Übergänge verschiedener Materialsysteme, welche innerhalb der letzten Jahre in der Köhler Arbeitsgruppe untersucht wurden. Da diese Übergänge nicht nur in Polymeren auftreten, sondern auch in Oligomeren und sogar in kleinen Molekülen, stellt Kapitel 4.6. diese Übergänge in einen generelleren Kontext und zeigt auf, wie Aggregation stattfindet und auf welchen unterschiedlichen Wegen die gemessenen Emissions- und Absorptionsspektren analysiert werden können.

Kapitel 4.7 bis 4.9 fokussieren sich auf den hybriden organisch-anorganischen Perowskiten $CH_3NH_3PbI_3$. Kapitel 4.7 beschäftigt sich mit der Analyse der temperatur- und anregungsdichtenabhängigen Emissionseigenschaften von $CH_3NH_3PbI_3$ zwischen 300 – 5 K. Damit war es möglich eine temperaturunabhängige kritische Anregungsdichte für verstärkte spontane Emission zu identifizieren. Ein zweiter Aspekt von Kapitel 4.7 beschäftigt sich mit dem Effekt des lokalen Erhitzens des Perowskiten bei niedrigen Temperaturen. Hier präsentiere ich die Entdeckung der Möglichkeit, bewusst Phasenänderungen durch geeignete Laseranregung in der Struktur zu induzieren, welche dann bei niedrigen Temperaturen kinetisch ausgefroren und letztlich eingeschlossen werden. Da die unterschiedlichen Phasen auch unterschiedliche Bandlücken besitzen, finden die zugehörigen Emissionen bei individuellen Wellenlängen statt. Zusätzlich konnte dieser Prozess als reversibel und höchst reproduzierbar identifiziert werden, was den Weg ebnet um dieses Phänomen prinzipiell für ein vollständig optisches Speichermedium auszunutzen.

Neben den deutlichen Änderungen der optischen Spektren während des Durchlaufens des tetragonal - orthorhombisch Phasenübergangs, zeigen hybride organisch-anorganische Perowskite zusätzlich eine kontinuierliche temperaturabhängige spektrale Verschiebung. Kapitel 4.8 arbeitet den Ursprung dieser Verschiebung heraus bei der gezeigt wird, dass die signifikante temperaturabhängige Gitterausdehnung von hybriden Perowskiten der dominante zugrundeliegende Prozess ist. Analysen an den

temperaturabhängigen Absorptions- und Emissionsspektren im Rahmen der Urbach Theorie erlauben des Weiteren, zwischen statischer und dynamischen Unordnung innerhalb des Materials zu unterscheiden. Dies wiederum liefert Einsichten inwiefern die morphologische Gestalt dieser Halbleiterklasse mit ihrer elektronischen Struktur verbunden ist.

Ein entscheidender Aspekt im Hinblick auf die Kommerzialisierung von Perowskit Solarzellen ist Kontrolle über die strukturelle Stabilität während der Prozessierung zu besitzen. Kapitel 4.9 beschreibt eine Machbarkeitsstudie bei der Perowskitschichten mit hoher Kristallinität erfolgreich mithilfe einer aerosolbasierten Kaltabscheidungs-methode prozessiert werden konnten. Da dieser ein trockener Prozess ist, bei dem das Ausgangsmaterial (Pulver) unabhängig vom Abscheidungsschritt präpariert wird, entkoppelt es Materialsynthese und Schichtbildung. Dies ist einzigartig im Vergleich zu allen anderen Prozessiermethoden für organisch-anorganische Perowskite.

Eine erweiterte Zusammenfassung der einzelnen Kapitel findet sich in Teil 3 „Overview of the Thesis“.

2. Introduction

2.1. Motivation

Driven by the desire for green energy supply and a simultaneous reduction of overall power consumption, the need for a new generation of highly efficient optoelectronic devices which offer the possibilities for an wide field of application as well as simple and low cost production at a large scale, has gained momentum within the last years.

At present, two classes of semiconductors are particularly promising to satisfy these requirements, which are organic semiconductors and hybrid organic-inorganic perovskites. For instance, organic semiconductors have impressively proven their commercial applicability in the field of display technology where, organic light emitting diodes (OLEDs) emerged as state of the art display technology. Furthermore, the power conversion efficiencies of organic solar cells have also steadily increased and are currently reaching 11.5%.[1] Also hybrid organic-inorganic perovskites have drawn enormous attention mainly in the solar cell community, where the power conversion efficiencies of perovskite based solar cell underwent a drastic increase within the last few years up to currently 22.1%.[1]

However, independent of the type of optoelectronic device and class of semiconducting material, a distinct knowledge and control on the charge carrier dynamics i.e. the dissociation of excitations or the transport of charge carriers is essential to obtain high device efficiencies.[2-4] These dynamics are inextricable linked with, and thus highly sensitive to the ordering and alignment within the active semiconducting material.[5-9] Thus, this thesis is concerned with the issue how changes in morphology modify the electronic structure and electronic interactions among chromophores and constituents of organic- and hybrid organic-inorganic semiconductors.

In the case of organic polymers, ordering processes have been mainly investigated upon cooling from the melt for flexible polymers like polystyrene or polydiacetylenes which typically undergo rod-to-coil phase transitions.[10-12] Such order-disorder transitions can also occur during the formation of thin films of organic conjugated polymers by spin-coating from solution. They have a more rigid character (rigid + semicrystalline) and are mainly used in organic solar cells. Despite their importance in optoelectronic devices,

surprisingly little is known on how the conjugated polymer chains align and pack, though this can have major impact on their corresponding electronic structure. The formation of "aggregates", i.e. domains with ordered, interacting chromophores is therefore an important issue in the field of organic semiconductor physics. Among other methods, a way to induce aggregate formation in conjugated polymer solutions is to decrease the solvent quality, which can be done in a very systematic way by lowering the temperature.[13,14]

As changes in the conformation of semiconductor materials also impact on their electronic structure, corresponding optical properties do so as well. Thus, temperature dependent optical steady-state spectroscopy is a highly attractive tool for investigating temperature induced order-disorder transition phenomena. Furthermore it is relatively easily accessible and, with it, detailed information about the morphology, ordering processes, as well as valuable information about the nature of the excited states of the investigated material can be obtained.

Therefore temperature dependent absorption and emission measurements were carried out for solutions of different conjugated polymers. They were carried out with the goal to develop a deep and a more generalized understanding on the aggregation behaviour of this materials and to gain knowledge on how the chain segments of the different structural phases electronically interact (chapter 4.2 to 4.6).

In addition to organic semiconductors, hybrid perovskites are also known to exist in different morphologies. In the case of perovskites, different morphologies refer to the different crystal structures such as cubic, tetragonal or orthorhombic structure of the unit cell which are known to depend on temperature.[15] Similar to the case of organic semiconductors, changes in the structure can have distinct impact on the electronic properties also in the case of hybrid perovskites.[16,17] Until now, fundamental knowledge on the origin of temperature dependent spectral shifts in the optical spectra are sparse. Furthermore the temperature dependent nature of the excited states remains under debate and thus needs further investigations. In that context, strategies to correlate the degree of disorder in hybrid perovskites with their optical spectra have also not yet been established, though they are highly desirable. To address these open issues, I carried out temperature dependent absorption and emission measurements on the hybrid

perovskite $CH_3NH_3PbI_3$, to investigate the impact of morphological changes of the crystal structure on the corresponding electronic properties (chapter 4.7 to 4.9).

In the following section 2.2, the physical origin of the optoelectronic properties of organic conjugated materials are introduced, including the impact of interacting constituents. As the class of hybrid perovskite semiconductors has come up only recently, section 2.3 then gives a brief historical overview of this new class of semiconducting material, followed by a summary of the origin of their optoelectronic properties.

2.2. Optical properties of organic semiconductors

Origin of the conducting properties and concept of disorder

Organic semiconductors mainly consist of carbon-hydrogen and carbon-carbon bonds. Depending on the binding partner, carbon can form energetically favourable hybrid orbitals from which single, double or triple bonds form whereby the electrons of the hybrid orbitals form covalent sigma bonds. In contrast to that, the electrons of the p-orbitals that are not involved in the hybridisation overlap and form a π-orbital (π-bond), whereby the corresponding electrons delocalise.

Conjugated polymers often are characterized by the alternation of single and double bonds, and the electrons in the π-orbitals delocalize over a number of repeating units. The occupied and unoccupied molecular states are separated by an energy gap. The highest occupied molecular orbital (HOMO) and the lowest unoccupied molecular orbital (LUMO) are usually bonding π and antibonding π^*-orbitals.

The length over which the electronic wave function can delocalize is called conjugation length. In real systems, this length is substantially limited by chemical defects and influenced by changes in the local dielectric constant, i.e. by its polarizability and by structural disorder of the polymer chain. As a consequence, the energy values of the individual HOMO and LUMO levels are Gaussian distributed and thus lead to an inhomogeneous broadening of the density of states (DOS), which in turn results also in a broadening of corresponding optical spectra as will be explained in more detail further below (Figure 1).[18]

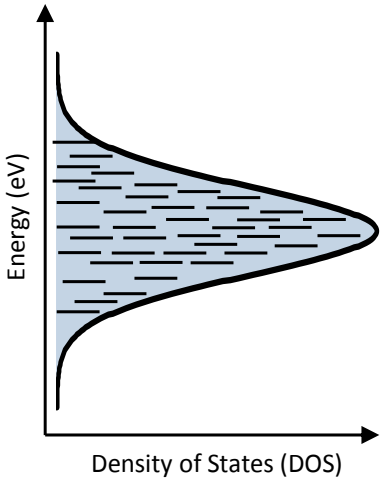

Figure 1: Illustration of the different energy levels of an ensemble of chromophores due to structural disorder, leading to a Gaussian distributed density of states (DOS).

Optical transitions

The fundamental basis to understand the absorption and emission spectra of conjugated polymers can be seen in the Franck-Condon-Principle. This principle says that electronic transitions between the electronic ground state S_0 and the first excited state S_1 occur significantly faster (in the order of 10^{-15} s) than the typical timescales of the motion of the corresponding atomic nucleus (typically in the range of 10^{-13} s). Therefore the configuration coordinate Q of the system is assumed to stay constant during a transition, so that the latter appears as a vertical transition in the energy diagram. Figure 2 illustrates the processes that occur for the absorption and emission of organic semiconductors.

In that picture, the potential energy curves (often approximated by a Morse potential) including their respective vibrational modes are indicated for both, the ground state S_0 and the first excited state S_1. The vibrational modes are labelled as $v = 0,1,2,3$ ... with their energy levels being separated by the constant vibrational energy $\hbar\omega_i$. In absorption, an electron is lifted from the lowest vibrational level of the electronic ground state into an arbitrary vibrational state of the S_1. It then relaxes non-radiatively to the lowest vibrational level of the S_1. Finally the excited state decays back to a certain vibrational level of the ground state via emitting a photon.

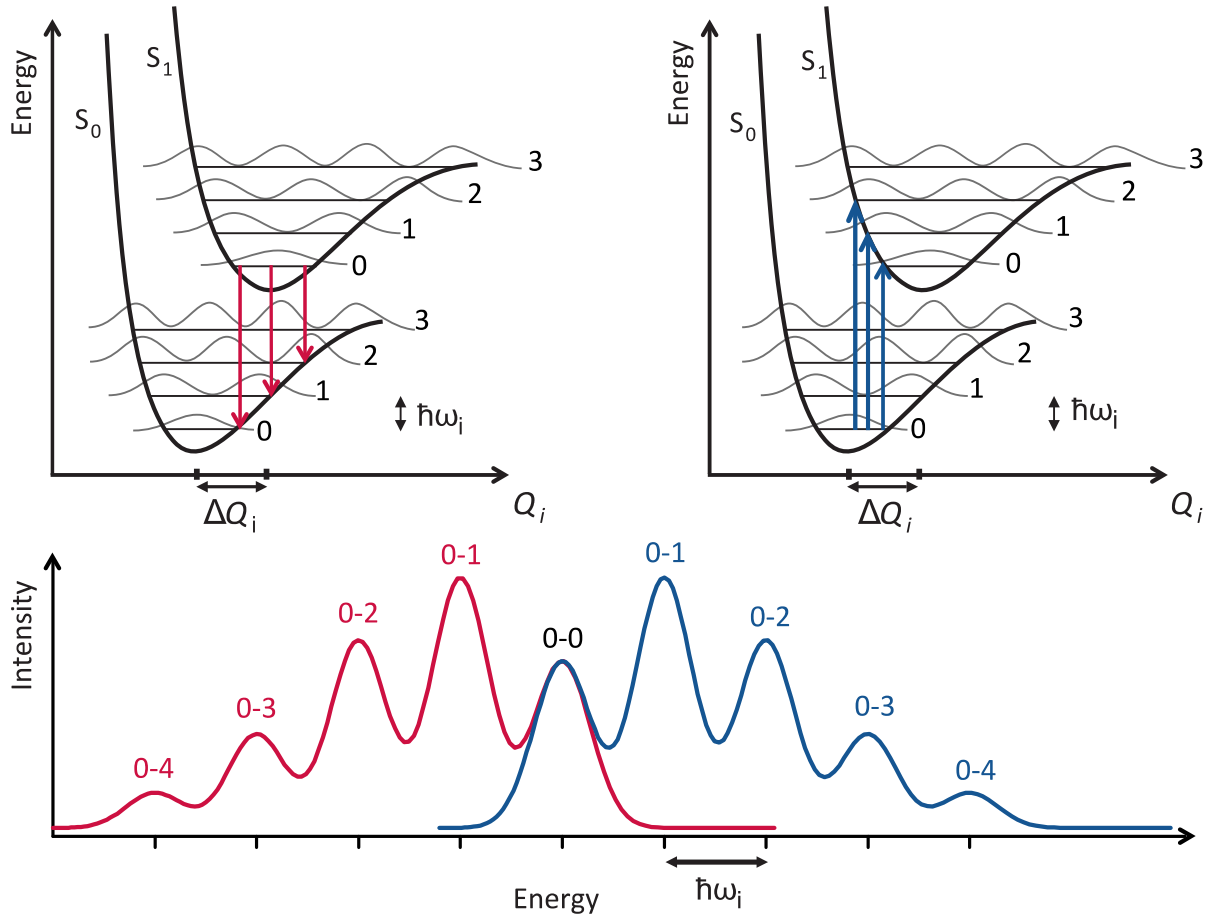

Figure 2: Top: Illustration of the various transitions in PL (left) and absorption (right) between the electronic ground state S_0 and excited state S_1. The potential energies of S_1 and S_0 together with their corresponding vibrational energy levels (here shown between 0 and 3) as a function of the configuration coordinate Q are shown. The displacement of the configuration coordinate between S_0 and S_1 is denoted as ΔQ. Furthermore the vibrational wave functions of the equidistant vibrational levels, energetically separated by $\hbar\omega_i$ are indicated as well. Bottom: Exemplary mirror-symmetric absorption (red) and emission (blue) spectra which result from the transitions, following the Frank-Condon-principle.

Here the intensities of transitions into the various vibrational states of the S_0 for emission and into the various vibrational states of the S_1 in the case of absorption depend on the overlap of the wave functions of initial and final state.[5,19] As the vibrational levels in both ground and excited state are equidistant (within the harmonic approximation), absorption and emission spectra both result as a composition of various energetically evenly spaced spectral features with a certain progression regarding their individual intensities (compare Figure 2). The latter is determined by the wave function overlap of initial and final state and is thus determined by the degree of displacement ΔQ of the configuration coordinate between the electronic ground and excited state.

In that context the Huang Rhys Parameter S is a measure of the strength of the electron-phonon-coupling and is correlated with ΔQ via:[20]

$$S = \frac{M\omega}{2\hbar}(\Delta Q)^2 \quad (1)$$

With M being the reduced mass and ω the vibrational energy. In the case of harmonic oscillators the relative transition strength of the progression of vibronic levels v is then given by:

$$I_v = \frac{S^v e^{-S}}{v!} \quad (2)$$

In the emission and absorption spectra of real systems the transition lines are not sharp as suggested by the above described model but broadened. In the case of the conjugated polymer systems that are investigated in this thesis, a Gaussian broadening due to their structural disorder can be assumed. According to the Franck-Condon-Principle, absorption and emission spectra have a mirror symmetry. On the other hand, this is not the case for conjugated polymers, which can be attributed to geometric relaxation and a distribution of conjugation lengths. Because all different domains/parts of the polymer absorb, usually a rather unstructured and broadened absorption spectrum is observed. In contrast to that, corresponding emission spectra often appear more structured and spectral features are more distinct due to the possibility of the excited states to relax towards lower energy sites of the polymer chain before the emission process takes place.

To model measured absorption and photoluminescence spectra of real systems, it is necessary to additionally consider the effect of the photon density-of-states of the surrounding medium on the emission rate of the investigated material. Here, from the Einstein relation it follows that the term $n(\hbar\omega) \cdot \hbar\omega$ has to be introduced with $n(\hbar\omega)$ being the refractive index of the investigated material system at photon energy $\hbar\omega$.[21] It than follows that the photoluminescence spectra $I_{PL}(\hbar\omega)$ and absorption spectra $I_{Abs}(\hbar\omega)$ of organic materials can be modelled by:[22-24]

$$I_{PL}(\hbar\omega) = [n(\hbar\omega) \cdot \hbar\omega]^3 \cdot \sum_v \frac{S^v e^{-S}}{v!} \cdot \Gamma \cdot \delta(\hbar\omega - (\hbar\omega_0 - v\hbar\omega_i)) \quad (3)$$

$$I_{Abs}(\hbar\omega) = n(\hbar\omega) \cdot \hbar\omega \cdot \sum_v \frac{S^v e^{-S}}{v!} \cdot \Gamma \cdot \delta(\hbar\omega - (\hbar\omega_0 + v\hbar\omega_i)) \quad (4)$$

$\hbar\omega_0$ corresponds to the photon energy of the 0-0 transition, Γ to the Gaussian peak function and δ represents the delta peak distribution. Note, that in the here developed model, only one vibrational mode with an energy value of $\hbar\omega_i$ is considered. The various energies of vibrations that are present in the investigated sample are typically assessed via Raman spectroscopy measurements.

In the past, the above derived modelling of the optical spectra has successfully applied to a variety of conjugated polymers.[23,25-29] Often an effective vibrational mode with an energy value between 0.17 eV – 0.18 eV is assumed, which is mainly due to the C=C symmetric stretching mode.

This single mode Franck Condon Analysis has therefore proven to be a simple applicable method to extract detailed information from measured PL or absorption spectra of conjugated polymers. On the other hand, as will be explained in detail in the next section, the optical properties and corresponding transitions can undergo significant changes when electronic coupling between polymer chains or chromophores is present. Therefore the applicability of the above developed modelling of the optical spectra is limited to the case of non-interacting single emitters (intrachain excitations). Modified and extended versions of the above developed model that take into account intermolecular interactions will be topic further below.

Impact of molecular coupling on optical properties - Evolution of H- and J- Aggregates

The aggregation of conjugated polymers due to attractive intermolecular interactions is a well-known phenomenon in the field of organic materials.[4,13,14,30-33] . In such cases, the excited state energies of involved constituents can split up and various possibilities for optical transitions can evolve. They depend on the relative orientation of the involved dipole moments, which can lead to a complex overall process. Therefore it appears beneficial to first consider the simplest possible system which is the strong interaction of two identical molecules labelled as molecule A and B (see also Figure 3 which illustrates the following considerations). In the framework of Kasha's theory,[34,35] the ground state of this dimer is then described by the Hamiltonian of the form $H = H_A + H_B + V_{AB}$, with H_A and H_B being the operators of the isolated molecules and V_{AB} represents a

intercoupling potential term. When solving corresponding Schrödinger equations one gets the ground state energy $E_{GS} = E_A + E_B + D$ with E_A and E_B being the corresponding ground state energies, and D being the negative energy value due to the van der Waals interactions between both molecules.

In the case of the excited state it is not possible to differ between excitation from molecule A or B, due to the assumption of two identical molecules. Therefore the coupling between the single molecules can be seen as either symmetric or antisymmetric so that the corresponding wave function reads as $\Psi_{E\pm} = \frac{1}{\sqrt{2}}(\Psi_A^*\Psi_B \pm \Psi_A\Psi_B^*)$. Using this wave function together with the Hamiltonian described above to solve the Schrödinger equation, it follows $E_{E\pm} = E_A^* + E_B + D' \pm \beta$. Here E_A^* is the energy of the excited molecule A and E_B the energy of the ground state of molecule B. Similar to before, D' corresponds to the energy of the van der Waals interactions between the two molecules in the excites state. β represents the energy of the transfer interaction between the molecules and results in a splitting of the excited state energies. Consequently the transition energy, being relevant for absorption measurements, is given by $\Delta E_{total} = \Delta E_A + \Delta D \pm \beta$ with $\Delta E_A = E_A^* - E_A$ being the excitation energy of a single molecule and ΔD reflects the difference between D' and D and is negative as usually $|D'| > |D|$. Due to its interaction, the dimer has two excited state levels which differ in energy by 2β. Depending on the relative orientation of the transition dipole moments in both molecules, there exist various scenarios for oscillator strengths of the transitions between the ground state and both excited states of the dimer. In that context one can differentiate between two limiting cases of relative dipole orientation:

One scenario applies when the molecules, or in more general the involved constituents align linearly straight in a sequential row. In that case the transition dipole moments add up, so that the lower excited state doubles its dipole moments, while in the higher excited state the dipole moments compensate to zero. As a consequence, the corresponding optical (absorption) transitions from the ground state into the higher energy excited state level carry no oscillator strength, while excitations into the lower excited state energy level are allowed. Therefore absorption and emission are red shifted compared to the monomer level, and the emission intensity is amplified. Consequently, the Stokes Shift is small in this case because transitions in both, absorption and emission take place between the same energy levels. Molecular aggregates, where the dipole

moments align in the this manner are typically called J-Aggregates (after E.E. Jelly,[36] or Scheibe-Aggregates after Scheibe).[37]

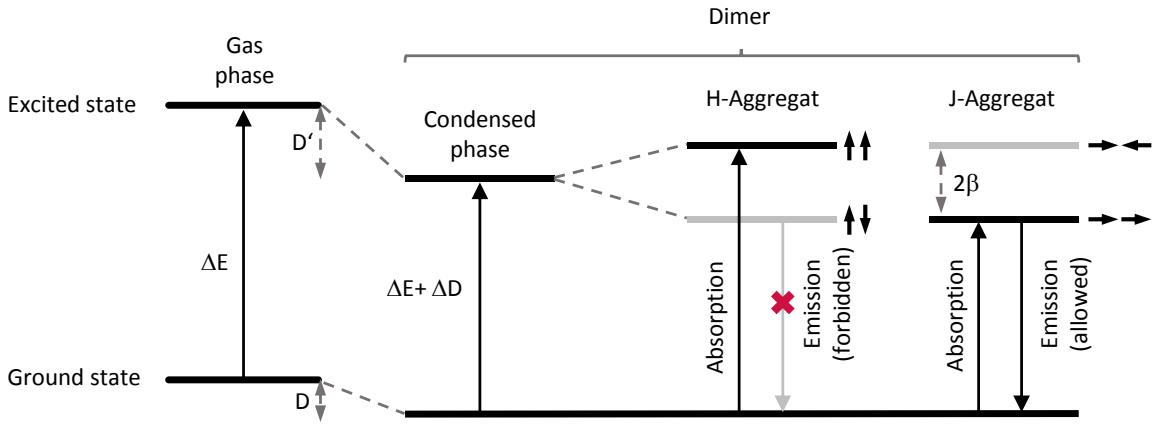

Figure 3: Illustration of the different energetic shifts and splitting of the energy levels occurring for the formation of an ideal dimer. The corresponding relative orientations of the transition dipoles for the two classes of aggregates are indicated as arrows.

In contrast to the above described case, a different class of aggregate results when the dipole moments of interacting molecules stack in a parallel coplanar fashion. Then the dipole moments add up in such a way, that they compensate to zero in the lower energy excited state level and double in the higher energy excited state, which is the exactly opposite behaviour compared to J-aggregates. As a consequence, absorption exclusively takes place to the higher energy level of the excited state, leading to a (hypsochromically) blue shifted absorption spectrum compared to the corresponding monomer spectrum. This absorption is then followed by non-radiative internal conversion of the excited state to the lower lying excited state energy level. Because the latter energy level does not carry any oscillator strength, the relaxation of the excited state to the ground state finally must occur non-radiatively. Therefore for a perfectly aligned coplanar stack at zero temperature, no emission spectrum is expected. In real systems, due to a non-perfect structural alignment of the constituents and temperature effects it is often possible to observe a weak emission. Here, because the energy levels of the absorption and of the (weak) emission differ, typically an enhanced Stokes Shift is observed. Due to its hypsochromically shifted absorption, this class of aggregates is referred to as H-aggregate.

Exciton bands in perfectly ordered idealised organic crystals

The above given description of the energy levels and values were developed for the simple case of two interacting molecules. This picture can now be expanded toward an infinite number of perfectly aligned constituents (in the absence of disorder). Here the dipole moments of the single molecules are approximated as a point dipole and furthermore, only nearest neighbour dipole-dipole interactions between adjacent molecules are considered. Using the same quantum mechanical approach as in the case for the dimer, it follows for the energies of the excited state as a function of the wave-vector of the exciton: $\Delta E(k) = \Delta E_{Monomer} + \Delta D \pm 2J \cos ka$ with $\Delta E_{Monomer}$ being the transition energy of the monomer, ΔD is the gas to-crystal-shift. Note that due to the energetic overlap of the large number of involved molecules, a band structure evolves. J refers to the degree of excitonic coupling which describes the transfer interaction between neighbouring molecules and is mainly determined by the transition dipole moments of the involved molecules. Due to the conservation of momentum, absorption of visible light only takes place for $k = 0$.[18] In the here described case of an ideal crystal, for each excited state energy level an exciton band forms with an energetic width of $4J$ (see Figure 4 for illustration).

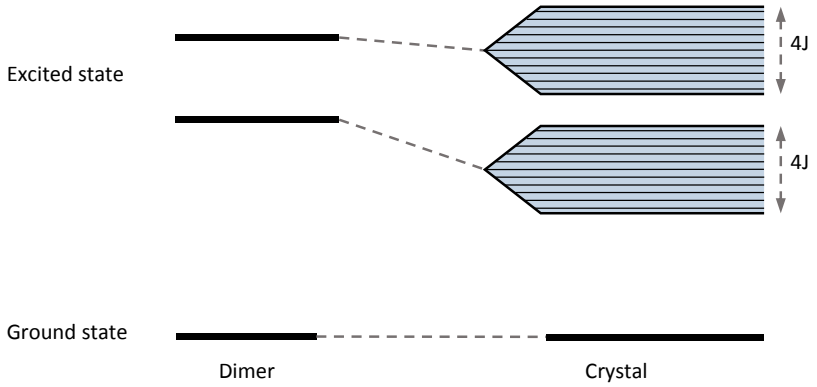

Figure 4: Transition of the splitted energy levels of a dimer toward the energy band structure of an idealised crystal consisting of dimers in which a large number of molecules are interacting within the excited state. The width of the bands is 4J and thus depends on the strength of the interaction between the molecules.

Within each band, excited states can in principle completely delocalize and move without restrictions. In a real system, thermally excited molecular dynamics as well as the energetic disorder need to be considered, which lead to a deviation compared to the behaviours of an ideal system.

Toward real systems: weakly interacting H- and J- Aggregates including vibronic coupling

To account for the static and dynamic disorder effects that occur in real polymeric systems, Spano and co-workers developed an extended theoretical model on the basis of Kasha's investigations.[38-41] The key development is the expansion of the wave function of the excited states by distinguishing between one-particle-states (where one molecule is in an electronic and also in a vibronic excited state, while all other molecule are in the ground state) and two-particle-states (one vibronically plus electronically excited molecule and another molecule which is in its electronic ground state but in an excited vibronic state). This leads to the energy schemes shown in Figure 5 for H- and J- aggregates. Note that no thermal effects, as well as no further disorder of the sites are yet considered. Every vibronic level of the excited state S_1 of a chromophore splits into an exciton band including its corresponding vibrational states. Its width is determined by the degree of electronic coupling strength and corresponding Franck-Condon-Factor.

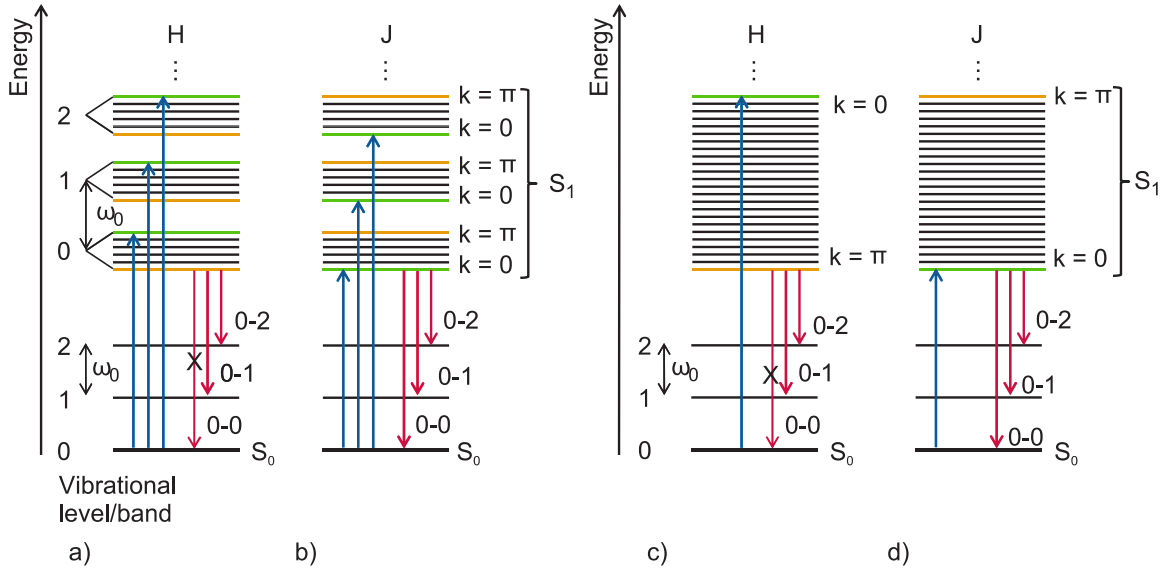

Figure 5: Scheme of the exciton bands in the weak coupling limit for H- (a) and J- aggregates (b), as well as the scheme of the exciton band in the strong coupling limit again for H- (c) and J-aggregates (d). In all cases, occurring transitions for absorption (blue) and emission (red) between S_0 and S_1 are indicated. From Ref 40

If this value is smaller than the vibrational quantum $\hbar\omega_0$, the vibrational bands are energetically separated which is called the weak-exciton-coupling-limit. In contrast to that, if the exciton bandwidth is large, they are superimposing and lead to a cumulated exciton band (Figure 5b). This regime is then referred to as strong-excitonic-coupling-

limit. The above described theory further gives the possibility to model the impact of coupling strength on the changes in the optical spectra. Figure 6 shows modelled absorption and emission spectra of H- and J-Aggregate type couplings of perfectly ordered chromophores, in each case for different degrees of coupling strength.

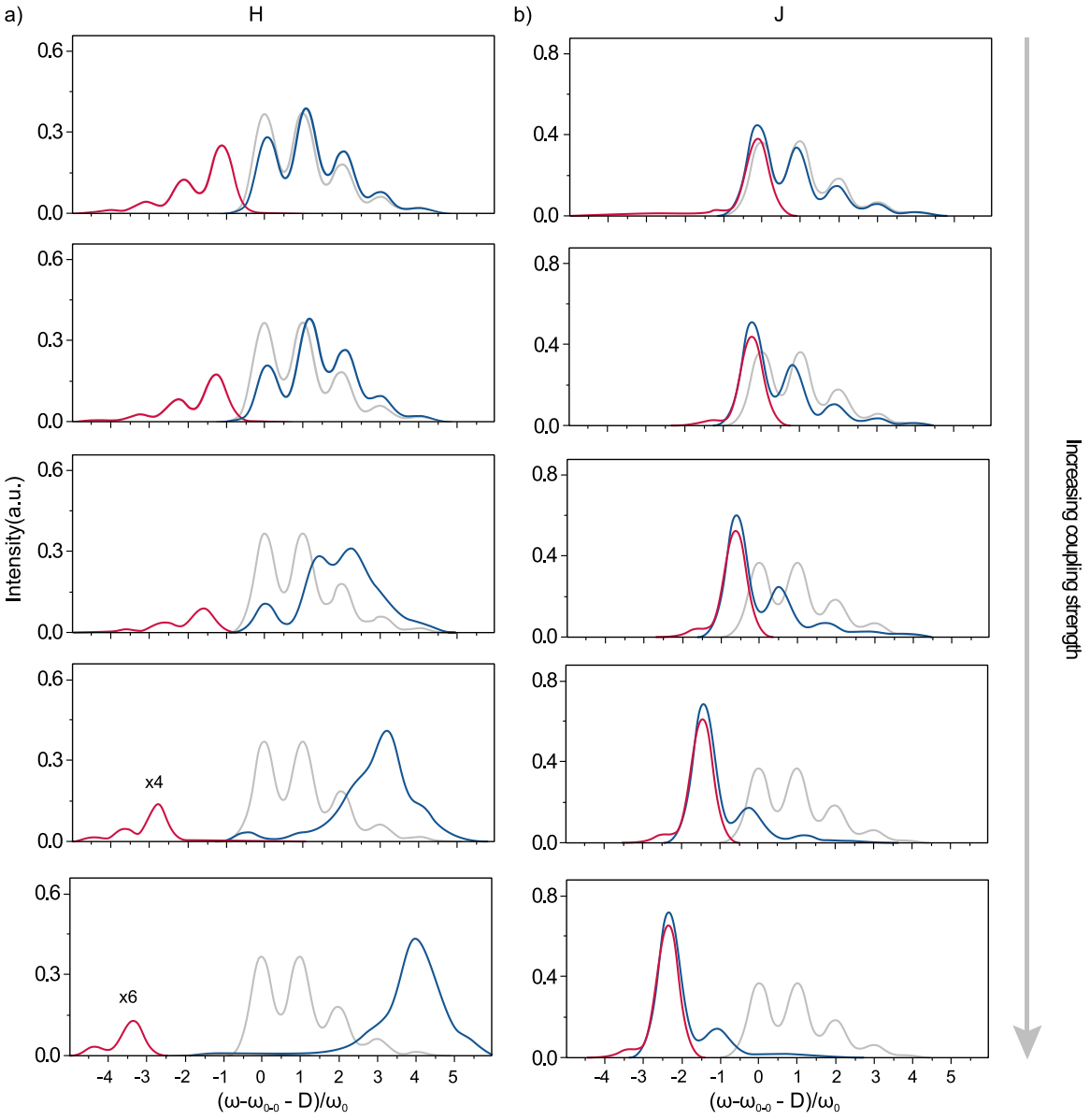

Figure 6: Calculated absorption (blue) and emission (red) spectra for (a) H-aggregates and (b) J-aggregates with a chain length of 20 repeating units. From top to bottom the coupling strength increases from $0.5\hbar\omega_i$ *to* $6\hbar\omega_i$*. Values are* $\hbar\omega_i$*=0.17 eV, S=1. From Ref 40*

In the case of H-Aggregates, for increasing coupling strength between the aggregated chromophores, both the $S_1 \leftarrow S_0$ 0-0 / 0-1 peak ratio in absorption, as well as the overall PL intensity decrease and the Stokes Shift between absorption and emission spectrum increases. The opposite behaviour is observed in the case of J-Aggregates.

Here for increasing coupling, the 0-0/0-1 peak ratio in absorption increases and the corresponding PL spectra exhibit an enhanced intensity. Furthermore the S_1-S_0 0-0 transitions of PL and absorption are in resonance, so that no Stokes Shift can be observed. When a perfectly ordered system at 0 K is assumed, the 0-0 Peak in the PL spectra is completely absent in the case of the H-aggregate due to the $k = 0$ selection rule.

However when static disorder is introduced into the investigated aggregate arrangement, symmetry is reduced which thus softens the selection rules where in turn the $S_1 \rightarrow S_0$ 0-0 transition becomes partly allowed in H-aggregates, while for J-aggregates the relative strength of the $S_1 \rightarrow S_0$ 0-0 transition decreases due to introduced localisation effects (Figure 7 left column).

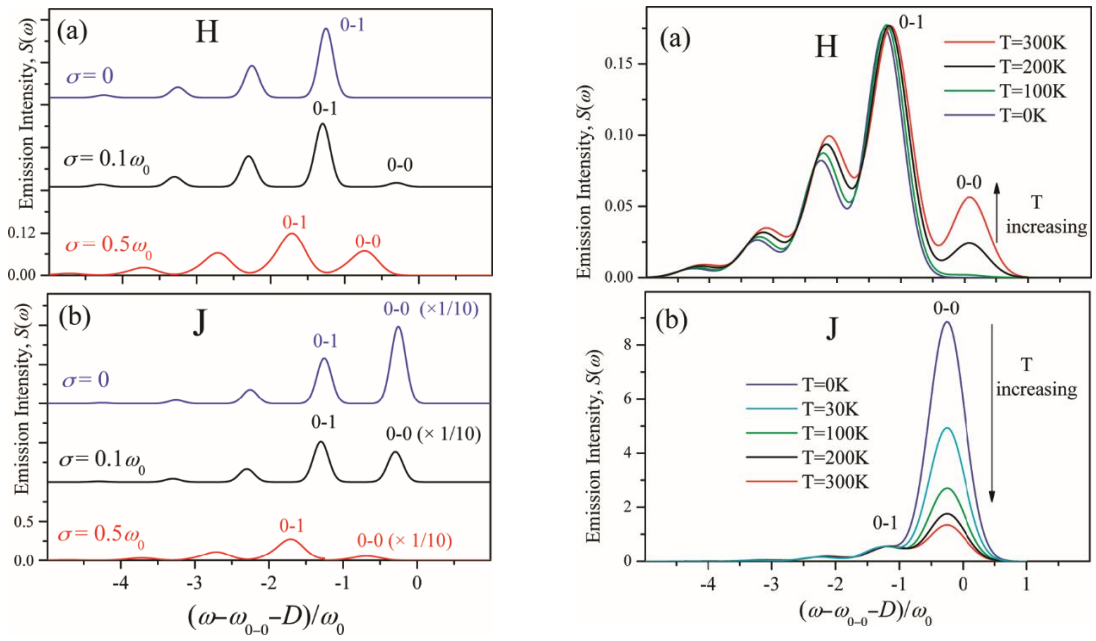

Figure 7: Simulated effect of disorder (left column) and temperature (right column) on the PL spectra of H- (top) and J-Aggregates (bottom). From Ref 40

The same spectroscopic behaviours can be observed when considering thermal effects (Figure 7 right column). Here the $S_1 \rightarrow S_0$ 0-0 transition becomes allowed in H-aggregates as exciton states straight above the bottom of the exciton band can be populated by thermal activation. For J-aggregates the $S_1 \rightarrow S_0$ 0-0 transition intensity decreases when thermally activated $k \neq 0$ states return to vibrationally excited electronic ground states. So in overall, static disorder as well as thermal effects degrade the general specific spectroscopic signatures of H- and J-aggregates.

FC Analysis of weakly interacting conjugated polymers

In the case of weakly interacting H-aggregates such as P3HT, Spano and co-workers have developed a modified Franck-Condon-Analysis to fit the absorption spectra of aggregated P3HT.[38,42] On the basis of the model which accounts for a single emitter discussed in above (equations 3 - 4), an additional term is introduced so that the Frank-Condon-fit changes to

$$I_{Abs}(\hbar\omega) = n(\hbar\omega)\cdot\hbar\omega\sum_v \frac{S^v}{v!}\left(1-\frac{We^{-S}}{2\hbar\omega_i}\left(\sum_{n\neq v}\frac{s^n}{n!(n-v)}\right)\right)^2 \Gamma\cdot\delta(\hbar\omega-(\hbar\omega_0+v\hbar\omega_i)) \qquad (5)$$

With W being the exciton bandwidth, n the vibrational quantum number and the other parameters defined as in equations 3 - 4. From fitting this modified FC-progression to the low energy side of the measured absorption spectrum of P3HT, it is possible to extract the exciton bandwidth and thus the degree of intermolecular coupling.

As described in previous section, in the absence of disorder and thermal effects, the 0-0 transition is forbidden in the case of H-aggregates. However in real systems this selection rule is relaxed and a diminished 0-0 transition can usually be observed in PL spectra of aggregated P3HT.[41] Furthermore in the case of weakly interacting H-aggregates, the relative intensities of the transitions in the higher vibrational states of the S_0 stay mainly unaffected compared to the corresponding case for a single emitter of P3HT.[38] Therefore it is possible to fit the PL spectrum of aggregated P3HT, using a modified Frank-Condon Progression taking into account the decreased intensity of the 0-0 transition described by,

$$I_{PL}(\hbar\omega) = [n(\hbar\omega)\cdot\hbar\omega]^3\left[\alpha\Gamma(\hbar\omega-\hbar\omega_0)+\sum_{v=1}\frac{S^v e^{-S}}{v!}\cdot\Gamma\cdot\delta(\hbar\omega-(\hbar\omega_0-v\hbar\omega_i))\right] \qquad (6)$$

With α being a scaling factor. This modified FC progression was successfully applied first by Clark et al. to analyse emission spectra of films of P3HT.[43] In summary, the presented model / modified Franck-Condon progressions are a powerful tool to analyze emission and absorption spectra of conjugated organic materials in various conformational states including aggregated phases where the coupling between the constituents has to be taken into account.

2.3. Optical properties of hybrid lead halide perovskites

Brief introduction and developments of perovskite based optoelectronic devices within the last years

The term perovskites originally refers to the calcium titanium oxide $CaTiO_3$, discovered by Gustav Rose in 1840 and named after the Russian mineralogist Lev Perovski.[44] Nevertheless materials which in general show a ABX_3 crystal structure, are typically said to have a perovskite structure.[45] The A position corresponds to a cation, B to a metal and X to an anion (Figure 8). In an idealised arrangement the crystal structure then consists of a BX_6 octahedral network with A ions in the interstices.[46]

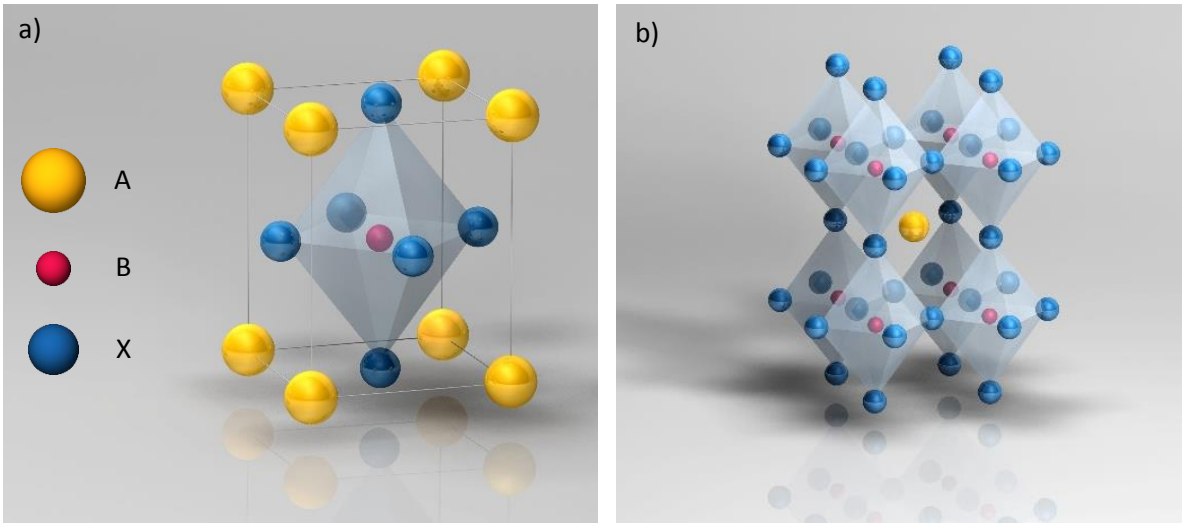

Figure 8: (a) Perovskite unit cell of the pseudocubic lattice showing the A cation in orange, the metal B cation in red, and the X anion in blue. (b) Representation of the perovskite lattice in terms of an anion corner-shared 3D network of $(BX_6)^{4-}$ octahedra, with B cations at their centers and A cations between them.

To form a perovskite, the different constituents have to satisfy the geometrical framework condition described by $t\sqrt{2}\,(r_B + r_X) = r_A + r_X$, where t is the so called tolerance factor with values between 0.8 and 1, while r_A, r_B, and r_X are the effective ionic radii for the A, B and X ions respectively.[45] As a consequence a high number of different perovskite materials with various compositions, structures and thus properties exist,[47,48] which have successfully been applied in a diversity of devices such as of transducers, modulators, capacitors and actuators.[49]

In 1978 hybrid organic-inorganic perovskites were characterised for the first time by Weber and co-workers.[50-52] This type of perovskite is classified by the chemical species of its constituents, where A is a monovalent organic cation (i.e. Methylammonium, Formamidinium or Octylammonium), B is a (semi-)metalic cation (i.e. Pb, Bi, Sn, Sb, Ge) and X is halide anion such as I, Br or Cl. Possible relevance as an active material in optoelectronic devices was shown by Mitzi and co-workers during the 1990's.[49,53-56] Starting with the first report of a perovskite based solar cell in 2009,[57] and following major breakthroughs in the fabrication and architecture in 2012,[58,59] the research field of hybrid organic-inorganic perovskites has gained incredible momentum until today. This is surely due to the rapid increase in power conversion efficiencies that have been demonstrated within the last few years, currently with a highest certified efficiency of 22.1%.[1] A further aspect that accounts for the enthusiasm on hybrid perovskites are the various additional fields of application which have developed within the last few years besides the main application in photovoltaics. Here since the year 2014 various works have demonstrated room temperature lasing from thin films, nanowires or nanocrystals of hybrid organic-inorganic perovskites which show low thresholds fluences and high quality factors.[60-71] Also the usage of hybrid perovskites in light emitting diodes has emerged within the last years,[72-81] where recently major improvements were made regarding their electroluminescence efficiency.[82] In that context, replacing the organic cation with the inorganic caesium has also proven to end up in an easy to process metal halide perovskite structure that shows promising photonic properties.[83,84]

In general, hybrid metal halide perovskites yield a high colour purity and are easy to synthesis from low cost abundant available materials. A further major point, making this class of materials highly attractive for light emitting applications, is the ability to easily tune the band gap and thus the optical properties by simple changes of the material composition.[85] It has been shown that the bandgap of the mixed perovskite $CH_3NH_3PbBr_xI_{3-x}$ can be tuned continuously between 1.5 eV up to 2.2 eV for increasing fraction X of the bromine halide.[86] When applying the same strategy to mixtures of bromide and chloride it is further possible to tune the bandgap within the higher spectral range up to more than 3.1 eV.[87,88] (see Figure 9 in the case of $CsPbX_3$, nanocrystals in solution). Recently tuning the optical bandgap was also achieved as a function of size of perovskite crystals on the nanoscale.[89,90] By employing perovskite crystals of different compositions and sizes into a host matrix it was even possible to achieve tuneable white

light emission.[89] Beside the use of hybrid perovskites in the field of photovoltaic and light emitting applications described above, further fields of applications have been explored recently. Hybrid halide perovskites were found to work as transistors,[56,91] and show applicability as memristors.[92-94]

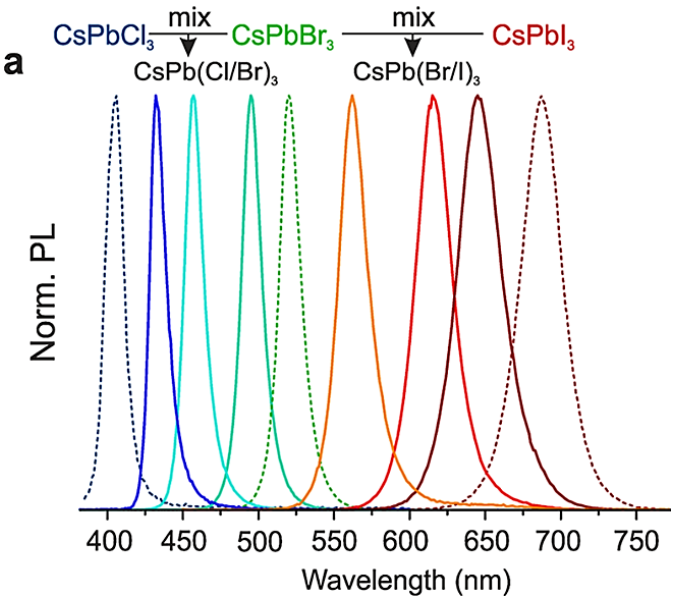

Figure 9: An overview of the PL spectra of samples obtained by mixing $CsPbBr_3$ NCs with either $CsPbCl_3$ or $CsPbI_3$ NCs in various ratios. From Reference [95]

Since perovskites also absorb in higher-energy spectral regions, a successful use as UV- and X-ray detectors could be shown as well,[96-102] which impressively demonstrate the wide field of possible applications for hybrid perovskites. Furthermore its high overall potential beyond the known applications is also demonstrated as they cover some intriguing physical effects that were discovered recently like photon recycling,[103] laser cooling,[104] or the existence of a hot phonon bottleneck.[105,106]

Beside all the fascination and excitement about this class of material, there are still some detrimental aspects, which still prevent its commercialisation. Until now, the perovskite active material which has shown best results in photovoltaics and thus is used in most research studies, contains lead as the metallic B cation. While it is classified as toxic,[107] the estimated amount of lead in case of a hypothetic commercialisation of perovskite photovoltaics fraction has been estimated as relatively low.[108] Nevertheless, its use in hybrid perovskite based devices is under heavy debate and thus efforts to find less toxic B cations alternatives are current topic. Here the successful use of less toxic metals or

semimetals like bismuth[109] or copper[110] in perovskite solar cells has been demonstrated, where tin-based perovskites have shown passable power conversion efficiencies of around 6%.[111-113]

A further drawback of hybrid perovskite based devices are their degradation and stability issues. Degradation can be induced by oxygen, light, moisture or temperature. Optimization of interfaces, materials, device architectures and the use of alternative hole-conductor materials in the case of solar cells have improved the stability within the last years, yet they are still limited to a non-commercial level.[114,115]

A further technical prerequisite for the commercialisation of perovskite based optoelectronic devices is the development of appropriate processing techniques which allow for precise control on film formation, film thickness and which are capable to upscaling. A variety of different methods were investigated in the last years. Most of them are based on the combination of two different compounds (typically from solutions) where at least one compound is a halide, leading to the formation of the perovskite crystals during (mostly) a drying process.[116] All methods reported so far have in common that the crystalline perovskite structure itself develops during film formation. As a result, material synthesis is interconnected with film processing. This implies that it is not possible to improve the quality of the perovskite without also modifying the film formation, and vice versa. Furthermore while most of the processing methods result in the formation of sub-µm thick perovskite layers, optimized for the use in photovoltaic applications, processing methods which deliver higher layer thickness, as would be desirable when used as X-ray detector, have not been presented so far.

As a final remark on the current state of the field it is worth mentioning that the main optoelectronic properties of the hybrid perovskites are due to the inorganic B and X components, so their character and general behaviours in principle are mainly that of inorganic semiconductors like GaAs or Si. Thus the application of established theories and models originally developed for inorganic semiconductors to the current field of hybrid perovskite appears reasonable. However many researchers which have just recently changed their focus of research toward hybrid perovskites are originally coming from different photovoltaic communities like organics, quantum dots or dye sensitized solar cells. Thus they are not necessarily familiar with the above mentioned theories and models of inorganic semiconductor, which might be a drawback for the field.

Origin of the optical properties of hybrid perovskites - Electronic structure

The optical properties of organic semiconductors are dominantly transitions between mostly the HOMO and LUMO levels of the chromophores, as described in section 2.2. The formation of bands is prevented by the relatively high degree of disorder in this class of materials. In contrast to this, due to its crystalline structure, hybrid perovskites clearly show a band structure, which was extensively investigated in the past by different theoretical approaches like density functional theory calculations,[15,117-122] or many-body perturbation theory.[123] Figure 10 shows an exemplary schematic illustration of the band structure of cubic $CH_3NH_3PbI_3$.

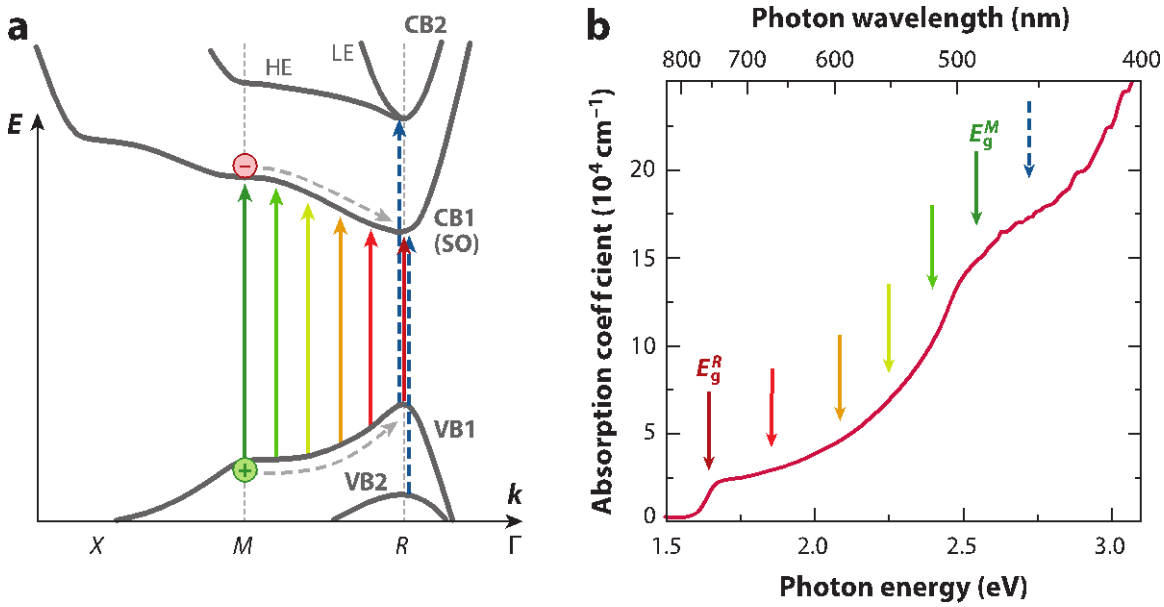

Figure 10: (a) Illustration of the electronic band structure of $CH_3NH_3PbI_3$. Coloured upward-pointing arrows represent allowed photoinduced electronic transitions. (b) Absorption spectrum showing that a continuum of electronic transitions between the R and M valleys leads to strong absorption across the visible range. Relaxation toward the R valley gives rise to a photoluminescence peak near 1.6 eV arising due to transitions from conduction band minimum to valence band maximum at the R point. From Reference [124]

It has been shown that the valence band consists mainly of iodine 5p-states with a small additional contribution from 6s-states of lead leading to a hybridisation between them, and that the conduction band is primary defined by the empty 6p-states of lead (compare Figure 11 of a projected DOS of tetragonal $CH_3NH_3PbI_3$).[119,121-123,125-128] This behaviour is similar to ionic materials, where typically the conduction band is predominantly defined by the electronic states of the cation and the valence band by the anion. From the density

of states of the different constituents of the $CH_3NH_3PbI_3$ in Figure 11 it also becomes clear, that the electronic contribution of the organic cation takes places several electron-volts below the valence band maximum.[15,123,127,129,130] From this, one can conclude that no electronic interaction takes place between the organic cation and the inorganic part of the hybrid perovskite. From this behaviour the actual role of the organic cation in hybrid perovskite can be uncovered and understood. Its main purpose can be seen in delivering a scaffold in which the inorganic framework forms corner sharing (PbI_2-) octahedral.

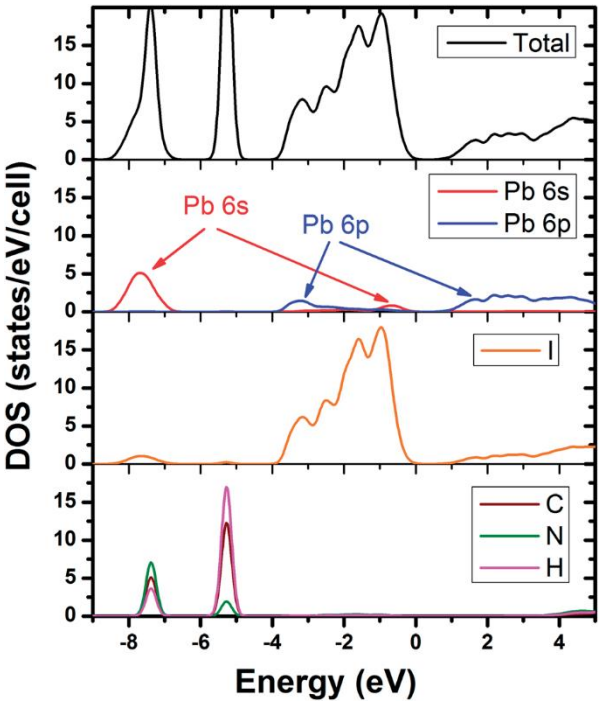

Figure 11: Projected density of states (DOS) of tetragonal $CH_3NH_3PbI_3$ showing elemental contributions to each band. From Ref [131]

In passing it should be mentioned that due to the presence of heavy lead and iodine, an elevated degree of spin-orbit-coupling was found in the hybrid perovskite, which impacts on the band structure, so that it lowers the band gap due to splitting of the conduction band.[117,122]

Optical transitions occur at the high symmetry R-point in the Brillouin Zone, where also the direct-bandgap nature becomes obvious as the minimum of the conduction band and the valence band maximum are at the same k-point. As a consequence absorption occurs without the need of any phonons which is reflected in the usually strong absorption onset observed at about 1.6 eV. From the band diagram it also becomes clear that the M

and R points are connected in the reciprocal space. This allows absorption in a wide wavelength range from which the continuous absorption above the band edge in the absorption spectra results.[15,118,119] After absorption into the conduction band, the photo-generated electrons then relax to the minimum of the conduction band at the R point, from which they decay back into the valence band under emission of a photon. Therefore the emission spectrum of an ideal hybrid perovskite consists of a single feature centred barely below the band edge.[132]

The description of the optical properties of hybrid perovskites are developed from the band structure properties so far. However, photo generated electrons and holes can be correlated due to their coulomb forces, so that they do not behave like two independent particles anymore. This behaviour results in their internal energy being lower than the bandgap energy E_g (Figure 12a).[18,133]

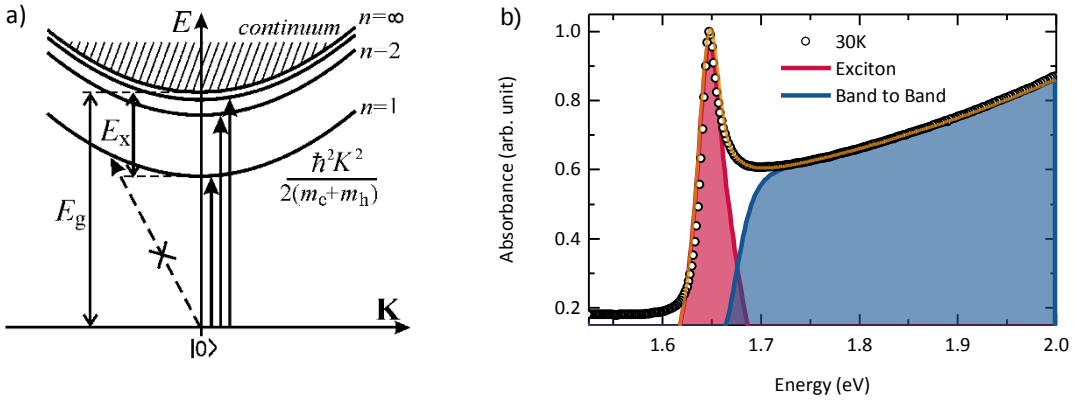

Figure 12: (a) Illustration of the exciton dispersion relations of a Wannier exciton in a direct semiconductor.[133] (b) Typical absorption spectra of $CH_3NH_3PbI_3$ at 30 K, which illustrates the contributions from excitons (red area) and band to band transitions (blue area) to the overall absorption spectrum. Here the measured spectrum was analysed by modelling the spectrum using Elliot's theory.[134]

Though reported values for exciton binding energies of hybrid perovskites can vary significantly,[124] they are generally in the range < 70 meV and are thus sufficiently low to allow a description of the corresponding excitons within the Wannier-Mott model. In the latter it is assumed that an electron in the conduction band can orbit around the hole, like an s-electron in a hydrogen atom.

The resulting energy levels of these bound states E_n are located below the band gap E_g and determined by a Rydberg like expression via:

$$E_n = E_g - \frac{\mu_{eff} e^4}{8h\varepsilon_r^2 \varepsilon_0^2} \frac{1}{n^2} \quad (7)$$

Where μ_{eff} is the effective reduced mass of the electron-hole system, ε_r the dielectric constant and n is a quantum number. While this Rydberg series of distinct exciton absorption peaks could be well resolved for highly pure inorganic semiconductors at lowest temperatures like GaAs,[135] or Cu_2O,[136] only one exciton absorption feature is observed in hybrid perovskites as shown in Figure 12 for the case of $CH_3NH_3PbI_3$. The increased linewidth of the exciton features is assumed to be due to disorder.

Temperature dependent morphological states of hybrid perovskites

It is well known that perovskites in general are prone to undergo structural changes of their unit cell as a function of temperature. Especially different degrees of tilting of the $(BX_6)^{4-}$ octahedral (see Figure 13 left column) leads to different crystal structures like cubic, tetragonal or orthorhombic.[47] Such a behaviour could also be observed for hybrid perovskites.[15,50,137] Moreover these structural phase transition can also impact on the band gap of the material and thus lead to a change in their corresponding optical properties.[138,139] For example, the architectural hybrid perovskite $CH_3NH_3PbI_3$ is known to be in a cubic phase for temperatures above 330 K,[140] adopts a tetragonal crystal structure within the temperature range of 330 – 160 K and is in an orthorhombic phase below 160 K.[15] While only subtle changes of the optical band gap at the cubic – tetragonal transition are observed,[141] a significant change in the optoelectronic properties of the perovskite takes place at the tetragonal - orthorhombic phase transition. During that phase transition the optical band gap increases by about 80 meV, and this is directly reflected in the absorption and emission spectra as reported by several groups in the past.[62,141-147]

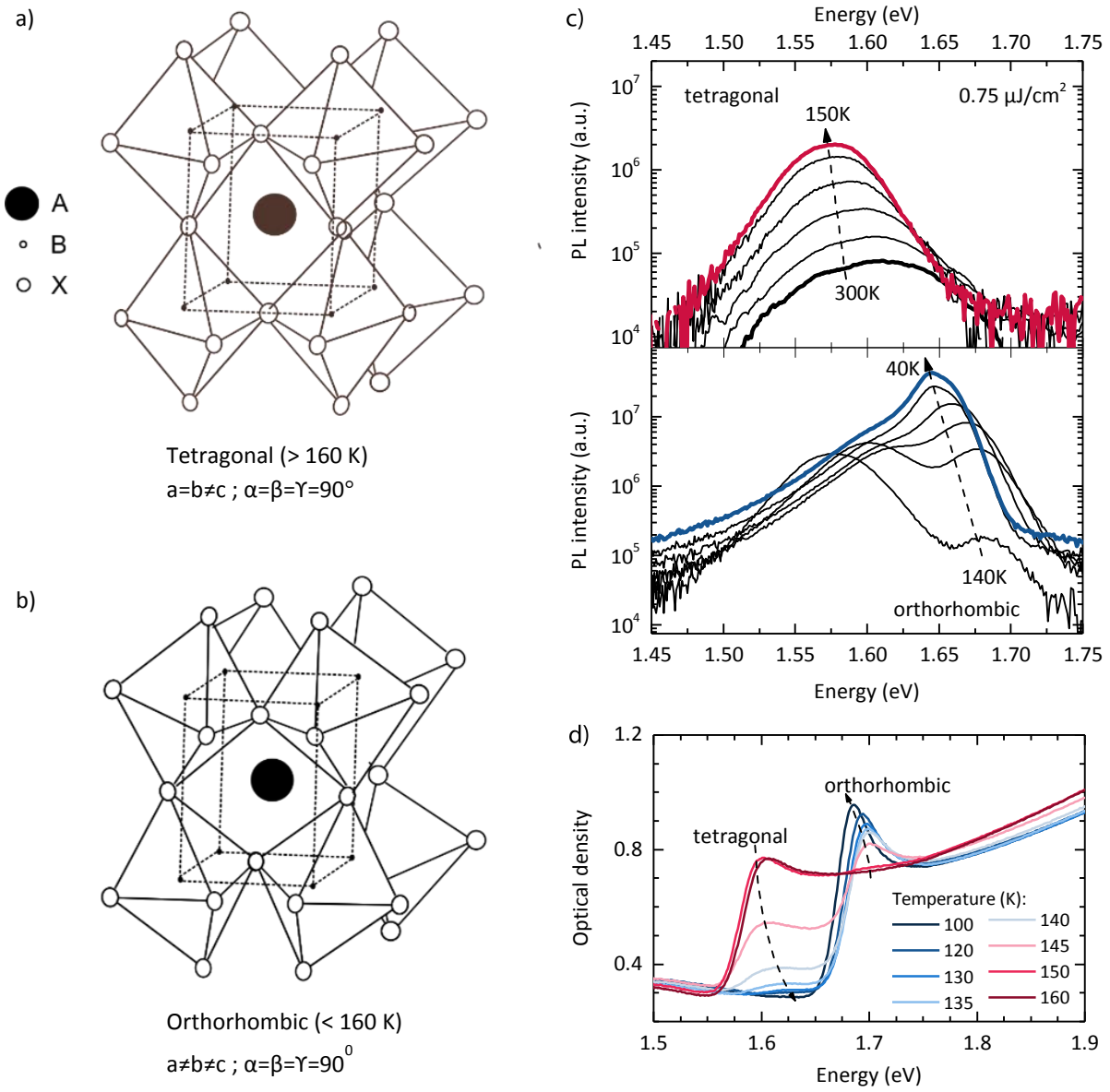

Figure 13: Crystal structures of the tetragonal (a) and orthorhombic (b) phase of $CH_3NH_3PbI_3$. Photoluminescence (c) and absorption (d) spectra of $CH_3NH_3PbI_3$ at different temperatures, from which the impact of structural phase change from tetragonal to orthorhombic crystal structure below 160 K on the optical properties can be seen (Absorption data from Tobias Meier).

This behaviour is illustrated in Figure 13 where absorption and emission spectra of $CH_3NH_3PbI_3$ for different temperatures between 300 K and 5 K are shown. While the detailed analysis of the temperature effects on the optical spectra of hybrid perovskites is focus of Chapter 4.7 and 4.8, the general ability of optical spectroscopy to investigate structural dynamics also for this class of material already becomes clear.

2.4 References

(1) NREL Solar efficiency chart. http://www.nrel.gov/ncpv/images/efficiency_chart.jpg (accessed 20 March 2016).

(2) Paquin, F.; Latini, G.; Sakowicz, M.; Karsenti, P.-L.; Wang, L.; Beljonne, D.; Stingelin, N.; Silva, C. Charge Separation in Semicrystalline Polymeric Semiconductors by Photoexcitation: Is the Mechanism Intrinsic or Extrinsic? *Physical Review Letters* **2011**, *106*, 197401.

(3) Pingel, P.; Zen, A.; Abellón, R. D.; Grozema, F. C.; Siebbeles, L. D. A.; Neher, D. Temperature-Resolved Local and Macroscopic Charge Carrier Transport in Thin P3HT Layers. *Advanced Functional Materials* **2010**, *20*, 2286.

(4) Scharsich, C.; Lohwasser, R. H.; Sommer, M.; Asawapirom, U.; Scherf, U.; Thelakkat, M.; Neher, D.; Köhler, A. Control of aggregate formation in poly(3-hexylthiophene) by solvent, molecular weight, and synthetic method. *Journal of Polymer Science Part B: Polymer Physics* **2012**, *50*, 442.

(5) Schubert, M.; Dolfen, D.; Frisch, J.; Roland, S.; Steyrleuthner, R.; Stiller, B.; Chen, Z.; Scherf, U.; Koch, N.; Facchetti, A.; Neher, D. Influence of Aggregation on the Performance of All-Polymer Solar Cells Containing Low-Bandgap Naphthalenediimide Copolymers. *Advanced Energy Materials* **2012**, *2*, 369.

(6) Duong, D. T.; Ho, V.; Shang, Z.; Mollinger, S.; Mannsfeld, S. C. B.; Dacuña, J.; Toney, M. F.; Segalman, R.; Salleo, A. Mechanism of Crystallization and Implications for Charge Transport in Poly(3-ethylhexylthiophene) Thin Films. *Advanced Functional Materials* **2014**, *24*, 4515.

(7) Kline, R. J.; McGehee, M. D.; Kadnikova, E. N.; Liu, J.; Fréchet, J. M. J. Controlling the Field-Effect Mobility of Regioregular Polythiophene by Changing the Molecular Weight. *Advanced Materials* **2003**, *15*, 1519.

(8) Noriega, R.; Rivnay, J.; Vandewal, K.; Koch, F. P. V.; Stingelin, N.; Smith, P.; Toney, M. F.; Salleo, A. A general relationship between disorder, aggregation and charge transport in conjugated polymers. *Nature Materials* **2013**, *12*, 1038.

(9) Ludwigs, S.: *P3HT Revisited – From Molecular Scale to Solar Cell Devices*; Springer Berlin Heidelberg, 2014.

(10) Lim, K. C.; Fincher, C. R.; Heeger, A. J. Rod-to-Coil Transition of a Conjugated Polymer in Solution. *Physical Review Letters* **1983**, *50*, 1934.

(11) Astakhova, T. Y.; Likhachev, V. N.; Vinogradov, G. A. Conformational rod-to-coil transition and solvatochromism of PDA solution. *Chemical Physics Letters* **1991**, *184*, 81.

(12) Lim, K. C.; Heeger, A. J. Spectroscopic and light scattering studies of the conformational (rod-to-coil) transition of poly(diacetylene) in solution. *The Journal of Chemical Physics* **1985**, *82*, 522.

(13) Köhler, A.; Hoffmann, S. T.; Bässler, H. An Order–Disorder Transition in the Conjugated Polymer MEH-PPV. *Journal of the American Chemical Society* **2012**, *134*, 11594.

(14) Knaapila, M.; Monkman, A. P. Methods for Controlling Structure and Photophysical Properties in Polyfluorene Solutions and Gels. *Advanced Materials* **2013**, *25*, 1090.

(15) Baikie, T.; Fang, Y.; Kadro, J. M.; Schreyer, M.; Wei, F.; Mhaisalkar, S. G.; Graetzel, M.; White, T. J. Synthesis and crystal chemistry of the hybrid perovskite $(CH_3NH_3)PbI_3$ for solid-state sensitised solar cell applications. *Journal of Materials Chemistry A* **2013**, *1*, 5628.

(16) Saba, M.; Quochi, F.; Mura, A.; Bongiovanni, G. Excited State Properties of Hybrid Perovskites. *Accounts of Chemical Research* **2016**, *49*, 166.

(17) D'Innocenzo, V.; Srimath Kandada, A. R.; De Bastiani, M.; Gandini, M.; Petrozza, A. Tuning the light emission properties by band gap engineering in hybrid lead halide perovskite. *Journal of the American Chemical Society* **2014**, *136*, 17730.

(18) Köhler, A.; Bässler, H.: Charges and Excited States in Organic Semiconductors. In *Electronic Processes in Organic Semiconductors*; Wiley-VCH Verlag GmbH & Co. KGaA, 2015; pp 87-191.

(19) Turro, N. J.: *Modern Molecular Photochemistry*; University Science Books, 1991.

(20) Ho, P. K. H.; Kim, J.-S.; Tessler, N.; Friend, R. H. Photoluminescence of poly(p-phenylenevinylene)–silica nanocomposites: Evidence for dual emission by Franck–Condon analysis. *The Journal of Chemical Physics* **2001**, *115*, 2709.

(21) Strickler, S. J.; Berg, R. A. Relationship between Absorption Intensity and Fluorescence Lifetime of Molecules. *The Journal of Chemical Physics* **1962**, *37*, 814.

(22) Köhler, A.; Bässler, H.: The Electronic Structure of Organic Semiconductors. In *Electronic Processes in Organic Semiconductors*; Wiley-VCH Verlag GmbH & Co. KGaA, 2015; pp 1-86.

(23) Khan, A. L. T.; Sreearunothai, P.; Herz, L. M.; Banach, M. J.; Köhler, A. Morphology-dependent energy transfer within polyfluorene thin films. *Physical Review B* **2004**, *69*, 085201.

(24) Khan, A. L. T.; Banach, M. J.; Köhler, A. Control of β-phase formation in polyfluorene thin films via Franck–Condon analysis. *Synthetic Metals* **2003**, *139*, 905.

(25) Saidani, M. A.; Benfredj, A.; Hamed, Z. B.; Romdhane, S.; Ulbricht, C.; Egbe, D. A. M.; Bouchriha, H. Franck-Condon analysis of the photoluminescence spectra of a triple-bond containing polymer as a solution and as a thin film. *Synthetic Metals* **2013**, *184*, 83.

(26) Hoffmann, S. T.; Scheler, E.; Koenen, J.-M.; Forster, M.; Scherf, U.; Strohriegl, P.; Bässler, H.; Köhler, A. Triplet energy transfer in conjugated polymers. III. An experimental assessment regarding the influence of disorder on polaronic transport. *Physical Review B* **2010**, *81*, 165208.

(27) Reish, M. E.; Huff, G. S.; Lee, W.; Uddin, M. A.; Barker, A. J.; Gallaher, J. K.; Hodgkiss, J. M.; Woo, H. Y.; Gordon, K. C. Thermochromism, Franck–Condon Analysis and Interfacial Dynamics of a Donor–Acceptor Copolymer with a Low Band Gap. *Chemistry of Materials* **2015**, *27*, 2770.

(28) Kanemoto, K.; Sudo, T.; Akai, I.; Hashimoto, H.; Karasawa, T.; Aso, Y.; Otsubo, T. Intrachain photoluminescence properties of conjugated polymers as revealed by long oligothiophenes and polythiophenes diluted in an inactive solid matrix. *Physical Review B* **2006**, *73*, 235203.

(29) Hoffmann, S. T.; Bässler, H.; Köhler, A. What Determines Inhomogeneous Broadening of Electronic Transitions in Conjugated Polymers? *The Journal of Physical Chemistry B* **2010**, *114*, 17037.

(30) Bencheikh, F.; Duché, D.; Ruiz, C. M.; Simon, J.-J.; Escoubas, L. Study of Optical Properties and Molecular Aggregation of Conjugated Low Band Gap Copolymers: PTB7 and PTB7-Th. *The Journal of Physical Chemistry C* **2015**, *119*, 24643.

(31) Cossiello, R. F.; Susman, M. D.; Aramendía, P. F.; Atvars, T. D. Z. Study of solvent-conjugated polymer interactions by polarized spectroscopy: MEH–PPV and Poly(9,9′-dioctylfluorene-2,7-diyl). *Journal of Luminescence* **2010**, *130*, 415.

(32) Kitts, C. C.; Vanden Bout, D. A. The effect of solvent quality on the chain morphology in solutions of poly(9,9′-dioctylfluorene). *Polymer* **2007**, *48*, 2322.

(33) Inganäs, O.; Salaneck, W. R.; Österholm, J. E.; Laakso, J. Thermochromic and solvatochromic effects in poly(3-hexylthiophene). *Synthetic Metals* **1988**, *22*, 395.

(34) Kasha, M. Energy Transfer Mechanisms and the Molecular Exciton Model for Molecular Aggregates. *Radiation Research* **1963**, *20*, 55.

(35) Kasha, M.; Rawls, H.; Ashraf El-Bayoumi, M. The exciton model in molecular spectroscopy. *Pure and Applied Chemistry* **1965**, *11*, 371.

(36) Jelley, E. E. Spectral Absorption and Fluorescence of Dyes in the Molecular State. *Nature* **1936**, *138*, 1009.

(37) Scheibe, G. Über die Veränderlichkeit der Absorptionsspektren in Lösungen und die Nebenvalenzen als ihre Ursache. *Angewandte Chemie* **1937**, *50*, 212.

(38) Spano, F. C. Modeling disorder in polymer aggregates: The optical spectroscopy of regioregular poly(3-hexylthiophene) thin films. *The Journal of Chemical Physics* **2005**, *122*, 234701.

(39) Yamagata, H.; Spano, F. C. Interplay between intrachain and interchain interactions in semiconducting polymer assemblies: The HJ-aggregate model. *The Journal of Chemical Physics* **2012**, *136*, 184901.

(40) Spano, F. C. The Spectral Signatures of Frenkel Polarons in H- and J-Aggregates. *Accounts of Chemical Research* **2010**, *43*, 429.

(41) Spano, F. C.; Silva, C. H- and J-Aggregate Behavior in Polymeric Semiconductors. *Annual Review of Physical Chemistry* **2014**, *65*, 477.

(42) Clark, J.; Chang, J.-F.; Spano, F. C.; Friend, R. H.; Silva, C. Determining exciton bandwidth and film microstructure in polythiophene films using linear absorption spectroscopy. *Applied Physics Letters* **2009**, *94*, 163306.

(43) Clark, J.; Silva, C.; Friend, R. H.; Spano, F. C. Role of Intermolecular Coupling in the Photophysics of Disordered Organic Semiconductors: Aggregate Emission in Regioregular Polythiophene. *Physical Review Letters* **2007**, *98*, 206406.

(44) Rose, G. Ueber einige neue Mineralien des Urals. *J. Prakt. Chem.* **1840**, *19*, 459.

(45) Goldschmidt, V. M. Die Gesetze der Krystallochemie. *Naturwissenschaften*, *14*, 477.

(46) Wells, A. F.: *Structural inorganic chemistry*; Oxford University Press, 2012.

(47) Glazer, A. The classification of tilted octahedra in perovskites. *Acta Crystallographica Section B* **1972**, *28*, 3384.

(48) Peńa, M. A.; Fierro, J. L. G. Chemical Structures and Performance of Perovskite Oxides. *Chemical Reviews* **2001**, *101*, 1981.

(49) Mitzi, D. B.: Synthesis, Structure, and Properties of Organic-Inorganic Perovskites and Related Materials. In *Progress in Inorganic Chemistry*; John Wiley & Sons, Inc., 2007; pp 1-121.

(50) Poglitsch, A.; Weber, D. Dynamic disorder in methylammonium-trihalogenoplumbates (II) observed by millimeter-wave spectroscopy. *The Journal of Chemical Physics* **1987**, *87*, 6373.

(51) Weber, D. $CH_3NH_3SnBr_xI_{3-x}$ (x = 0-3), a tin(II) system with a cubic perovskite structure. *Zeitschrift fuer Naturforschung* **1978**, *33b*, 862.

(52) Weber, D. $CH_3NH_3PbX_3$, a Pb(II)-System with Cubic Perovskite Structure. *Zeitschrift fuer Naturforschung* **1978**, *33b*, 1443.

(53) Mitzi, D. B.; Feild, C. A.; Harrison, W. T. A.; Guloy, A. M. Conducting Tin Halides with a Layered organic-based Perovskite Structure. *Nature* **1994**, *369*, 467.

(54) Mitzi, D. B.; Feild, C. A.; Schlesinger, Z.; Laibowitz, R. B. Transport, Optical, and Magnetic Properties of the Conducting Halide Perovskite $CH_3NH_3SnI_3$. *Journal of Solid State Chemistry* **1995**, *114*, 159.

(55) Mitzi, D. B.; Wang, S.; Feild, C. A.; Chess, C. A.; Guloy, A. M. CONDUCTING LAYERED ORGANIC-INORGANIC HALIDES CONTAINING (110)-ORIENTED PEROVSKITE SHEETS. *Science* **1995**, *267*, 1473.

(56) Kagan, C. R.; Mitzi, D. B.; Dimitrakopoulos, C. D. Organic-inorganic hybrid materials as semiconducting channels in thin-film field-effect transistors. *Science* **1999**, *286*, 945.

(57) Kojima, A.; Teshima, K.; Shirai, Y.; Miyasaka, T. Organometal Halide Perovskites as Visible-Light Sensitizers for Photovoltaic Cells. *Journal of the American Chemical Society* **2009**, *131*, 6050.

(58) Kim, H. S.; Lee, C. R.; Im, J. H.; Lee, K. B.; Moehl, T.; Marchioro, A.; Moon, S. J.; Humphry-Baker, R.; Yum, J. H.; Moser, J. E.; Gratzel, M.; Park, N. G. Lead iodide perovskite sensitized all-solid-state submicron thin film mesoscopic solar cell with efficiency exceeding 9%. *Scientific Reports* **2012**, *2*, 591.

(59) Lee, M. M.; Teuscher, J.; Miyasaka, T.; Murakami, T. N.; Snaith, H. J. Efficient Hybrid Solar Cells Based on Meso-Superstructured Organometal Halide Perovskites. *Science* **2012**, *338*, 643.

(60) Chen, S.; Roh, K.; Lee, J.; Chong, W. K.; Lu, Y.; Mathews, N.; Sum, T. C.; Nurmikko, A. A Photonic Crystal Laser from Solution Based Organo-Lead Iodide Perovskite Thin Films. *ACS Nano* **2016**, *10*, 3959.

(61) Deschler, F.; Price, M.; Pathak, S.; Klintberg, L. E.; Jarausch, D.-D.; Higler, R.; Hüttner, S.; Leijtens, T.; Stranks, S. D.; Snaith, H. J.; Atatüre, M.; Phillips, R. T.; Friend, R. H. High Photoluminescence Efficiency and Optically Pumped Lasing in Solution-Processed Mixed Halide Perovskite Semiconductors. *The Journal of Physical Chemistry Letters* **2014**, *5*, 1421.

(62) Xing, G.; Mathews, N.; Lim, S. S.; Yantara, N.; Liu, X.; Sabba, D.; Gratzel, M.; Mhaisalkar, S.; Sum, T. C. Low-temperature solution-processed wavelength-tunable perovskites for lasing. *Nature Materials* **2014**, *13*, 476.

(63) Zhang, Q.; Ha, S. T.; Liu, X.; Sum, T. C.; Xiong, Q. Room-Temperature Near-Infrared High-Q Perovskite Whispering-Gallery Planar Nanolasers. *Nano Letters* **2014**, *14*, 5995.

(64) Fu, Y.; Zhu, H.; Schrader, A. W.; Liang, D.; Ding, Q.; Joshi, P.; Hwang, L.; Zhu, X. Y.; Jin, S. Nanowire Lasers of Formamidinium Lead Halide Perovskites and Their Stabilized Alloys with Improved Stability. *Nano Letters* **2016**, *16*, 1000.

(65) Liao, Q.; Hu, K.; Zhang, H.; Wang, X.; Yao, J.; Fu, H. Perovskite Microdisk Microlasers Self-Assembled from Solution. *Advanced Materials* **2015**, *27*, 3405.

(66) Zhu, H.; Fu, Y.; Meng, F.; Wu, X.; Gong, Z.; Ding, Q.; Gustafsson, M. V.; Trinh, M. T.; Jin, S.; Zhu, X. Y. Lead halide perovskite nanowire lasers with low lasing thresholds and high quality factors. *Nature Materials* **2015**, *14*, 636.

(67) Xing, J.; Liu, X. F.; Zhang, Q.; Ha, S. T.; Yuan, Y. W.; Shen, C.; Sum, T. C.; Xiong, Q. Vapor Phase Synthesis of Organometal Halide Perovskite Nanowires for Tunable Room-Temperature Nanolasers. *Nano Letters* **2015**, *15*, 4571.

(68) Dhanker, R.; Brigeman, A. N.; Larsen, A. V.; Stewart, R. J.; Asbury, J. B.; Giebink, N. C. Random lasing in organo-lead halide perovskite microcrystal networks. *Applied Physics Letters* **2014**, *105*, 151112.

(69) Sutherland, B. R.; Hoogland, S.; Adachi, M. M.; Wong, C. T.; Sargent, E. H. Conformal organohalide perovskites enable lasing on spherical resonators. *ACS Nano* **2014**, *8*, 10947.

(70) Stranks, S. D.; Wood, S. M.; Wojciechowski, K.; Deschler, F.; Saliba, M.; Khandelwal, H.; Patel, J. B.; Elston, S. J.; Herz, L. M.; Johnston, M. B.; Schenning, A. P.; Debije, M. G.; Riede, M. K.; Morris, S. M.; Snaith, H. J. Enhanced Amplified Spontaneous

Emission in Perovskites Using a Flexible Cholesteric Liquid Crystal Reflector. *Nano Letters* **2015**, *15*, 4935.

(71) Saliba, M.; Wood, S. M.; Patel, J. B.; Nayak, P. K.; Huang, J.; Alexander-Webber, J. A.; Wenger, B.; Stranks, S. D.; Horantner, M. T.; Wang, J. T.; Nicholas, R. J.; Herz, L. M.; Johnston, M. B.; Morris, S. M.; Snaith, H. J.; Riede, M. K. Structured Organic-Inorganic Perovskite toward a Distributed Feedback Laser. *Advanced Materials* **2016**, *28*, 923.

(72) Tan, Z.-K.; Moghaddam, R. S.; Lai, M. L.; Docampo, P.; Higler, R.; Deschler, F.; Price, M.; Sadhanala, A.; Pazos, L. M.; Credgington, D.; Hanusch, F.; Bein, T.; Snaith, H. J.; Friend, R. H. Bright light-emitting diodes based on organometal halide perovskite. *Nature Nanotechnology* **2014**, *9*, 687.

(73) Kim, Y. H.; Cho, H.; Heo, J. H.; Kim, T. S.; Myoung, N.; Lee, C. L.; Im, S. H.; Lee, T. W. Multicolored organic/inorganic hybrid perovskite light-emitting diodes. *Advanced Materials* **2015**, *27*, 1248.

(74) Hoye, R. L.; Chua, M. R.; Musselman, K. P.; Li, G.; Lai, M. L.; Tan, Z. K.; Greenham, N. C.; MacManus-Driscoll, J. L.; Friend, R. H.; Credgington, D. Enhanced performance in fluorene-free organometal halide perovskite light-emitting diodes using tunable, low electron affinity oxide electron injectors. *Advanced Materials* **2015**, *27*, 1414.

(75) Kumawat, N. K.; Dey, A.; Narasimhan, K. L.; Kabra, D. Near Infrared to Visible Electroluminescent Diodes Based on Organometallic Halide Perovskites: Structural and Optical Investigation. *ACS Photonics* **2015**, *2*, 349.

(76) Li, G.; Rivarola, F. W.; Davis, N. J.; Bai, S.; Jellicoe, T. C.; de la Pena, F.; Hou, S.; Ducati, C.; Gao, F.; Friend, R. H.; Greenham, N. C.; Tan, Z. K. Highly Efficient Perovskite Nanocrystal Light-Emitting Diodes Enabled by a Universal Crosslinking Method. *Advanced Materials* **2016**, *28*, 3528.

(77) Li, G.; Tan, Z. K.; Di, D.; Lai, M. L.; Jiang, L.; Lim, J. H.; Friend, R. H.; Greenham, N. C. Efficient light-emitting diodes based on nanocrystalline perovskite in a dielectric polymer matrix. *Nano Letters* **2015**, *15*, 2640.

(78) Wang, J.; Wang, N.; Jin, Y.; Si, J.; Tan, Z. K.; Du, H.; Cheng, L.; Dai, X.; Bai, S.; He, H.; Ye, Z.; Lai, M. L.; Friend, R. H.; Huang, W. Interfacial control toward efficient and low-voltage perovskite light-emitting diodes. *Advanced Materials* **2015**, *27*, 2311.

(79) Bade, S. G.; Li, J.; Shan, X.; Ling, Y.; Tian, Y.; Dilbeck, T.; Besara, T.; Geske, T.; Gao, H.; Ma, B.; Hanson, K.; Siegrist, T.; Xu, C.; Yu, Z. Fully Printed Halide Perovskite Light-Emitting Diodes with Silver Nanowire Electrodes. *ACS Nano* **2016**, *10*, 1795.

(80) Gil-Escrig, L.; Miquel-Sempere, A.; Sessolo, M.; Bolink, H. J. Mixed Iodide-Bromide Methylammonium Lead Perovskite-based Diodes for Light Emission and Photovoltaics. *The Journal of Physical Chemistry Letters* **2015**, *6*, 3743.

(81) Qin, X.; Dong, H.; Hu, W. Green light-emitting diode from bromine based organic-inorganic halide perovskite. *Science China Materials* **2015**, *58*, 186.

(82) Cho, H.; Jeong, S. H.; Park, M. H.; Kim, Y. H.; Wolf, C.; Lee, C. L.; Heo, J. H.; Sadhanala, A.; Myoung, N.; Yoo, S.; Im, S. H.; Friend, R. H.; Lee, T. W. Overcoming the electroluminescence efficiency limitations of perovskite light-emitting diodes. *Science* **2015**, *350*, 1222.

(83) Xu, Y.; Chen, Q.; Zhang, C.; Wang, R.; Wu, H.; Zhang, X.; Xing, G.; Yu, W. W.; Wang, X.; Zhang, Y.; Xiao, M. Two-Photon-Pumped Perovskite Semiconductor Nanocrystal Lasers. *Journal of the American Chemical Society* **2016**, *138*, 3761.

(84) Zhang, X.; Lin, H.; Huang, H.; Reckmeier, C.; Zhang, Y.; Choy, W. C.; Rogach, A. L. Enhancing the Brightness of Cesium Lead Halide Perovskite Nanocrystal Based Green Light-Emitting Devices through the Interface Engineering with Perfluorinated Ionomer. *Nano Letters* **2016**, *16*, 1415.

(85) Saparov, B.; Mitzi, D. B. Organic-Inorganic Perovskites: Structural Versatility for Functional Materials Design. *Chemical Reviews* **2016**, *116*, 4558.

(86) Noh, J. H.; Im, S. H.; Heo, J. H.; Mandal, T. N.; Seok, S. I. Chemical Management for Colorful, Efficient, and Stable Inorganic–Organic Hybrid Nanostructured Solar Cells. *Nano Letters* **2013**, *13*, 1764.

(87) Kumawat, N. K.; Dey, A.; Kumar, A.; Gopinathan, S. P.; Narasimhan, K. L.; Kabra, D. Band Gap Tuning of $CH_3NH_3Pb(Br_{1-x}Cl_x)_3$ Hybrid Perovskite for Blue Electroluminescence. *ACS Applied Materials & Interfaces* **2015**, *7*, 13119.

(88) Comin, R.; Walters, G.; Thibau, E. S.; Voznyy, O.; Lu, Z.-H.; Sargent, E. H. Structural, optical, and electronic studies of wide-bandgap lead halide perovskites. *Journal of Materials Chemistry C* **2015**, *3*, 8839.

(89) Pathak, S.; Sakai, N.; Wisnivesky Rocca Rivarola, F.; Stranks, S. D.; Liu, J.; Eperon, G. E.; Ducati, C.; Wojciechowski, K.; Griffiths, J. T.; Haghighirad, A. A.; Pellaroque, A.; Friend, R. H.; Snaith, H. J. Perovskite Crystals for Tunable White Light Emission. *Chemistry of Materials* **2015**, *27*, 8066.

(90) Sichert, J. A.; Tong, Y.; Mutz, N.; Vollmer, M.; Fischer, S.; Milowska, K. Z.; Garcia Cortadella, R.; Nickel, B.; Cardenas-Daw, C.; Stolarczyk, J. K.; Urban, A. S.; Feldmann, J. Quantum Size Effect in Organometal Halide Perovskite Nanoplatelets. *Nano Letters* **2015**, *15*, 6521.

(91) Chin, X. Y.; Cortecchia, D.; Yin, J.; Bruno, A.; Soci, C. Lead iodide perovskite light-emitting field-effect transistor. *Nature Communications* **2015**, *6*, 7383.

(92) Yan, K.; Peng, M.; Yu, X.; Cai, X.; Chen, S.; Hu, H.; Chen, B.; Gao, X.; Dong, B.; Zou, D. High-performance perovskite memristor based on methyl ammonium lead halides. *Journal of Materials Chemistry C* **2016**, *4*, 1375.

(93) Yoo, E. J.; Lyu, M.; Yun, J. H.; Kang, C. J.; Choi, Y. J.; Wang, L. Resistive Switching Behavior in Organic-Inorganic Hybrid $CH_3NH_3PbI_{3-x}Cl_x$ Perovskite for Resistive Random Access Memory Devices. *Advanced Materials* **2015**, *27*, 6170.

(94) Gu, C.; Lee, J. S. Flexible Hybrid Organic-Inorganic Perovskite Memory. *ACS Nano* **2016**, *10*, 5413.

(95) Nedelcu, G.; Protesescu, L.; Yakunin, S.; Bodnarchuk, M. I.; Grotevent, M. J.; Kovalenko, M. V. Fast Anion-Exchange in Highly Luminescent Nanocrystals of Cesium Lead Halide Perovskites ($CsPbX_3$, X = Cl, Br, I). *Nano Letters* **2015**, *15*, 5635.

(96) Domanski, K.; Tress, W.; Moehl, T.; Saliba, M.; Nazeeruddin, M. K.; Grätzel, M. Working Principles of Perovskite Photodetectors: Analyzing the Interplay Between Photoconductivity and Voltage-Driven Energy-Level Alignment. *Advanced Functional Materials* **2015**, *25*, 6936.

(97) Maculan, G.; Sheikh, A. D.; Abdelhady, A. L.; Saidaminov, M. I.; Haque, M. A.; Murali, B.; Alarousu, E.; Mohammed, O. F.; Wu, T.; Bakr, O. M. $CH_3NH_3PbCl_3$ Single Crystals: Inverse Temperature Crystallization and Visible-Blind UV-Photodetector. *The Journal of Physical Chemistry Letters* **2015**, *6*, 3781.

(98) Náfrádi, B.; Náfrádi, G.; Forró, L.; Horváth, E. Methylammonium Lead Iodide for Efficient X-ray Energy Conversion. *The Journal of Physical Chemistry C* **2015**, *119*, 25204.

(99) Ramasamy, P.; Lim, D. H.; Kim, B.; Lee, S. H.; Lee, M. S.; Lee, J. S. All-inorganic cesium lead halide perovskite nanocrystals for photodetector applications. *Chem Commun (Camb)* **2016**, *52*, 2067.

(100) Wang, F.; Mei, J.; Wang, Y.; Zhang, L.; Zhao, H.; Zhao, D. Fast Photoconductive Responses in Organometal Halide Perovskite Photodetectors. *ACS Applied Materials & Interfaces* **2016**, *8*, 2840.

(101) Wei, H.; Fang, Y.; Mulligan, P.; Chuirazzi, W.; Fang, H.-H.; Wang, C.; Ecker, B. R.; Gao, Y.; Loi, M. A.; Cao, L.; Huang, J. Sensitive X-ray detectors made of methylammonium lead tribromide perovskite single crystals. *Nature Photonics* **2016**, *10*, 333.

(102) Yakunin, S.; Sytnyk, M.; Kriegner, D.; Shrestha, S.; Richter, M.; Matt, G. J.; Azimi, H.; Brabec, C. J.; Stangl, J.; Kovalenko, M. V.; Heiss, W. Detection of X-ray photons by solution-processed lead halide perovskites. *Nature Photonics* **2015**, *9*, 444.

(103) Pazos-Outon, L. M.; Szumilo, M.; Lamboll, R.; Richter, J. M.; Crespo-Quesada, M.; Abdi-Jalebi, M.; Beeson, H. J.; Vrucinic, M.; Alsari, M.; Snaith, H. J.; Ehrler, B.; Friend, R. H.; Deschler, F. Photon recycling in lead iodide perovskite solar cells. *Science* **2016**, *351*, 1430.

(104) Ha, S.-T.; Shen, C.; Zhang, J.; Xiong, Q. Laser cooling of organic–inorganic lead halide perovskites. *Nature Photonics* **2015**, *10*, 115.

(105) Price, M. B.; Butkus, J.; Jellicoe, T. C.; Sadhanala, A.; Briane, A.; Halpert, J. E.; Broch, K.; Hodgkiss, J. M.; Friend, R. H.; Deschler, F. Hot-carrier cooling and photoinduced refractive index changes in organic-inorganic lead halide perovskites. *Nature Communications* **2015**, *6*, 8420.

(106) Yang, Y.; Ostrowski, D. P.; France, R. M.; Zhu, K.; van de Lagemaat, J.; Luther, J. M.; Beard, M. C. Observation of a hot-phonon bottleneck in lead-iodide perovskites. *Nature Photonics* **2015**, *10*, 53.

(107) Needleman, H. Lead Poisoning. *Annual Review of Medicine* **2004**, *55*, 209.

(108) Fabini, D. Quantifying the Potential for Lead Pollution from Halide Perovskite Photovoltaics. *The Journal of Physical Chemistry Letters* **2015**, *6*, 3546.

(109) Park, B. W.; Philippe, B.; Zhang, X.; Rensmo, H.; Boschloo, G.; Johansson, E. M. Bismuth Based Hybrid Perovskites $A_3Bi_2I_9$ (A: Methylammonium or Cesium) for Solar Cell Application. *Advanced Materials* **2015**, *27*, 6806.

(110) Cortecchia, D.; Dewi, H. A.; Yin, J.; Bruno, A.; Chen, S.; Baikie, T.; Boix, P. P.; Grätzel, M.; Mhaisalkar, S.; Soci, C.; Mathews, N. Lead-Free $MA_2CuCl_xBr_{4-x}$ Hybrid Perovskites. *Inorganic Chemistry* **2016**, *55*, 1044.

(111) Lee, S. J.; Shin, S. S.; Kim, Y. C.; Kim, D.; Ahn, T. K.; Noh, J. H.; Seo, J.; Seok, S. I. Fabrication of Efficient Formamidinium Tin Iodide Perovskite Solar Cells through SnF_2-Pyrazine Complex. *Journal of the American Chemical Society* **2016**, *138*, 3974.

(112) Hao, F.; Stoumpos, C. C.; Cao, D. H.; Chang, R. P. H.; Kanatzidis, M. G. Lead-free solid-state organic-inorganic halide perovskite solar cells. *Nature Photonics* **2014**, *8*, 489.

(113) Noel, N. K.; Stranks, S. D.; Abate, A.; Wehrenfennig, C.; Guarnera, S.; Haghighirad, A.-A.; Sadhanala, A.; Eperon, G. E.; Pathak, S. K.; Johnston, M. B.; Petrozza, A.; Herz, L. M.; Snaith, H. J. Lead-free organic-inorganic tin halide perovskites for photovoltaic applications. *Energy & Environmental Science.* **2014**, *7*, 3061.

(114) Berhe, T. A.; Su, W.-N.; Chen, C.-H.; Pan, C.-J.; Cheng, J.-H.; Chen, H.-M.; Tsai, M.-C.; Chen, L.-Y.; Dubale, A. A.; Hwang, B.-J. Organometal halide perovskite solar cells: degradation and stability. *Energy & Environmental Science.* **2016**, *9*, 323.

(115) Gujar, T. P.; Thelakkat, M. Highly Reproducible and Efficient Perovskite Solar Cells with Extraordinary Stability from Robust $CH_3NH_3PbI_3$: Towards Large-Area Devices. *Energy Technology* **2016**, *4*, 449.

(116) Stranks, S. D.; Nayak, P. K.; Zhang, W.; Stergiopoulos, T.; Snaith, H. J. Formation of thin films of organic-inorganic perovskites for high-efficiency solar cells. *Angewandte Chemie International Edition* **2015**, *54*, 3240.

(117) Even, J.; Pedesseau, L.; Katan, C.; Kepenekian, M.; Lauret, J.-S.; Sapori, D.; Deleporte, E. Solid-State Physics Perspective on Hybrid Perovskite Semiconductors. *The Journal of Physical Chemistry C* **2015**, *119*, 10161.

(118) Even, J.; Pedesseau, L.; Katan, C. Analysis of Multivalley and Multibandgap Absorption and Enhancement of Free Carriers Related to Exciton Screening in Hybrid Perovskites. *The Journal of Physical Chemistry C* **2014**, *118*, 11566.

(119) Mosconi, E.; Amat, A.; Nazeeruddin, M. K.; Grätzel, M.; De Angelis, F. First-Principles Modeling of Mixed Halide Organometal Perovskites for Photovoltaic Applications. *The Journal of Physical Chemistry C* **2013**, *117*, 13902.

(120) Tanaka, K.; Takahashi, T.; Ban, T.; Kondo, T.; Uchida, K.; Miura, N. Comparative study on the excitons in lead-halide-based perovskite-type crystals $CH_3NH_3PbBr_3$ $CH_3NH_3PbI_3$. *Solid State Communications* **2003**, *127*, 619.

(121) Brivio, F.; Walker, A. B.; Walsh, A. Structural and electronic properties of hybrid perovskites for high-efficiency thin-film photovoltaics from first-principles. *APL Materials* **2013**, *1*, 042111.

(122) Even, J.; Pedesseau, L.; Jancu, J.-M.; Katan, C. Importance of Spin–Orbit Coupling in Hybrid Organic/Inorganic Perovskites for Photovoltaic Applications. *The Journal of Physical Chemistry Letters* **2013**, *4*, 2999.

(123) Brivio, F.; Butler, K. T.; Walsh, A.; van Schilfgaarde, M. Relativistic quasiparticle self-consistent electronic structure of hybrid halide perovskite photovoltaic absorbers. *Physical Review B* **2014**, *89*, 155204.

(124) Herz, L. M. Charge-Carrier Dynamics in Organic-Inorganic Metal Halide Perovskites. *Annual Review of Physical Chemistry* **2016**, *67*, 65.

(125) Zhu, X.; Su, H.; Marcus, R. A.; Michel-Beyerle, M. E. Computed and Experimental Absorption Spectra of the Perovskite $CH_3NH_3PbI_3$. *The Journal of Physical Chemistry Letters* **2014**, *5*, 3061.

(126) Lang, L.; Yang, J.-H.; Liu, H.-R.; Xiang, H. J.; Gong, X. G. First-principles study on the electronic and optical properties of cubic ABX_3 halide perovskites. *Physics Letters A* **2014**, *378*, 290.

(127) Filippetti, A.; Mattoni, A. Hybrid perovskites for photovoltaics: Insights from first principles. *Physical Review B* **2014**, *89*, 125203.

(128) Yin, W. J.; Shi, T.; Yan, Y. Unique properties of halide perovskites as possible origins of the superior solar cell performance. *Advanced Materials* **2014**, *26*, 4653.

(129) Borriello, I.; Cantele, G.; Ninno, D. Ab initioinvestigation of hybrid organic-inorganic perovskites based on tin halides. *Physical Review B* **2008**, *77*, 235214.

(130) Wang, Y.; Gould, T.; Dobson, J. F.; Zhang, H.; Yang, H.; Yao, X.; Zhao, H. Density functional theory analysis of structural and electronic properties of orthorhombic perovskite $CH_3NH_3PbI_3$. *Physical Chemistry Chemical Physics* **2014**, *16*, 1424.

(131) Brenner, T. M.; Egger, D. A.; Kronik, L.; Hodes, G.; Cahen, D. Hybrid organic—inorganic perovskites: low-cost semiconductors with intriguing charge-transport properties. *Nature Reviews Materials* **2016**, *1*, 15007.

(132) Wehrenfennig, C.; Liu, M.; Snaith, H. J.; Johnston, M. B.; Herz, L. M. Homogeneous Emission Line Broadening in the Organo Lead Halide Perovskite $CH_3NH_3PbI_{3-x}Cl_x$. *The Journal of Physical Chemistry Letters* **2014**, *5*, 1300.

(133) Pelant, I.; Valenta, J.: *Luminescence spectroscopy of semiconductors*; Oxford University Press, 2012.

(134) Elliott, R. J. Intensity of Optical Absorption by Excitons. *Physical Review* **1957**, *108*, 1384.

(135) Weisbuch, C.; Benisty, H. Microcavities in Ecole Polytechnique Fédérale de Lausanne, Ecole Polytechnique (France) and elsewhere: past, present and future. *physica status solidi (b)* **2005**, *242*, 2345.

(136) Baumeister, P. W. Optical Absorption of Cuprous Oxide. *Physical Review* **1961**, *121*, 359.

(137) Stoumpos, C. C.; Malliakas, C. D.; Kanatzidis, M. G. Semiconducting tin and lead iodide perovskites with organic cations: phase transitions, high mobilities, and near-infrared photoluminescent properties. *Inorganic Chemistry* **2013**, *52*, 9019.

(138) Yin, W. J.; Yang, J. H.; Kang, J.; Yan, Y. F.; Wei, S. H. Halide perovskite materials for solar cells: a theoretical review. *Journal of Materials Chemistry A* **2015**, *3*, 8926.

(139) Stoumpos, C. C.; Kanatzidis, M. G. The Renaissance of Halide Perovskites and Their Evolution as Emerging Semiconductors. *Accounts of Chemical Research* **2015**, *48*, 2791.

(140) Jacobsson, T. J.; Schwan, L. J.; Ottosson, M.; Hagfeldt, A.; Edvinsson, T. Determination of Thermal Expansion Coefficients and Locating the Temperature-Induced Phase Transition in Methylammonium Lead Perovskites Using X-ray Diffraction. *Inorganic Chemistry* **2015**, *54*, 10678.

(141) Milot, R. L.; Eperon, G. E.; Snaith, H. J.; Johnston, M. B.; Herz, L. M. Temperature-Dependent Charge-Carrier Dynamics in $CH_3NH_3PbI_3$ Perovskite Thin Films. *Advanced Functional Materials.* **2015**, *25*, 6218.

(142) Fang, H.-H.; Raissa, R.; Abdu-Aguye, M.; Adjokatse, S.; Blake, G. R.; Even, J.; Loi, M. A. Photophysics of Organic-Inorganic Hybrid Lead Iodide Perovskite Single Crystals. *Advanced Functional Materials* **2015**, *25*, 2378.

(143) Kong, W.; Ye, Z.; Qi, Z.; Zhang, B.; Wang, M.; Rahimi-Iman, A.; Wu, H. Characterization of an abnormal photoluminescence behavior upon crystal-phase transition of perovskite $CH_3NH_3PbI_3$. *Physical Chemistry Chemical Physics.* **2015**, *17*, 16405.

(144) Yasuhiro, Y.; Toru, N.; Masaru, E.; Atsushi, W.; Yoshihiko, K. Near-band-edge optical responses of solution-processed organic–inorganic hybrid perovskite $CH_3NH_3PbI_3$ on mesoporous TiO_2 electrodes. *Applied Physics Express* **2014**, *7*, 032302.

(145) Wehrenfennig, C.; Liu, M.; Snaith, H. J.; Johnston, M. B.; Herz, L. M. Charge carrier recombination channels in the low-temperature phase of organic-inorganic lead halide perovskite thin films. *APL Materials* **2014**, *2*, 081513.

(146) Wu, K.; Bera, A.; Ma, C.; Du, Y.; Yang, Y.; Li, L.; Wu, T. Temperature-dependent excitonic photoluminescence of hybrid organometal halide perovskite films. *Physical Chemistry Chemical Physics* **2014**, *16*, 22476.

(147) D'Innocenzo, V.; Grancini, G.; Alcocer, M. J.; Kandada, A. R.; Stranks, S. D.; Lee, M. M.; Lanzani, G.; Snaith, H. J.; Petrozza, A. Excitons versus free charges in organo-lead tri-halide perovskites. *Nature Communications* **2014**, *5*, 3586.

(148) Wu, Z.; Petzold, A.; Henze, T.; Thurn-Albrecht, T.; Lohwasser, R. H.; Sommer, M.; Thelakkat, M. Temperature and Molecular Weight Dependent Hierarchical Equilibrium Structures in Semiconducting Poly(3-hexylthiophene). *Macromolecules* **2010**, *43*, 4646.

(149) Martín, J.; Nogales, A.; Martín-González, M. The Smectic–Isotropic Transition of P3HT Determines the Formation of Nanowires or Nanotubes into Porous Templates. *Macromolecules* **2013**, *46*, 1477.

3. Overview of the Thesis

The primary goal of the thesis is to obtain a fundamental knowledge on how changes in morphology modify the electronic structure and interactions among chromophores and constituents of organic- and hybrid organic-inorganic semiconductors. To achieve this goal, the thesis consists of eight manuscripts, where five focus on organic semiconductors (chapters 4.2 – 4.6), while three deal with the hybrid organic-inorganic perovskite $CH_3NH_3PbI_3$ (chapters 4.7 – 4.9) (see Figure 14c). Chapter 4.2 focuses on identifying the nature of temperature induced order-disorder transitions of the conjugated polymer P3HT and how material properties like polydispersity and molecular weight impact on this transition. With this knowledge, it was then possible to perform a proper analysis of the temperature dependent photoluminescence spectra of P3HT (Figure 14a), which is focus of chapter 4.3. Here the results of structural investigation were combined with the analysis on the temperature dependent optical spectra. This allowed me to, (i), interpret and understand the temperature dependent ordering processes of P3HT and their signatures on corresponding optical spectra within the entire investigated temperature range, (ii), it was possible for the first time, to identify two different aggregate species of P3HT at low temperatures using optical spectroscopy. The knowledge about the analysis methods of the optical spectra derived in chapters 4.2 and 4.3, were then used to investigate energy transfer processes between disordered and ordered domains (also induced by temperature) of the conjugated polymer MEHPPV (see Figure 14b) described in Chapter 4.4. By doing this, contributions from disordered and ordered phases in the transient absorption spectra of MEHPPV at low temperature could be identified, which allowed me to conclude that an ultrafast energy transfer of excited states from the disordered phase to planarized chain segments occurs. Once the excited state dynamics between the ordered and disordered phase of MEHPPV were clarified, we consecutively went on to also investigate the excited state dynamics that occur within the aggregated phase of MEHPPV (chapter 4.5). By combining broadband transient absorption spectroscopy with coherent ultrafast electronic 2D spectroscopy, exciton relaxation and energy transfer dynamics in the aggregated phase are revealed. In the Köhler group, temperature induced order-disorder transitions could not only be observed in P3HT or MEHPPV, but also in a variety of different materials, including low band gap polymers, conjugated oligomers and even in small molecules. Chapter 4.6 therefore summarizes

and reviews the results on all materials so far investigated and puts temperature induced order-disorder transitions into a more general context. It discusses general parameters that influence these ordering dynamics and shows how optical spectroscopy can be used to gain information on the different conformational states of the investigated organic materials. Phase transitions not only occur in organic conjugated material but are also known to take place in another class of solar cell material, which are hybrid organic-inorganic perovskites.

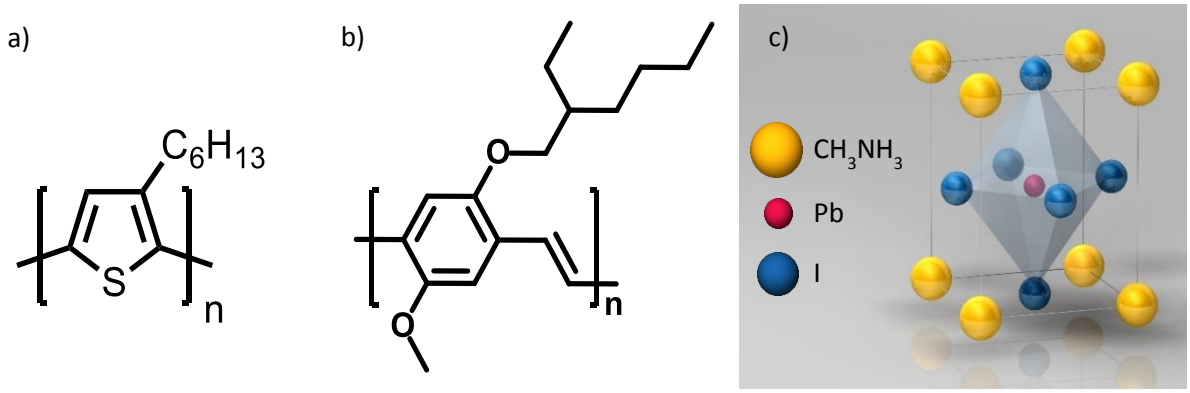

Figure 14: Chemical structures of (a) Poly(3-hexylthiophene) (P3HT), used in chapters 4.2 and 4.3, (b) Poly[2-methoxy-5-(2-ethylhexyloxy)-1,4-phenylenevinylene] (MEH-PPV) used in chapters 4.4 and 4.5 and (c) the crystal unit cell of the organic-inorganic perovskite methylammonium lead iodide ($CH_3NH_3PbI_3$ or $MAPbI_3$) used in chapters 4.7 to 4.9.

Chapter 4.7 to 4.9 deal with the hybrid organic-inorganic perovskite $CH_3NH_3PbI_3$. Similar to the case of the neat organic semiconductors, the focus of the works is to gain a deep knowledge and even control on the different morphological states of the investigated material. The optical properties of organic-inorganic perovskites are also sensitive to their morphology and it is furthermore known that they adopt different crystal structures (e.g. tetragonal, orthorhombic) depending on temperature. Chapter 4.7 thus deals with the analysis of the temperature dependent emission properties of $CH_3NH_3PbI_3$ between 300 – 5 K. I found that there is a temperature independent critical excitation density for amplified spontaneous emission. A further important aspect of this chapter is the discovery to reproducibly induce, probe and erase the tetragonal crystal structure at low temperatures, where intrinsically an orthorhombic crystal structure is present by exposing the sample to appropriate laser fluences. To also understand the temperature dependent shift of the optical band gap which is present in $CH_3NH_3PbI_3$, chapter 4.8 presents an analysis on temperature dependent absorption and emission spectra in the

framework of Urbach theory, which also clarifies the aspect of the different types of disorder in the material. In regard to commercialisation of perovskite solar cells, a crucial aspect is the structural stability during the processing. Chapter 4.9 describes a proof of principle work where perovskite layers with high crystallinity could be successfully processed using the aerosol deposition method. As the latter is a dry process where the source material (powder) is prepared independently, it decouples the material synthesis and layer formation, which is unique compared to all other processing methods for organic-inorganic perovskites.

The Impact of Polydispersity and Molecular Weight on the Order – Disorder Transition in Poly(3-hexylthiophene)

In chapter 4.2 I investigated the impact of polydispersity and molecular weight on the temperature induced order-disorder transition in P3HT in solutions of THF. For decreasing temperature, spectral dynamics in both, absorption and corresponding PL spectra are observed. Analysing the data, it becomes clear that the order-disorder transition of P3HT occurs in three major steps which are for decreasing temperature: (i) planarization of the disordered phase, (ii) aggregate formation (iii) planarization of the aggregated phase. To analyse the spectral changes in a detailed and quantitative way, a decomposition of the measured absorption spectra is necessary to distinguish between the spectral contributions of the disordered phase and aggregated phase. From these spectral decompositions it was possible to calculate the relative fraction of aggregated chains in the investigated solution at a certain temperature. Furthermore the usage of specially synthesised and thus well-defined P3HT with different chain lengths yet low polydispersity allowed us to study the impact of polydispersity and chain length on the phase transition. From the temperature dependent fraction of aggregate for P3HTs with different chain lengths a clear correlation between the critical transition temperature at which the order-disorder transition takes place (indicated by a significant increase of fraction of aggregate) and the chain length of P3HT was observed (Figure 15a). In addition we could even show that this correlation can be understood in the framework of a mean-field theory that describes a coil globule transition of polymers. This could be seen from the overall good quality of the fit to the data, which also allowed us to extract relevant parameters like the theta temperature of P3HT in THF. As a second parameter

that impacts on the phase transition, we identified the influence of polydispersity on the shape of the transition. In that context, shape corresponds to the steepness of increase of the temperature dependent fraction of aggregate (Figure 15b). We compared the temperature dependent fraction of aggregates in two batches of P3HT, which both have the same molecular weight / chain length, yet clearly differ in their polydispersity. The specially synthesised P3HT had a PDI = 1.16 in contrast to a PDI = 2.0 for the "high PDI" compound which was chosen to be in the range of typical values that can be found for commercially available P3HTs. Here a more gradual and smeared out increase of the fraction of aggregate within the transition temperature region was observed.

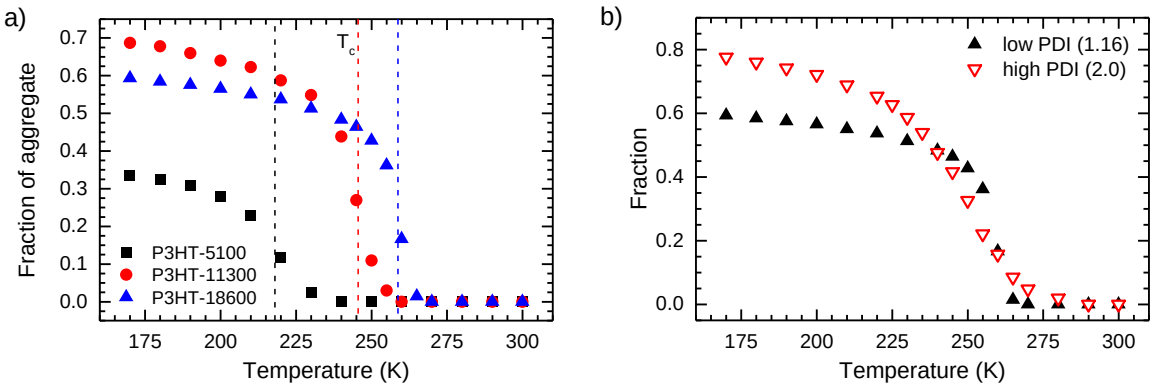

Figure 15: (a) Fraction of aggregates in the solution as a function of temperature for the three P3HTs with different molecular weight. (b) Comparison between the fraction of aggregates of P3HT with low PDI and P3HT with high PDI as a function of temperature.

This behaviour could be well explained when considering the correlation between the critical temperature of the transition and the chain length of the polymers. In this context a wide distribution of chain lengths directly results in a corresponding wide distribution of critical transition temperatures. These are intermixing when an ensembles of polymer chains with high PDI is investigated, which then results in the observed disproportionally smearing out of the temperature dependent fraction of aggregate transition. From this result the phase transition was associated to be rather first order than to have a second order nature.

Spectroscopic Signature of Two Distinct H-Aggregate Species in Poly(3-hexylthiophene)

With the knowledge about the temperature dependent conformation dynamics of P3HT in solution from chapter 4.2, it appeared straightforward to extend our analysis on the temperature dependent optical spectra of P3HT towards a detailed investigation on the basis of the PL data which is presented in chapter 4.3. The investigated P3HT solution showed a phase transition with the first spectral features from an aggregated phase arising below a temperature of 270 K. Within the transition temperature region we applied our spectral decomposition approach to the photoluminescence (PL) spectra and obtained the PL spectra of only the aggregated phase. We were able to observe that the emission spectrum of that aggregated phase undergoes drastic changes within the temperature range between 265 K down to 160 K (Figure 16a).

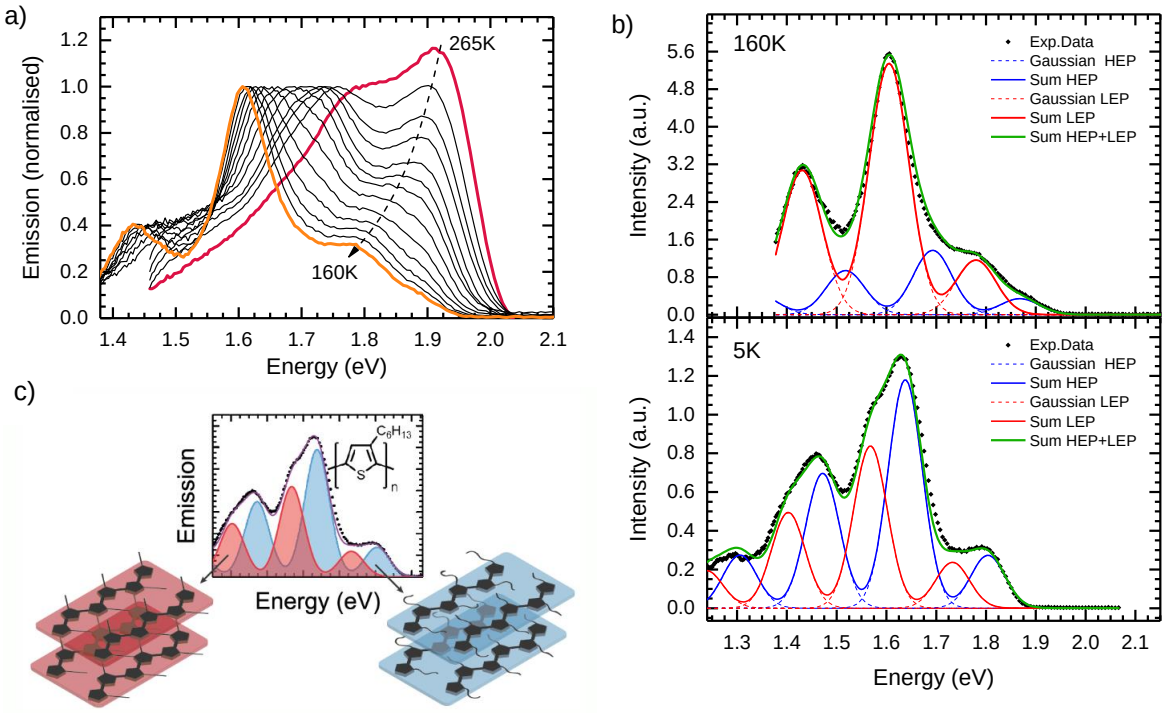

Figure 16: (a) Fluorescence spectra of aggregated P3HT in the temperature range from 265 to 160 K where the polymer chains are in fluid solution. The spectra are normalized to the intensity of the $S_1 \rightarrow S_0$ 0–1 feature. (b) Modified Franck–Condon analysis (green solid line) of the fluorescence spectra (black squares) of P3HT aggregates at 160 and 5 K using a superposition of a higher energy vibronic progression (HEP) (blue solid line) and a lower energy vibronic progression (LEP) (red solid line). (c) Sketch illustrating the interpretation of the two different PL progressions toward different aggregate species with crystalline backbone yet different degree in side chain order.

First I interpreted red shift of the overall PL spectrum for decreasing temperature as a planarization of the aggregated chains. Second, I considered the changes in the peak ratio of the$S_1 \rightarrow S_0$ 0-0/0-1 transition in the framework of a theoretical model of weakly interacting aggregates developed by Spano and co-workers which describes the impact of intermolecular coupling between aggregated chains on their optical properties. This allowed me to identify an increase in intermolecular coupling for decreasing temperature. Concomitantly it suggests a rather disordered and only weakly interacting character of the aggregated chains within the temperature range straight below the aggregation onset, that changes to a more ordered and more strongly interacting chains as temperature is reduced.

Furthermore from applying Franck-Condon Analysis on the temperature dependent PL data down to 5 K, it became clear that the spectra could only be modelled in a satisfying way when an additional vibronic progression was introduced to the FC Analysis (Figure 16b). This suggested the existence of different aggregate species (Figure 16c). This scenario could then further be proofed by carrying out additional spectroscopic approaches such as time resolved emission spectroscopy and steady-state emission spectroscopy for different excitation wavelengths. Furthermore the same vibrational progressions as in solution were also found at low temperature for corresponding films of the P3HT that we investigated. This allowed us to compare our work to the results of a past work where the identical batch of P3HT was investigated via scattering experiments.[148,149] That work studied the structural evolution of P3HT when cooling from the melt toward room temperature, where it undergoes a similar order-disorder transition than in our case in solution. Using this, we were able to draw an overall picture of the different dynamics and morphological states that occur when P3HT is cooled and undergoes an order-disorder transition. First, the surprisingly small intermolecular coupling of the aggregated phase in a small temperature range below the transition temperature can be interpreted to stem from a structural phase where the backbones are layer separated yet they and also the side chains still are disordered. For lower temperatures we find the main chains are ordered, yet the side chain are disordered. At the lowest temperatures measured, both, backbone and side chains are ordered.

Ultrafast Energy Transfer between Disordered and Highly Planarized Chains of Poly[2-methoxy-5-(2-ethylhexyloxy)-1,4-phenylenevinylene] (MEH-PPV)

In this work we investigated the energy transfer between disordered and highly planarized chains of the conjugated polymer MEHPPV. To do so, we first performed temperature dependent absorption and emission spectroscopy. Comparable to the previous works on P3HT, three different temperature regions could also be observed for MEHPPV, which occur for decreasing temperature in a sequence of (i) planarization of the disordered phase, (ii) order-disorder transition (iii) planarization of the aggregated phase (Figure 17a). After performing spectral decomposition it becomes clear that the aggregated phase of MEH-PPV consists of highly planar chain segments with low intermolecular coupling between the chains. This was concluded from the shape of the neat absorption and emission spectra of the aggregated phase, which had mirror image character and yield very high $S_1 \rightarrow S_0$ 0-0/0-1 peak ratios. We then calculated the temperature dependent fraction of aggregates from both, absorption and emission data (Figure 17b). It turned out that the fraction of aggregate increases steeply within the temperature range between 180 K – 160 K and saturates for lower temperatures. While the fraction of aggregate calculated from the absorption data yields a maximum value of approximately 30% aggregated chains at a temperature of 120 K, the fraction of aggregate calculated from PL suggests that the entire emission stems from the aggregated phase below 160 K.

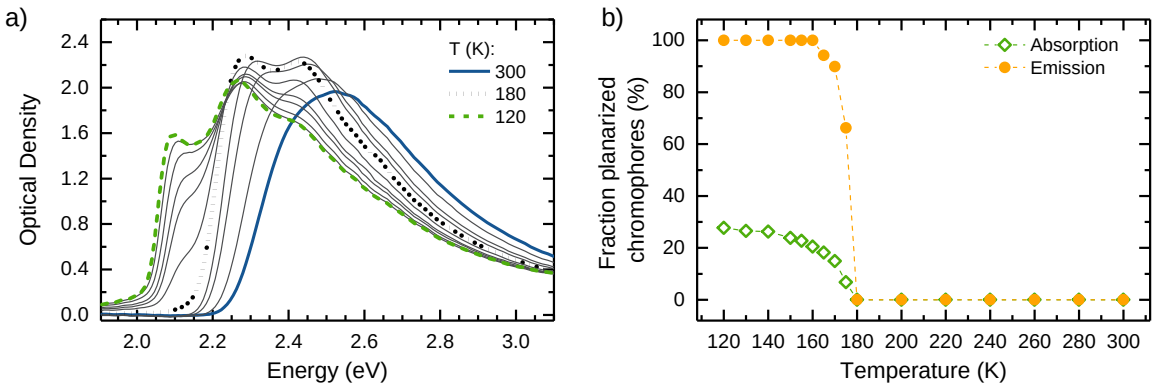

Figure 17: (a) Steady-state absorption spectra of MEH-PPV in MTHF for different temperatures, between 300, and 120 K. (b) Fraction of planarized chromophores as a function of temperature obtained from the absorption spectra (open green diamonds) and from the emission spectra (orange dots).

This difference suggests an efficient energy transfer from the disordered toward the ordered phase which we then investigated in detail using fs-transient absorption spectroscopy. We used our knowledge on the spectral decomposition of both, absorption spectra (from chapter 4.2) and emission spectra (from chapter 4.3) of aggregated polymer solutions at low temperature, and we applied these techniques to the time resolved transient absorption spectra. In a first step we considered the transient absorption spectrum of aggregated MEHPPV solution at 120 K at an excitation energy of 2.12 eV where exclusively the planar chain segments were excited. Here, by appropriate normalizing the 120 K PL spectrum to the stimulated emission (SE) part of the transient absorption spectrum, it was possible to extract the spectral shape of the ground state bleach (GSB) of the planarized chain segments. Using the thereby obtained spectra of both SE and GSB of the ordered chain segments then allowed us to also decompose low temperature transient absorption spectra with a higher excitation energy at 2.48 eV, where also the disordered phase absorbs. Figure 18a shows the corresponding decomposed transient absorption spectrum, 1 ps after excitation, where, in addition to the contribution from planarized chain segments (red area), also a certain contribution from the disordered phase (blue area) to the overall ground state bleach is evident. As a function of time, the relative amount of the latter contribution reduces, while the relative amount of GSB from planarized chains increases (Figure 18b).

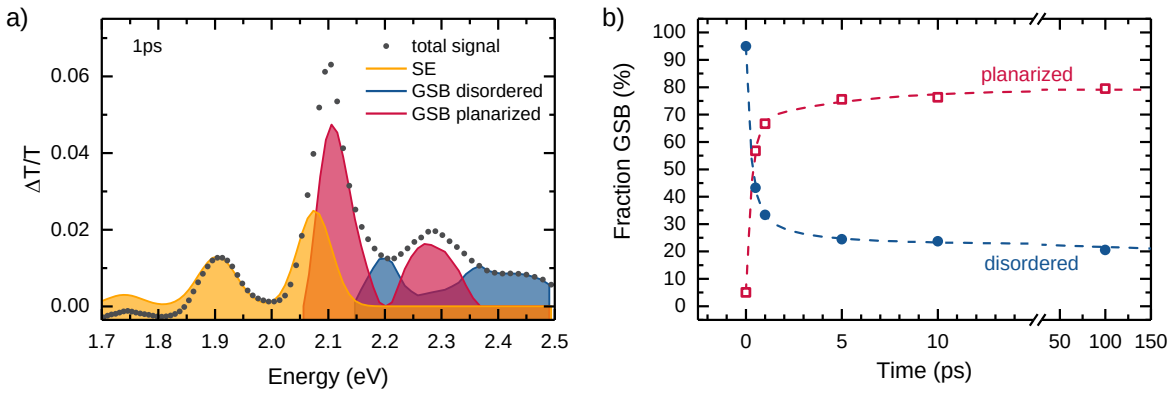

Figure 18: (a) Pump–probe spectra for excitation at 2.48 eV (where coiled chains absorb) at 120 K for a time delay of 1 ps after excitation. In addition to the total ΔT/T signal (dots), the contributions of SE, GSB from disordered chromophores, and the GSB from the planarized chromophores are indicated by orange, blue, and red solid lines, respectively. (b) Percentage of the ground-state bleach signal that is due to planarized chromophores (open square symbols) or to disordered chromophores (filled round symbols) as a function of time. The dashed line is a guide to the eye.

From this behaviour an efficient energy transfer from disordered towards highly planarized chain segments, on the timescales of a few picoseconds could be inferred. From the short timescale we further suggested that both, disordered and planarized chain segments must be in a close proximity.

Relaxation dynamics and exciton energy transfer in the low-temperature phase of MEH-PPV

Chapter 4.4 focuses on the energy transfer *from* the disordered *to* planarized chains of aggregated MEHPPV in solution at low temperatures. Spurred from these results, in Chapter 4.5 we consequently moved on to perform a detailed analysis on the excited state dynamics *within* the planarized aggregated phase of MEHPPV in solution. To do so, we performed ultrafast transient absorption spectroscopy as well as coherent electronic two-dimensional spectroscopy. To exclude additional dynamics occurring from energy transfer processes from the disordered to the aggregated phase, we excited our sample only at low energies where absorption is entirely due to the aggregated phase. In order to identify relaxation processes within the aggregated phase, we used excitation energies of 2.03 eV, which only excites the most planarized chain segments, and 2.1 eV, which excites the aggregated phase also at slightly higher energy allowing for relaxation processes. In general the transient absorption spectra at low T exhibited various distinct bands due to stimulated emission and ground-state-bleach signals (Figure 19a). The well resolved character of the spectra allowed to analyse the spectral moments of the individual bands which are defined as $M_0(T) = \sum_{v_1}^{v_2} I(v,T) \cdot \Delta v$ and $M_1(T) = \frac{1}{M_0(T)} \sum_{v_1}^{v_2} v \cdot I(v,T) \cdot \Delta v$, where $I(v,T)$ reflects the intensity of absorption change at a certain population time T and frequency v. Δv is the frequency interval between the data points and $v_1$and v_2 define the summation limits of each band. First, by calculating the zero-order moments M_0 we were able to analyse the population dynamics which revealed to have a complex character. Due to the broad distribution of polymer chains that was present in our sample (PDI=4), the complex population dynamics could be due to a broad distribution of rates or arise from several distinct kinetic processes. In the first case, an appropriate description is a stretched exponential decay model. From this it is possible to identify two time regimes with different slopes when plotting the data in a Kohlrausch-Williams-Watts representation (Figure 19b).

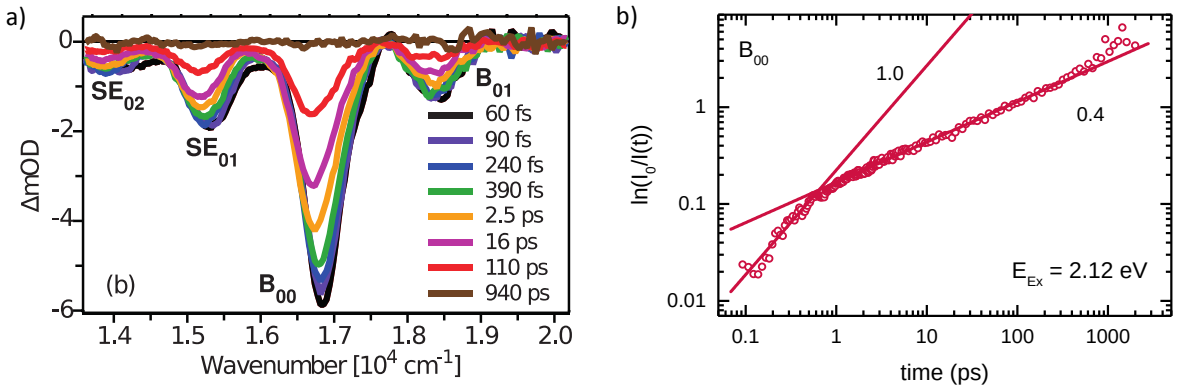

Figure 19: (a) Selection of transient absorption spectra at 140 K and different population times upon excitation at 2.10 eV. (b) Kohlrausch-Williams-Watts representation of the zero order moment decay of the B_{00} band at 140 K upon excitation at 2.10 eV.

The behaviour at short times characterized by a slope of unity indicated a vanishing dispersion of the excited state where energetic relaxation to nearest neighbours with lower energy occurs via single jumps. This results in the fact that lower energy sites become subsequently unavailable for other adjacent excitations, from which the decreased slope in Figure 19b at longer times with a value of 0.4 results. The latter is between the limits of 0.5 and 1/3, which are expected for Förster transfer from a random ensemble of donors to a dilute array of acceptors in a 3D and a 2D case respectively.

In the second case a multi exponential approach using four exponentials also fitted the measured data and revealed for time constants. However, both models ended up in the same attempt to distinguish between a fast and a slow regime, with dynamics occurring on time scales faster or longer than tens of nanoseconds respectively. In the multimode model the obtained time constants of about 40 ps and 320 ps in the slow dynamic regime were ascribed to the $S_1 \rightarrow S_0$ relaxation of the excited states at the bottom of the density of states of the aggregated phase. For the stretched exponential model we could show that an additional dispersive energy transfer dynamic has to be considered at longer times.

Consequently we also performed an analysis on the spectral shifts that occur in the transient absorption spectra as a function of time by calculating the first spectral moment of the different spectral bands M_1. For excitation energy of 2.03 eV no significant spectral shifts could be observed. In contrast to this, for an excitation energy of 2.1 eV all bands

shift to the red as a function of time, where we were able to distinguish between two time constants being in the ranges of 200-250 fs and 4 ps.

The same spectral shift behaviour with the same two time constants could also be extracted from the coherent 2D spectroscopy measurements (see Figure 20a for two 2D plots). Here we focused on the spectral region of the B_{00} band, where the amplitude of red shift increased with excitation energy (Figure 20b), similar to the results from transient absorption. From global analysis of the 2D data we were also able to identify a further fast decay component in the sub 30 fs range. Taking all results into account we were finally able to develop a detailed picture on the occurring dynamics within the aggregated phase of MEHPPV.

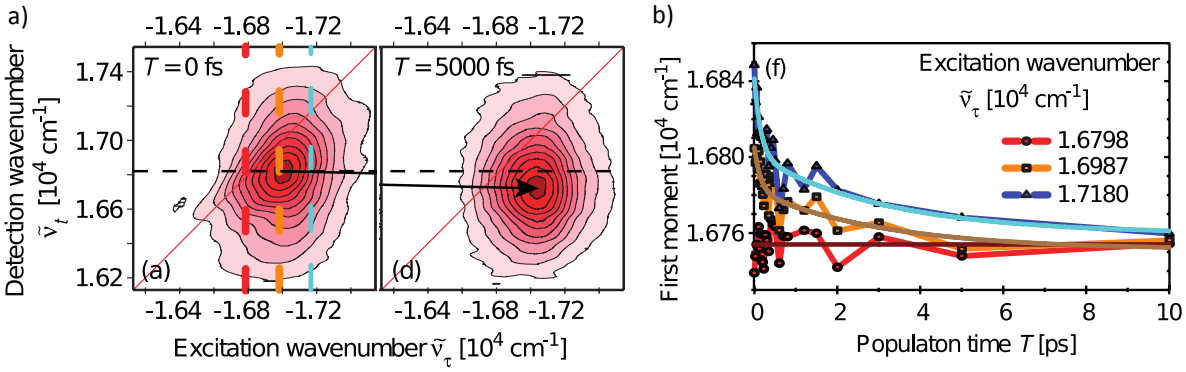

Figure 20. (a) Selection of measured (normalized) 2D spectra of MEH-PPV at different population times T as indicated in the inset. Contour lines display signal levels from 5% (light pink) to 95% (dark red) in steps of 10%. (b) Temporal evolution of the first moment (i.e., average spectral position) of the signal along the detection axis (symbols) for the different excitation wavenumbers shown by the vertical lines in panel (a). Overlaid solid lines show the best individual bi-exponential fit of each trace

Figure 21 illustrates the measured spectral dynamics with their different time constants toward the corresponding physical dynamics. First, the time constant in the 30 fs range is ascribed to a localization process of the initially delocalized excited state on smaller domains. This process is followed by an exciton relaxation process, populating the bottom of the density of states within a 200-250 ps time scale. Due to the time evolution of the features in the 2D spectra, we were able to associate the 4 ps time constant to arise from spectral diffusion of the excitons within the exciton density of states towards the lowest energy states of the aggregated phase.

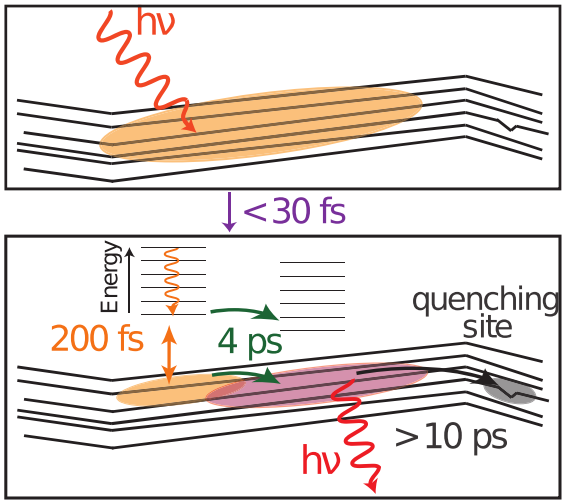

Figure 21: Illustration of the different dynamics with their corresponding time constants.

Afterwards, either radiative relaxation or further energy transfer towards defect states occur on timescales on the tens to hundreds of picoseconds.

The Temperature Induced Order-Disorder Transition in Solutions of Conjugated Polymers Probed by Optical Spectroscopy

While the aggregation of π-conjugated materials is known to significantly impact on the photophysics of thin films and optoelectronic devices, only little is known about the nature and the general mechanisms on how such aggregates form. In chapter 4.2 – 4.5 the conjugated polymers P3HT and MEHPPV were investigated, where in both compounds aggregate formation occurs upon cooling. In addition, other conjugated polymers such as polyfluorene with octyl sidechains (PFO) or the poly(p-phenylene ethynylene) derivative MEHPPE are also known to show order-disorder transitions. In the Köhler group, temperature induced order-disorder transitions were observed also for oligo PPV, the low bandgap polymer PCPDTBT, and for the small molecule DTS(FBTTH$_2$)$_2$ within the last years. In chapter 4.6, I compare and discuss how temperature induced aggregate formation in solution is manifested in a range of conjugated homopolymers, a low-bandgap-type donor-acceptor polymer and in low molecular weight compounds. To do so I first considered the temperature dependent absorption spectra of the different compounds (Figure 22).

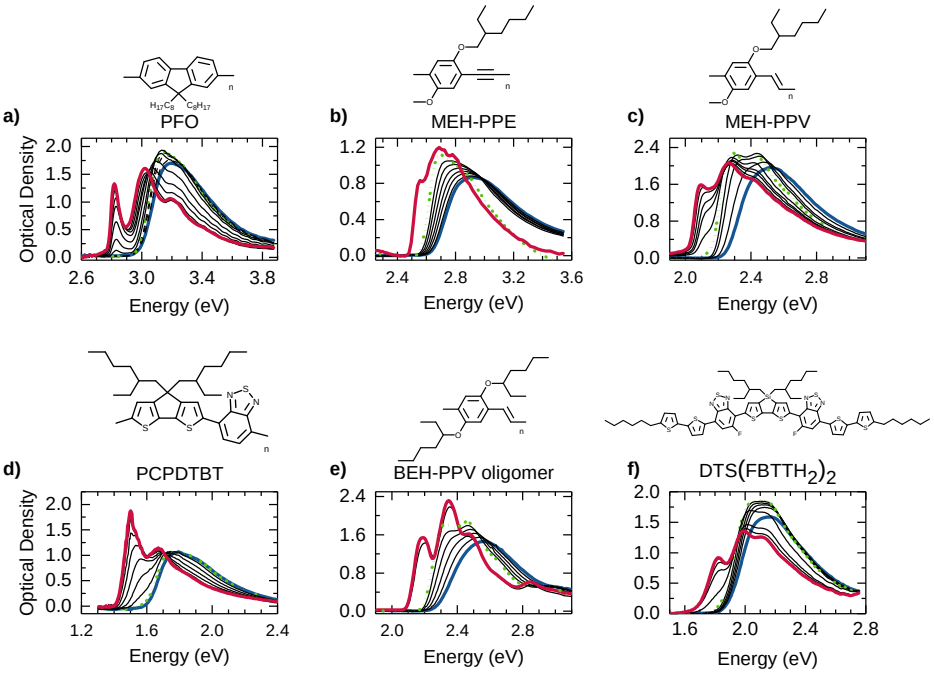

Figure 22: Temperature dependent absorption spectra of the investigated material systems in MTHF solution showing aggregation behaviour. The chemical structure is indicated on top of each panel. For each compound, the spectrum measured at the highest temperature, at a temperature directly above the phase transition, and at the lowest temperature are indicated in blue, green (dotted) and red respectively.

It became clear that all compounds show the same temperature dependent three step process upon cooling that is (i) planarization of the disordered phase, (ii) aggregate formation (iii) planarization of the aggregated phase. To gain further insights into the nature of the order-disorder transition and to identify the spectral character of the pure phases, I discuss different approaches to decompose the measured absorption spectra. From the decomposition, the temperature dependent fraction of aggregate can be obtained. When comparing the fraction of aggregate of all investigated materials, it became clear that the critical transition temperature and the steepness of the transition depend sensitively on the material. However the occurrence of an order-disorder transition is a general property of all compounds investigated.

To identify the nature of the phase transition, we first reconsider the results on the temperature induced aggregate formation of different batches of P3HT. Here we show that the transition temperature depends on the chain length and can be described in the framework of a mean-field model developed by Sanchez for coil globule transition. By further taking into account the results of the order-disorder transition of the molecule DTS(FBTTH$_2$)$_2$, the impact of polydispersity on the phase transition can be identified, which is smearing out the temperature dependence of the transition due to the distribution of molecular weights and associated transition temperatures. These findings, reveal the nature of the order-disorder transition to be first order. In the following we show that the mechanism of the aggregation process can be understood as a coil-globule process, where the chain expands before it collapses into a highly ordered dense state.

We furthermore discuss the role of side chains in the aggregation process. They can have major impact on the collapse process, which depends on whether the side chains induce structural disorder or support to planarize the backbone. The impact of different side chain order on the aggregation process and the correlated optical spectra is then discussed for aggregated P3HT, where at lowest temperatures the existence of two different PL progressions is observed. These progressions are associated with different crystal structures that differ in their side chain order, while their main chains are ordered. To explain the energetic shift in the optical spectra between the two structures, we highlight the role of environmental polarization, as the two structures differ in the degree of long range order. The latter affects the electrostatic van der Waal type interaction between the chromophores, leading to different polarization energies for

both structures. We point out the importance of future investigations to clarify the impact of the changes in polarisation energies between the different morphologies on the optical spectra. Finally, it is possible to derive a summarized picture, which correlates the temperature dependent conformational states to the optical spectra (Figure 23).

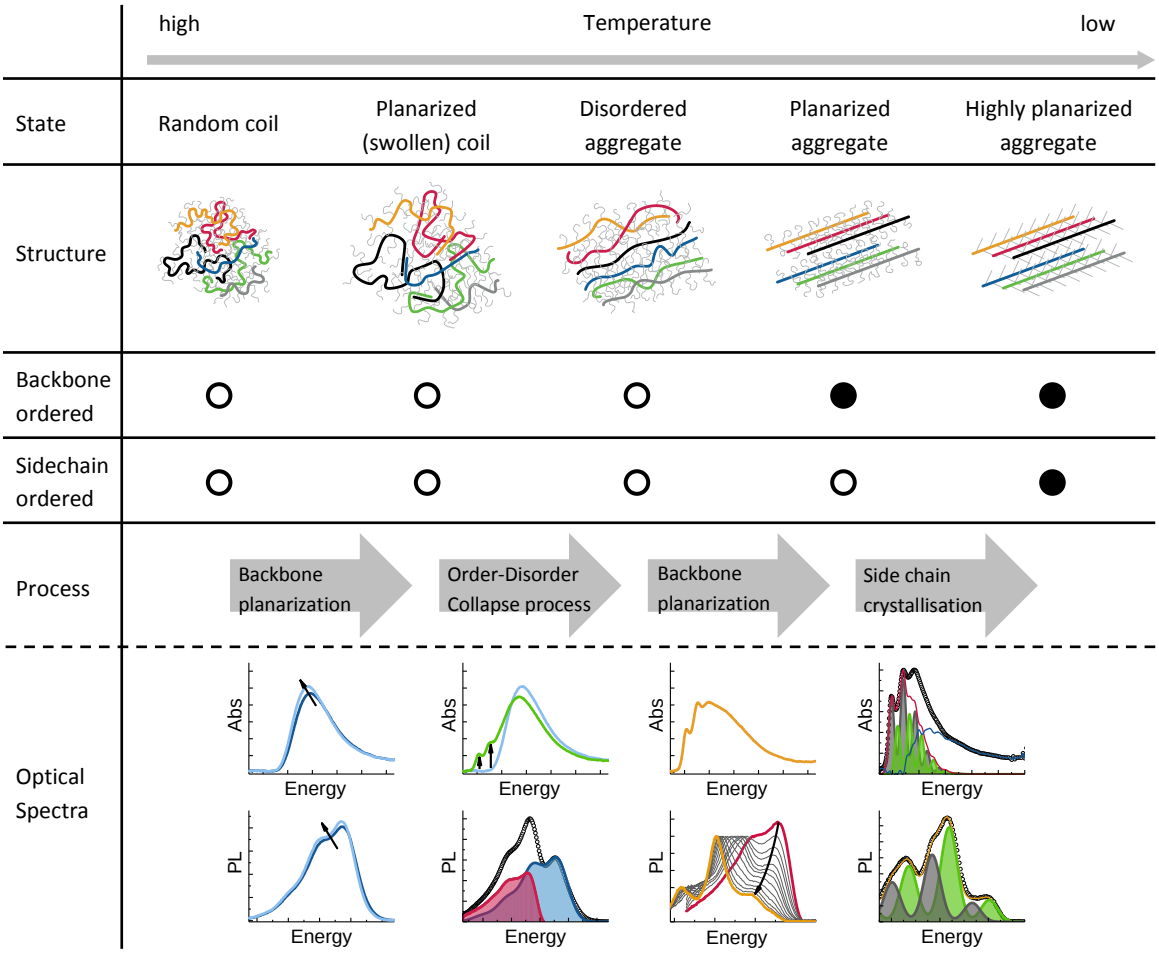

Figure 23: Summary of the changes that can occur in morphology and optical spectra upon cooling a solution of π-conjugated materials.

Reversible Laser Induced Amplified Spontaneous Emission from Coexisting Tetragonal and Orthorhombic Phases in Hybrid Lead Halide Perovskites

Within the last view years, organic-inorganic mixed halide perovskites caused enormous attraction in the solar cell community, convincing with high device performances and the possibility for low cost production. In 2014, low threshold levels for amplified stimulated emission showed that mixed halide perovskites can also be used as easy to fabricate lasers with high quality factors. All these outstanding properties are mainly attributed to the high crystallinity of the perovskite structure. In this context, an interesting aspect of these perovskite materials is that most of them can exist in different crystal structures depending on the temperature. Here, similar to the organic material systems that were investigated in chapters 4.2 – 4.6, changes in the (crystal) structures also can have significant impact on the optical properties of these perovskite materials. In the first section of this chapter we investigate the temperature dependent PL properties of the hybrid perovskite $CH_3NH_3PbI_3$, which is known to be in a tetragonal phase at high temperatures (330 K – 163 K) and in an orthorhombic phase at low temperatures (< 163 K). For cooling within the temperature range of 300 K – 160 K, we observe a single PL feature, attributed to emission from the tetragonal phase, which shifts to the red. However, when further decreasing the temperature below 160 K, a new blue shifted PL feature evolves at the expense of intensity of the PL from the tetragonal phase. It is attributed to PL from the orthorhombic phase and also shifts to the red upon further decreasing the temperature down to 5 K. When repeating the temperature dependent PL measurements at a higher excitation fluence amplified spontaneous emission (ASE) features can be observed in both phases. We further could observe a temperature threshold for this process, similar to a fluence threshold that is normally observed in literature. This effect could be understood when taking into account thermally activated non-radiative decay channels which we also observed. With that, we succeeded in calculating a temperature independent threshold exciton density required for ASE in both phases.

After having understood the temperature dependent PL dynamics of the perovskite in its different structural phases, we performed further analysis of the emission spectrum at lowest temperatures. Here we were able to show that a second PL feature can be induced when the sample is exposed to a high fluence excitation (Figure 24). We interpret this

discovery to arise from local heating during excitation with high fluence from which a modification of the crystal structure toward the tetragonal phase is induced. The latter is then kinetically frozen in when the high intensity laser is turned off.

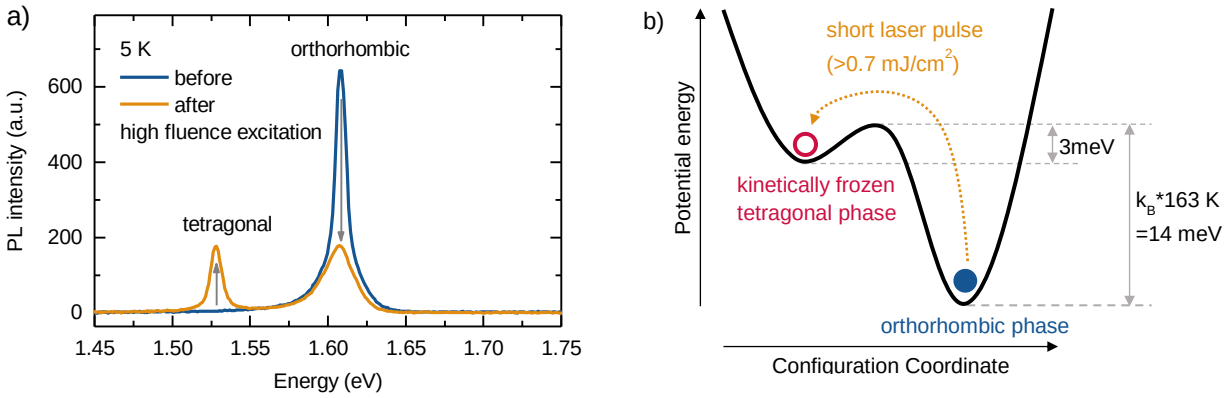

Figure 24. (a) The emission spectrum of perovskite film at 5 K before (blue line) and after (orange line) high fluence (1615 μJ/cm⁻²) excitation, recorded with a fluence of 21 μJ/cm⁻². (b) Schematic illustrating how illumination by an intense laser pulse can induce the formation of a metastable trapped tetragonal phase.

Figure 24b illustrates the proposed scenario. We found this interpretation corroborated by several aspects. Due to the spectral shape and lifetime, we could exclude that the induced PL feature originates from a bound exciton of the orthorhombic phase, as it is sometimes found in literature. Moreover, the spectral position of the induced feature perfectly met the expected value which was obtained when extrapolating the temperature dependent red shift of the tetragonal PL toward 5 K. Furthermore, the metastable nature of the induced phase could be identified, as it vanished for mild heating of the sample. Evidence for the temperature induced heating that occurs during laser excitation was then given by investigating the PL spectra during high fluence excitation, where we observed an additional broad PL band at lower spectral energies. It could be associated to arise from a superposition of various PL peaks of the tetragonal phase with different peak energies. This appeared evident when considering (i) the spectral behaviour of the low energy band when changing the excitation fluence, (ii) the above described temperature dependence of the PL peak position and (iii) assuming a temperature gradient across the Gaussian excitation profile on the sample. Using the knowledge about the metastable nature of the induced tetragonal phase at 5 K, we also succeeded to detrap the induced tetragonal phase by local heating due to appropriate

laser excitation of the sample. The detrapping of the kinetically frozen in tetragonal phase was seen upon a certain excitation fluence and became faster for increasing fluence.

Since we showed that the tetragonal phase can be induced and detrapped all optically by choosing appropriate laser fluences, we finally did a proof of principle demonstration to use $CH_3NH_3PbI_3$ as an all optical memory device. To this end we used high- mid- and low fluences to perform write- erase- and read processes of the tetragonal phase respectively, which could be probed by the PL peak intensities of the two phases (Figure 25).

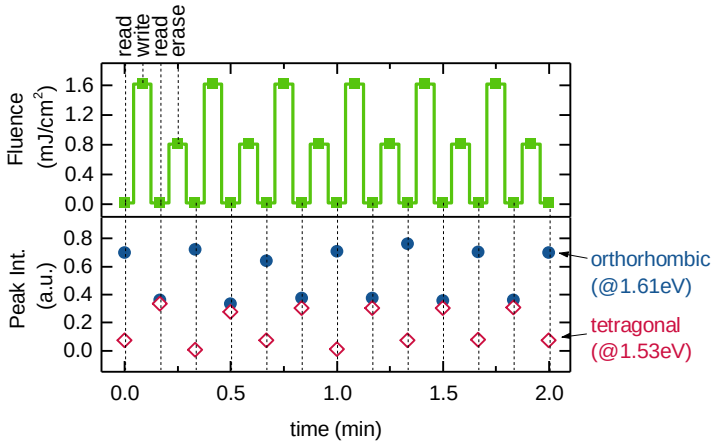

Figure 25 (Lower panel) Peak intensities at 5 K of the ASE at 1.61 eV (blue dots) in the orthorhombic phase and of the ASE at 1.53 eV (red diamonds), attributed to the tetragonal phase. The peak intensities were recorded using a fluence of 21 μJ/cm^{-2} (= "read" mode) after previous illumination with pulses at a fluence of 1615 μJ/cm^{-2} (= "write" mode) or at 811 μJ/cm^{-2} (= "erase" mode) as illustrated in the upper panel.

It was possible to perform reproducible sequences of write-read-erase cycles. Finally, spatially resolved PL mapping before/after writing and after an erase process further revealed the reproducible nature of the laser induced phase change.

Effect of Thermal and Structural Disorder on Electronic Structure of Hybrid Perovskite Semiconductor $CH_3NH_3PbI_3$

In this chapter, the temperature dependence of the optical properties of $CH_3NH_3PbI_3$ from room temperature to 6 K is investigated. In both, the tetragonal (T > 163 K) and the orthorhombic (T < 163 K) phase of $CH_3NH_3PbI_3$, the band gap (from both absorption

and photoluminescence measurements) decreases with decrease in temperature - in contrast to what is normally seen for many inorganic semiconductors such as Si, GaAs, GaN etc. By temperature dependent X-ray measurements we find that in $CH_3NH_3PbI_3$, the temperature coefficient of thermal expansion is large and accounts for the positive temperature coefficient of the band gap. We also performed spectral analysis of the temperature dependent absorptions spectra in the framework of Elliot's theory. With it we succeeded to distinguish between spectral contributions from excitons and band to band transitions. Further analysing the temperature dependent linewidth of the excitonic contribution reveals, that the orthorhombic phase is the better ordered one compared to the tetragonal phase at higher temperatures. Further considering the temperature dependent absorption spectra, we identified an Urbach focus point (Figure 26a) in both phases which demonstrates the possibility to analyse the low energy edge of the excitonic peak in the framework of the Urbach formalism. In the latter, we found the Urbach energy, which is related to the degree of disorder in the sample, to be surprisingly small for solution processed semiconductors.

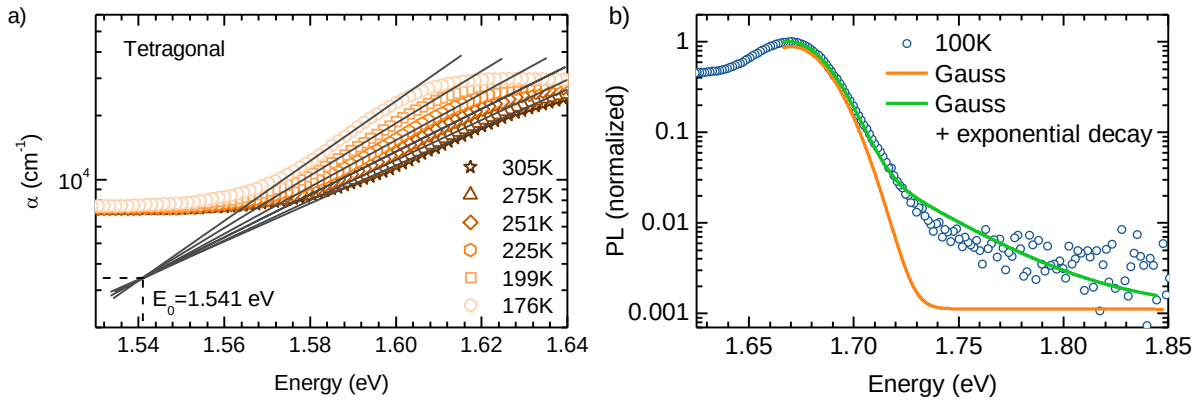

Figure 26: (a) Logarithmic representation of absorption coefficient as a function of photon energy at different temperatures in the tetragonal phase of $CH_3NH_3PbI_3$. Linear fits to the absorption edges end up in a common Urbach focus at 1.541 eV. (b) Normalized PL spectrum of $CH_3NH_3PbI_3$ at 100 K (blue dots) together with fits of the higher energy PL edge using a single Gaussian (orange line) or a Gaussian + exponential (green line) function

When analysing the temperature dependent Urbach energy we were able to distinguish between static and dynamic disorder in the sample. I could also observe this discrimination of disorder in the temperature dependent photoluminescence spectra. By differentiating between Gaussian and exponential contributions to the shape of the PL it was possible to analyse the impact of static and dynamic disorder on the spectra.

Overall, our study establishes a methodology using optical techniques for the concise characterisation of disorder in new perovskite materials

Compact Layers of Hybrid Halide Perovskites Fabricated via the Aerosol Deposition Process – Uncoupling Material Synthesis and Layer Formation

Metal halide perovskites have attracted enormous attention within the last few years in the solar cell community and also, more recently in the LED sector. A main factor of that success can be attributed to their capability of combining both, superior charge transport properties due to their crystalline nature, together with a high versatility in combining and/or mixing of different constituents to tune their optoelectronic properties. On the other hand a clear limitation of this class of material can be seen in the inseparability of material synthesis and layer formation. In the past, a variety of different methods have been presented to properly form layers of halide perovskites. Mostly they are based on the combination of two different compounds (typically from solutions) where at least one compound is a halide, leading to the formation of the perovskite crystals during (mostly) a drying process. All methods reported so far have in common that the crystalline perovskite structure itself develops during film formation. As a result, material synthesis is interconnected with film processing. This implies that it is not possible to improve the quality of the perovskite without also modifying the film formation, and vice versa. To this end we used the aerosol deposition method to process layers of the hybrid perovskite $CH_3NH_3PbI_3$.

The method is commonly used to produce dense ceramic coatings at room-temperature directly from a bulk powder that is transferred into an aerosol and then spray-coated onto a substrate where the dense films are formed without any temperature treatment (see Figure 27a).The dry nature of the AD process is in contrast to the already used sol-gel spray coating methods that have been applied to hybrid perovskites so far. In the latter, the constituents for the halide perovskite are deposited by a spray and the reaction occurs during the drying process of the film, whereas in the AD process the ready-made crystalline perovskite powder is deposited. We finally succeeded to form $CH_3NH_3PbI_3$ perovskite layers by aerosol deposition.

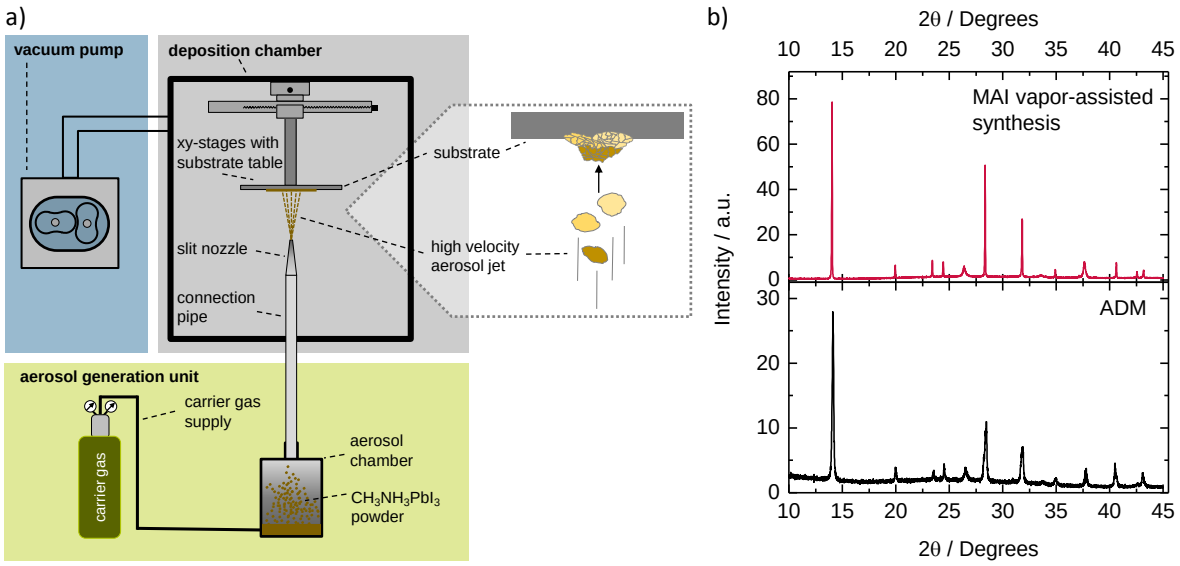

Figure 27: (a) Schematic representation of an AD setup with its typical components. The zoomed area at the right-hand side illustrates the film formation process in more detail. (b) XRD patterns of a reference film produced by a vapor-assisted crystallization approach (red) and the AD-processed film (black).

The films show typical optical properties, high crystalline quality, compactness and good contact to underlying layers. Furthermore the absence of any features from PbI_2 incorporations from the measured XRD patterns (Figure 27b) proofs the non-destructive character of the process.

In summary, I have demonstrated that disorder – order transitions in organic semiconductors can be analyzed through careful optical spectroscopy, and that they can be described as first-order phase transitions with certain general features as detailed in Chapter 4.2 – 4.6. In a similar way, a phase transition from tetragonal to orthorhombic phases in a hybrid perovskite can dominate the optical spectra and can be exploited for an all-optical memory device. For both classes of materials, temperature dependent absorption and photoluminescence measurements were found to be a powerful and effective technique to study excited states.

4. Publications

4.1. Individual Contributions to Joint Publications

1. **The Impact of Polydispersity and Molecular Weight on the Order – Disorder Transition in Poly(3-hexylthiophene)**
   Fabian Panzer, Heinz Bässler, Ruth Lohwasser, Mukundan Thelakkat and Anna Köhler,
   Journal Physical Chemistry Letters 5 (**2014**) 2742–2747

   Based on data taken in the framework in my diploma thesis, I analysed and interpreted the spectra, and together with Heinz Bässler and Anna Köhler I wrote the manuscript.

2. **Spectroscopic Signature of Two Distinct H-Aggregate Species in Poly(3-hexylthiophene)**
   Fabian Panzer, Michael Sommer, Heinz Bässler, Mukundan Thelakkat, Anna Köhler
   Macromolecules 48 (**2015**) 1543–1553

   Using P3HT synthesised by Michael Sommer, I prepared all samples (films and solutions) used. I performed all temperature dependent steady-state absorption and emission measurements. Furthermore I performed all site selective emission measurements and time resolved PL measurements. I performed all Franck-Condon Analysis and interpreted the data. Together with Anna Köhler and Heinz Bässler I wrote the manuscript.

3. **Ultrafast Energy Transfer between Disordered and Highly Planarized Chains of Poly[2-methoxy-5-(2-ethylhexyloxy)-1,4-phenylenevinylene] (MEH-PPV)**
   Thomas Unger, Fabian Panzer, Cristina Consani, Federico Koch, Tobias Brixner, Heinz Bässler and Anna Köhler
   ACS Macro Letters 4 (**2015**) 412-416

   I prepared the solutions measured. I measured all temperature dependent steady-state absorption and emission spectra. I performed all analysis on the steady-state data (including the Franck-Condon analysis on the aggregate absorption spectrum). I interpreted the data and wrote the part of the manuscript which relates to the steady-state data. I furthermore reviewed and edited the overall manuscript and graphs.

4. **Relaxation dynamics and exciton energy transfer in the low-temperature phase of MEH-PPV**
   Cristina Consani, Federico Koch, Fabian Panzer, Thomas Unger, Anna Köhler and Tobias Brixner
   The Journal of Chemical Physics 142 (**2015**) 212429

   I prepared the solutions that were measured. I measured all steady-state absorption and emission spectra used in the manuscript. I analysed the transient absorption data which described the population dynamics in the framework of a broad rate distribution by using a Kohlrausch-Williams-Watts (KWW) representation of the experimental data. I was heavily involved in the discussion of the results and interpretation of the findings. Furthermore I wrote minor parts of the manuscript and reviewed the overall manuscript.

5. **The Temperature Induced Order-Disorder Transition in Solutions of Conjugated Polymers Probed by Optical Spectroscopy**
   Fabian Panzer, Heinz Bässler, Anna Köhler
   Invited Feature Article, The Journal of Physical Chemistry B (prepared for submission)

   I conceived the idea and designed the structure of the manuscript. I performed all additional temperature dependent absorption and emission measurements for BEH-PPV (Polymer and Oligomers), MEH-PPE and PFO. I analysed the temperature dependent absorption and emission spectra for MEH-PPE, PFO, BEH-PPV (Polymer and Oligomer). I interpreted the data. Together with Anna Köhler and Heinz Bässler I wrote the manuscript. I furthermore reviewed and edited the overall manuscript and graphs and developed the overall summary table.

6. **Reversible Laser Induced Amplified Spontaneous Emission from Coexisting Tetragonal and Orthorhombic Phases in Hybrid Lead Halide Perovskites**
   Fabian Panzer, Sebastian Baderschneider, Tanaji Gujar, Thomas Unger, Marius Jakoby, Sergey Bagnich, Heinz Bässler, Jürgen Köhler, Ralf Moos, Mukundan Thelakkat, Richard Hildner, Anna Köhler
   Advanced Optical Materials (**2016**), DOI: 10.1002/adom.201500765

   I conceived the idea and designed the experiments under supervision from Anna Köhler and Ralf Moos. I performed all temperature dependent and fluence dependent steady-state emission measurements. I assisted Sebastian Baderschneider to carry out the spatial resolved measurements. Together with Anna Köhler and Richard Hildner I wrote the manuscript.

7. **Effect of Thermal and Structural Disorder on Electronic Structure of Hybrid Perovskite Semiconductor $CH_3NH_3PbI_3$**
Shivam Singh, Cheng Li, Fabian Panzer, K. L. Narasimhan, Anna Gräser, Tanaji P. Gujar, Anna Köhler, Mukundan Thelakkat, Sven Huettner, and Dinesh Kabra
(**2016**) submitted

Based on the PL data which were taken for the manuscript "Reversible Laser Induced Amplified Spontaneous Emission from Coexisting Tetragonal and Orthorhombic Phases in Hybrid Lead Halide Perovskites" I performed further analysis on the PL data. I fitted the high energy edge of the PL spectra at different temperatures and analysed the obtained fit parameters. I calculated and interpreted the temperature dependent Stokes shift. I interpreted the temperature dependent PL data and wrote the part of the manuscript which correlates to the PL data. I was heavily involved in the interpretation of the measured and analysed data. I furthermore reviewed and edited the overall manuscript and graphs.

8. **Compact Layers of Hybrid Halide Perovskites Fabricated via the Aerosol Deposition Process – Uncoupling Material Synthesis and Layer Formation**
Fabian Panzer, Dominik Hanft, Tanaji Gujar, Frank-Julian Kahle, Mukundan Thelakkat, Anna Köhler, Ralf Moos
Materials 9 (**2016**), 277

I assisted Dominik Hanft with the aerosol deposition of the perovskite powder and Tanaji Gujar taking the SEM images. I performed the absorption and emission measurements of the sample. I analysed and prepared all measured data and wrote the manuscript.

4.2. The Impact of Polydispersity and Molecular Weight on the Order – Disorder Transition in Poly(3-hexylthiophene)

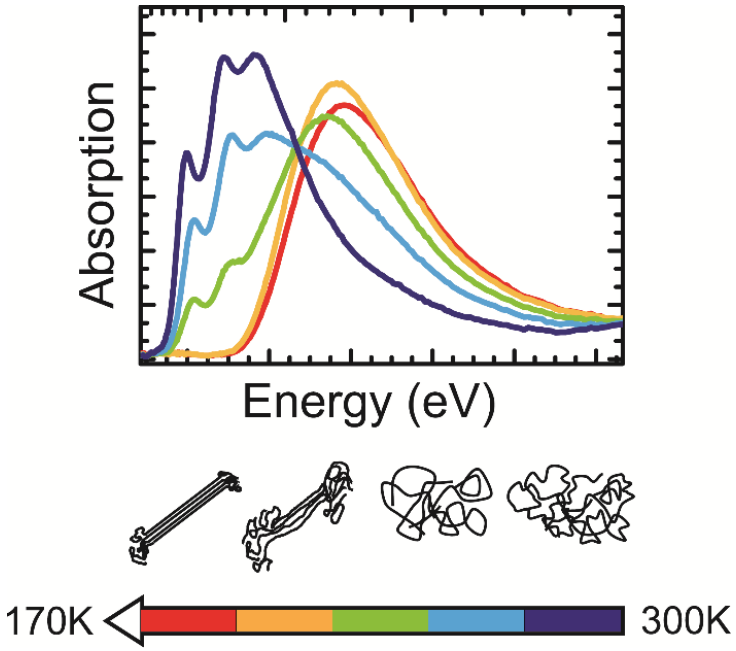

Fabian Panzer, Heinz Bässler, Ruth Lohwasser, Mukundan Thelakkat and Anna Köhler

Published in
The Journal of Physical Chemistry Letters
DOI: 10.1021/jz5009938

THE JOURNAL OF PHYSICAL CHEMISTRY Letters

Letter

pubs.acs.org/JPCL

The Impact of Polydispersity and Molecular Weight on the Order–Disorder Transition in Poly(3-hexylthiophene)

Fabian Panzer,[†,‡] Heinz Bässler,[‡] Ruth Lohwasser,[‡,§] Mukundan Thelakkat,[‡,§] and Anna Köhler*[,†,‡]

[†]Experimental Physics II, [‡]Bayreuth Institute of Macromolecular Science, and [§]Applied Functional Polymers, Macromolecular Chemistry 1, University of Bayreuth, 95540 Bayreuth, Germany

Supporting Information

ABSTRACT: Conjugated poly(3-hexylthiophene) (P3HT) chains are known to exist at least in two distinct conformations: a coiled phase and a better ordered aggregated phase. Employing steady state absorption and fluorescence spectroscopy, we measure the course of aggregation of P3HT in tetrahydrofuran (THF) solution within a temperature range of 300 K to 170 K. We show that aggregation is a temperature controlled process, driven by a thermodynamic order–disorder transition. The transition temperature increases with the molecular weight of the chains and can be rationalized in the theory of Sanchez. This implies a smearing out of the phase transition in samples with increasing polydispersity and erodes the signature of a first order phase transition. The detection of a hysteresis when undergoing cooling/heating cycles further substantiates this reasoning.

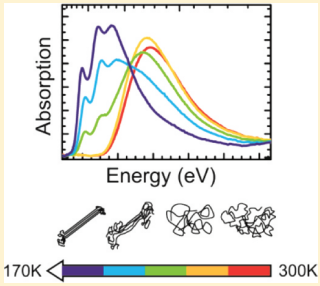

SECTION: Glasses, Colloids, Polymers, and Soft Matter

It is well-known that upon cooling a solution of a conjugated polymer such as polydiacetylene,[1,2] poly(*p*-phenylenevinylene),[3,4] polyfluorene[5] and polythiophene,[6−8] aggregation occurs. A signature of this phenomenon is the red-shift of absorption and fluorescence spectra accompanied by spectral narrowing. This indicates that in the aggregated phase, the polymer chains are more extended and consequently more ordered. Since in conjugated polymers change in carrier transport is predominantly disorder-controlled, there is a strong endeavor[9] to understand how to introduce short-range order in electronic devices such as field-effect transistors, organic solar cells, or organic light-emitting diodes (OLEDs) with conjugated polymers as active materials. Since the polymer films are usually processed from solution, strategies are needed toward the formation of ordered structures that exist already in solution and are preserved during solution processing.[10] To this end, we characterize aggregation in solution of poly(3-hexylthiophene) (P3HT), which is a preferred material used for efficient organic solar cells. Stimulated by preceding work on poly(2-methoxy-5-(2′ethyl-hexoxy)-1,4-phenylene-vinylene) (MEH-PPV) in solution, we studied the aggregation of P3HT in tetrahydrofuran (THF) solution as a function of temperature, molecular weight, and polydispersity. In essence we find that aggregation is, in principle, a first-order transition from a coil to an ordered phase that is smeared out with progressing polydispersity of the chains because the transition temperature depends on molecular weight.

For our studies, we used P3HTs synthesized by a modified Grignard metathesis reaction method as described elsewhere.[11] Due to this synthetic method, the samples have a very low polydispersity index (PDI) and thus a very narrow molar mass distribution. The number-average molecular weight (M_n) and the weight-average molecular weight (M_w) were measured by gel permeations chromatography (GPC) in THF with polystyrene as the calibration standard as well as matrix-assisted laser desorption ionization-time-of-flight mass spectroscopy (MALDI-TOF MS). The polydispersity indices of the low PDI samples were obtained by the GPC data, while the numbers of repeating units, i.e., the degree of polymerization (DP), were determined from the MALDI-TOF measurements, within an experimental uncertainty of 2 repeating units. Commercial P3HT (P3HT-COM) was purchased from American Dye Sources Ltd. (ADS), Canada, and shows a comparable molecular weight to P3HT-19, but a higher PDI of 2.0. Table 1 gives an overview of the relevant properties of the

Table 1. Overview of the Used Materials and Their Corresponding Properties: The Number-Average Molecular Weight (M_n) (Obtained by Both GPC and MALDI-TOF Measuerments), Weight-Average Molecular Weight (M_w), Resulting Polydispersity Index (PDI = M_w/M_n), and Degree of Polymersiation (DP) (Obtained by MALDI-TOF Measurements)

method	GPC			MALDI-TOF MS	
notation	M_n (g/mol)	M_w (g/mol)	PDI	M_n (g/mol)	DP
P3HT-5	5100	6300	1.22	3200	19
P3HT-11	11 300	12 500	1.11	7100	43
P3HT-19	18 600	21 600	1.16	12 400	74
P3HT-34	34 200	39 400	1.15	24 000	144
P3HT-COM	18 800	38 400	2.04	n.a.	n.a.

Received: May 19, 2014
Accepted: July 17, 2014
Published: July 17, 2014

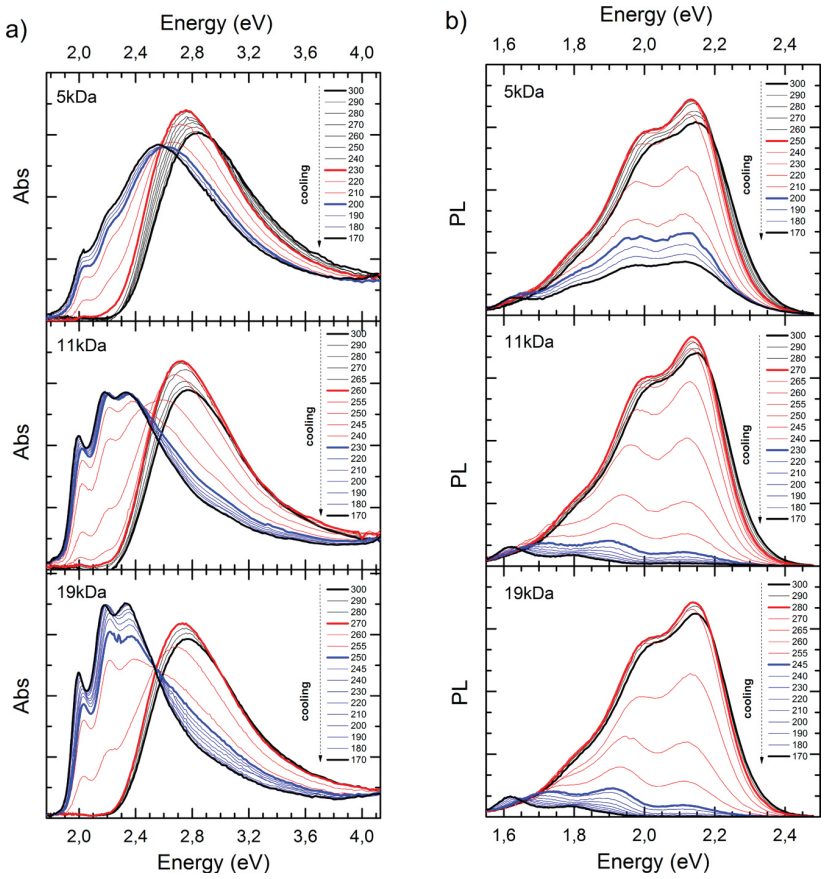

Figure 1. Temperature-dependent absorption (a) as well as corresponding emission spectra (b) for the three Polymers P3HT-5100 (top), P3HT-11 (middle) and P3HT-19 (bottom) in THF, differing in their molecular weight. The spectra are taken from 300 to 170 K in steps of 10 K (usually) or 5 K (near the transition temperature).

used materials including the notation used. We like to note that in the P3HT series used here, the polymer chains do not fold up to a size-exclusion chromatography (SEC) molecular weight of ~20 kg/mol (MALDI ~ 12 kg/mol) both in bulk and in thin films on cooling from melt.[12]

All samples were dissolved in THF at a concentration of 0.1 mg/mL. To ensure that all of the polymer chains are completely dissolved, the solutions were heated to 40−50 °C and stirred for about 10 to 30 min, depending on the molecular weight. Absorption and emission spectra at different temperatures were recorded with a home-built setup. The solutions were filled into a fused silica cuvette with 1 mm path length and put into a temperature-controlled continuous flow cryostat (Oxford instruments). In order to minimize the light intensity impinging on the sample, we use two correlated monochromators for incident as well as transmitted light. The latter is recorded by a silicon diode and a lock-in-amplifier.

For emission measurements, the xenon lamp and the first monochromator are replaced via a shutter by a diode laser with an excitation wavelength at 405 nm (3.06 eV), exciting the sample at a shallow angle. Emission is recorded by the same detection unit. This ensures recording absorption and fluorescence spectra at the same sample spot and temperature immediately after one another. All spectra were corrected for the transmission of the setup, using an oriel calibration lamp. Sample heating or cooling was done in a stepwise fashion with a heating or cooling rate of 2K per min and waiting 45 min before taking the measurement at a given temperature. Absorption as well as emission spectra for the three polymers with different molecular weight and low polydispersity (P3HT-19, P3HT-11, and P3HT-5) were measured within the temperature range from 300 to 170 K, which is the glass temperature of THF (Figure 1). While decreasing the temperature from 300 K down to 170 K, we were able to observe three distinct temperature ranges (see Table 2 for an overview of all relevant temperatures and shifts).

Table 2. Overview of the Corresponding Concrete Values of the Discussed Three Temperature Ranges for Three Samples with Low Polydispersity

polymer	range 1 Abs (Pl) (K)	range 2 (K)	range 3 (K)
P3HT-19	300−270 (280)	265−250	250−170
P3HT-11	300−260 (270)	250−230	230−170
P3HT-5	300−230 (250)	220−200	200−170

At 300 K, the absorption spectra are broad and structureless. When cooling from 300 K to the onset of the phase transition (temperature range 1), the maxima of the spectra feature a red shift by 35−50 meV, accompanied by an increase in intensity of about 10%.

When further decreasing the temperature and entering the temperature range 2, a vibrational resolved absorption spectrum appears with a S_1-S_0 0−0 feature (A_1) at 2.0 eV and a

dx.doi.org/10.1021/jz5009938 | J. Phys. Chem. Lett. 2014, 5, 2742−2747

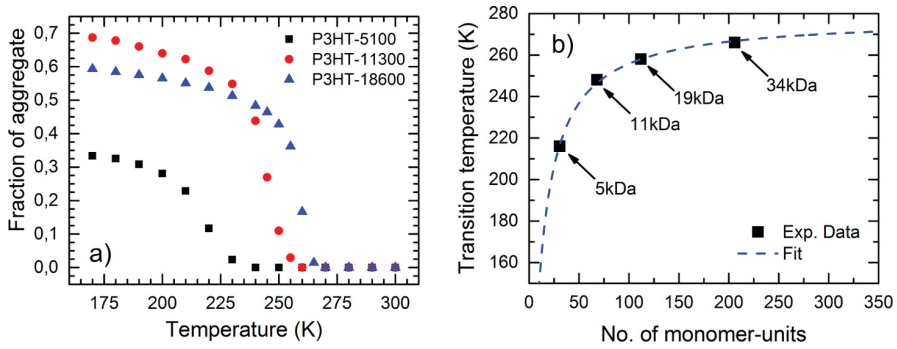

Figure 2. (a) Fraction of aggregates in the solution as a function of temperature for the three different P3HTs. (b) The dependence between the critical transition temperature and molecular weight and a fit using eq 2.

vibrational satellite at 2.2 eV (A_2 feature). At the same time, absorption from the high energy region (above 2.5 eV) is decreasing and an isosbestic point at about 2.5 eV is observed. These main spectral changes take place within a small temperature range of approximately 20−30K. Upon subsequent cooling, the A_1-Peak shifts toward lower energies and becomes more intense.

At 300 K, all the fluorescence spectra are more structured compared to the corresponding absorption spectra with a main emission peak at approximately 2.16 eV and a second peak at about 1.99 eV. Within temperature range 1, i.e., between 300 K and the onset of the phase transition, the emission of the samples shifts to lower energies and the overall intensity increases. This is in analogy to absorption spectra. Within temperature range 2, a distinct loss of intensity and simultaneously change in the ratio between the peaks at 2.15 and 2.0 eV can be observed. This effect is more pronounced for P3HT-19 and P3HT-11. At temperatures below the phase transition (temperature range 3), a structured low energy emission spectra can be observed. For both P3HT-19 and P3HT-11 emission from the former pronounced peak at 2.15 eV vanishes. Instead a low energy peak at 1.9 eV appears at 240 K that shifts to 1.8 eV at 170 K. This is complementary to the behavior of the low energy peak observed in corresponding absorption spectra. In contrast to P3HT-19 and P3HT-11 within this temperature range, the emission spectrum of P3HT-5 is more intense and basically retains its original structure except for additional spectral broadening.

In general, the broad absorption and corresponding emission spectra observed within the first temperature range (e.g., at 300 K) can be associated with P3HT chains in the coiled state,[13,14] while the red-shifted, well-structured absorption and emission spectra observed with the temperature below the phase transition (e.g., at 170 K) are assigned to weakly interacting H-type aggregates in which the chains are more planar and more extended.[15−18] Therefore, we interpret the data shown in Figure 1 as the signature of a temperature-induced stepwise phase transition from coiled phase toward aggregated P3HT. The observed initial red shift within the first temperature range is associated with an increase in conjugation length of the coiled phase,[19] and a concomitant increase in oscillator strength of the polymer chains.[20] This is the signature of an initial planarization process of the coiled chains within the first temperature range. The existence of an isosbestic point at 2.5 eV in the absorption spectra within the second temperature regime indicates that P3HT chains are gradually transformed from coiled to an aggregated state.[21] Within the temperature range 3 the aggregate absorption spectra bear out a further redshift. This can be a signature of an increase in conjugation length due to an improved planarization of the aggregates or to spectral diffusion due to energy transfer within aggregates. The strong decrease in overall intensity compared to emission from coiled phase demonstrates that in the aggregated phase the chains form H-aggregates.[8]

In order to further investigate the temperature-dependent conformational behavior of P3HT in solution, the measured absorption spectra were deconvoluted into the spectra of the aggregated and coiled polymer chains, following the approach of Scharsich et al.[22] Here the absorption spectrum of pure coiled phase was scaled to the high energy shoulder of the respective spectra and subtracted acquiring the fraction of pure aggregate absorption. Taking into account the difference of oscillator strength between coiled and aggregated polymer chains as described in the Supporting Information, the fraction of aggregates f_{aggr} in solution was obtained as a function of temperature for all three samples (Figure 2a). Here we can see that aggregation starts at lower temperatures for lower molecular weights (P3HT-19 at 265 K, P3HT-11 at 255 K, and P3HT-5 at 230 K). Below these temperatures, all samples show a steep increase in aggregate fraction within a temperature range of about 20−30 K. After that, the fraction of aggregate saturates for these three samples toward the lowest measured temperature. At 170 K, the maximum fraction of aggregates reached is 60% for P3HT-19, 70% for P3HT-11, and 32% for P3HT-5. These values (especially for P3HT-19 and P3HT-11) are consistent with typical values found in the literature,[8,22,23] indicating that the maximum fraction of aggregate is independent of the way the samples are prepared.

The experiments demonstrate that molecular weight of the polymers used has a significant influence on which temperature the transition takes place. We infer the critical temperature from the inflection point in the fraction of aggregate as a function of temperature:

$$\left.\frac{\partial^2 f_{aggr}}{\partial T^2}\right|_{T_c} = 0 \qquad (1)$$

Figure 2b shows that the obtained critical temperatures T_c increase as a function of the number of monomer units for four polymers.

Based upon mean field theory, Sanchez showed that an infinite chain undergoes a second-order phase transition from a swollen coil to a collapsed globule upon cooling below a critical

dx.doi.org/10.1021/jz5009938 | J. Phys. Chem. Lett. 2014, 5, 2742−2747

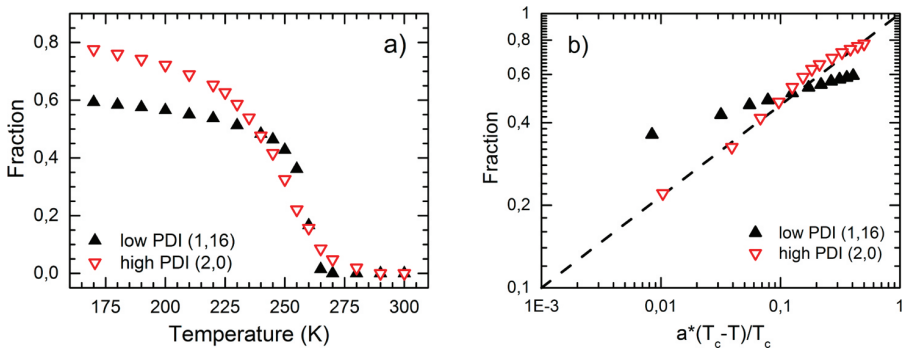

Figure 3. Comparison between the fraction of aggregates of P3HT-19 with low PDI and P3HT-COM with high PDI, (a) as a function of temperature, and (b) as a function of the reduced temperature $a((T_c - T)/T_c)$ plotted double logarithmically. Here, the dashed line indicates a slope of 0.33, representing the expected course for a second order phase transition.

(transition) temperature T_c.[24] In finite systems, this transition becomes pseudo-second order and depends on the chain stiffness. The theory predicts that the critical temperature scales with the number of repeat units N of the chains as

$$\frac{\theta - T_c}{T_c} = \frac{\varphi}{\sqrt{N}} \tag{2}$$

where φ is a constant that depends on the chain stiffness and the so-called theta temperature θ is the critical temperature of an infinite chain. Figure 2b shows that eq 2 provides an excellent fit for T_c as a function of the monomer units and thus the molecular weight of the polymer chains, with fitting parameters $\varphi = 8.7 \pm 0.3$ and $\theta = (278 \pm 1)$ K.

Experiments on samples with similar molecular weight yet different polydispersity (P3HT-COM) shed further light on the nature of this transition. Figure 3a reveals clear differences regarding the temperature dependence of the fraction of aggregates. On one hand, the maximum fraction of aggregate at around 77% for P3HT-COM at a temperature of 170 K is approximately 20% higher compared to the corresponding value for P3HT-19. Furthermore, the shape of the transition seems to be more undefined and more continuous for the P3HT-COM sample compared to the samples with low polydispersity. By contrast, the critical temperatures T_c for the samples with low and high polydispersity are nearly identical, indicating that in this case polydispersity plays no role. If a coil−globule transition in an infinite chain was a second-order transition, it should be described by

$$f_{aggr}(T) \sim \left(\frac{T_c - T}{T_c}\right)^a, \quad a = 0.33 \tag{3}$$

where f_{aggr} is the fraction of the ordered chains.[3] In order to identify the order of the transition, we plotted f_{aggr} versus the reduced temperature $(T_c - T)/T_c$ on a double logarithmic scale (Figure 3b). The dashed line indicates a slope of 0.33, representing a second-order phase transition. The good quality of the fit for the data of P3HT-COM (PDI = 2.0) is, indeed, reminiscent as a second order phase transition. However, for the sample P3HT-19 with low polydispersity, a clear deviation from the second-order course (dashed line in Figure 3b) is obvious. Therefore, we conclude that polydispersity determines the temperature-dependent shape and any assignment to a second order phase transition is accidental. As the transition temperature depends on molecular weight, obviously a broad distribution of chain lengths for high PDI samples smears out the shape of the transition. Considering the steep transition for the low PDI sample, we conclude that in the limit of a well-defined chain length the transition is of first order. This is in accordance with the work of Cone et al. on the formation of the β-phase in poly(9,9′-dioctylfluorene) (PFO).[5]

Figure 4 shows that in P3HT-19, there is a hysteresis regarding the fraction of aggregates observed upon sample

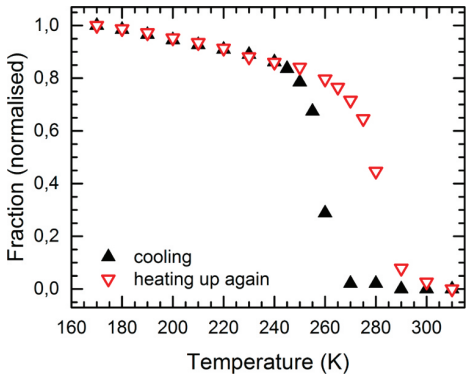

Figure 4. Normalized intensity of the A_1-Peak gathered from absorption spectra while going through a cooling/heating cycle. Waiting time to ensure thermal stability within the solution was set to 45 min between every temperature.

cooling and heating. In order to asses a possible influence of waiting time between two consecutive 10 K temperature jumps, the waiting time was increased up to 90 min. Here we found that the waiting time has virtually no effect on the hysteresis (see SI). This suggests that the hysteresis is linked to an enhanced thermal stability of planarized structures. It was suggested this may be due to side chain ordering occurring after aggregation of the main chains[25] which could lead to different polymorphs.[26] However, we cannot rule out the possibility that the formation or dissolution of the aggregates during stepwise sample cooling or heating is kinetically hindered which is often the case in first order transitions. Experiments with different heating/cooling rates would be required to tell this possibility.

In summary, we show that the aggregation of P3HT in solution by lowering temperature can be described as a phase transition from coiled phase toward aggregated P3HT. The process is a sequence of swelling of the coiled phase, formation of aggregates, and further planarization of the aggregate. This is consistent with recent simulation of the initial crystallization

dx.doi.org/10.1021/jz5009938 | J. Phys. Chem. Lett. 2014, 5, 2742−2747

process of P3HT in solution.[25] The authors conclude that this nucleation process is the sequence of three steps, i.e., ring orientation, elongation of the main chain and, finally ordering the side chains. The bathochromic shift of the unstructured absorption spectrum of P3HT above T_c is likely to be a signature of the first step. We find that the subsequent elongation of the chains and their concomitant collapse to ordered aggregates appears as a thermodynamic first order process.

Our results are corroborated by Monte Carlo simulations by Kolinski and co-workers, who constrast the nature of the coil−globule transition for flexible and for stiffer polymers.[27] They find that, whereas flexible chains collapse to an essentially Gaussian, tight random coil, finite length polymers that have a considerable degree of stiffness collapse into an ordered state such as a rod-like bundle. Kolinski et al. compare this collapse to the denatured-to-native transition in globular proteins. The simulations predict that upon lowering the temperature, the dimensions of the stiffer chains first increase until the chain suddenly undergoes a pseudo-first-order phase transition to an ordered dense state. Kolinski and co-workers attribute the initial increase in chain dimension to the dominance of freezing out rotational degrees of freedom over attractive interactions. They suggest this prepares the chain just above the transition in conformation composed of stiff sections connected by "flexible" linkages, which thus primes the polymer to collapse into an ordered structure.

The dependence between molecular weight of the used polymer and the critical temperature of the transition can be rationalized in terms of the theory of Sanchez. In samples with higher polydispersity, realized in commercial samples, there is a superposition of different transition temperatures of chains of different lengths. This obscures the first-order character of the transition. The hysteresis regarding the fraction of ordered chains upon undergoing cooling/heating cycles is tentatively attributed to side chain ordering.

■ ASSOCIATED CONTENT

Supporting Information

Determination of oscillator strength in the aggregate, impact of waiting time on the hysteresis of the fraction of aggregates. This material is available free of charge via the Internet at http://pubs.acs.org.

■ AUTHOR INFORMATION

Corresponding Author

*E-Mail: anna.koehler@uni-bayreuth.de.

Notes

The authors declare no competing financial interest.

■ ACKNOWLEDGMENTS

We acknowledge financial support by the Bavarian State Ministry of Science, Research, and the Arts through the Collaborative Research Network 'Solar Technologies go Hybrid' and by the German Science Foundation DFG through the doctoral training center GRK1640. We thank Günter Reiter from Albert-Ludwigs-Universität Freiburg for helpful discussion.

■ REFERENCES

(1) Rughooputh, S. D. D. V.; Bloor, D.; Phillips, D.; Jankowiak, R.; Schütz, L.; Bässler, H. Fluorescence Studies of Polydiacetylenes in 2-Methyltetrahydrofuran Vitreous Glasses at Low Temperatures. *Chem. Phys.* **1988**, *125*, 355−373.

(2) Chance, R. R.; Patel, G. N.; Witt, J. D. Thermal Effects on the Optical Properties of Single Crystals and Solution-Cast Films of Urethane Substituted Polydiacetylenes. *J. Chem. Phys.* **1979**, *71*, 206−211.

(3) Köhler, A.; Hoffmann, S. T.; Bässler, H. An Order-Disorder Transition in the Conjugated Polymer MEH-PPV. *J. Am. Chem. Soc.* **2012**, *134*, 11594−11601.

(4) Pichler, K.; Halliday, D. A.; Bradley, D. D. C.; Burn, P. L.; Friend, R. H.; Holmes, A. B. Optical Spectroscopy of Highly Ordered Poly(*p*-phenylene vinylene). *J. Phys.: Condens. Matter* **1993**, *5*, 7155.

(5) Cone, C. W.; Cheng, R. R.; Makarov, D. E.; Vanden Bout, D. A. Molecular Weight Effect on the Formation of Beta Phase Poly(9,9′-dioctylfluorene) in Dilute Solutions. *J. Phys. Chem. B* **2011**, *115*, 12380−12385.

(6) Ferreira, B.; da Silva, P. F.; Seixas de Melo, J. S.; Pina, J.; Macanita, A. Excited-State Dynamics and Self-Organization of Poly(3-hexylthiophene) (P3HT) in Solution and Thin Films. *J. Phys. Chem. B* **2012**, *116*, 2347−2355.

(7) Berson, S.; De Bettignies, R.; Bailly, S.; Guillerez, S. Poly(3-Hexylthiophene) Fibers for Photovoltaic Applications. *Adv. Funct. Mater.* **2007**, *17*, 1377−1384.

(8) Clark, J.; Chang, J.-F.; Spano, F. C.; Friend, R. H.; Silva, C. Determining Exciton Bandwidth and Film Microstructure in Polythiophene Films Using Linear Absorption Spectroscopy. *Appl. Phys. Lett.* **2009**, *94*, 163306.

(9) Duong, D. T.; Ho, V.; Shang, Z.; Mollinger, S.; Mannsfeld, S. C. B.; Dacuña, J.; Toney, M. F.; Segalman, R.; Salleo, A. Mechanism of Crystallization and Implications for Charge Transport in Poly(3-ethylhexylthiophene) Thin Films. *Adv. Funct. Mater.* **2014**, n/a−n/a.

(10) Khan, A. L. T.; Sreearunothai, P.; Herz, L. M.; Banach, M. J.; Köhler, A. Morphology-Dependent Energy Transfer within Polyfluorene Thin Films. *Phys. Rev. B* **2004**, *69*, 085201.

(11) Lohwasser, R. H.; Thelakkat, M. Toward Perfect Control of End Groups and Polydispersity in Poly(3-hexylthiophene) via Catalyst Transfer Polymerization. *Macromolecules* **2011**, *44*, 3388−3397.

(12) Singh, C. R.; Gupta, G.; Lohwasser, R.; Engmann, S.; Balko, J.; Thelakkat, M.; Thurn-Albrecht, T.; Hoppe, H. Correlation of Charge Transport with Structural Order in Highly Ordered Melt-Crystallized Poly(3-hexylthiophene) Thin Films. *J. Polym. Sci., Part B: Polym. Phys.* **2013**, *51*, 943−951.

(13) Hotta, S.; Rughooputh, S. D. D. V.; Heeger, A. J.; Wudl, F. Spectroscopic Studies of Soluble Poly(3-alkylthienylenes). *Macromolecules* **1987**, *20*, 212−215.

(14) Brown, P. J.; Thomas, D. S.; Köhler, A.; Wilson, J. S.; Kim, J.-S.; Ramsdale, C. M.; Sirringhaus, H.; Friend, R. H. Effect of Interchain Interactions on the Absorption and Emission of Poly(3-hexylthiophene). *Phys. Rev. B* **2003**, *67*, 064203.

(15) Clark, J.; Silva, C.; Friend, R. H.; Spano, F. C. Role of Intermolecular Coupling in the Photophysics of Disordered Organic Semiconductors: Aggregate Emission in Regioregular Polythiophene. *Phys. Rev. Lett.* **2007**, *98*, 206406.

(16) Park, Y. D.; Lee, H. S.; Choi, Y. J.; Kwak, D.; Cho, J. H.; Lee, S.; Cho, K. Solubility-Induced Ordered Polythiophene Precursors for High-Performance Organic Thin-Film Transistors. *Adv. Funct. Mater.* **2009**, *19*, 1200−1206.

(17) Oh, J. Y.; Lee, T. I.; Myoung, J.-M.; Jeong, U.; Baik, H. K. Coating on a Cold Substrate Largely Enhances Power Conversion Efficiency of the Bulk Heterojunction Solar Cell. *Macromol. Rapid Commun.* **2011**, *32*, 1066−1071.

(18) Spano, F. C. Absorption in Regio-Regular Poly(3-hexyl)-Thiophene Thin Films: Fermi Resonances, Interband Coupling and Disorder. *Chem. Phys.* **2006**, *325*, 22−35.

(19) Hoffmann, S. T.; Bässler, H.; Köhler, A. What Determines Inhomogeneous Broadening of Electronic Transitions in Conjugated Polymers? *J. Phys. Chem. B* **2010**, *114*, 17037−17048.

(20) Valeur, B. Absorption of UV−Visible Light. In *Molecular Fluorescence*; Wiley-VCH Verlag GmbH: Weinheim, Germany, 2001; pp 20−33.
(21) Cohen, M. D.; Fischer, E. 588. Isosbestic Points. *J. Chem. Soc. (Resumed)* **1962**, 3044.
(22) Scharsich, C.; Lohwasser, R. H.; Sommer, M.; Asawapirom, U.; Scherf, U.; Thelakkat, M.; Neher, D.; Köhler, A. Control of Aggregate Formation in Poly(3-hexylthiophene) by Solvent, Molecular Weight, and Synthetic Method. *J. Polym. Sci., Part B: Polym. Phys.* **2012**, *50*, 442−453.
(23) Nagarjuna, G.; Baghgar, M.; Labastide, J. A.; Algaier, D. D.; Barnes, M. D.; Venkataraman, D. Tuning Aggregation of Poly(3-hexylthiophene) within Nanoparticles. *ACS Nano* **2012**, *6*, 10750−10758.
(24) Sanchez, I. C. Phase Transition Behavior of the Isolated Polymer Chain. *Macromolecules* **1979**, *12*, 980−988.
(25) Takizawa, Y.; Shimomura, T.; Miura, T. Simulation Study of the Initial Crystallization Processes of Poly(3-hexylthiophene) in Solution: Ordering Dynamics of Main Chains and Side Chains. *J. Phys. Chem. B* **2013**, *117*, 6282−6289.
(26) Koch, F. P. V.; Heeney, M.; Smith, P. Thermal and Structural Characteristics of Oligo(3-hexylthiophene)s $(3HT)_n$, $n = 4−36$. *J. Am. Chem. Soc.* **2013**, *135*, 13699−13709.
(27) Kolinski, A.; Skolnick, J.; Yaris, R. The Collapse Transition of Semiflexible Polymers. A Monte Carlo Simulation of a Model System. *J. Chem. Phys.* **1986**, *85*, 3585−3597.

Supporting information to:

The impact of polydispersity and molecular weight on the order-disorder transition in P3HT

Fabian Panzer[†], Heinz Bässler[‡], Ruth Lohwasser[§], Mukundan Thelakkat[§], Anna Köhler[†].

[†]Experimental Physics II and Bayreuth Institute of Macromolecular Science, University of Bayreuth, 95540 Bayreuth, Germany

[‡]Bayreuth Institute of Macromolecular Science, University of Bayreuth, 95440 Bayreuth, Germany

[§]Applied Functional Polymers, Macromolecular Chemistry 1 and Bayreuth Institute of Macromolecular Science, University of Bayreuth, 95440 Bayreuth, Germany

Determination of oscillator strength in the aggregate:

We derived the relative change in oscillator strength between the aggregated and coiled phase, $\varepsilon_{agg}/\varepsilon_{coil}$, as described in detail in the supporting informations of J. Clark et al[1] and in C. Scharsich et al[2], using

$$\frac{A_{aggregate}}{A_{coil}} = -\frac{\varepsilon_{aggregate}}{\varepsilon_{coil}}$$

with the areas taken from the shades regions as illustrated in Fig. S1. Using the change in oscillator strength thus derived and the change observed in the absorption spectra upon cooling, the fraction of aggregated chains was derived.

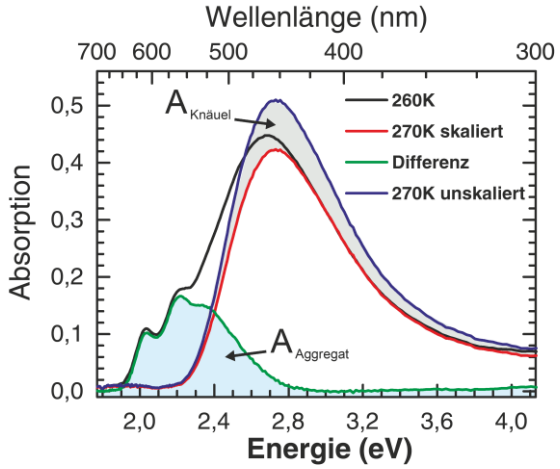

Figure S1: Exemplary illustration of the procedure to determine the change in oscillator strength between coiled and aggregated phase of P3HT. The required areas A_{coil} and $A_{aggregate}$ are highlighted.

For comparison, we have also determined the fraction of aggregates by considering the intensity of the A_1-Absorption peak of the aggregate as a function of temperature. Both methods yield the same temperature dependence (see Figure S2).

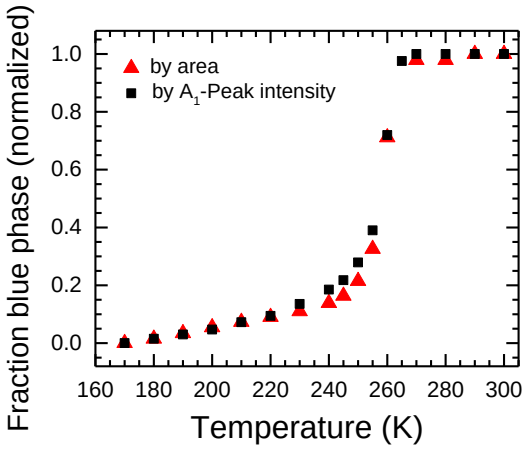

Figure S2: Normalised fraction of coiled phase derived by two different methods as a function of temperature.

Impact of waiting time on the hysteresis of the fraction of aggregates:

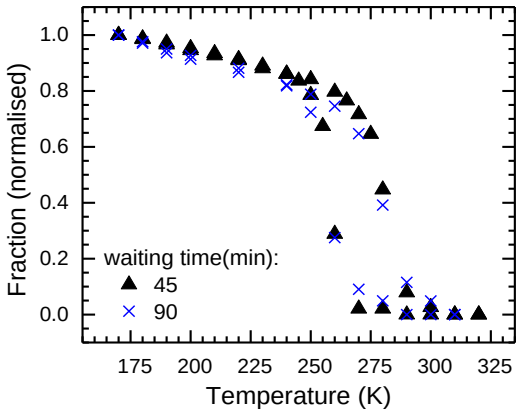

Figure S3: Normalised fraction of aggregate as a function of temperature while going through a cooling/heating cycle for two different waiting times between two consecutive temperatures.

References:

(1) Clark, J.; Chang, J.-F.; Spano, F. C.; Friend, R. H.; Silva, C. *Applied Physics Letters* **2009**, *94*, 163306.

(2) Scharsich, C.; Lohwasser, R. H.; Sommer, M.; Asawapirom, U.; Scherf, U.; Thelakkat, M.; Neher, D.; Kohler, A. *J Polym Sci Pol Phys* **2012**, *50*, 442.

4.3. The Spectroscopic Signature of Two Distinct H-Aggregate Species in Poly(3-hexylthiophene)

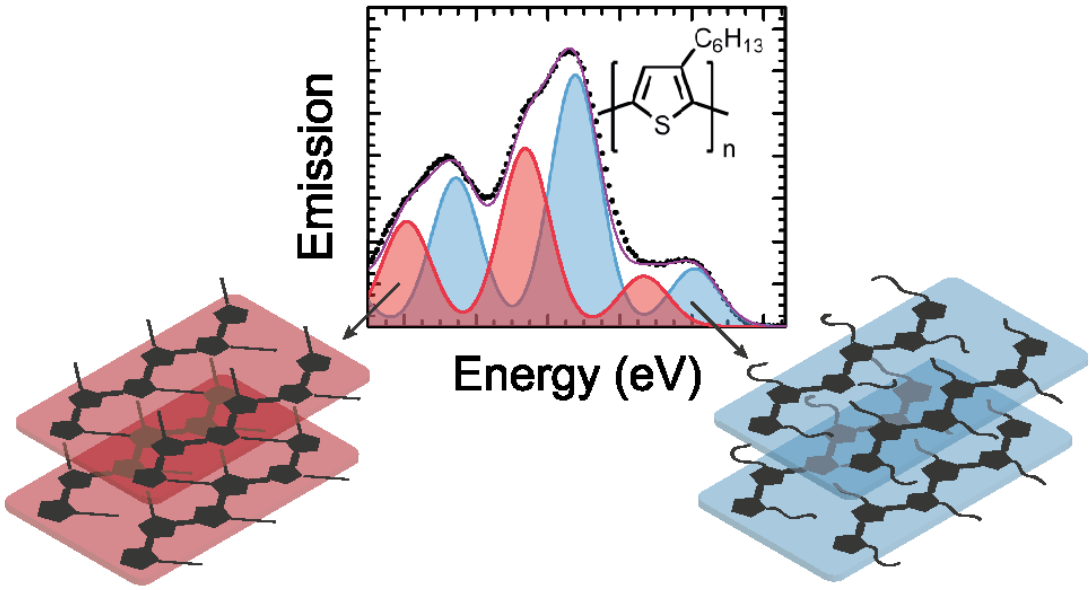

Fabian Panzer, Michael Sommer, Heinz Bässler, Mukundan Thelakkat and Anna Köhler

Published in
Macromolecules
DOI: 10.1021/acs.macromol.5b00129

Macromolecules

Article

pubs.acs.org/Macromolecules

Spectroscopic Signature of Two Distinct H-Aggregate Species in Poly(3-hexylthiophene)

Fabian Panzer,[†,‡] Michael Sommer,[§] Heinz Bässler,[‡] Mukundan Thelakkat,[§] and Anna Köhler*[,†,‡]

[†]Experimental Physics II, [‡]Bayreuth Institute of Macromolecular Research (BIMF), and [§]Applied Functional Polymers, Macromolecular Chemistry I, University of Bayreuth, 95540 Bayreuth, Germany

Supporting Information

ABSTRACT: In an endeavor to correlate the optoelectronic properties of π-conjugated polymers with their structural properties, we investigated the aggregation of P3HT in THF solution within a temperature range from 300 to 5 K. By detailed steady-state, site-selective, and time-resolved fluorescence spectroscopy combined with Franck−Condon analyses, we show that below a certain transition temperature (265 K) aggregates are formed that prevail in different polymorphs. At 5 K, we can spectroscopically identify two H-type aggregates with planar polymer backbones yet different degree of order regarding their side chains. Upon heating, the H-character of the aggregates becomes gradually eroded, until just below the transition temperature the prevailing "aggregate" structure is that of still phase-separated, yet disordered main and side chains. These conclusions are derived by analyzing the vibrational structure of the spectra and from comparing the solution spectra with those obtained from thin films that were cooled slowly from the melting temperature to room temperature and that had been analyzed previously by various X-ray techniques. In addition, site selectively recorded fluorescence spectra show that there is—dependent on temperature—energy transfer from higher energy to lower energy aggregates. This suggests that they must form clusters with dimensions of the exciton diffusion length, i.e., several nanometers in diameter.

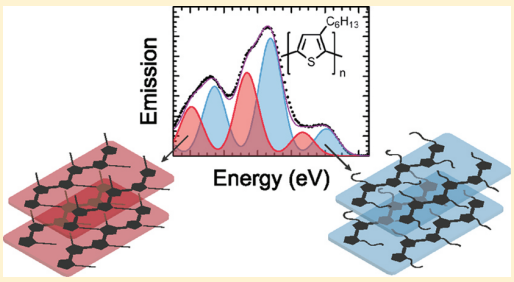

1. INTRODUCTION

A characteristic feature of organic solids is that electronic coupling among the constituting elements is weak yet it controls their optoelectronic properties. Deliberate or unintentional modification of the morphology has therefore a significant impact on the electronic properties such as the transport of charge carriers and the dissociation of excitations, i.e., excitons.[1−4] Currently there is strong endeavor toward understanding and controlling the relation between film morphology and electronic structure in devices such as solar cells and field effect transistors, using conjugated polymers as active elements, with a view to improve their performance.[5,6] Even though, understanding the formation of self-assembled structures in rigid or semirigid conjugated polymers which are typically processed out of solution is still less studied, especially compared to the large body of work established for flexible, nonconjugated polymers.

A material that emerged as a workhorse, notably in field of organic photovoltaics,[7−11] is regioregular poly(3-hexylthiophene) (P3HT). Since the discovery that in regioregular P3HT the charge carrier mobility measured in the field effect transistor configuration is much higher than in regiorandom P3HT,[12−14] much effort is currently spent on the understanding and improvement of structural order on P3HT. Depending on solvent, temperature, molecular weight, and sample preparation, it can exist in an amorphous phase with coiled chain conformations or in an aggregated phase containing planarized chains with some propensity to form semicrystalline domains.[11] These aggregates can be of an H-type or of a J-type nature, depending on the strength of interchain to intrachain coupling. The transition from one coupling regime to the other—reported in particular for P3HT nanofibers—depends sensitively to molecular weight and regioregularity of the sample.[15−18] It is also well established that P3HT can adopt different morphologies; i.e., it is polymorph.[19−23] In different morphologies, the separation and orientation of the polymer segments are different with the consequence that the electronic properties depend on the morphology.[24]

It is important to realize that, while being a workhorse, P3HT is not a singular case but rather a model for other technologically useful conjugated polymers. All of them have more or less stiff backbones and are therefore prone to adopt semicrystalline morphologies. For example, the poly(p-phenylene) derivative MEH-PPV has been shown to undergo a similar disorder−order phase transition upon cooling a solution similar P3HT,[25] and the polyfluorene derivative PFO is well-known for adopting an amorphous phase or an ordered β-phase.[26]

In structural studies including various techniques of X-ray diffraction and microscopy, different polymorphs of P3HT-

Received: January 21, 2015
Revised: February 18, 2015
Published: February 27, 2015

DOI: 10.1021/acs.macromol.5b00129
Macromolecules 2015, 48, 1543−1553

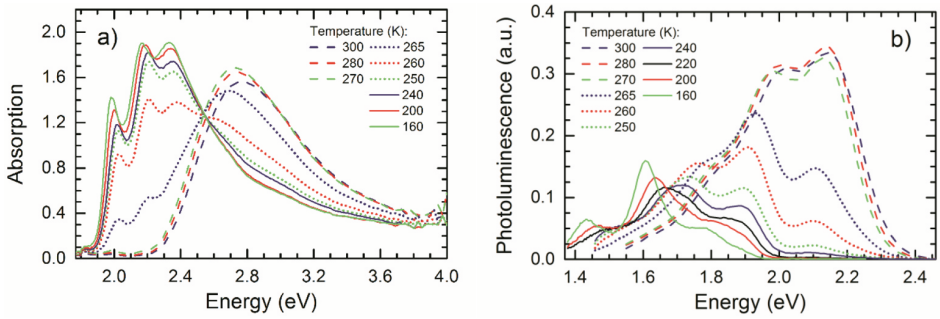

Figure 1. Absorption (a) as well as fluorescence spectra (b) of P3HT in THF solution for different temperatures. Spectra that belong to the three inherent temperature ranges described in the text are indicated with different lines (dashed, dotted, and straight). Emission spectra were corrected for the relative changes in absorption at 3.06 eV (being the excitation energy for all fluorescence spectra).

aggregates have been identified. For example, the work of Prosa et al. and Mena-Osteritz et al. identified H-aggregates with interdigitated side chains that form on graphite surfaces or, to a small amount, under certain spin-casting conditions.[27,28] They can also be prepared by self-seeding approaches.[29] This polymorph of P3HT is frequently referred to as "form II".[23,27] More common, however, are H-aggregates with noninterdigitating, noncrystalline side chains,[27,30−32] also known as "form I".[23,27] They form in a layer structure of separated main and side chains, where the main chains may adopt either a liquid, smectic-like packing, or a regular, crystalline packing. While the latter is thermodynamically more stable, its formation is frequently kinetically hindered.

These structural techniques provide valuable insight into the existing polymer morphologies and their formation processes. They can, however, be too elaborate or time-consuming to be applied routinely to the characterization of films that are to be used in device structures. A comparatively fast and simple approach to identify the presence of different H-aggregates in films (or solutions) is to measure their fluorescence spectra, yet this method requires that the spectral signatures of different polymorphs be known.

Here, we have studied the formation of H-aggregates in solution of tetrahydrofuran (THF) upon continuous cooling from room temperature to 5 K with the aim to identify the evolution of their spectral signatures. We find that the spectral shape of the H-aggregate emission evolves continuously. From the first appearance of aggregate emission at 265 K, the spectrum changes from a vibrational structure that essentially matches that of a nonaggregated chain to one with a strongly suppressed 0−0 transition peak at 160 K and below. Importantly, closer inspection identifies emission from two distinct, coexisting polymorphs. Notably, these two polymorphs are not the "form I" and "form II" mentioned in the literature (ref 19). Rather, they are two variants of "form I". Thus, the fluorescence features are assigned to H-aggregates in a layer structure of separated main and side chains. In both polymorphs, the main chain is crystalline and the side chains are noninterdigitated. Higher energy emission results for a polymorph with disordered side chains while lower energy emission is observed for a polymorph with crystalline (and still noninterdigitated) side chains. Emission from both polymorphs is also observed and assigned to in neat thin films, which is the form in which P3HT is used in optoelectronic devices.

2. EXPERIMENTAL SECTION

2.1. Sample Preparation. For our studies, we used P3HT synthesized by a modified Grignard metathesis reaction method as described elsewhere.[33] Because of this synthetic method, the sample has a very narrow molar mass distribution and thus a very low dispersity index (D = 1.16). The number-average molecular weight (M_n = 18 600 g/mL) and the weight-average molecular weight (M_w = 21 600 g/mL) were measured by gel permeations chromatography (GPC) in tetrahydrofuran (THF) with polystyrene as a calibration standard. The number of repeating units was determined to 74 ± 2 by MALDI-TOF measurements. The sample thus contains exactly one tail-to-tail defect that is distributed along the entire chain.[34] For all solution measurements, we dissolved the polymer in THF at a concentration of 0.2 mg/mL. To ensure that all of the polymer chains are completely dissolved, the solution was heated to 40−50 °C and stirred for about 30 min, so that no macroscopic particles could be observed any more. For the measurements, the solution was filled in a 1 mm cuvette that could be sealed and inserted into a cryostat.

To carry out measurements on thin films, two films of P3HT were spin-coated with 2000 rpm for 60 s from 10 mg/mL THF solution onto silicon wafers covered with a natural oxide layer in nitrogen atmosphere. One film was heated subsequently in nitrogen atmosphere to 250 °C, i.e., above the melting temperature of P3HT at 230 °C,[30] and cooled slowly to room temperature at a rate of 1 K/min using a programmable heating plate (Model HP60 from Torrey Pines Scientific Inc.). In contrast to that, the other film was used without any further treatments after spin-coating.

2.2. Steady-State Absorption and Emission Measurements. To measure steady-state absorption as well as emission spectra for different temperatures, we used a home-built setup that allows us to record absorption and fluorescence spectra at the same sample spot immediately after each other for each temperature step. In brief, the sample (a 1 mm cuvette with solution or a film) was placed in an Oxford Instruments cryostat. Sample heating or cooling was done in a stepwise fashion with a rate of about 2 K/min and an equilibration time of 30 min before taking the measurement. For absorption measurements, the light from a xenon lamp was dispersed through a first monochromator M1, transmitted through the sample, dispersed through a second monochromator M2, and eventually recorded by a silicium diode connected to a lock-in amplifier.

For emission measurements a flip mirror switched the incident light to a diode laser with excitation wavelength 405 nm. The laser beam was incident onto the sample at an angle of about 60° to the normal. The resulting fluorescence was dispersed through the monochromator M2 and recorded by the silicium diode connected to the lock-in amplifier. The spectra were corrected for the transmission of the setup. A more detailed description of the setup can be found elsewhere.[35]

To measure the emission in a site selective fashion, we replaced the diode laser by a pulsed Nd:YAG laser with a pulse width of 7 ns. Tunable excitation was obtained by converting the 355 nm pulse by an optical parametric oscillator from GWU that covers a continuous spectral range from 410 to 710 nm. The resulting emission was then

DOI: 10.1021/acs.macromol.5b00129
Macromolecules 2015, 48, 1543−1553

recorded using a glass fiber connected to a spectrograph (Oriel MS125) with an attached CCD camera (Andor iDus DU420).

2.3. Time-Resolved Emission Measurements. Time-dependent emission spectra were recorded using a streak camera setup, with the sample held again in a cryostat from Oxford Instruments. Light from a 80 MHz pulsed Chameleon II laser from Coherent was frequency doubled by a second-harmonics generator to provide an excitation energy of 3 eV. The emitted light was diffracted through an Acton SP-2300i spectrograph and eventually recorded by an Optronis SC-10 streak camera combined with a TSU12-10 deflection unit and a SRU-BA detection unit.

3. RESULTS

3.1. Temperature Dependence of the Aggregate Emission. For a detailed spectroscopic investigation of the P3HT electronic structure in the aggregated phase, we measured absorption as well as emission spectra in THF solution within the temperature range from 300 K down to the melting point of THF (Figure 1), which is at about 160 K.[36] As discussed in detail in previous work,[35] P3HT undergoes a disorder−order transition upon cooling. In the spectra shown in Figure 1, three regimes can be discerned. In the temperature range from 300 to 270 K, i.e., above the phase transition temperature, the absorption spectra are broad and structureless, indicating that the chains are disordered.[14,37] The bathochromic shift by 40 meV of the maxima and the increase in intensity of about 7% that is observed upon cooling from 300 to 270 K indicate an increased conjugation length that suggests a swelling-up process of the chain backbone. This red-shift and intensity increase are also reflected in the associated fluorescence spectra, which are overall more structured, featuring a $S_1 \rightarrow S_0$ 0−0 emission peak at 2.15 eV and a vibrational satellite at about 2.0 eV. When lowering the temperature from 265 to 250 K, a vibrationally resolved absorption spectrum appears with a $S_1 \leftarrow S_0$ 0−0 feature at 2.0 eV. The spectra at different temperatures feature an isosbestic point at 2.53 eV. This is the signature of the occurrence of a phase transition from the disordered to a more ordered phase.[35] The associated changes in the fluorescence spectra have been attributed to the emergence of an additional emission feature with a 0−0 peak at 1.90 eV that overlaps with the 0−1 emission feature of the disordered phase and that grows in relative intensity at the expense of the emission from the disordered phase upon cooling to 250 K. This additional emission has been assigned to the fluorescence of the ordered phase. Upon subsequent cooling in the temperature range below the phase transition, i.e., from 240 to 160 K, the 0−0 absorption peak of the ordered phase shifts toward lower energies and becomes more intense, while the 0−0 emission peak of the ordered phase appears to reduce in intensity. Both absorption and emission spectra feature a very similar bathochromic shift.

The analysis and interpretation of the development evident in the spectral part attributed to the aggregated phase require a deconvolution of the emission from disordered and ordered phases. The procedure is illustrated in Figure 2. We consider that the fluorescence spectrum well above the phase transition temperature, e.g. at 280 K, contains only emission from the disordered phase. To confirm this, Figure 2a illustrates that the 280 K fluorescence spectrum can be modeled satisfactorily in terms of a Franck−Condon progression.[38] This implies that the energy dependence of the photoluminescence $P(\hbar\omega)$, normalized to the cube of the refractive index n (assumed to be constant within the investigated spectral range), to the cube

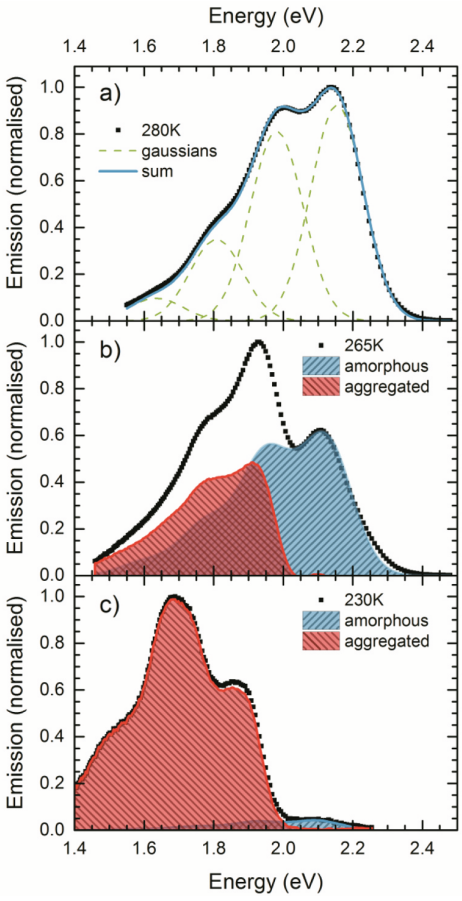

Figure 2. Illustration of isolating the fluorescence spectra of the aggregate phase at selected temperatures. (a) The 280 K fluorescence of the amorphous phase (black squares) is modeled by a Franck−Condon analysis (blue solid line) using an effective mode (green dashed line). (b, c) The 280 K spectrum (blue) is scaled to the high-energy tail of the 265 and 230 K emission spectra (black squares). The difference between the two spectra (red) is assigned to emission from the aggregated phase.

of the photon energy $\hbar\omega$ and to the intensity of the 0−0 vibrational peak I_{0-0}, is given by

$$\frac{P(\hbar\omega)}{n^3(\hbar\omega)^3 I_{0-0}} \sim \sum_{m=0} \frac{S^m}{m!} \Gamma\delta[\hbar\omega - (E_0 - mE_d)] \quad (1)$$

where $S = 1.1$ is the Huang−Rhys factor of an effective vibrational mode with energy $E_d = 0.175$ eV,[4] Γ is the Gaussian line width function with the standard deviation σ, and E_0 denotes the energy of the 0−0 transition. Once the phase transition sets in, i.e., for temperatures below 265 K, the spectra cannot be modeled as progressions from one emitting state. As mentioned above, we consider the spectra to result from the superposition of emission from the disordered and ordered, aggregated phase. To isolate the emission from the aggregated phase, the 280 K emission spectrum is scaled to the high-energy side of the actual emission spectra between 265 and 160 K (here changes in E_0 and σ were allowed to account for the temperature dependency of these two parameters; see Figure S1 in the Supporting Information) and subtracted. The remaining emission is attributed to the aggregate phase (Figure 2b,c).

DOI: 10.1021/acs.macromol.5b00129
Macromolecules 2015, 48, 1543−1553

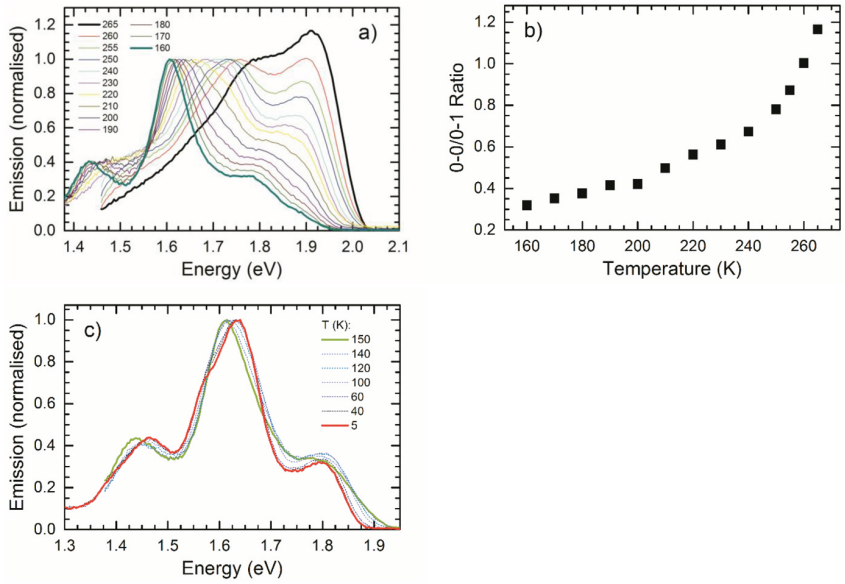

Figure 3. (a) Fluorescence spectra of aggregated P3HT in the temperature range from 265 to 160 K where the polymer chains are in fluid solution. The spectra are normalized to the intensity of the $S_1 \rightarrow S_0$ 0−1 feature. (b) Temperature dependence of the ratio of the 0−0/0−1 features of the $S_1 \rightarrow S_0$ transition in the same range. (c) Fluorescence spectra of aggregated P3HT recorded at temperatures between 160 and 5 K, where THF is crystalline.

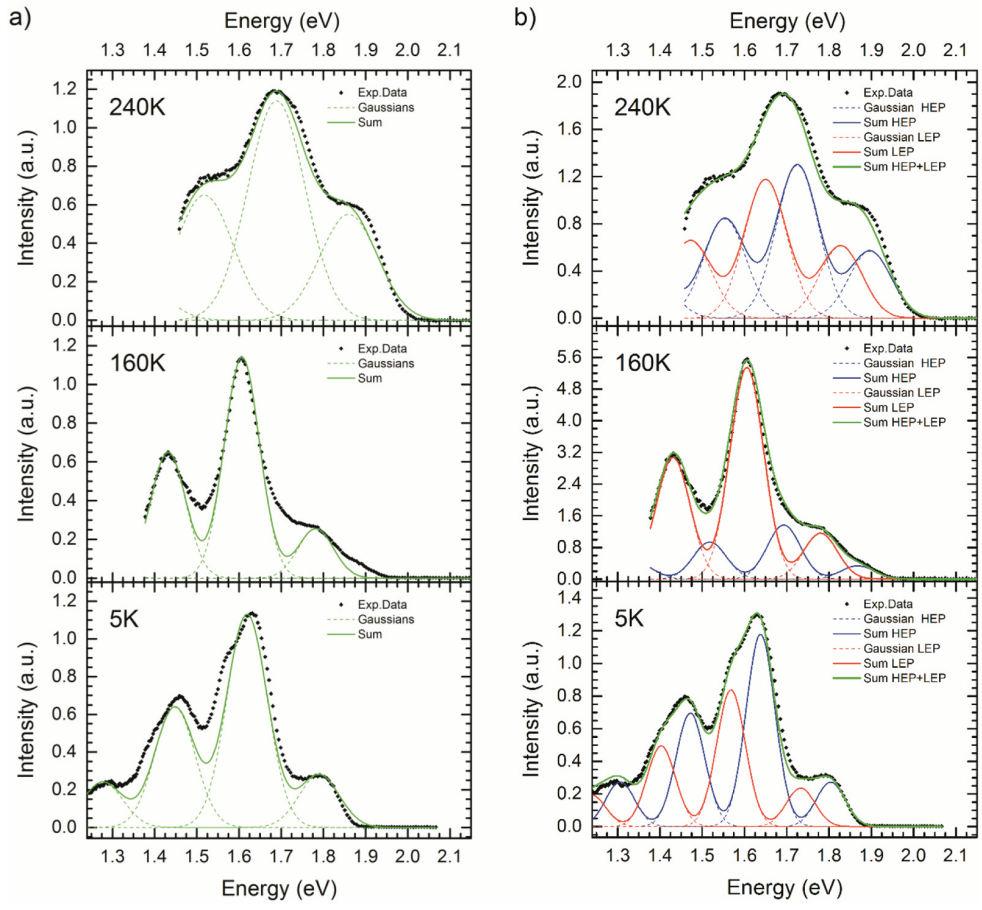

Figure 4. (a) Modified Franck−Condon analysis according to eq 2 (green solid line) of the fluorescence spectra (black squares) of P3HT aggregates at 240, 160, and 5 K using a single vibronic progression (green dotted line). (b) The same as in (a) but using a superposition of a higher energy progression (HEP) (blue solid line) and a lower energy progression (LEP) (red solid line).

DOI: 10.1021/acs.macromol.5b00129
Macromolecules 2015, 48, 1543−1553

Figure 3a shows the normalized spectra of aggregate emission in the temperature range of 265−160 K. Note the change in abscissa scale between Figures 2 and 3. The spectra show a pronounced 0−0 feature at 1.9 eV, which shifts to 1.77 eV while decreasing the temperature down to 160 K. Remarkably, the ratio of the 0−0/0−1 vibrational peak intensities decreases continuously from about 1.2 at 265 K to 0.3 at 160 K (Figure 3b). Additional emission spectra were also measured for the temperature range between 160 and 5 K (Figure 3c). Since below 160 K THF is in a crystalline phase,[36] the spectra correspond to P3HT chains embedded in a rigid THF matrix. This preludes major conformal changes. Accordingly, there is only a minor bathochromic shift when decreasing the temperature from 150 to 5 K. In this temperature range it was not possible to measure absorption spectra because the THF matrix is opaque.

3.2. Evidence for Two Different Aggregate Phases. While the deconvolution of the fluorescence spectra described above is sufficient for an overall assessment of evolution of the character of the aggregates, it is unable to account for important details regarding the identification of their structure. For this reason we carried out a modified (compared to eq 1) Franck−Condon analysis based upon the approach by Clark et al.[39] It takes into account the decrease of the 0−0 peak intensity in the fluorescence spectra when the chromophores form H-aggregates. The fluorescence is then described by

$$\frac{P(\hbar\omega)}{n^3(\hbar\omega)^3} \sim \alpha\Gamma(\hbar\omega - E_0) + \sum_{m=1} \frac{S^m}{m!}\Gamma\delta \times [\hbar\omega - (E_0 - mE_d)] \quad (2)$$

The term $\alpha\Gamma(\hbar\omega - E_0)$, in which α is the scaling factor, accounts for the fact that in a disordered H-aggregate the 0−0 feature of the fluorescence spectrum is suppressed. For a perfectly ordered H-aggregate, α would be zero since the 0−0 transition was symmetry-forbidden. The symbols take the same meaning than for eq 1. The scaling factor α, the energy E_0 of the 0−0 transition, and the standard deviation σ of the Gaussian line width were allowed to change with temperature, while the Huang−Rhys parameter S = 1.1 and the effective vibrational mode energy E_d = 0.175 eV were kept constant. Figure 4a shows three emission spectra at representative temperatures. While the spectrum at 240 K can be described satisfactory by a single progression with one effective vibrational mode, deviations between the Franck−Condon analysis and the experimental data appear at 160 K. In particular, the data show an additional shoulder at 1.9 eV and a less structured spectral shape that cannot be accommodated when using one progression. Using additional and/or different vibrational modes does not help to overcome these deviations in spectral shape and furthermore cannot be used to explain the additional observed emission intensity in the range of 1.9 eV, being higher than the proposed 0−0 energy at 1.8 eV. At 5 K, the vibrational peaks at 1.62 and 1.45 eV carry additional low-energy shoulders that cannot be modeled in terms of a single Franck−Condon progression, even when hypothetically considering additional/altered vibrational modes.

As an alternative approach, we considered the superposition of two similar, modified Franck−Condon progressions according to eq 2, i.e., a higher energy progression (HEP) with a 0−0 transition centered at about 1.9 eV for the 160 K spectrum and a lower energy progression (LEP) shifted by about 80 meV to lower energies (see Figure 4b). It turns out that the superposition of the HEP and LEP provides an excellent fit to the experimental spectra in the entire temperature range, while analyzing the low-temperature spectra in terms of a single modified Franck−Condon progression was unsuccessful. Figure 5 shows the relevant spectral parameters.

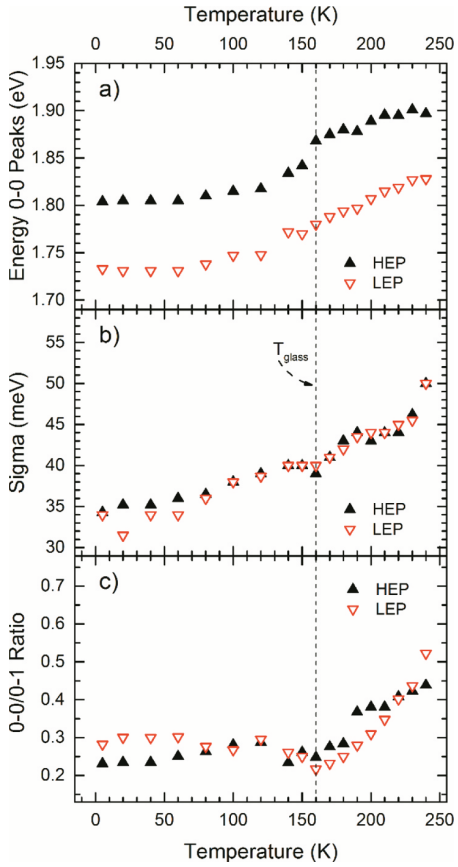

Figure 5. Fit parameters derived from the modified Franck−Condon analysis of the fluorescence spectra of P3HT aggregates using two energetic different progressions (HEP, LEP) as a function of temperature. (a) Energies of the 0−0 emission, (b) standard deviations σ of the 0−0 feature, and (c) ratio of 0−0 and 0−1 emission. The dashed vertical line indicates the glass transition temperature of THF.

The 0−0 energy of the LEP (HEP) fluorescence spectrum shifts from 1.91 eV (1.83 eV) at 240 K to 1.8 eV (1.72 eV) to 5 K, while the energy difference between the HEP and the LEP is temperature independent (Figure 5a). Within the experimental uncertainty both the Gaussian disorder parameter σ and the ratio of 0−0/0−1 emission peaks are the same for the HEP and LEP. The disorder parameter decreases continuously from 50 meV at 240 K to 35 meV at 5 K (Figure 5b). The 0−0/0−1 ratios behave similarly and decrease as a function of temperature, starting at values at around 0.5 at 240 K and saturating in the range of 0.23−0.28 for the lowest temperatures (Figure 5c). Thus, the spectral analysis of the fluorescence spectra suggests the spectra to arise from the superposition of two emissions that have the same H-type nature and that are subject to the same inhomogeneous broadening yet that differ in transition energy by about 80 meV.

The necessity to involve two Franck−Condon progressions instead of only one is also borne out by an analysis of the absorption spectra. To do this, we use a modified Franck−

DOI: 10.1021/acs.macromol.5b00129
Macromolecules 2015, 48, 1543−1553

Condon Fit developed by Spano et al.[40−43] which takes into account the influence of intermolecular coupling on the absorption spectrum of aggregates.

$$\frac{A(\hbar\omega)}{n(\hbar\omega)} \sim \sum_{m=0} \frac{S^m}{m!}\left(1 - \frac{We^{-S}}{2E_d}\left(\sum_{n\neq m} \frac{s^n}{n!(n-m)}\right)\right)^2 \times \Gamma\delta[\hbar\omega - (E_0 + mE_d)] \quad (3)$$

where W defines the exciton bandwidth (and n being the vibrational quantum number).

The difference between the Franck−Condon (FC) progression simulating the absorption of the aggregated phase and the experimental spectra, i.e., the residue, should represent the absorption spectrum of P3HT in the disordered phase. We find that similar to the case of emission, modeling the spectra using only one progression (see Figure S2 in the Supporting Information) is unsuccessful. The sharp 0−0 peak at about 1.9 eV limits the Gaussian line width of the Franck−Condon analysis and results in a residue that reveals a vibronic progression and overall shape that are at variance with the absorption spectra of the disordered phase shown in Figure 1a. Successful modeling of the absorption spectra is, however, possible by using a superposition of two progressions according to eq 3. The two progressions have a spectral offset of about 100 meV, comparable to that in emission. Figure 6 shows the absorption measured at 160 K, along with the two FC progressions, their superposition, and the residue. The progressions used an exciton bandwidth of W = 70 meV. Analogous to the simulation of the fluorescence spectra of the aggregates, we used constant values of S = 1.1 and E_d = 0.175 eV while the energy E_0 of the 0−0 transition and the standard deviation σ of the Gaussian line width were allowed to change with temperature. Using two progressions, the residue matches well with the absorption of disordered P3HT (cf. Figure 1a). Thus, the analysis of the absorption spectra corroborates the conclusion of two H-aggregates drawn from the analysis of the fluorescence spectra.

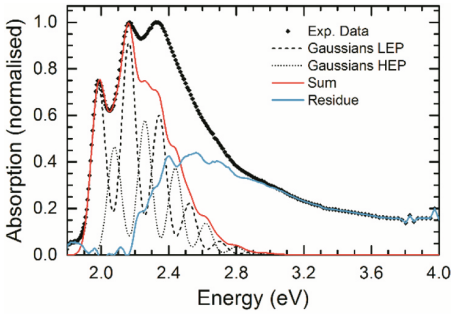

Figure 6. Absorption spectra of P3HT (black squares) at 160 K as well as the Franck−Condon analysis (red solid line) according to eq 3 using two progressions (black dashed and dotted lines).

The temperature dependence of the Gaussian disorder parameter σ as well as the energy E_0 of the $S_1 \leftarrow S_0$ 0−0 transition obtained from the analyses of the absorption and emission spectra are compared in Figure 7 for the lower energy progression LEP. The data for the higher energy progression HEP are analogous. Both parameters, σ as well as E_0, continuously decrease while cooling down the solution, with E_0 decreasing by 60 meV from 2.04 eV at 260 K down to 1.98 eV for 160 K (Figure 7a), and σ reducing by 14 meV from 57 meV toward 43 meV within the same temperature range (Figure 7b). The Stokes shift between the 0−0 features in absorption and emission is about 200 meV almost independent of the temperature (see Figure S3 in the Supporting Information). This comparable evolution of the progressions in absorption and emission is consistent with the existence of two H-aggregates that differ only slightly.

Further evidence for the presence of two different aggregate phases is derived from experiments employing the site selection technique. When scanning the excitation energy E_{ex} from 2.070 to 1.865 eV, the fluorescence spectra change in a characteristic way (Figure 8). This is most obvious in the 5 K emission spectrum. For excitation within a spectral range from 2.070 to 1.938 eV, the fluorescence spectrum changes only marginally and is characteristic of the higher energy (HEP) aggregate. When exciting at 1.908 eV a low-energy shoulder on the 0−1 feature appears. Upon further decreasing of E_{ex} to 1.865 eV, the 0−1 feature of HEP shifts by approximately 20 meV because tail states of the distribution of HEP states are addressed. In addition to this, the 0−1 transition of the lower energy aggregate (LEP) spectrum becomes the dominant feature. This is an unequivocal proof that the HEP and LEP emissions originate from different aggregates. It also demonstrates that at 5 K there is little communication between the two different aggregates. Otherwise, the fluorescence from the lower energy aggregates should be sensitized by exciting higher energy aggregates, contrary to experiment.

At 160 K, there are subtle differences in the evolution of the spectra upon scanning E_{ex} compared to the 5 K spectra. Again, the site selectively excited fluorescence from the aggregates is a superposition of emission from the higher energy progression

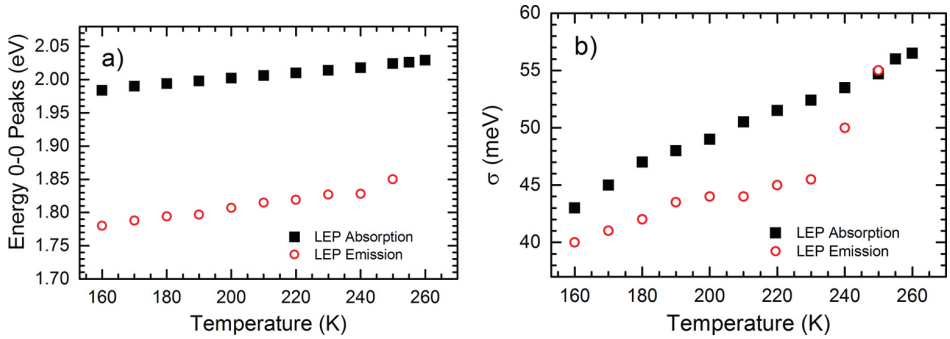

Figure 7. (a) Energies of the $S_1 \rightarrow S_0$ 0−0 peaks and (b) standard deviation σ for the low-energy progression (LEP) in absorption and emission.

DOI: 10.1021/acs.macromol.5b00129
Macromolecules 2015, 48, 1543−1553

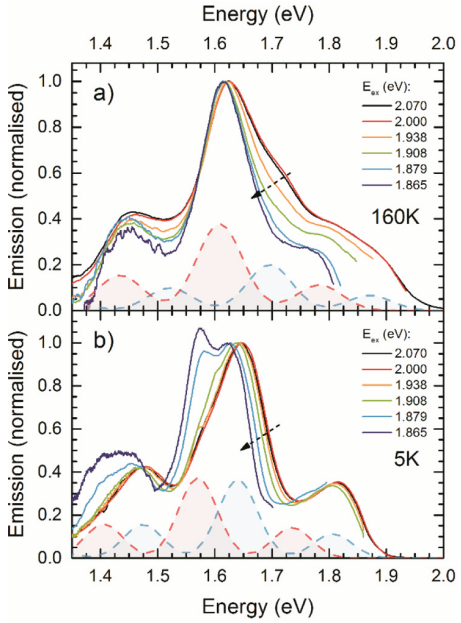

Figure 8. Fluorescence spectra (solid lines) of P3HT aggregates in THF parametric in the excitation energy E_{ex} (a) at 160 K and (b) at 5 K. The spectra are normalized to the intensity of the 0−1 feature. Spectra of corresponding HEP and LEP at those temperatures are also illustrated by dashed lines with filled area. The arrows indicate the direction of decreasing excitation energy.

and from the lower energy progression. In contrast to the 5 K spectra, the LEP is the dominant feature. Moreover, the spectral position of the LEP—traced most easily by considering its 0−1 peak at about 1.62 eV—remains nearly stationary when scanning E_{ex} from 2.070 to 1.865 eV, whereas the emission from the HEP shifts bathochromic by 18 meV (see Figure S4 for FC analysis on the site selected spectra). It seems that at 160 K there is temperature-dependent energy transfer from HEP to LEP which is frozen out at 5 K. This energy transfer from HEP to LEP at 160 K can also be seen when considering the time-dependent aggregate fluorescence spectra. Figure 9 shows spectra recorded within a time window of 15 ps for different times up to 6 ns after the excitation pulse at a temperature of 160 K. The spectra are normalized to unity at the approximate energy of the LEP 0−0 feature near 1.78 eV. It is evident how with increasing time the spectra reduce in relative intensity at the spectral positions corresponding to the 0−0 and 0−1 vibrational peaks of the HEP, i.e., at about 1.9 and 1.7 eV, whereas the relative intensity of the LEP 0−1 peak at about 1.6 eV increases. While a detailed analysis of the time dependence of this energy transfer is beyond the scope of the present paper, Figure 9 clearly corroborates the evidence for two emitting species brought forward by the site selectively recorded steady-state fluorescence spectra of Figure 8.

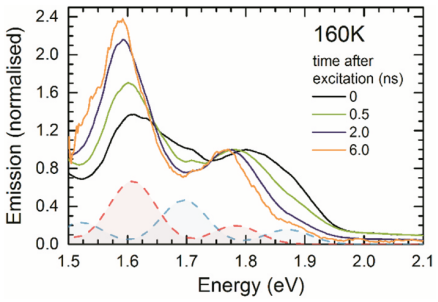

Figure 9. Normalized emission spectra (solid lines) of P3HT in THF for different times after the excitation pulse at 160 K. The spectra are normalized to unity at about 1.8 eV. For clarity, corresponding HEP and LEP are also illustrated by dashed blue and red lines.

3.3. Nature of the Two Aggregate Phases. Having ascertained the occurrence of two distinct, albeit similar, H-aggregate phases for P3HT in THF at temperatures below the phase transition, we were wondering first whether it would be possible to assign the spectra to specific P3HT morphologies and second whether the two different aggregate phases of P3HT that we identified in solution can exist also in a bulk film. To answer this question, we recorded emission spectra of differently prepared P3HT films on silicon wafers at a temperature of 5 K for different excitation energies E_{ex}. One film ("heated") was heated to 250 C under nitrogen and then cooled down slowly as described in the Experimental Section, while the other one ("as cast") was measured as spin-coated without any further treatment (Figure 10). This sample preparation protocol follows the approach taken by Wu et al.,[30] who studied the morphology of such films by X-ray scattering.

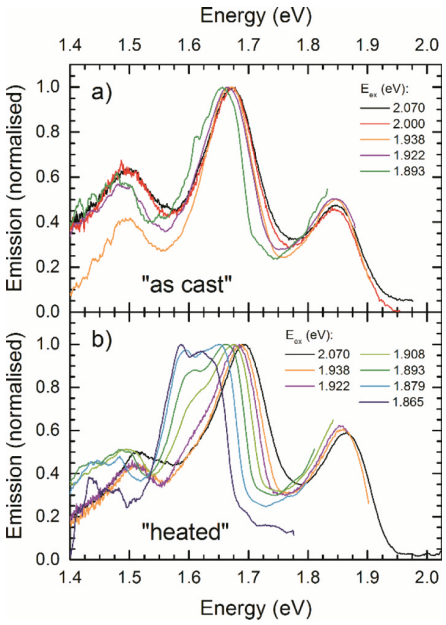

Figure 10. Normalized emission spectra of P3HT films at a temperature of 5 K for different excitation energies E_{ex}: (a) as-cast film; (b) a treated ("heated) film as described in the text.

The spectral shape of the emission spectrum of the "as-cast" film undergoes only minor changes when decreasing excitation energy E_{ex}. For excitation at 2.070 eV, it features a 0−0 vibrational peak at about 1.85 eV, a 0−1 peak at about 1.675 eV, and a 0−2 peak at about 1.50 eV. As evident most clearly when considering the 0−1 peak, the spectra shift to the red by only about 20 meV upon reducing the excitation energy by 177 meV to 1.893 eV. In contrast to this, the shape of the emission spectrum for the film, which was heated above its melting temperature, changes significantly for different excitation

DOI: 10.1021/acs.macromol.5b00129
Macromolecules 2015, 48, 1543−1553

energies. It appears to be made up by the superposition of two progressions. The higher energy progression has a 0−0 peak at about 1.85 eV and it is dominant for excitation at 2.070 eV, while roughly 80 meV below, a lower energy progression can be made out that is dominant for excitation at 1.865 eV. Analogous to the qualitative spectral changes for P3HT in THF at 5 K (Figure 8b), this LEP is first evident as an emerging shoulder in the 0−1 peak for excitation at 1.908 eV and then shifts to the red and becomes more and more intense for decreasing excitation energy. By comparing Figures 10b and 8b, it becomes obvious that the two aggregate phases (HEP and LEP) are formed both in THF solution and also when slowly cooling a P3HT film from above its melting temperature to room temperature.

4. DISCUSSION

The results obtained so far may be briefly summarized as follows. Figures 1−3 show that upon reducing the temperature of a THF solution of P3HT a transition from a phase with disordered chain conformations to a phase with ordered chains takes place. The emission from the ordered phase can be extracted, and it displays a continuous red-shift and concomitant reduction of the relative 0−0 peak intensity. From the analysis of the spectra in Figures 4−7, it becomes evident that absorption and emission of the ordered phase originate from two distinct, albeit similar, species. The two excitation features are both of the same H-type character (indicated by the same low value of the 0−0 peak intensity), are subject to the same degree of disorder (manifested in σ), and are separated by about 80 meV. The site-selective and time-dependent spectra of Figures 8−10 corroborate the evidence for two distinct excited states, which indicate that at elevated temperature energy transfer from the higher to the lower energy state can occur and that both H-type aggregates can also prevail in thin films when the processing conditions are chosen suitably.

4.1. Temperature Dependence of the Aggregate Emission. The emission spectra of aggregated conjugated polymers such as P3HT have been discussed in terms of the weakly interacting H/J aggregate model developed by Spano and co-workers.[39,42,44,45] This model considers chromophores that interact weakly by dipole−dipole coupling with a coupling energy that is less than the mean vibrational energy of the emission or absorption spectra. The resulting absorption and emission spectra of the H-type (= parallel dipole moments between the interacting chromophores) or J-type (= collinear dipole moments) aggregates still display a vibrational structure, albeit the intensities of the vibrational peaks are modified. In particular, the ratio between the 0−0 and 0−1 vibrational peaks depends strongly on the strength and character of the interchromophore coupling, yet also on the disorder present in the sample and on the sample temperature. In general, a 0−0/0−1 emission peak ratio that is enhanced compared to that prevailing in the nonaggregated chromophore indicates a J-type coupling, while a reduced emission peak ratio results from an H-type coupling. Upon reducing the temperature, the relative intensity of the 0−0 decreases (increases) further for a H-type (J-type) aggregate. The presence of disorder, quantified by the standard deviation σ of the inhomogeneously broadened Gaussian line shape, significantly moderates these effects.[46] We interpret the data shown in Figure 3a,b in this framework of weakly interacting H/J-aggregates.

The low-temperature emission spectrum taken at 160 K has a characteristic H-type aggregate character. This is evident from its vibrational structure that features a low 0−0/0−1 peak ratio and from the fact that it cannot be modeled using one or two common Franck−Condon progressions as expressed in eq 1. Rather, it requires the use of two similar, modified Franck−Condon progressions with reduced 0−0 peak as given by eq 2. Upon *raising* the temperature up to 265 K, the intensity of the 0−0 increases. Several factors contribute to this change in vibrational structure. (i) For a given value of interchain coupling and disorder in an H-aggregate, the relative intensity of the 0−0 peak increases with temperature and can approach the 0−0/0−1 ratio in the unaggregated molecule.[46] (ii) In addition, Figure 5b shows that in our sample the disorder itself increases with temperature, which further enhances the increase in the relative 0−0 intensity. (iii) This is intensified by thermal expansion upon heating, which increases the interchain distance thus reducing the interchain coupling. (iv) The observed hypsochromic shift upon raising the temperature suggests a reduction in conjugation length, implying an increase in interchain coupling that would counteract to some extent the increase in 0−0 caused by points i to iii.[46] The combination of these factors results in the observed overall increase in relative 0−0 peak intensity with temperature. Paradoxically at 265 K, the aggregate spectrum closely resembles that of a non-aggregated chain, except for the spectral position, as can be seen from Figure 2b. Evidently, the symmetry reasons that cause the 0−0 peak to vanish for a perfect weakly interacting H-aggregate at 0 K are lifted by temperature and disorder.

4.2. Evidence for Two Different Aggregate Phases. Testimony to the coexistence of two similar yet distinct weakly interacting H-type aggregates in THF solution is given (i) by the need to invoke two modified Franck−Condon progressions to model the emission and absorption data (Figures 4 and 6), (ii) by the ability to excite the two different aggregates selectively (Figure 8), and (iii) by the time-dependent fluorescence spectra at 160 K (Figure 9), where the spectral features at the position of the higher energy progression decay faster than the ones corresponding to the lower energy progression. These observations allow no other interpretation. The same two H-type aggregates also form in a thin film when it has been heated and allowed to cool slowly, while only one H-type aggregate prevails in a spin-cast film (Figure 10). Comparison of the spectra obtained from both films for excitation at 2.070 eV identifies the emission in the spin-cast film as arising from the higher energy progression. Thus, in a thin film structure, both polymorphs can be formed, yet the formation of the lower energy polymorph is kinetically hindered and requires suitable processing conditions. While several polymorphs of P3HT H-aggregates have been identified in structural studies, e.g., on the basis of wide-angle X-ray scattering and scanning tunneling microscopy,[23,27,28,30,31,47] the signatures of different polymorphs in optical spectroscopy have, to our knowledge, not been reported.

4.3. Nature of the Two Aggregate Phases. P3HT is known to exist in different phases that have been identified by structural studies.[27,28,30,31,47−49] Wu et al. used DSC, small-angle and wide-angle X-ray scattering, and AFM to investigate the structure of a P3HT film prepared in the same way and using material from the same batch as we use in our work.[30] They investigate the structural changes of P3HT upon cooling from the melt. In the isotropic melt, both the main chain and side chains are uncorrelated. For ease of reference, we shall call

DOI: 10.1021/acs.macromol.5b00129
Macromolecules 2015, 48, 1543−1553

this *phase 1*. It corresponds to morphology of the disordered phase in solution. Upon cooling below the melting point, the P3HT chains aggregate to form a layer structure of spatially separated main and side chains.[49] Both main and side chains are still disordered and liquid-like. We refer to this as *phase 2*. It exists only within a small temperature range until about 20 °C below the melting point. Upon further cooling, the main chains condense into a regular two-dimensional array. The polythiophene backbone is planar and crystallized while the side chains are still disordered (*phase 3*). Finally, when cooling below 50 °C, the chains adopt a three-dimensional crystalline topology with both main chains and side chains packed in a regular, ordered fashion (*phase 4*). By employing scanning electron microscopy and wide-angle X-ray scattering on P3HT nanowires and P3HT nanotubes in porous templates, Martín et al. confirm this basic sequence of structural ordering.[47] Very recently, the existence of two phases with planar backbone, one with ordered and one with disordered side chains, has also been reported by Brambilla et al. on the basis of Raman measurements.[48]

The phases 1 to 4 described here correspond to Figures 5e to 4b in Martín et al.[47] Note that the formation of the thermodynamically more favorable crystalline phases 3 and 4 can be kinetically hindered.[30] Independent of the processing method (cooling from melt, cooling a solution, reducing solution quality), the self-assembly process applies to about half of the material, with the other half remaining amorphous.[4,30,35]

These phases 1−4 are all characterized by side chains that are not interdigitated. In addition, a phase with interdigitated side chains has been reported (referred to as form II crystals). As mentioned above, such a structure can be formed under certain circumstances, e.g., on a graphite surface due to interfacial interactions,[28,31] when the polymer is subjected to other constraints during processing,[27] or in highly ordered single crystals grown from solution.[29] Since the interdigitated structure is accompanied by an increased π-stacking distance, it is easily converted, e.g. by moderate heating, to a thermodynamically more favorable structure with denser backbone packing, where π-stacking is optimized by placing the side chains into a noninterdigitated structure, tilted away from the backbone.[27,31] In particular, cooling from the melt leads to noninterdigitated structures.[27,30]

A key result of the present investigation is the recognition that in a P3HT film that has been slowly cooled from above the melting point to room temperature, the same two different H-aggregate species are found as in THF solution below the disorder−order phase transition. This is documented by Figures 8 and 10 and provides a link between the spectroscopy of those aggregates and their microscopic structure revealed in the recent structural studies. It allows to assign the fluorescence spectra of the higher energy (HEP) and lower energy (LEP) H-aggregates formed upon cooling P3HT in solution (see Figures 8 and 10). We can rule out an assignment of the HEP or LEP emission to an interdigitated H-aggregate structure for two reasons. First, as already mentioned, the interdigitated structure does not form upon cooling from a melt.[27,30] Second, in the interdigitated structure, the π-stacking distance is increased.[27,31] This would imply a reduced H-type coupling and thus concomitant a higher 0−0/0−1 ratio for the HEP or the LEP emission, at variance with experiment. Based on our observation that HEP and LEP emission are characterized by the same ratio of the 0−0/0−1 emission peaks (Figure 5), it is straightforward to attribute the HEP and LEP emission to phases 3 and 4, respectively. These are the aggregates with crystallized main chains yet disordered side chains and those with crystalline main and side chains. The two associated polymorphs have very similar interchain coupling, differing only regarding the degree of side-chain order.

The energy difference of about 70 meV between HEP and LEP is somewhat surprising. Evidently it arises from the fact that correlation between the laminar stacks is lost in phase 3 where the side chains separating the layers are disordered and liquid-like, while it is preserved in the phase 4 due to the crystalline side chains. Thus, this shift seems to reflect the impact of interactions between different lamellar stacks on the excited states energies, while ratio of the 0−0/0−1 emission peaks is controlled mostly by the interaction within one stack.

The conclusion that in phases 3 and 4 the polymer backbone is crystalline requires some specifying comment. In a molecular crystal such as an anthracene crystal, the S_1-S_0 0−0 transitions in absorption and emission are resonant, i.e., there is no Stokes shift, and they are homogeneously broadened. In contrast, this is not the case for the absorption and fluorescence spectra of the HEP and LEP features. By comparing Figures 1 and 5, it is evident that the 0−0 features of the fluorescence are offset from those in absorption by 100−200 meV, and they bear out an inhomogeneous broadening with a standard deviation of about 40 meV. The temperature-dependent Stokes shift can in part be attributed to spectral diffusion.[50,51] This spectral diffusion and the inhomogeneous broadening are clear evidence for the presence of energetic disorder. Such disorder can arise from two causes, namely a variation in the polarization of the environment or a variation in the conjugation length of the chromophore. Since inhomogeneous line broadening and spectral diffusion (Figures 5b and 5a, respectively) are identical for both polymorphs, it follows that the different degree of order in the side chains cannot be the main source for the energetic disorder. Thus, we argue that the polythiophene chromophores constituting the lamellar stack of H-aggregates do not have identical conjugation length. Rather, there is some distribution in conjugation length, despite the overall lamellar arrangement. Another contribution to the Stokes shift arises from the exciton band structure of the H-aggregate. In a disordered H-aggregate, absorption takes place to the top of the exciton band while emission occurs from its bottom. That bandwidth separation is roughly given by We^{-S}, where W is the free exciton bandwidth and S is the Franck−Condon factor.[42] Using the experimentally obtained values of W = 70 meV and S = 1.1, we obtain a value of 23 meV for this contribution to the Stokes shift.

Finally, we discuss whether and how the phase 2 relates to our spectroscopic measurements. Phase 2 is the structure that Wu et al. and Martin et al. reported to consist of spatially separated main and side chains without lamellar crystals. This phase prevails in samples when cooling from the melt for a small temperature range below the melting point only.[30,35] In the context of Figures 2b and 3a we already mentioned that there is a small temperature range just below the onset of aggregation upon cooling, say at 265 and 260 K, where the emission from the aggregate phase is clearly red-shifted from that of the disordered phase, yet the vibrational structures of the two emissions are nearly identical. It implies that the interchain coupling is already sufficiently strong to reduce the excited state energy, yet the prevailing disorder erodes any signature of an H-aggregate in the 0−0 to 0−1 peak ratio. The spectroscopic signature of the emission just below the onset of

DOI: 10.1021/acs.macromol.5b00129
Macromolecules 2015, 48, 1543−1553

aggregation is fully consistent with the morphology suggested for phase 2. We thus associate phase 2 with the emission spectra of the aggregated domains shown in Figure 3c. Obviously, upon further cooling this evolves into the crystalline phases 3 and 4 with the associated typical H-aggregate spectra showing the suppressed 0−0 peak.

4.4. An Estimate of the Domain Size. Having identified the polymorphs causing the HEP and LEP, we now consider which additional information we can extract from the site-selective and time-dependent experiments (Figures 8−10) regarding the microstructure of the P3HT H-aggregates. At 5 K, emission from phase 4 is observed when it is directly excited, e.g., by using an excitation energy of 1.865 eV. In contrast, when the excitation addresses phase 3, e.g., by exciting at 2.000 eV, emission is only seen from that phase, yet not from phase 4. Evidently, at 5 K, there is no energy transfer from the lamellar structure with still disordered side chains to the lamellae with crystalline side chains. This applies to both the neat film (Figure 10) and the frozen THF solution (Figure 8). Energy transfer from phase 3 to phase 4 does, however, occur when the temperature is raised to 160 K. For excitation at 2.070 eV, the dominant part of the emission is due to the lower energy all-crystalline phase 4, yet with a minor contribution from the actually excited phase 3 with the noncrystalline side chains (Figure 8). The time-dependent fluorescence spectra (Figure 9) indicate that this transfer takes place on a time scale of a few nanoseconds. These observations allow for an estimate regarding the size and distribution of the polymorphs.

(i) The appearance of energy transfer implies that the two polymorphs must be sufficiently close. For the concentration used here, this entails that an aggregated ensemble in solution must contain both polymorphs.

(ii) The facts that the energy transfer takes place not on an ultrafast time scale but rather on the comparatively slow nanosecond range and that some emission from the higher energy phase remains to be seen in the steady-state spectrum for excitation at 2.000 and 2.070 eV suggest that each polymorph must have a size that exceeds twice the exciton diffusion range at that temperature.

A typical exciton diffusion length at room temperature is about 5−10 nm.[52] However, in an inhomogeneously broadened density of states distribution the exciton diffusion length decreases with decreasing temperature.[53] Here the characteristic parameter is the ratio between the standard deviation of the Gaussian density of states distribution (σ) and k_BT. When decreasing σ/k_BT from 2 (equivalent to T = 300 K and σ = 52 meV) to 4 (equivalent to about 150 K), the exciton diffusion length decreases by a factor of roughly 5, i.e., to a value of 1−2 nm.[53] Thus, the observed energy transfer implies a polymorph size with a diameter exceeding a few nanometers. The overall structural picture that emerges is that of an aggregated ensemble that contains both a layered crystalline polymorph with crystalline side chains and one with disordered side chains, with both polymorphs extending over at least a few nanometers. A possible overall scenario is that of a layered crystalline polymorph with crystalline side chains (phase 4) in the center and a surrounding layered crystalline polymorph with disordered side chains (phase 3), embedded in the remaining amorphous phase.

■ ASSOCIATED CONTENT

Ⓢ Supporting Information

Figures containing the experimental as well as theoretical temperature-dependent Stokes shift of the LEP as well as Franck−Condon analysis of aggregate absorption spectrum at 160 K, using one progression; fitted parameters E_0 and σ from the FC analysis on the coiled emission spectrum as a function of temperature; FC analysis on the site-selected emission spectra at 5 and 160 K at excitation of 2.070 and 1.865 eV as well as corresponding fraction of HEP and LEP phase. This material is available free of charge via the Internet at http://pubs.acs.org.

■ AUTHOR INFORMATION

Corresponding Author

*E-mail: anna.koehler@uni-bayreuth.de (A.K.).

Present Address

M.S.: Department of Macromolecular Chemistry, University of Freiburg, Stefan-Meier.-Str. 31, 79104 Freiburg, Germany.

Notes

The authors declare no competing financial interest.

■ ACKNOWLEDGMENTS

We acknowledge financial support by the Bavarian State Ministry of Science, Research, and the Arts through the Collaborative Research Network 'Solar Technologies go Hybrid', by the German Science Foundation DFG through the doctoral training center GRK1640 and by the Federal Ministry of Education and Research (BMBF) through the project "OLYMP". We thank Marie-Luis Panzer for the help with the TOC Graphic. Furthermore, we thank Alexander Rudnick for the assistance with the site selective measurements.

■ REFERENCES

(1) Pingel, P.; Zen, A.; Abellón, R. D.; Grozema, F. C.; Siebbeles, L. D. A.; Neher, D. *Adv. Funct. Mater.* **2010**, *20*, 2286−2295.
(2) Kline, R. J.; McGehee, M. D.; Kadnikova, E. N.; Liu, J. S.; Frechet, J. M. J. *Adv. Mater.* **2003**, *15*, 1519−1522.
(3) Paquin, F.; Latini, G.; Sakowicz, M.; Karsenti, P.-L.; Wang, L.; Beljonne, D.; Stingelin, N.; Silva, C. *Phys. Rev. Lett.* **2011**, *106*, 197401.
(4) Scharsich, C.; Lohwasser, R. H.; Sommer, M.; Asawapirom, U.; Scherf, U.; Thelakkat, M.; Neher, D.; Köhler, A. *J. Polym. Sci., Part B: Polym. Phys.* **2012**, *50*, 442−453.
(5) Koch, F. P. V.; Rivnay, J.; Foster, S.; Müller, C.; Downing, J. M.; Buchaca-Domingo, E.; Westacott, P.; Yu, L.; Yuan, M.; Baklar, M.; Fei, Z.; Luscombe, C.; McLachlan, M. A.; Heeney, M.; Rumbles, G.; Silva, C.; Salleo, A.; Nelson, J.; Smith, P.; Stingelin, N. *Prog. Polym. Sci.* **2013**, *38*, 1978−1989.
(6) Duong, D. T.; Toney, M. F.; Salleo, A. *Phys. Rev. B* **2012**, *86*, 205205.
(7) Berson, S.; De Bettignies, R.; Bailly, S.; Guillerez, S. *Adv. Funct. Mater.* **2007**, *17*, 1377−1384.
(8) Zen, A.; Saphiannikova, M.; Neher, D.; Grenzer, J.; Grigorian, S.; Pietsch, U.; Asawapirom, U.; Janietz, S.; Scherf, U.; Lieberwirth, I.; Wegner, G. *Macromolecules* **2006**, *39*, 2162−2171.
(9) Chasteen, S. V.; Carter, S. A.; Rumbles, G. *Proc. SPIE* **2005**, 59380J−59380J-11.
(10) Hiorns, R. C.; de Bettignies, R.; Leroy, J.; Bailly, S.; Firon, M.; Sentein, C.; Khoukh, A.; Preud'homme, H.; Dagron-Lartigau, C. *Adv. Funct. Mater.* **2006**, *16*, 2263−2273.
(11) Huang, Y.; Kramer, E. J.; Heeger, A. J.; Bazan, G. C. *Chem. Rev.* **2014**, *114*, 7006−7043.
(12) Kim, Y.; Cook, S.; Tuladhar, S. M.; Choulis, S. A.; Nelson, J.; Durrant, J. R.; Bradley, D. D. C.; Giles, M.; McCulloch, I.; Ha, C.-S.; Ree, M. *Nat. Mater.* **2006**, *5*, 197−203.

DOI: 10.1021/acs.macromol.5b00129
Macromolecules 2015, 48, 1543−1553

(13) Sirringhaus, H.; Brown, P. J.; Friend, R. H.; Nielsen, M. M.; Bechgaard, K.; Langeveld-Voss, B. M. W.; Spiering, A. J. H.; Janssen, R. A. J.; Meijer, E. W.; Herwig, P.; de Leeuw, D. M. *Nature* **1999**, *401*, 685−688.
(14) Brown, P. J.; Thomas, D. S.; Kohler, A.; Wilson, J. S.; Kim, J. S.; Ramsdale, C. M.; Sirringhaus, H.; Friend, R. H. *Phys. Rev. B* **2003**, *67*, 064203.
(15) Martin, T. P.; Wise, A. J.; Busby, E.; Gao, J.; Roehling, J. D.; Ford, M. J.; Larsen, D. S.; Moulé, A. J.; Grey, J. K. *J. Phys. Chem. B* **2012**, *117*, 4478−4487.
(16) Paquin, F.; Yamagata, H.; Hestand, N. J.; Sakowicz, M.; Bérubé, N.; Côté, M.; Reynolds, L. X.; Haque, S. A.; Stingelin, N.; Spano, F. C.; Silva, C. *Phys. Rev. B* **2013**, *88*, 155202.
(17) Baghgar, M.; Labastide, J. A.; Bokel, F.; Hayward, R. C.; Barnes, M. D. *J. Phys. Chem. C* **2014**, *118*, 2229−2235.
(18) Baghgar, M.; Labastide, J.; Bokel, F.; Dujovne, I.; McKenna, A.; Barnes, A. M.; Pentzer, E.; Emrick, T.; Hayward, R.; Barnes, M. D. *J. Phys. Chem. Lett.* **2012**, *3*, 1674−1679.
(19) Koch, F. P.; Heeney, M.; Smith, P. *J. Am. Chem. Soc.* **2013**, *135*, 13699−13709.
(20) Poelking, C.; Andrienko, D. *Macromolecules* **2013**, *46*, 8941−8956.
(21) Yuan, Y.; Zhang, J.; Sun, J.; Hu, J.; Zhang, T.; Duan, Y. *Macromolecules* **2011**, *44*, 9341−9350.
(22) Guo, Y.; Wang, L.; Han, Y.; Geng, Y.; Su, Z. *Polym. Chem.* **2014**, *5*, 1938−1944.
(23) Brinkmann, M. *J. Polym. Sci., Part B: Polym. Phys.* **2011**, *49*, 1218−1233.
(24) Noriega, R.; Rivnay, J.; Vandewal, K.; Koch, F. P. V.; Stingelin, N.; Smith, P.; Toney, M. F.; Salleo, A. *Nat. Mater.* **2013**, *12*, 1038−1044.
(25) Köhler, A.; Hoffmann, S. T.; Bässler, H. *J. Am. Chem. Soc.* **2012**, *134*, 11594−11601.
(26) Cone, C. W.; Cheng, R. R.; Makarov, D. E.; Vanden Bout, D. A. *J. Phys. Chem. B* **2011**, *115*, 12380−12385.
(27) Prosa, T. J.; Winokur, M. J.; McCullough, R. D. *Macromolecules* **1996**, *29*, 3654−3656.
(28) Mena-Osteritz, E.; Meyer, A.; Langeveld-Voss, B. M. W.; Janssen, R. A. J.; Meijer, E. W.; Bauerle, P. *Angew. Chem., Int. Ed.* **2000**, *39*, 2680−2684.
(29) Rahimi, K.; Botiz, I.; Stingelin, N.; Kayunkid, N.; Sommer, M.; Koch, F. P. V.; Nguyen, H.; Coulembier, O.; Dubois, P.; Brinkmann, M.; Reiter, G. *Angew. Chem., Int. Ed.* **2012**, *51*, 11131−11135.
(30) Wu, Z. Y.; Petzold, A.; Henze, T.; Thurn-Albrecht, T.; Lohwasser, R. H.; Sommer, M.; Thelakkat, M. *Macromolecules* **2010**, *43*, 4646−4653.
(31) Kline, R. J.; DeLongchamp, D. M.; Fischer, D. A.; Lin, E. K.; Richter, L. J.; Chabinyc, M. L.; Toney, M. F.; Heeney, M.; McCulloch, I. *Macromolecules* **2007**, *40*, 7960−7965.
(32) Köse, M. E. *J. Phys. Chem. C* **2011**, *115*, 13076−13082.
(33) Lohwasser, R. H.; Thelakkat, M. *Macromolecules* **2011**, *44*, 3388−3397.
(34) Kohn, P.; Huettner, S.; Komber, H.; Senkovskyy, V.; Tkachov, R.; Kiriy, A.; Friend, R. H.; Steiner, U.; Huck, W. T. S.; Sommer, J.-U.; Sommer, M. *J. Am. Chem. Soc.* **2012**, *134*, 4790−4805.
(35) Panzer, F.; Bässler, H.; Lohwasser, R.; Thelakkat, M.; Köhler, A. *J. Phys. Chem. Lett.* **2014**, *5*, 2742−2747.
(36) Lebedev, B. V.; Rabinovich, I. B.; Milov, V. I.; Lityagov, V. Y. *J. Chem. Thermodyn.* **1978**, *10*, 321−329.
(37) Hotta, S.; Rughooputh, S. D. D. V.; Heeger, A. J.; Wudl, F. *Macromolecules* **1987**, *20*, 212−215.
(38) Ho, P. K. H.; Kim, J.-S.; Tessler, N.; Friend, R. H. *J. Chem. Phys.* **2001**, *115*, 2709−2720.
(39) Clark, J.; Silva, C.; Friend, R. H.; Spano, F. C. *Phys. Rev. Lett.* **2007**, *98*, 206406.
(40) Spano, F. C. *J. Chem. Phys.* **2005**, *122*, 234701.
(41) Spano, F. C. *Chem. Phys.* **2006**, *325*, 22−35.
(42) Spano, F. C. *Acc. Chem. Res.* **2010**, *43*, 429−439.
(43) Spano, F. C.; Clark, J.; Silva, C.; Friend, R. H. *J. Chem. Phys.* **2009**, *130*, 074904.
(44) Clark, J.; Chang, J. F.; Spano, F. C.; Friend, R. H.; Silva, C. *Appl. Phys. Lett.* **2009**, *94*, 163306.
(45) Yamagata, H.; Spano, F. C. *J. Chem. Phys.* **2012**, *136*, 184901.
(46) Yamagata, H.; Hestand, N. J.; Spano, F. C.; Köhler, A.; Scharsich, C.; Hoffmann, S. T.; Bässler, H. *J. Chem. Phys.* **2013**, *139*, 114903.
(47) Martín, J.; Nogales, A.; Martín-González, M. *Macromolecules* **2013**, *46*, 1477−1483.
(48) Brambilla, L.; Tommasini, M.; Botiz, I.; Rahimi, K.; Agumba, J. O.; Stingelin, N.; Zerbi, G. *Macromolecules* **2014**, *47*, 6730−6739.
(49) Hugger, S.; Thomann, R.; Heinzel, T.; Thurn-Albrecht, T. *Colloid Polym. Sci.* **2004**, *282*, 932−938.
(50) Bässler, H. *Phys. Status Solidi B* **1993**, *175*, 15−56.
(51) Hoffmann, S. T.; Bässler, H.; Koenen, J.-M.; Forster, M.; Scherf, U.; Scheler, E.; Strohriegl, P.; Köhler, A. *Phys. Rev. B* **2010**, *81*, 115103.
(52) Bjorgaard, J. A.; Kose, M. E. *J. Phys. Chem. C* **2014**, *118*, 5756−5761.
(53) Athanasopoulos, S.; Emelianova, E. V.; Walker, A. B.; Beljonne, D. *Phys. Rev. B* **2009**, *80*, 195209.

DOI: 10.1021/acs.macromol.5b00129
Macromolecules 2015, 48, 1543−1553

Supporting information to:

Spectroscopic Signature of Two Distinct H-Aggregate Species in Poly(3-hexylthiophene)

Fabian Panzer[†], Michael Sommer[§], Heinz Bässler[‡], Mukundan Thelakkat[§], Anna Köhler[†].*

[†]Experimental Physics II and Bayreuth Institute of Macromolecular Science, University of Bayreuth, 95540 Bayreuth, Germany

[‡]Bayreuth Institute of Macromolecular Science, University of Bayreuth, 95440 Bayreuth, Germany

[§]Applied Functional Polymers, Macromolecular Chemistry 1 and Bayreuth Institute of Macromolecular Science, University of Bayreuth, 95440 Bayreuth, Germany

E_0 and σ of the modelled coiled emission spectrum as a function of temperature:

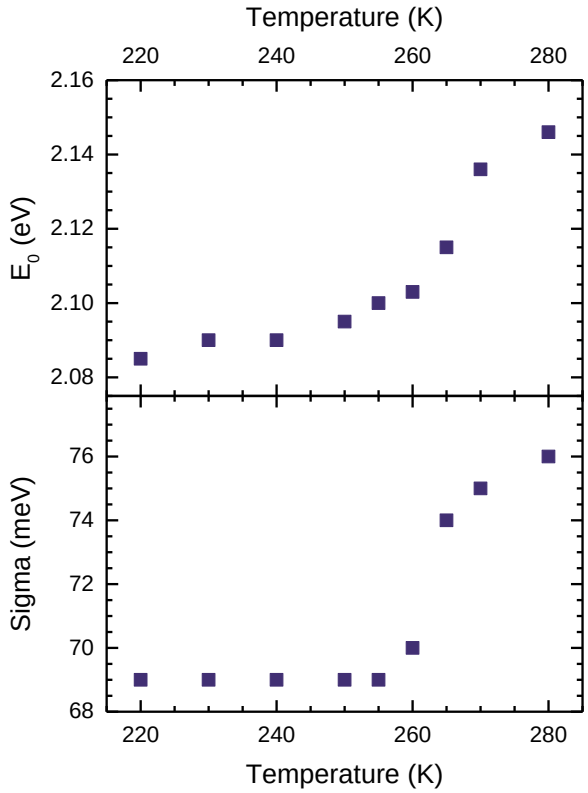

Figure S1: Fit-parameters inferred from Franck-Condon analysis of the fluorescence spectra of P3HT in the amorphous phase as a function of temperature. (a) Energies of the 0-0-emission, (b) standard deviations σ of the 0-0 feature.

Modelling emission form amorphous phase at temperatures below 220 K was not possible due to the fact that emission from this phase completely vanished below this temperature and only aggregate emission was observed.

Franck Condon Analysis of Absorption spectrum at 160 K:

We also performed Franck Condon Analysis on the absorption spectrum at 160 K, using one progression Due to the decreased line width of the gaussians, it is not possible to model the measured spectrum in a satisfying way. Furthermore the resulting residue shows a very structured shape especially in the lower energy region between 1.9 and approximately 2.9 eV.

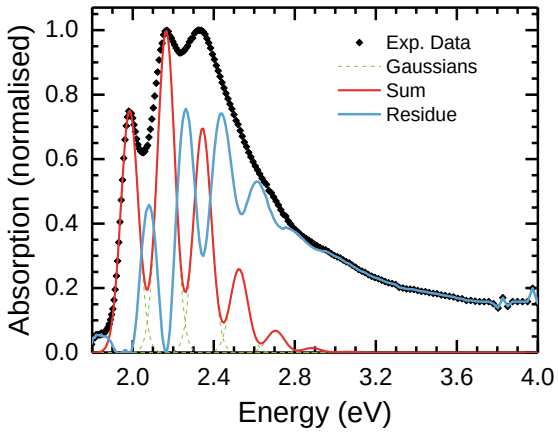

Figure S2: Absorption spectra of P3HT (black squares) at 160 K, as well as the Franck-Condon analysis (red) according to eq. 3 using one progressions and the resulting residue (blue).

Temperature dependent Stokes Shift of LEP phase:

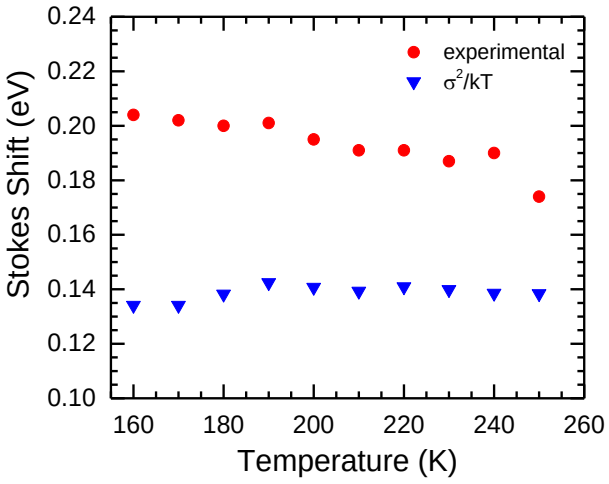

Figure S3: Experimentally as well as theoretical estimated Stokes Shift as a function of temperature.

The experimental Stokes shift was obtained by considering the energetic difference between the 0-0 peaks in emission and corresponding absorption spectrum of the LEP (red dots).

Resulting Stokes Shift from hopping theory is obtained using the expression:

$$\Delta\epsilon \sim \frac{\sigma^2}{kT}$$

The temperature dependent values of sigma were obtained from the FC-Analysis and are shown in Figure 5 in the manuscript.

FC-Analysis using two progressions (HEP/LEP) on the site selected emission spectra

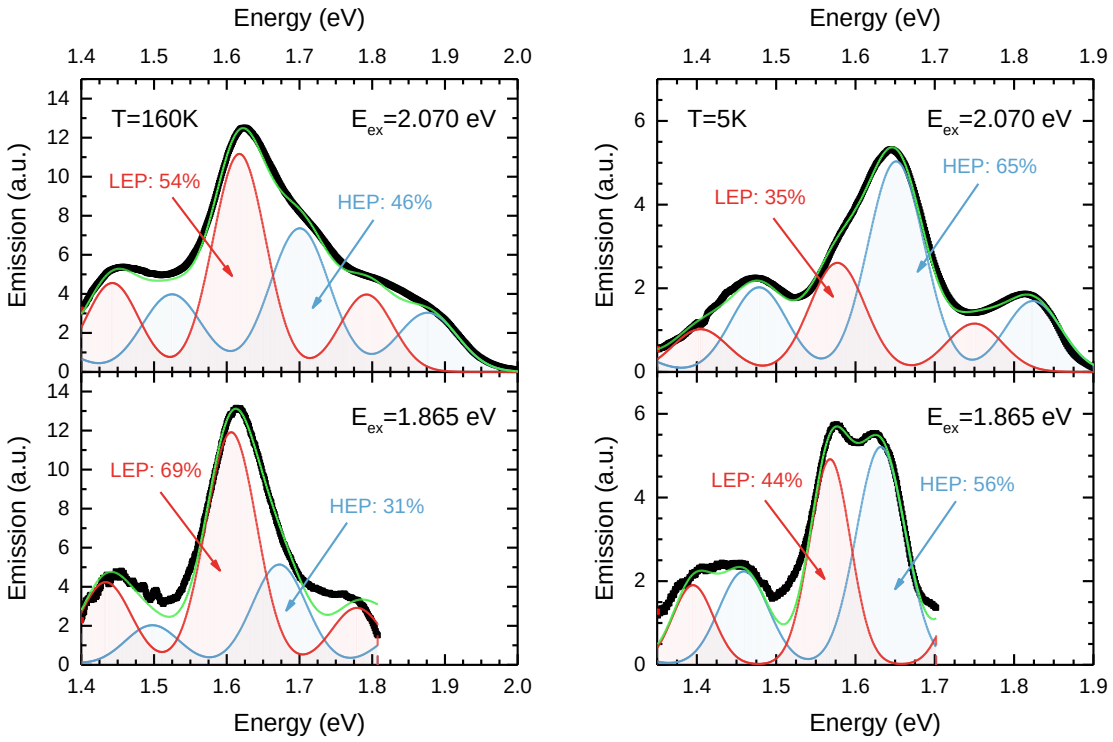

Figure S4: Site selected (top: 2.070 eV; bottom: 1.865 eV) emission spectra at 160 K (left) and 5 K (right) and corresponding FC-Analysis using eq. 2 and two progressions LEP and HEP.

4.4. Ultrafast Energy Transfer between Disordered and Highly Planarized Chains of Poly[2-methoxy-5-(2-ethylhexyloxy)-1,4-phenylenevinylene] (MEH-PPV)

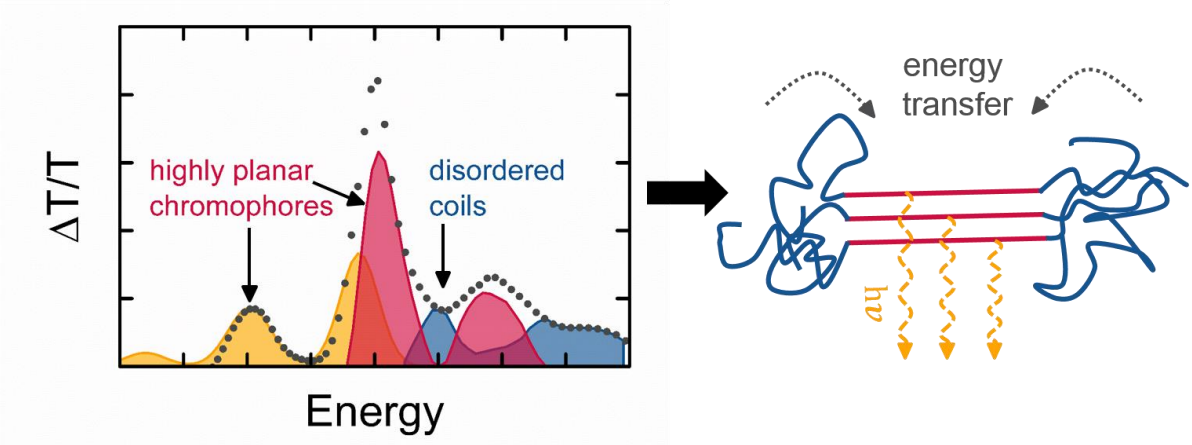

Thomas Unger, Fabian Panzer, Cristina Consani, Federico Koch, Tobias Brixner, Heinz Bässler and Anna Köhler

Published in
ACS Macro Letters
DOI: 10.1021/acsmacrolett.5b00133

ACS Macro Letters

Letter

pubs.acs.org/macroletters

Ultrafast Energy Transfer between Disordered and Highly Planarized Chains of Poly[2-methoxy-5-(2-ethylhexyloxy)-1,4-phenylenevinylene] (MEH-PPV)

Thomas Unger,[†,‡] Fabian Panzer,[†,‡] Cristina Consani,[§] Federico Koch,[§] Tobias Brixner,[§,∥] Heinz Bässler,[‡] and Anna Köhler*[,†,‡]

[†]Experimental Physics II, University of Bayreuth, 95540 Bayreuth, Germany

[‡]Bayreuth Institute of Macromolecular Research (BIMF), University of Bayreuth, 95440 Bayreuth, Germany

[§]Institut für Physikalische und Theoretische Chemie and [∥]Center for Nanosystems Chemistry (CNC), Universität Würzburg, Am Hubland, 97074 Würzburg, Germany

Supporting Information

ABSTRACT: Upon cooling a solution of poly[2-methoxy-5-(2-ethylhexyloxy)-1,4-phenylenevinylene] (MEH-PPV), a phase transition occurs, leading to the formation of aggregates. We have studied the dynamics of singlet excitons in MEH-PPV solution below the critical temperature of the phase transition using steady-state photoluminescence measurements and pump−probe fs-spectroscopy at different temperatures. Spectral analysis indicates the coexistence of disordered chromophores with highly planarized chromophores. The high planarity is evidenced by a remarkably high 0−0/0−1 peak ratio in the spectra. By spectrally separating the contributions of either type of chromophore to the pump−probe signal we find that energy transfer takes place within less than 1 ps from disordered, unaggregated chain segments to highly planarized, aggregated chain segments. The short time scale of the energy transfer indicates intimate intermixing of the planarized and disordered polymeric chromophores.

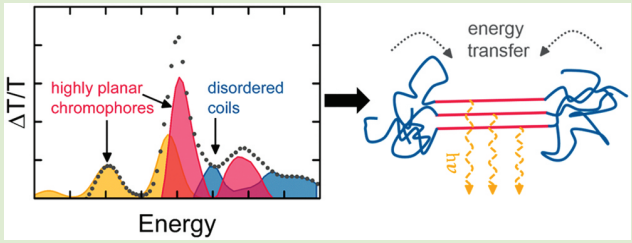

Conjugated polymers are prone to aggregation in solution.[1−3] Below a critical transition temperature that depends on the chain length,[4] isolated and more or less coiled chains tend to aggregate with a concomitant increase of their effective conjugation length. A manifestation of this phenomenon is the appearance of lower-energy absorption and fluorescence bands so that the spectra exhibit an isosbestic point. Absorption spectra demonstrate, nevertheless, that both phases coexist well below the phase transition temperature with the fractional contribution of the ordered phase increasing upon further cooling. On the other hand, the fluorescence comes almost exclusively from the ordered phase. This is a signature of efficient energy transfer between both phases.

The purpose of the current work was to unravel the interplay between the disordered and ordered phases, identify the nature of both phases and measure of rate of energy transfer between them. As a test material, we chose MEH-PPV in solution as a prototypical π-conjugated polymer for which a wealth of information is already existing, employing steady-state absorption and fluorescence spectroscopy, as well as time-resolved pump−probe spectroscopy within a broad temperature range. Based on spectral decomposition techniques and adopting Spano et al.'s H/J-aggregate model,[5] we are able to associate the room temperature phase with disordered chains or chain segments, while, in the aggregated phase, chains or chain segments prevail that are extended with predominant J-type character. From the observation that energy transfer from the disordered to the planarized chromophores occurs on a subps time scale we will conclude that both types of chromophores are intimately connected, for example, by forming an array of extended chains surrounded with a "hairy" surface of coiled chains.

For the investigation, we used MEH-PPV that was purchased from American Dye Source Ltd. (ADS). It was dissolved in methyltetrahydrofuran (MTHF) at a concentration of 0.2 mg/mL. To ensure that all of the polymer chains are completely dissolved, the solution was heated to 50−60 °C and stirred for about 10 h until no macroscopic particles could be observed. The experiments were performed in a temperature range between 300 and 120 K where MTHF is liquid.[6] Steady-state absorption and emission spectra at different temperatures were recorded with a home-built setup. The solutions were filled into a 1 mm fused silica cuvette and put in a temperature-controlled continuous flow cryostat (Oxford Instruments). In order to minimize the light intensity impinging on the sample, we used two correlated monochromators for incident as well as transmitted light. The latter was recorded by a silicon diode and a lock-in-amplifier.

Received: February 19, 2015
Accepted: March 26, 2015

DOI: 10.1021/acsmacrolett.5b00133
ACS Macro Lett. 2015, 4, 412−416

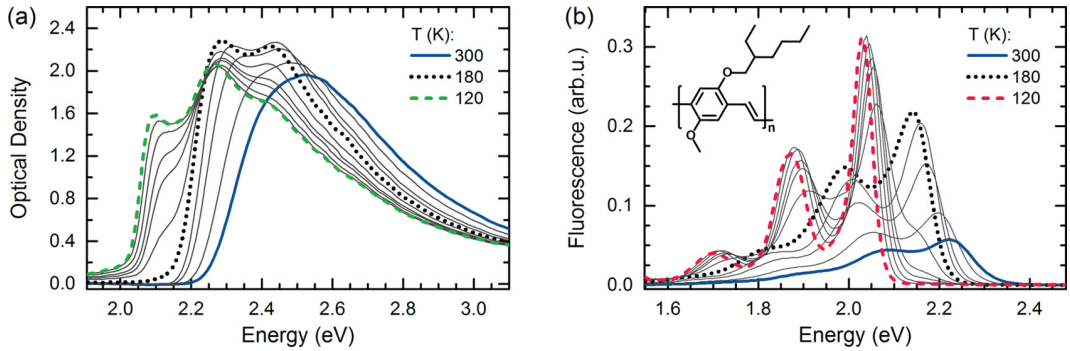

Figure 1. Steady-state (a) absorption and (b) fluorescence spectra of MEH-PPV in MTHF for different temperatures, that is, at 300, 260, 220, 200, 180, 175, 170, 170, 165, 155, 140, and 120 K. Fluorescence spectra were corrected for the relative changes in absorption at the excitation energy (3.06 eV).

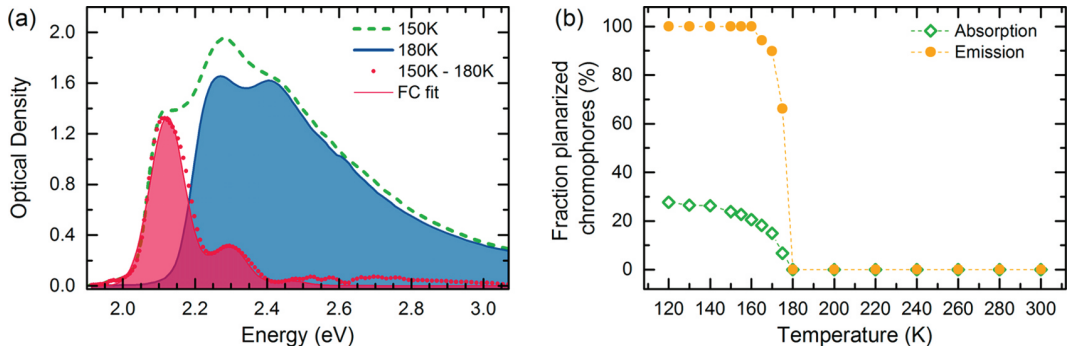

Figure 2. (a) Absorption spectrum at 150 K (green dashed line) together with the absorption spectrum of the disordered phase (filled blue curve) that was measured at 180 K and subsequently normalized to match the high energy tail of the 150 K absorption spectrum. The difference between the 150 and 180 K spectra is shown by the red dots. This difference spectrum can be reproduced by a Franck−Condon progression (filled red curve). (b) Fraction of planarized chromophores as a function of temperature obtained from the absorption spectra (open green diamonds) and from the emission spectra (orange dots), as described in the Supporting Information.

For steady-state emission measurements, the xenon lamp and the first monochromator were replaced via a shutter by a diode laser with an excitation wavelength at 405 nm (3.06 eV), exciting the sample at a shallow angle. Emission was recorded by the same detection unit. This ensured recording absorption and fluorescence spectra at the same sample spot and temperature immediately after one another. All spectra were corrected for the transmission of the setup, using an Oriel calibration lamp. Sample heating or cooling was done in a stepwise fashion with a heating or cooling rate of 2 K per min and waiting 30 min before taking the measurement at a given temperature to ensure thermal equilibrium within the sample.

The transient absorption data with excitation at 2.48 eV (pulse length 190 fs) were obtained using a 100 kHz setup from Coherent Ltd., as described in more detail in the Supporting Information (SI). In brief, the pump-pulse fluence was set to about 10 μJ/cm^2 to keep the pump−probe signal linear with fluence (see Figure S1). The spectra were recorded using a lock-in amplifier and a monochromator with a silicon diode. To obtain transient absorption data with excitation at 2.12 eV (pulse length 42 fs), a 1 kHz setup from Spectra Physics was employed. Here also excitation pulse energies were low enough to keep the signal in the linear regime.

Figure 1 shows the absorption and photoluminescence (PL) spectra of MEH-PPV in MTHF solution in the temperature range between 300 and 120 K. In absorption, the 300 K spectrum is vibrationally unresolved with a maximum at 2.5 eV (Figure 1a). It is associated with disordered coil-like polymer chains.[7−9] Upon cooling to 180 K, the spectra shift to the red by about 80 meV. They continuously acquire vibrational structure and a 0−0 feature near 2.3 eV develops. In contrast, the emission spectrum at 300 K shows vibrational structure with $S_1 \rightarrow S_0$ 0−0, 0−1, 0−2 peaks at 2.23, 2.07, and 1.89 eV, respectively (Figure 1b). When lowering the temperature from 300 to 180 K, the spectra shift to the red by about 80 meV similar to the behavior in absorption. This is accompanied by a continuous increase in overall intensity, where the area beneath the spectrum at 180 K more than triples compared to the area at 300 K (see Figure S2 in SI for energetic shifts of the S_1−S_0 0−0 peak and area under the spectra as a function of temperature). Thus, upon cooling until 180 K, absorption and emission spectra shift to the red and become more intense. This indicates that the conjugated segments of the chain become more extended, although their overall chain conformation still corresponds to that of a disordered coil conformation.[4,10,11] This is similar to the behavior that was recently observed when cooling solutions of P3HT,[2,4] as well as PCPDTBT.[12]

When further cooling below 180 K, a new absorption (emission) peak near 2.1 eV (2.05 eV) appears and grows in intensity at the expense of absorption (emission) from coiled chains. It is assigned to the absorption (emission) of planarized MEH-PPV chain segments in aggregates.[7] Below 170 K, emission from the coiled chains vanishes and the fluorescence spectrum is dominated by the planarized chromophores. This is consistent with earlier work,[7] and has been attributed to the

DOI: 10.1021/acsmacrolett.5b00133
ACS Macro Lett. 2015, 4, 412−416

occurrence of a disorder−order transition. The PL spectra of the planarized chromophores bear out a bathochromic shift from 2.053 to 2.026 eV upon further cooling from 170 to 120 K and the associated absorption spectra shift by the same amount (Figure S2).

To gain detailed information about the absorption from the planarized chains or chain segments requires decomposition of the measured spectra below 180 K. Here we followed a scaling approach, similar to that in Reference 13, which we already used for decomposing absorption spectra of aggregated P3HT in solution.[2,4] This approach is applicable to MEH-PPV because the spectra bear out an isosbestic point at 2.24 eV in the temperature range of 180 to 140 K (Figure 1a), which is an unambiguous evidence that a transition from a coiled to an ordered phase is occurring.[14,15] Figure 2a illustrates the decomposition approach and shows the measured absorption spectrum at 150 K (green dashed line) together with the normalized absorption spectrum of the disordered phase measured at 180 K (filled blue curve). The difference between these spectra (red dots) is attributed to absorption from planarized chromophores with peaks at 2.1 and 2.3 eV. A Franck−Condon analysis of this absorption spectrum (filled red curve) from the planarized chromophores yields a Huang−Rhys parameter of S = 0.25, an I_{0-0}/I_{0-1} ratio = 4, an effective vibrational mode of E_d = 170 meV and a Gaussian line width of σ = 48 meV. In the framework of the H/J-aggregate model developed by Spano and co-workers,[5] such a high I_{0-0}/I_{0-1} ratio is a signature of strong coupling along the polymer chain (intrachain) in the aggregated phase and correspondingly weak coupling between different polymer chains (interchain). The same high ratio applies to coupling along a linear arrangement of chromophores and to coupling between chromophores in an adjacent, face-to-face arrangement, respectively. Similar remarkably high I_{0-0}/I_{0-1} ratios have been observed for fully planarized single crystals of P3HT.[16] This appears to be a signature of ordered domains of π-conjugated chains in general, tractable in terms of Spano et al.'s theory.[5] The fraction of planarized chromophores as a function of temperature is displayed in Figure 2b. It was obtained from the absorption fraction of planarized chain segments, taking into account the relative change in oscillator strength between disordered and planarized chain segments, as detailed in the SI.

From the absorption data we infer that below the critical transition temperature, the percentage of planarized chromophores increases continuously, saturating at a maximum value of about 30% at 120 K. In contrast, the percentage of fluorescence from planarized chromophores increases steeply below the transition temperature, until below 160 K, emission results entirely from the planarized chromophores. The fact that emission results entirely from planarized chromophores though they make up only 30% of the total composition implies efficient energy transfer from disordered to planarized chromophores.

Figure 3 shows the transient absorption spectrum of MEH-PPV in solution at 120 K, excited at 2.12 eV and probed between 2.5 and 1.7 eV with a delay time of 75 fs. As the disordered chains do not absorb for excitation at 2.12 eV, we assign the peak observed near 2.3 eV to the ground-state bleach (GSB) of the $S_1 \rightarrow S_0$ 0−1 transition of the planarized chromophores. The feature near 2.1 eV is the superposition of the ground-state bleach of the 0−0 transition of the planarized chromophores (as evident from Figure 1a) and the associated stimulated emission (SE). Accordingly, the feature centered

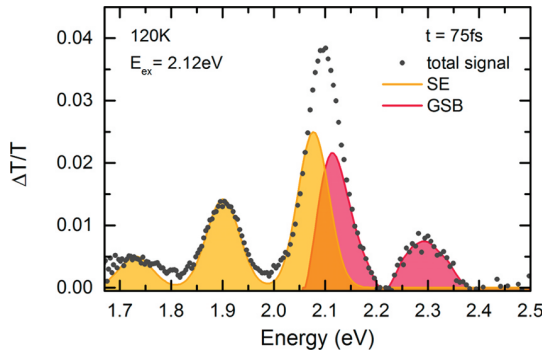

Figure 3. Pump−probe spectrum (gray dots) taken at 120 K, 75 fs after excitation at 2.12 eV, where only the planarized chains absorb. The spectrum is decomposed into the contributions from stimulated emission (SE, filled orange curve) and ground-state bleach (GSB, filled red curve). The SE contribution was obtained by normalizing the 120 K PL spectrum to match the 1.9 eV SE peak. The GSB contribution was obtained by subtracting the normalized 120 K PL spectrum from the total $\Delta T/T$ signal.

near 1.9 eV is assigned to the 0−1 feature of the stimulated emission transition (SE 0−1). Since the fluorescence spectrum of the planarized chromophores is evident in Figure 1b, it is possible to spectrally decompose the 0−0 feature of the pump−probe spectrum into the contributions from GSB and SE. To this end, we take the 120 K photoluminescence (PL) spectrum and normalize it in such a way that the 0−1 peak of the PL spectrum matches the 1.9 eV $\Delta T/T$ signal in intensity, taking into account a slight spectral shift of about 10 meV between the steady-state and the time-resolved spectra. Subtraction of the 120 K PL spectrum from the $\Delta T/T$ signal yields the spectrum associated with the ground-state bleach.

From this spectral decomposition we find a 0−0/0−1 ratio of the GSB that significantly exceeds unity, similar to that of the absorption spectra obtained for the planarized chromophores from steady-state data (Figure 2a). In a recent publication,[17] absorption spectra of aggregated MEH-PPV were simulated theoretically resulting in a significantly smaller 0−0/0−1 ratio compared to this work, mainly due to an underestimated contribution of the coiled phase to the overall absorption spectrum.

When exciting a sample held at 120 K with 2.48 eV, Figure 2a tells us that 95% of the absorbing chromophores are in a disordered conformation. Yet already at 1 ps after excitation, the GSB signal shows signatures of both disordered and planarized chromophores. This is documented by Figure 4 in which pump−probe spectra are shown that are detected after a delay time of 1 and 5 ps.

Spectra at further delay times are listed in the SI. Based on the same decomposition routine as above, the total GSB signal, due to disordered chromophores and to planarized chromophores, was obtained. We then used the GSB signal from the planarized chains derived in Figure 3, normalized it appropriately, and subtracted it from the total GSB signal to derive the GSB contribution of the disordered chain, analogous to the spectral decomposition approach described above. The relative contribution of planarized and of disordered chromophores obtained by this procedure is displayed in Figure 5 as a function of time. In both, Figures 4 and 5, we see that the contribution due to the lower-energy, planarized chromophores grows at the expense of the higher-energy, disordered chromophores.

DOI: 10.1021/acsmacrolett.5b00133
ACS Macro Lett. 2015, 4, 412−416

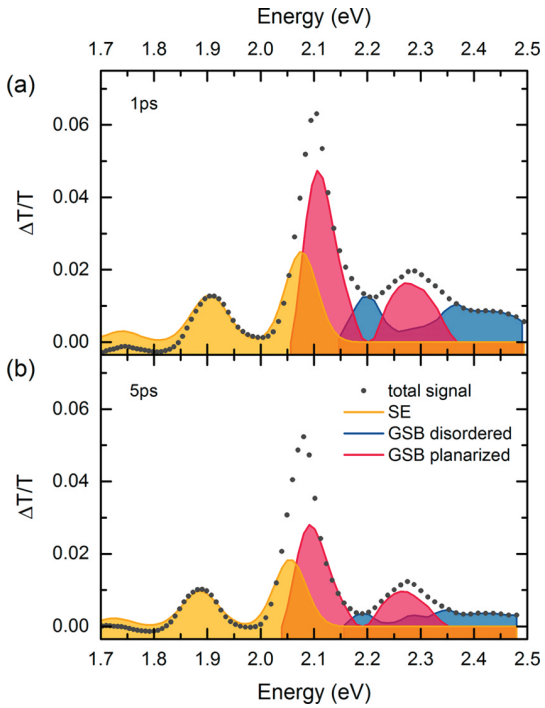

Figure 4. Pump–probe spectra for excitation at 2.48 eV (where coiled chains absorb) at 120 K for different time delays after excitation, that is, (a) 1 and (b) 5 ps. In addition to the total $\Delta T/T$ signal (dots), the contributions of SE, GSB from disordered chromophores, and the GSB from the planarized chromophores are indicated by orange, blue, and red solid lines, respectively.

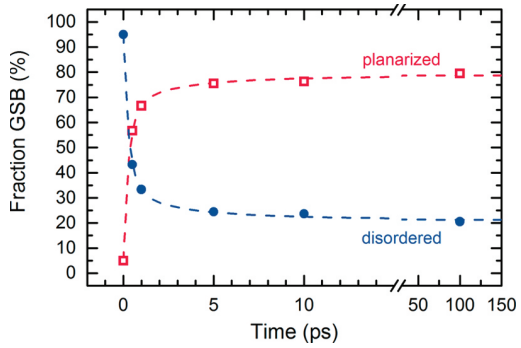

Figure 5. Percentage of the ground-state bleach signal that is due to planarized chromophores (open square symbols) or to disordered chromophores (filled round symbols) as a function of time. The dashed line is a guide to the eye, indicating a decay/growth pattern with an initial exponential decay/growth, followed by a stretched-exponential decay/growth.

We interpret the rising contribution from the planarized chromophores to result from energy transfer from the higher-energy disordered chromophores that is completed within a few ps. A similarly rapid energy transfer from disordered to ordered chain segments has been observed also in polyfluorene (PFO) thin films.[18] Such a fast transfer is incompatible with long-range energy transfer from isolated coiled chains to planarized chains (see SI). It rather suggests that planarized and coiled chromophores are in close proximity, for example, by planarized chain segments forming an ordered cluster surrounded by more disordered coiled chains or chain segments, which was also proposed recently.[19,20] Since experimental and theoretical previous work suggests that MEH-PPV forms planarized segments above a certain concentration,[7,21] the planarized segments are more likely to arise from coalescing chains than by self-folding.

In structures where acceptor chromophores are embedded in a matrix of donor chromophores, energy transfer is characterized by a kinetics comprising several components.[22−24] Initially, fast monoexponential decay of the donor emission prevails due to energy transfer to immediately adjacent acceptor sites. In a second step, the decay becomes dispersive since energy transfer takes place over a range of distances and in a multistep fashion. Both transfer types, that is, (parallel) transfer over a range of distances and (sequential) multistep transfer, have been shown to result in a stretched-exponential decay law,[25−31] also referred to as Kohlrausch–Williams–Watts (KWW) decay law[32]

$$I(t) = I_0 \exp\left[-\left(\frac{t}{t_0}\right)^{\beta}\right]$$

where β is a parameter that accounts for the deviation from nonexponentiality. β takes the value of 0.5 in the case of Förster-type energy transfer. In the long-time limit, finally, the donor decay is dominated by those donor chromophores that decay naturally before energy transfer to distant acceptor sites can occur. The donor emission thus asymptotically approaches the natural donor decay lifetime. Figure 5 indicates that the temporal evolution of the GSB contributions of disordered chromophores and of planarized chromophores is consistent with such a picture. The dashed lines indicate such a decay/growth pattern with an initial exponential decay/growth with about 300 fs lifetime, followed by a stretched-exponential with β = 0.5 and a characteristic time in the range of 1 ps. Similar values and quality of fit result when using a multiexponential approach.

In passing we mention that, in Figure 4, we consider that the slight difference between the measured $\Delta T/T$ signal at 1.75 eV and the SE (derived from the normalized PL spectra) indicates some excited-state absorption from disordered chromophores.

We now consider the decay of the pump–probe signal near 2.1 eV. This is interpreted as the decay of the excitations on the planarized segments. Figure 6 reveals a decay that is not exactly exponential yet approaches an exponential decay with a lifetime of about 350 ps. Such deviation from monoexponentiality is an ubiquitous phenomenon not only in energy-transfer studies but also in time-resolved fluorescence studies on conjugated polymers.[24] It is usually associated with residual trapping at unidentified traps such as oxidation products with a time-dependent trapping rate that translates into a dispersive decay law, described in terms of the Kohlrausch–Williams–Watts (KWW) decay law,[32] mentioned above. An exponent of 0.8 indicates that a small fraction of aggregate excitations are lost via a weakly dispersive exciton motion toward unidentified scavengers such as electron traps that are ubiquitous in π-conjugated polymers.[33−35]

In conclusion, in addition to the observed ultrafast energy transfer and implied core–shell structure of the aggregates, an intriguing aspect of the present work relates to the decomposition of the absorption spectra of MEH-PPV in MTHF solution near and below the transition temperature. At first glance, the overall spectra shown in Figure 2 resemble the absorption spectra of weakly interacting H-aggregates in P3HT, bearing out an apparent ratio of the 0–0 and 0–1 features of

DOI: 10.1021/acsmacrolett.5b00133
ACS Macro Lett. 2015, 4, 412−416

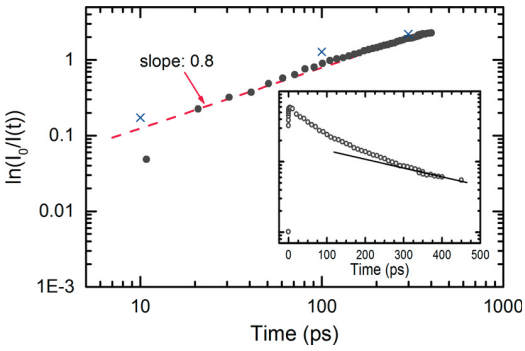

Figure 6. Decay of $\Delta T/T$ at 2.07 eV (dots) for E_{Ex} = 2.48 eV at 120 K, presented in a Kohlrausch–Williams–Watts (KWW) plot for times >10 ps. The red dashed line indicates a slope of 0.8, as discussed in the text. For comparison, the blue crosses indicate the values obtained for the area below the GSB + SE 0–0 band centered at 2.1 eV (=zeroth spectral moment). Slight deviation at early time scales originate from a spectral band shift. The inset shows $\Delta T/T$ at 2.07 eV plotted in a semilogarithmic fashion, with the solid line indicating a mono-exponential decay function with a lifetime of 350 ps.

less than unity. Separating those spectra disproves this conjecture. It turns out that the isolated spectrum of the planarized chromophores is mirror-symmetric with the fluorescence spectrum, thus, implying a high planarity of the aggregated chains. In fact, comparison of the emission spectra indicates the planarized chromophores in MEH-PPV to be as planar as ladder-type poly(*p*-phenylene) (MeLPPP), where covalent bridges enforce a rigid, flat structure and which recently has shown room temperature Bose–Einstein condensation of cavity exciton-polaritons.[36]

■ ASSOCIATED CONTENT

Supporting Information

Details on transient absorption setup. Relative change of area under emission spectra and spectral shift of emission and absorption as a function of temperature. Details on the calculation of the fraction of planarized chains, relative change of oscillator strength as a function of temperature. Transient absorption spectra for further times after excitation. Estimation of energy transfer range. This material is available free of charge via the Internet at http://pubs.acs.org.

■ AUTHOR INFORMATION

Corresponding Author

*E-mail: anna.koehler@uni-bayreuth.de.

Notes

The authors declare no competing financial interest.

■ ACKNOWLEDGMENTS

We acknowledge financial support by the Bavarian State Ministry of Science, Research, and the Arts through the Collaborative Research Network "Solar Technologies go Hybrid", by the German Science Foundation DFG through the doctoral training center GRK1640 and by the Federal Ministry of Education and Research (BMBF) through the Project "OLYMP".

■ REFERENCES

(1) Yamagata, H.; Hestand, N. J.; Spano, F. C.; Köhler, A.; Scharsich, C.; Hoffmann, S. T.; Bässler, H. *J. Chem. Phys.* **2013**, *139*, 114903.
(2) Scharsich, C.; Lohwasser, R. H.; Sommer, M.; Asawapirom, U.; Scherf, U.; Thelakkat, M.; Neher, D.; Köhler, A. *J. Polym. Sci., Part B: Polym. Phys.* **2012**, *50*, 442–453.
(3) Cone, C. W.; Cheng, R. R.; Makarov, D. E.; Vanden Bout, D. A. *J. Phys. Chem. B* **2011**, *115*, 12380–12385.
(4) Panzer, F.; Bässler, H.; Lohwasser, R.; Thelakkat, M.; Köhler, A. *J. Phys. Chem. Lett.* **2014**, *5*, 2742–2747.
(5) Yamagata, H.; Spano, F. C. *J. Chem. Phys.* **2012**, *136*, 184901.
(6) Aycock, D. F. *Org. Process Res. Dev* **2007**, *11*, 156–159.
(7) Köhler, A.; Hoffmann, S. T.; Bässler, H. *J. Am. Chem. Soc.* **2012**, *134*, 11594–11601.
(8) Mirzov, O.; Scheblykin, I. G. *Phys. Chem. Chem. Phys.* **2006**, *8*, 5569–5576.
(9) Schwartz, B. J. *Annu. Rev. Phys. Chem.* **2003**, *54*, 141–172.
(10) Hsu, J.-H.; Fann, W.; Tsao, P.-H.; Chuang, K.-R.; Chen, S.-A. *J. Phys. Chem. A* **1999**, *103*, 2375–2380.
(11) Wood, P.; Samuel, I. D. W.; Schrock, R.; Christensen, R. L. *J. Chem. Phys.* **2001**, *115*, 10955–10963.
(12) Scharsich, C.; Fischer, F. S. U.; Wilma, K.; Hildner, R.; Ludwigs, S.; Köhler, A. Manuscript in preparation, 2015.
(13) Collison, C. J.; Rothberg, L. J.; Treemaneekarn, V.; Li, Y. *Macromolecules* **2001**, *34*, 2346–2352.
(14) Scheibe, G. *Angew. Chem.* **1937**, *50*, 212–219.
(15) Cohen, M. D.; Fischer, E. *J. Chem. Soc.* **1962**, 3044–3052.
(16) Rahimi, K.; Botiz, I.; Agumba, J. O.; Motamen, S.; Stingelin, N.; Reiter, G. *RSC Adv.* **2014**, *4*, 11121–11123.
(17) Yamagata, H.; Hestand, N. J.; Spano, F. C.; Köhler, A.; Scharsich, C.; Hoffmann, S. T.; Bässler, H. *J. Chem. Phys.* **2013**, *139*, 114903.
(18) Khan, A. L. T.; Sreearunothai, P.; Herz, L. M.; Banach, M. J.; Köhler, A. *Phys. Rev. B* **2004**, *69*, 085201.
(19) Lee, C. K.; Hua, C. C.; Chen, S. A. *Macromolecules* **2013**, *46*, 1932–1938.
(20) Peteanu, L. A.; Sherwood, G. A.; Werner, J. H.; Shreve, A. P.; Smith, T. M.; Wildeman, J. *J. Phys. Chem. C* **2011**, *115*, 15607–15616.
(21) De Leener, C.; Hennebicq, E.; Sancho-Garcia, J.-C.; Beljonne, D. *J. Phys. Chem. B* **2009**, *113*, 1311–1322.
(22) Brunner, K.; Tortschanoff, A.; Warmuth, C.; Bässler, H.; Kauffmann, H. F. *J. Phys. Chem. B* **2000**, *104*, 3781–3790.
(23) Mollay, B.; Lemmer, U.; Kersting, R.; Mahrt, R. F.; Kurz, H.; Kauffmann, H. F.; Bässler, H. *Phys. Rev. B* **1994**, *50*, 10769–10779.
(24) Herz, L. M.; Silva, C.; Grimsdale, A. C.; Müllen, K.; Phillips, R. T. *Phys. Rev. B* **2004**, *70*, 165207.
(25) Klafter, J.; Shlesinger, M. F. *Proc. Natl. Acad. Sci. U.S.A.* **1986**, *83*, 848–851.
(26) Klafter, J.; Blumen, A. *Chem. Phys. Lett.* **1985**, *119*, 377–382.
(27) Palmer, R. G.; Stein, D. L.; Abrahams, E.; Anderson, P. W. *Phys. Rev. Lett.* **1984**, *53*, 958–961.
(28) Budimir, J.; Skinner, J. L. *J. Chem. Phys.* **1985**, *82*, 5232–5241.
(29) Blumen, A.; Zumofen, G.; Klafter, J. *Phys. Rev. B* **1984**, *30*, 5379–5382.
(30) Klafter, J.; Blumen, A. *J. Chem. Phys.* **1984**, *80*, 875–877.
(31) Mollay, B.; Kauffmann, H. F. *J. Chem. Phys.* **1992**, *97*, 4380–4397.
(32) Williams, G. Molecular aspects of multiple dielectric relaxation processes in solid polymers. *Electric Phenomena in Polymer Science*; Springer: Berlin Heidelberg, 1979; Vol. 33, pp 59–92.
(33) Nicolai, H. T.; Kuik, M.; Wetzelaer, G. A. H.; de Boer, B.; Campbell, C.; Risko, C.; Brédas, J. L.; Blom, P. W. M. *Nat. Mater.* **2012**, *11*, 882–887.
(34) Köhler, A. *Nat. Mater.* **2012**, *11*, 836–837.
(35) Mikhnenko, O. V.; Kuik, M.; Lin, J.; van der Kaap, N.; Nguyen, T.-Q.; Blom, P. W. M. *Adv. Mater.* **2014**, *26*, 1912–1917.
(36) Plumhof, J. D.; Stöferle, T.; Mai, L.; Scherf, U.; Mahrt, R. F. *Nat. Mater.* **2014**, *13*, 247–252.

DOI: 10.1021/acsmacrolett.5b00133
ACS Macro Lett. 2015, 4, 412–416

Supporting information to:

Ultrafast energy transfer between disordered and highly planarized chains of Poly[2-methoxy-5-(2-ethylhexyloxy)-1,4-phenylenevinylene] (MEH-PPV)

Thomas Unger[†,‡], Fabian Panzer[†,‡], Cristina Consani[#], Federico Koch[#], Tobias Brixner[#,‖], Heinz Bässler[‡], Anna Köhler[†,‡,*]

[†]Experimental Physics II

University of Bayreuth, 95540 Bayreuth, Germany

[‡]Bayreuth Institute of Macromolecular Research (BIMF)

University of Bayreuth, 95440 Bayreuth, Germany

[#]Institut für Physikalische und Theoretische Chemie, Universität Würzburg,

Am Hubland, 97074 Würzburg, Germany

[‖] Center for Nanosystems Chemistry (CNC), Universität Würzburg, Am Hubland,

97074 Würzburg, Germany

1. Description of the transient absorption setup with excitation at 2.1eV

Transient absorption measurements with excitation at 2.48 eV were performed with a 100 kHz setup, consisting of a RegA9000 regenerative amplifier system from Coherent that delivered pulses, centered at 800 nm with a pulse width of about 190 fs as confirmed by an autocorrelator. 12% of the intensity was used to create the probe light externally in a YAG-crystal in the range from 480 to 1300 nm. The remaining intensity pumped a dual-pass optical parametric amplifier to produce the excitation pulses in the range from 2.48 eV to 2.0 eV. The pump beam diameter was about 200 µm to ensure homogeneous excitation. For the measurements, the pump pulse fluence was set to about 10 µJ/cm^2, at which the pump-probe signal was linear with fluence (see Figure S1). Spectra were recorded using a lock-in amplifier and a monochromator with a silicon diode.

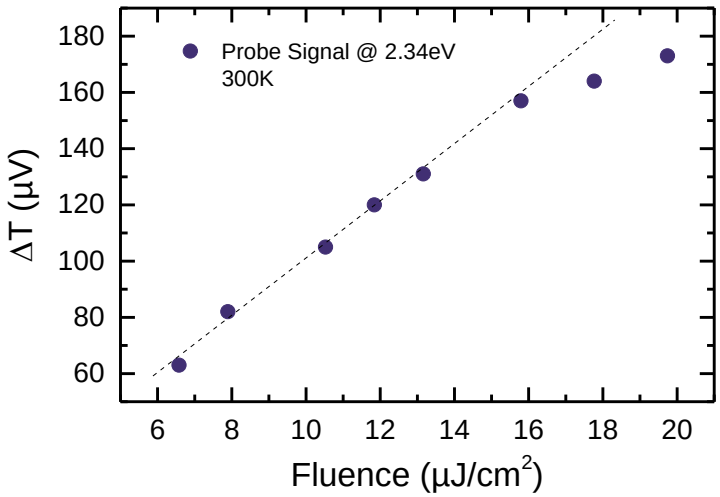

Figure S1: Pump-probe signal as a function of fluence, probed at an energy of 2.34 eV.

For the transient absorption measurements exciting at 2.1 eV, the sample was filled in a 0.3 mm thick cell and placed in a continuous-flow cryostat (Oxford Instruments) operated with liquid nitrogen. The 42 fs excitation pulses at 2.1 eV were generated by a commercial parametric amplifier (TOPAS, Light Conversion), pumped by the output of a 1 kHz regenerative amplifier (Spitfire Pro, Spectra Physics) delivering 120 fs, 2.5 mJ pulses at 800 nm. The white-light continuum used as a probe beam was generated by focusing a small fraction of the 800 nm pulses in a CaF2 window. Pump and probe diameters at the sample position were 50 µm and 30 µm, respectively. Also in this case, we used excitation-pulse energies (1.8 nJ) within the linear regime of excitation, where exciton-exciton annihilation processes are negligible.

2. Changes of steady-state absorption and emission spectra as a function of temperature

The relative change of area under the measured emission spectrum was normalized to the area under the measured spectrum at a temperature of 300 K. Upon cooling down to 180 K, the area continuously increases and finally triples at 180 K (Figure S2a). Spectral shifts of emission and absorption spectra were determined by considering the energetic position of the S_1-S_0 0-0 peaks. In emission this was easily possible within the whole measured temperature range. In contrast to that, simple determination of the S_1-S_0 0-0 peak from the spectrally unresolved absorption spectra of the disordered phase was not possible (Figure S2b).

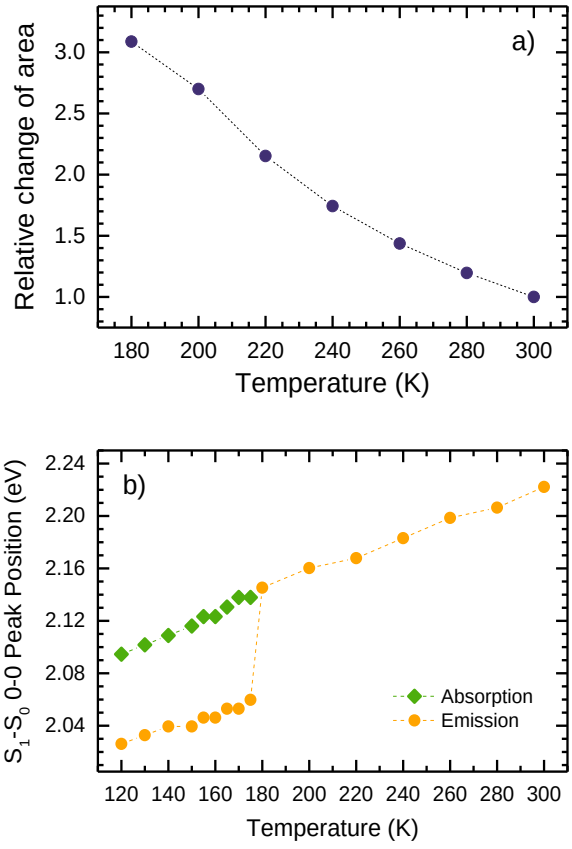

Figure S2: (a) Relative change in area under emission spectra, normalised to the area at 300 K. (b) Energetic position of the S_1-S_0 0-0 peaks of the aggregated phase (< 180 K) and disordered phase (>180 K).

3. Calculating the fraction of aggregates from absorption spectra

The fraction of aggregated chains f_{agg} as a function of temperature is calculated by

$$f_{agg} = F * f_{absaggr}$$

where $f_{absaggr}$ is the fraction of aggregate absorption from the measured absorption spectrum and F is the relative change of oscillator strength between disordered and aggregated chain conformation. We derived the relative change in oscillator strength between the aggregated and disordered phase, $\varepsilon_{aggregate}/\varepsilon_{disordered}$, similar to the approach which is described in detail in the supporting informations of previous works by Clark et al.[1] and Scharsich et al.[2], using

$$\frac{A_{aggregate}}{A_{disordered}} = -\frac{\varepsilon_{aggregate}}{\varepsilon_{disordered}} = F$$

with the areas taken from the shaded regions as illustrated in Figure S3.

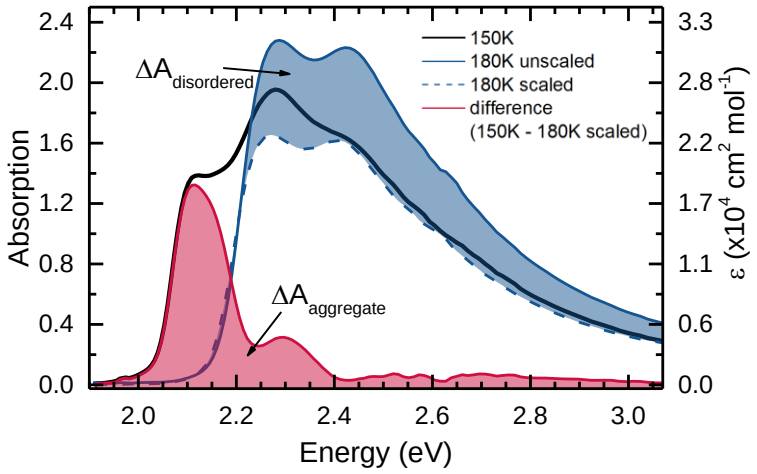

Figure S3: Exemplary illustration of the procedure to determine the change in oscillator strength between coiled and aggregated phase of MEH-PPV. The required areas $A_{disordered}$ and $A_{aggregate}$ are highlighted.

From this approach, the relative change in oscillator strength between disordered and aggregated phase can be obtained within the temperature range between 180 K and 140 K, which is found to be near unity (Figure S4).

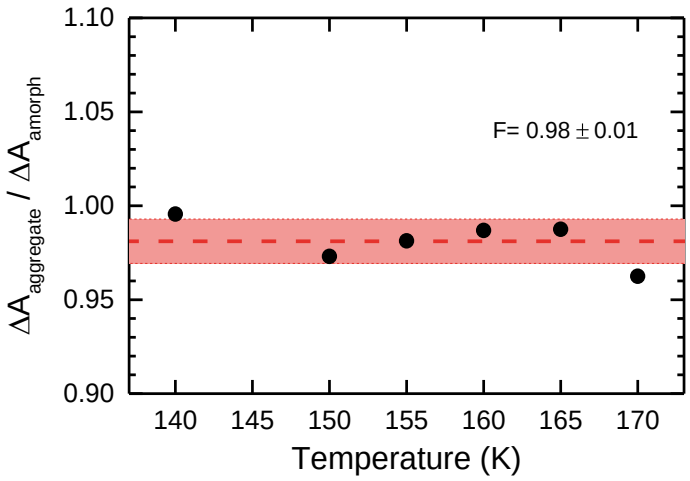

Figure S4: Relative change of oscillator strength between disordered and aggregated phase as a function of temperature.

4. Transient absorption spectra

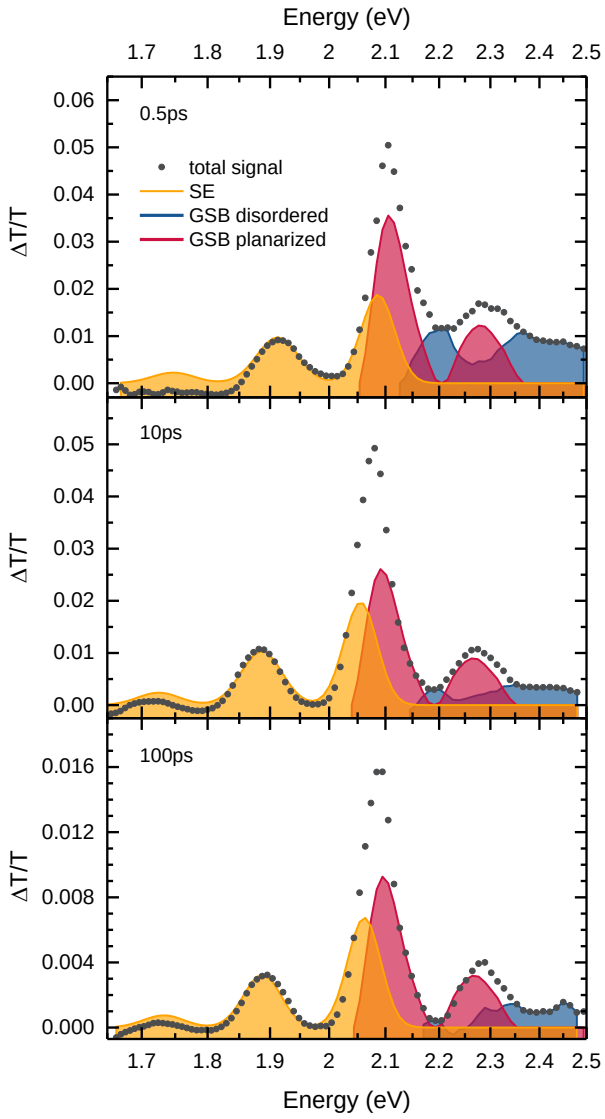

Figure S5: Pump-probe spectra for excitation at 2.48 eV (where coiled chains absorb) at 120 K for different time delays after excitation, i.e. (a) 0.5 ps, (b) 10 ps and (c) 100 ps. In addition to the total ΔT/T signal (dots), the contributions of SE, GSB from disordered chromophores and the GSB from the planarized chromophores are indicated by orange, blue and red solid lines, respectively.

5. Estimate of energy transfer range

We will argue that the short timescale of energy transfer (< 1 ps) is not compatible with long-range energy transfer from coiled to planarized chains. Transfer from coiled to planarized chains is completed within 1 ps. Thus, a generous upper limit for the transfer rate k is 1×10^{12} s^{-1}.

Suppose the transfer takes place from a coiled chromophore to a planarized chromophore that are separated by a long distance R. "Long", in this context, in particular implies that the distance separating the centres of mass of the two chromophores is larger than their size. Thus, the point-dipole approximation applies. Let us suppose further that coupling between these chromophores is weak and that relaxation within S_1 has occurred prior to energy transfer, so that the energy transfer can be presumed to be of a Förster-type nature.

In the case of Förster-type energy transfer, the energy transfer rate k from one chromophore to another at a distance R is given by

$$k = \frac{1}{\tau_0}\left(\frac{R_0}{R}\right)^6, \qquad (1)$$

where τ_0 is the lifetime of the donor chromophore in the absence of the acceptor chromophore and R_0 is the Förster radius. The Förster radius depends on the mutual orientation of the two chromophores, the refractive index of the surrounding medium, the fluorescence quantum yield of the donor chromophore and the spectral overlap between the donor emission and the acceptor absorption. Solving eq. (1) for R yields

$$R = \frac{R_0}{\sqrt[6]{\tau_0 k}}. \qquad (2)$$

For the lifetime of the donor chromophore we take a lifetime of 500 ps, which is typical for π-conjugated polymers[3] and which is consistent with the data shown in Figure 5 in the manuscript. Typical Förster radii are in the range of a few nanometers, with 5 nm being a generous upper limit for R_0 when all parameters are maximized.[4]

Thus, an upper limit for the distance between the two chromophores is $\boldsymbol{R} \leq 1.8$ nm. This estimate demonstrates that energy transfer occurring on a picosecond timescale implies proximity between donor and acceptor chromophores.

Addendum – Estimate of the maximum Förster radius of 5 nm:

R_0 is given by:[4]

$$\frac{R_0}{nm} = 2.108 * 10^{-2} \left\{ \kappa^2 \Phi_D^0 n^{-4} \int_{\lambda}^{0} I_\lambda^D(\lambda) \left[\frac{\varepsilon_A(\lambda)}{dm^3 mol^{-1} cm^{-1}} \right] \left(\frac{\lambda}{nm} \right)^4 d\lambda \right\}^{1/6}$$

with κ^2 being the dipole orientation factor, Φ_D^0 the fluorescence quantum yield of the donor in the absence of the acceptor, *n* the refractive index of the solvent medium, ε_A the molar extinction coefficient of the donor and I_λ^D the donor emission spectrum normalized to an area value of unity. Φ_D^0 can at most be unity, and the refractive index cannot be lower than 1. For the extinction coefficient of the donor we take a maximum constant value of 10^5 cm^2 mol^{-1},[5] i.e. we assume a step function. So far, all values have been assumed to take the maximum value that is allowed by theory.

Let us presume that the overlap of donor and acceptor extends over a range of 100 nm, say, from 500 to 600 nm. Note that this is again a generous estimate and that typical values are smaller. Inserting these values into the above equation and carrying out the integral leads to R_0=3.7 nm as maximum possible Förster radius.

Thus, allowing for some margin, presuming a value of R_0=5 nm is a generous upper limit.

References:

1. Clark, J.; Chang, J.-F.; Spano, F. C.; Friend, R. H.; Silva, C. *Applied Physics Letters* **2009,** 94, (16), 163306.
2. Scharsich, C.; Lohwasser, R. H.; Sommer, M.; Asawapirom, U.; Scherf, U.; Thelakkat, M.; Neher, D.; Köhler, A. *J Polym Sci Pol Phys* **2012,** 50, (6), 442-453.
3. Ariu, M.; Lidzey, D. G.; Sims, M.; Cadby, A. J.; Lane, P. A.; Bradley, D. D. C. *Journal of Physics: Condensed Matter* **2002,** 14, (42), 9975.
4. Lakowicz, J. R., *Principles of fluorescence spectroscopy*. Springer US: 2006.
5. See, e.g. Chapter 5 in Turro, N. J., Modern Molecular Photochemistry, University Science Books,1991

4.5. Relaxation dynamics and exciton energy transfer in the low-temperature phase of MEH-PPV

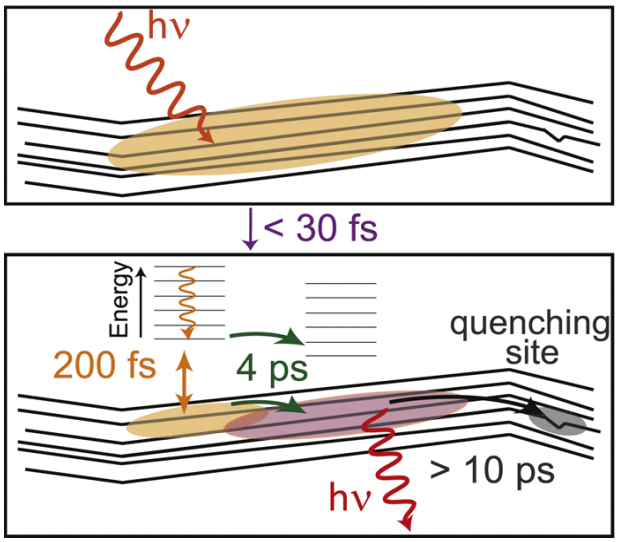

Cristina Consani, Federico Koch, Fabian Panzer, Thomas Unger, Anna Köhler and Tobias Brixner

Published in
The Journal of Chemical Physics
DOI: 10.1063/1.4918645

Relaxation dynamics and exciton energy transfer in the low-temperature phase of MEH-PPV

Cristina Consani,[1] Federico Koch,[1] Fabian Panzer,[2] Thomas Unger,[2] Anna Köhler,[2] and Tobias Brixner[1,3,a)]

[1]*Institut für Physikalische und Theoretische Chemie, Universität Würzburg, Am Hubland, 97074 Würzburg, Germany*

[2]*Lehrstuhl Experimentalphysik II, Universität Bayreuth, Universitätsstraße 30, 95440 Bayreuth, Germany*

[3]*Center for Nanosystems Chemistry (CNC), Universität Würzburg, Am Hubland, 97074 Würzburg, Germany*

(Received 2 February 2015; accepted 8 April 2015; published online 21 April 2015)

Understanding the effects of aggregation on exciton relaxation and energy transfer is relevant to control photoinduced function in organic electronics and photovoltaics. Here, we explore the photoinduced dynamics in the low-temperature aggregated phase of a conjugated polymer by transient absorption and coherent electronic two-dimensional (2D) spectroscopy. Coherent 2D spectroscopy allows observing couplings among photoexcited states and discriminating band shifts from homogeneous broadening, additionally accessing the ultrafast dynamics at various excitation energies simultaneously with high spectral resolution. By combining the results of the two techniques, we differentiate between an initial exciton relaxation, which is not characterized by significant exciton mobility, and energy transport between different chromophores in the aggregate. © *2015 AIP Publishing LLC.* [http://dx.doi.org/10.1063/1.4918645]

I. INTRODUCTION

Molecular functional materials are currently subject to extensive studies because of their applications in organic electronics and photovoltaics. Among these materials, conjugated polymers are particularly attractive as they combine high absorption cross sections with low-cost production and deposition over flexible substrates.[1–3] However, typical efficiencies of solar cells based on conjugated polymers are currently limited to <11%.[4]

The key parameters to understand photoinduced function in these devices are the interactions of polymer structural units (monomers), both within a single polymer chain and between neighboring polymer chains in aggregates. Indeed, such interactions affect the relaxation time scale of the excited states, the population yield of mobile excitons versus nonmobile species (e.g., excimers), the capability to transport the absorbed energy over long distances, the formation of charge-transfer states, and their dissociation into free charges in proximity of the donor-acceptor interface. Particularly, the efficiency of energy transport from the bulk of the donor material towards the interface with the acceptor is among the factors that have a significant influence on the performance of organic photovoltaic devices.

Conformational disorder, which is among the distinctive characteristics of conjugated polymers, has profound effects on the dynamics of excitons and energy transfer. Together with spatial variations in the polarization of the environment, conformational disorder breaks the conjugation along the polymer chains and forms short conjugated segments called "conformational subunits."[5,6] Absorption of a photon populates exciton states which are initially delocalized over several conformational subunits but localize on sub-100 fs time scales on smaller domains due to dynamic coupling between electronic and nuclear degrees of freedom.[7] On a longer time scale, electronic energy transfer is typically described in terms of a sequence of Förster energy transfer steps between localized excitons,[8,9] although intermediate regimes characterized by coherent intrachain energy transfer have been reported for Poly[2-methoxy-5-(2-ethylhexyloxy)-1,4-phenylenevinylene] (MEH-PPV) in chloroform.[10] The dynamics of energy transfer differs significantly along the polymer chain (intrachain) and between different polymer chains (interchain). The latter is typically one to two orders of magnitude faster than intrachain energy transfer,[11–14] explaining the more efficient energy transport observed in films as compared to isolated polymer chains in solution.[12,15,16]

The picture of exciton dynamics described above applies in general for conjugated polymers. However, the dynamics of the photoexcited species, as well as the rate, the efficiency, and the length scale of energy transport, can differ strongly for different systems. Additionally, the photophysics of conjugated polymers and their aggregates depends not only on the chemical nature of the compound but also on its structure and morphology.[12,17–21] Hence, understanding the key factors controlling exciton dynamics requires the capability to control the structure of the aggregate. A possibility in this respect is to use systems where both aggregation and the morphology of the self-aggregated state can be controlled by external parameters.

In this paper, we investigate the low-temperature self-aggregated phase of the polymer MEH-PPV in solution. In MEH-PPV, two classes of chromophores have been observed, one emitting at higher energy ("blue sites") than the other ("red sites").[22–25] The picture emerging from single-molecule spectroscopy suggests that MEH-PPV can be found in two distinct conformational classes, and that the relative amount

a)Electronic mail: brixner@phys-chemie.uni-wuerzburg.de

of blue and red sites in a single chain is controlled by the presence of interactions between segments of the polymer chain that are brought into contact by chain folding. The red sites have been repeatedly ascribed to planarized segments characterized by an increased conjugation length compared to the blue sites.[25,26] It was also suggested that the formation of the red sites might be related to aggregation.[22,27] Recent studies showed that concentrated solutions of MEH-PPV in 2-methyltetrahydrofuran (MeTHF) undergo a phase transition from a coiled conformation ("blue phase"), characteristic of room temperature, to an aggregated and planarized phase at low temperatures ("red phase"), characterized by very long conjugation length.[28] The phase transition is accompanied by the appearance of a low-energy band in both the absorption and emission spectra.[28,29] In the following, we will refer to the blue (red) phase as coiled (aggregated) phase.

Although the ultrafast dynamics of the room-temperature coiled phase of MEH-PPV has been extensively studied both in solution and films,[14,18,24,30,31] knowledge on the ultrafast dynamics of the aggregated red phase is still sparse. In the following, we use broadband transient absorption spectroscopy and coherent electronic two-dimensional (2D) spectroscopy to observe the exciton relaxation and energy transfer dynamics in the planarized aggregated phase of MEH-PPV. Combining the results from these experiments allows us to individuate two regimes of energy relaxation in the aggregated phase of MEH-PPV. In particular, we separate the initial exciton relaxation within a manifold of excitons sharing a common ground state (relaxation without significant energy transport) from the energy hopping between excitonic states located on different polymer segments. Furthermore, we show that the average time scale for energy hopping in the aggregated phase is comparable with the typical values reported for the red-emitting sites in single molecules.

II. EXPERIMENTAL METHODS

MEH-PPV was purchased from Sigma Aldrich (CAS 138184-36-8). Gel permeation chromatography measurements were performed (PSS Polymer Standards Service Gmbh in Mainz) using polystyrene as the calibration standard and solving the MEH-PPV in 1,2,4-trichlorbenzol at a temperature of 150 °C to make sure that it was completely dissolved. This measurement provided the weight-average molecular weight of the batch of sample used for our experiments (M_w = 218.8 kDa) and the number-average molecular weight (M_n = 58.12 kDa), resulting in a dispersity of $D = M_w/M_n$ = 3.76. The sample was dissolved in distilled MeTHF (Sigma Aldrich) at a concentration of 0.2 mg/ml. The solution was stirred and heated at ≈40–45 °C for 24 h, until no macroscopic particles could be observed anymore. Absorption and emission spectra at different temperatures were recorded with a home-built setup which is described in detail elsewhere.[32]

For the time-resolved measurements, the 0.3 mm thick sample cell was placed in a continuous-flow cryostat (Oxford Instruments) operated with liquid nitrogen. Upon cooling the sample from room temperature to 140 K, an optical density of ≈0.4 OD at 2.11 eV was achieved.

The light source for the ultrafast spectroscopy experiments was a commercial Spitfire Pro-regenerative amplifier (Spectra Physics) providing 120 fs, 2.5 mJ pulses at 800 nm with a repetition rate of 1 kHz. A small portion (<1 μJ) of the 800 nm pulses beam was focused onto a CaF_2 window to generate the white-light continuum probe. About one quarter of the laser intensity was used to pump a commercial non-collinear parametric amplifier (TOPAS White, Light Conversion) to generate the tunable excitation pulses. For the experiments described here, the excitation pulses were centered at 2.10 eV and 2.03 eV and pulse lengths were 42 fs and 60 fs, respectively. Beam diameters at the sample position were ≈50 μm and ≈30 μm for the excitation and probe beams, respectively. For all the experiments, we made sure that excitation-pulse energies were within the linear regime of excitation, where exciton-exciton annihilation processes are negligible (see also Fig. S1 in the supplementary material).[33,80] For the transient absorption experiments, photon flux of 9.4×10^{13} photons/cm^2 and 4.9×10^{14} photons/cm^2 were used upon 2.10 eV and 2.03 eV excitation, respectively.

The setup for 2D spectroscopy was described extensively elsewhere.[34] Briefly, 35 fs excitation pulses centered at 2.10 eV were generated by the TOPAS White and split into four replicas, which served as three excitation pulses and local oscillator in an inherently phase-stabilized fully noncollinear four-wave mixing setup with heterodyne detection. The time delay between the local oscillator and the third pulse was set to 2.8 ps. The coherence time τ was sampled in steps of $\Delta\tau$ = 5.5 fs, covering a range of ±143 fs. Scattering contributions may lead to distortions of the 2D signals and possible errors in the phasing procedure, since they add up to the projection of the signal on the detection axis. This might lead to errors in the phasing procedure or misinterpretation of cross-peaks and oscillating contributions. Therefore, it is important to efficiently subtract these undesired scattering contributions. Working with samples in the liquid phase often requires circulation of the sample to reduce photodamage, but this might lead to dynamic scattering. This dynamic scattering can be effectively reduced by double-modulation lock-in detection.[35] In our experiment, where the sample is still above the glass temperature but is not circulated inside the cryostat, we can perform scattering correction by acquiring certain scattering contributions at each delay point and subtracting them from the spectral interferograms before Fourier evaluation of the data.[36] In addition to our scattering correction routine, we added a polarizer in the signal beam to reduce remaining unpolarized scattered light. Data sets were phased to spectrally resolved pump-probe data acquired in the same setup (see also Fig. S2 in the supplementary material[80]). Optical signals were recorded with a CCD-array spectrometer (Acton SpectraPro 2500i equipped with PIXIS 2K CCD camera).

III. RESULTS AND ANALYSIS

A. Transient absorption

Figure 1(a) shows the normalized steady-state $S_1 \leftarrow S_0$ absorption (red solid) and $S_1 \rightarrow S_0$ emission spectra (red

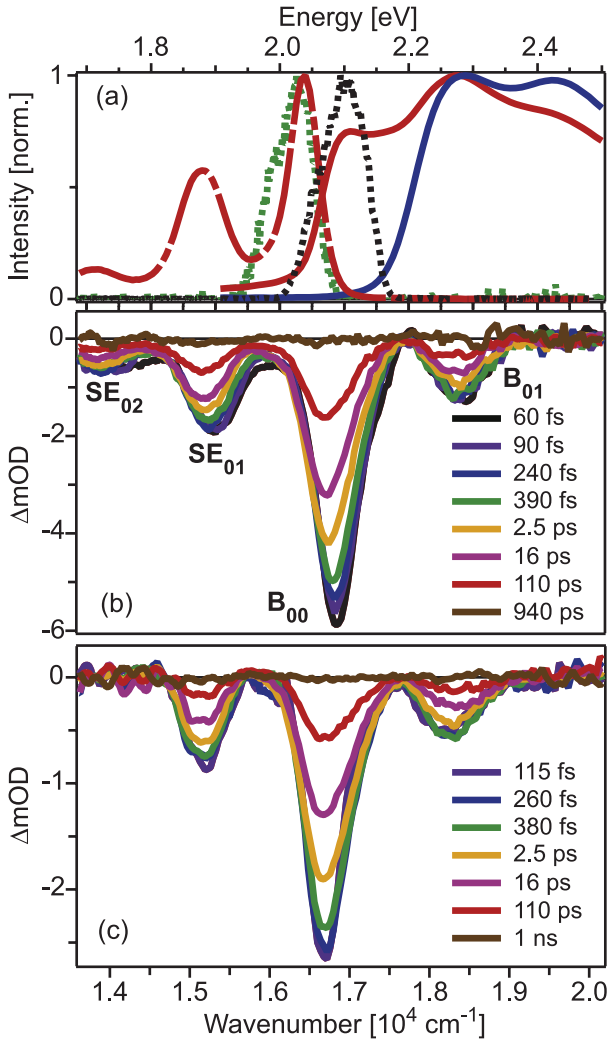

FIG. 1. (a) Static absorption (solid) and emission (dashed dotted) of the aggregated phase (red) and coiled phase (blue) of MEH-PPV at 140 K and 180 K, respectively. The laser spectra used in the experiments are also shown (black and green dotted). Selection of transient absorption spectra at 140 K and different population times upon excitation at (b) 2.10 eV (1.69×10^4 cm^{-1}) and (c) 2.03 eV (1.64×10^4 cm^{-1}).

dashed-dotted) of MEH-PPV at 140 K, together with the spectra of the laser pulses used for the experiments (black and green dotted lines). The low-energy absorption feature at 2.1 eV only appears below a critical temperature (here 180 K, see also the steady-state absorption at temperatures immediately above the phase transition, plotted in blue in Fig. 1(a)) and is attributed to the 0–0 transition of the aggregated phase.[28] The emission at 140 K is characterized by three major bands at 2.04 eV, 1.88 eV, and 1.71 eV, which are ascribed to the 0–0, 0–1, and 0–2 transitions, respectively.

Selections of transient absorption spectra of the aggregated phase of MEH-PPV at 140 K and different population times T are shown for excitation at 2.10 eV (Fig. 1(b)) and 2.03 eV (Fig. 1(c)). No significant difference in the dynamics is observed by lowering the temperature to 120 K (Fig. S3 in the supplementary material[80]). As it is the purpose of this study to selectively investigate the dynamics in the aggregated phase, we did not excite the sample at energies higher than 2.1 eV, where absorption from a fraction of the sample in the coiled phase may still be present. For both excitation energies, the transient signals are dominated by three major negative bands at ≈2.27 eV, ≈2.08 eV, and ≈1.88 eV. A fourth small negative band at ≈1.72 eV is evident upon 2.10 eV excitation; upon 2.03 eV excitation, the noise in this spectral region is comparable with the expected magnitude of such a feature. By comparing the shape and energy position of the observed bands with the inverted static absorption and emission (see Fig. 1(a)), we can ascribe the negative feature at 2.27 eV to the ground-state bleach of the vibronic 0–1 transition and we will refer to this band as B_{01} in the following. The band at 2.08 eV (B_{00} in the following) contains contributions from both the ground-state bleach and the stimulated emission (SE) of the 0–0 transition, while the negative bands at ≈1.88 eV (SE_{01}) and ≈1.72 eV (SE_{02}) arise from SE from the 0–1 and 0–2 vibronic transitions, respectively. No clear signatures of excited-state absorption (positive ΔOD signals) are observed in the entire investigated spectral range.

Interestingly, the ground-state bleach signal in the 2.10–2.50 eV region does not resemble the steady-state absorption, but it appears as the mirror image of the stimulated emission. Since no signatures of excited-state absorption are detected in this spectral region, the discrepancy between bleach and steady-state absorption must be ascribed to the fact that only a fraction of the steady-state absorption stems from the states absorbing at 2.10 eV, i.e., from the aggregated phase. Although a precise determination of the fraction of MEH-PPV in the planarized conformation is still pending, the formation of the planarized chromophores is expected to affect only a fraction of the sample. In fact, in conjugated polymers typically between 40% and 60% of the polymer chains can form planarized chromophores.[32,37] Thus, we assign the steady-state absorption above 2.10 eV that is not reflected in a transient bleach signal to the contribution from the coiled phase.

For both excitation energies, the transient absorption signal decays non-exponentially and completely recovers in less than 1 ns (Fig. S4 in the supplementary material[80]). The most pronounced difference between the evolution of the transient signals at the two excitation energies is observed in the sub-10 ps dynamics. Upon excitation at 2.10 eV, all the bands show a shift to lower energies, most pronounced in the SE (Fig. 1(b)). The amplitude of this shift is almost completely suppressed when the excitation is tuned to the lowest edge of the aggregated-phase absorption at 2.03 eV (Fig. 1(c)).

In general, broadband transient absorption data can be described globally by assuming kinetic models with rates that are independent from the detection wavenumber. Such global description allows identifying the spectral features associated with different processes through their time evolution. However, when the transient spectra show pronounced spectral shifts on time scales comparable with the population relaxation (such as in Fig. 1(b)), the results from such a global analysis can be difficult to interpret.

Here, we follow a different approach. Since the transient absorption signals are dominated by well-separated bleach and SE bands, an analysis of the spectral moments of these bands can be performed to disentangle different molecular processes. We define the spectral moments $M_0^{(i)}$ and $M_1^{(i)}$ of

the three major bands i (i = B_{01}, B_{00} and SE_{01}) according to

$$M_0^{(i)}(T) = \sum_{\nu=\nu_1^{(i)}}^{\nu_2^{(i)}} I(\nu,T) \cdot \Delta\nu, \tag{1a}$$

$$M_1^{(i)}(T) = \frac{1}{M_0^{(i)}(T)} \sum_{\nu=\nu_1^{(i)}}^{\nu_2^{(i)}} \nu \cdot I(\nu,T) \cdot \Delta\nu, \tag{1b}$$

where $I(\nu,T)$ is the absorbance change at frequency ν and population time T, $\nu_1^{(i)}$ and $\nu_2^{(i)}$ are the frequency summation limits for each band i, and $\Delta\nu$ is the frequency interval between data points. As long as bands are not overlapping, the band integrals $M_0^{(i)}$ (zero-order moments) are not sensitive to variations in the shape or position of the bands, but probe exclusively the population dynamics. The first spectral moments $M_1^{(i)}(T)$ correspond to the average spectral positions of the bands and allow us to directly monitor band shifts.

Figures 2(a) and 2(b) depict $M_0^{(i)}(T)$ for 2.10 eV and 2.03 eV excitation, respectively (symbols). At both excitation energies, the temporal evolution of the band integrals appears as a non-exponential decay. *A priori*, due to the wide distribution of polymer lengths and possible conformations in our sample, the measured temporal evolution could arise either (I) from a broad distribution of rates or (II) from several distinct kinetic processes. We will now proceed to analyze the observed population dynamics both via model I and model II and provide arguments for both of them. However, we stress that the main conclusion of our work, i.e., the characterization of the dynamics of exciton relaxation and transport within the aggregated phase, will be based on the band-shift analysis that is completely independent from the choice of the population-kinetics model.

Kinetics in case I can be modelled with a stretched exponential function according to $M_0^{(i)}(T) = A \cdot e^{-(\frac{T}{\tau})^{\beta}}$ with amplitude A, characteristic time τ, and distribution width β. This stretched exponential form is also known as Kohlrausch-Williams-Watts (KWW) function.[38] A number of theoretical treatments have shown that the stretched exponential is recovered when modelling independent, parallel single-step processes on one hand yet, on the other hand, also for sequential, multistep processes on disordered structures.[38–45] In particular, energy-dispersive hopping in disordered organic semiconductors is characterized by a KWW-like behaviour.[8,46,47] In that case, the double logarithmic plot $\ln(I(T=0)/I(T))$ of the signal intensity I versus the time T typically shows two regimes (see Fig. S5 in the supplementary material[80]). For short times, a slope β of unity—equivalent to an exponential decay—indicates vanishing dispersion. This is commonly interpreted

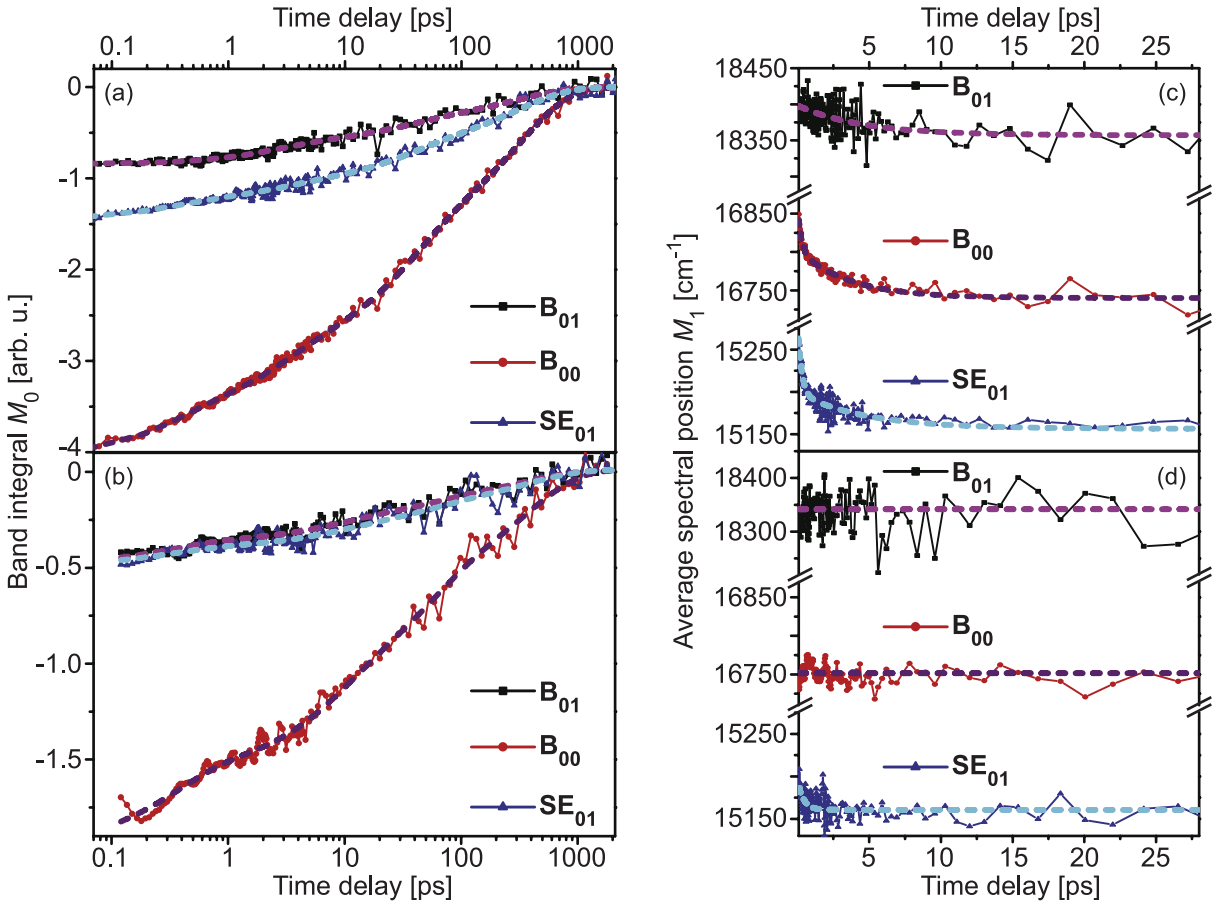

FIG. 2. Spectral moments of the three major bands observed in the transient absorption experiments as a function of the population time T: integrated intensity $M_0^{(i)}$ (Eq. (1a)) of the three major bands for excitation at (a) 2.10 eV and (b) 2.03 eV and their average spectral position $M_1^{(i)}$ (Eq. (1b)) upon excitation at (c) 2.10 eV and (d) 2.03 eV. Consistent with the results of the maximum entropy method analysis, the temporal dependence of the spectral moments is fitted by a multi-exponential kinetics (dashed lines).

to designate energetic relaxation by jumps to lower energy nearest neighbors. Subsequently, lower energy sites immediately adjacent to an excitation are no further available. Thus, at longer times, jumps to non-nearest neighbours prevail and the slope β acquires a value near 0.5. Note that values of $\beta = 1/2$ and $\beta = 1/3$ are expected for Förster transfer from a random ensemble of donors to a dilute array of acceptors in a 3D and 2D case, respectively.

In case II, a multiexponential fit function $M_0^{(i)}(T) = \sum_{j=1}^{4} A_j \cdot e^{-\frac{T}{\tau_j}}$, with amplitudes A_j and characteristic times τ_j, is suitable. Both models are approximately consistent with our experimental data (Fig. S6 in the supplementary material[80]). In order to attempt a discrimination without initial bias, the maximum entropy method (MEM) is employed, via the open-source program MemExp,[48,49] to simulated data for models I and II and to the experimental data (Fig. S7 in the supplementary material[80] shows exemplary results for $M_0^{(B_{00})}$). The MEM analysis of the experimental data contains four distinct time scale peaks (Figs. S4, S7, and S8[80]) and thus more clearly resembles model II rather than model I. Thus, we further discuss our results in terms of a multi-exponential fit. Fit constants are listed in Table I. Note that despite the use of a multi-exponential model, the retrieved time constants may be distributed; thus for the following discussion, the values reported in Table I must be interpreted as the average time constants of different rate distributions. The fit results for model I are listed in Table S1 of the supplementary material.[80]

The temporal evolution of the average spectral position $M_1^{(i)}(T)$ of the three major bands is plotted in Figs. 2(c) and 2(d) for excitation at 2.10 eV and 2.03 eV, respectively, and fit results are again reported in Table I. Upon excitation at 2.10 eV, all bands show a red-shift which is completed within the first 15 ps. The bleach band (B_{01}) shifts mono-exponentially towards lower wavenumbers on a ≈4 ps time scale (see also the τ_2^s values in Table I). A red-shift with similar time constants is observed also in the average spectral position of bands B_{00} and SE_{01}, preceded by an additional fast ($\tau_1^s \approx 200 - 250$ fs) red-shift. Noteworthy, the amplitude of the ≈4 ps red-shift is virtually identical (42 ± 3 cm^{-1}) for the B_{01} and SE_{01} bands.

The sub-300 fs shift appears exclusively in bands containing contributions from SE, thus we ascribe it to processes occurring in the excited state. The lack of such contribution in the B_{01} band is a further indication that no significant excited-state absorption is contributing to the signal in this spectral region.

Upon excitation at 2.03 eV (Fig. 2(d)), no spectral evolution is observed in the three bands, except for a very small initial red-shift on a sub-500 fs time scale in the SE_{01} band.

B. Coherent 2D spectroscopy

Coherent electronic 2D spectroscopy can be seen as an extension of transient absorption spectroscopy, where the time-dependent molecular signal is measured as a function of both the excitation and detection frequency. In coherent 2D spectroscopy, the molecular response to the interaction with three electromagnetic fields is measured as a function of three time delays. For each fixed population time T (between the second and third pulse), Fourier transformation of the emitted signal with respect to the time delay τ between the first two pulses, and t between the third pulse and the signal, yields the excitation and detection axes, respectively. Since the 2D signal and its time evolution allow mapping of electronic couplings and correlations between initial and final electronic states during molecular relaxation, respectively, coherent 2D spectroscopy is particularly suitable to characterize processes of energy transfer in complex systems.[50–52] In the following, we apply coherent 2D spectroscopy to discriminate between band shifts and homogeneous broadening in the temporal evolution of the aggregated-phase signal of MEH-PPV, as well as to observe exciton dynamics and energy transfer at several excitation energies with high frequency resolution.

Figures 3(a)-3(d) show a selection of 2D spectra of MEH-PPV in the aggregated phase for four different population times T. Data are acquired at 140 K with the excitation pulses shown in Fig. 1(a) (black dotted), thus the lowest transition band of the aggregated phase is selectively investigated. At all population times, the 2D spectra are dominated by a single feature, containing contributions from the bleach and SE of the $0 \rightarrow 0$ transition (see also Fig. 1(b)). No clear signatures of excited-state absorption are detected.

TABLE I. Characteristic time constants obtained from a multi-exponential global fit of the integrated signals $M_0^{(i)}(T)$ and from the independent fits of the average spectral position $M_1^{(i)}(T)$ of the three major bands ($i = B_{01}$, B_{00}, and SE_{01}) of the transient absorption data described in Sec. III A.

	Excitation energy Temperature	2.10 eV 120 K	2.10 eV 140 K	2.03 eV 140 K
Population decay $M_0(T)$ $M_0(T) = \sum_{j=1}^{4} A_j e^{-\frac{T}{\tau_j}}$	τ_1 (fs)	220 ± 50	290 ± 40	240 ± 60
	τ_2 (ps)	2.6 ± 0.2	2.5 ± 0.3	5 ± 2
	τ_3 (ps)	41 ± 4	32 ± 3	41 ± 8
	τ_4 (ps)	320 ± 20	312 ± 11	380 ± 50
Band shift $M_1^{B_{01}}(T)$	τ_1^s (fs)	…	…	…
	τ_2^s (ps)	3.9 ± 0.8	4.8 ± 0.8	…
Band shift $M_1^{B_{00}}(T)$	τ_1^s (fs)	200 ± 80	230 ± 70	<100
	τ_2^s (ps)	2.9 ± 0.5	3.6 ± 0.6	…
Band shift $M_1^{SE_{01}}(T)$	τ_1^s (fs)	170 ± 40	250 ± 50	400 ± 200
	τ_2^s (ps)	2.8 ± 0.6	4.7 ± 1.1	…

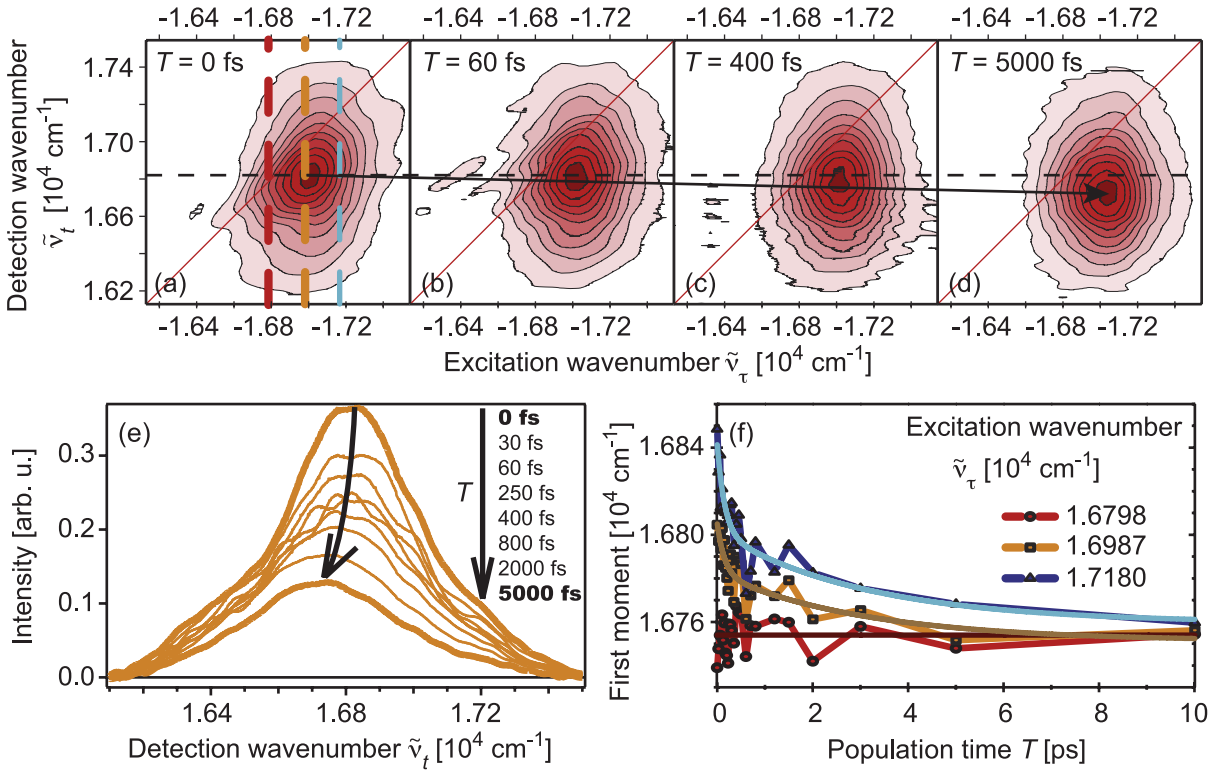

FIG. 3. Selection of experimentally retrieved (normalized) 2D spectra of MEH-PPV at different population times T: (a) 0 fs, (b) 60 fs, (c) 400 fs, and (d) 5000 fs. Contour lines display signal levels from 5% (light pink) to 95% (dark red) in steps of 10%. The dashed horizontal line marks the $T = 0$ average spectral position of the 2D signal at $\widetilde{\nu}_\tau = 1.6987 \times 10^4$ cm^{-1}, while the black arrow indicates the shift of the 2D signal towards lower detection wavenumbers as a function of the population time T. (e) Spectral evolution of the signal along the detection axis for excitation at $\widetilde{\nu}_\tau = 1.6987 \times 10^4$ cm^{-1} (orange vertical dashed line in panel (a)). (f) Temporal evolution of the first moment (i.e., average spectral position) of the signal along the detection axis (symbols) for the different excitation wavenumbers shown by the vertical lines in panel (a). Overlayed solid lines show the best individual bi-exponential fit of each trace.

The most prominent features in these spectra are the initial elongation of the signal along the ($-\widetilde{\nu}_\tau = \widetilde{\nu}_t$) diagonal, which disappears on a time scale of <100 fs, and the continuous red-shift of the 2D signal along the detection axis $\widetilde{\nu}_t$ (see the horizontal dashed line and solid arrow in Figs. 3(a)-3(d)).

The temporal evolution of the 2D signal can be inspected by performing a global analysis and constructing two-dimensional decay-associated spectra (2D-DAS).[53–55] The 2D-DAS are not required for further analysis but are reported in Fig. S9 and discussed in Sec. S3 of the supplementary material[80] for completeness. In the following, we focus on the spectral evolution of the 2D signal along $\widetilde{\nu}_t$ for different (fixed) values of $\widetilde{\nu}_\tau$. One exemplary spectral evolution is plotted in Fig. 3(e) for $\widetilde{\nu}_\tau = 1.6987 \times 10^4$ cm^{-1} (i.e., along the dashed orange cut in Fig. 3(a)). Similar to the analysis of the transient absorption data, at each $\widetilde{\nu}_\tau$, we quantify the temporal evolution of the average spectral position of the signal by calculating the first spectral moment $M_1(\widetilde{\nu}_\tau, T)$ (see Eq. (1b)). The $M_1(\widetilde{\nu}_\tau, T)$ at three different $\widetilde{\nu}_\tau$ values are plotted in Fig. 3(f) and show that the red-shift is absent (within our signal-to-noise ratio) when exciting at the lowest edge of the MEH-PPV absorption band (red) and increases in amplitude upon increasing $\widetilde{\nu}_\tau$ (orange and blue). Independent of $\widetilde{\nu}_\tau$, the band shift is almost complete within 10 ps and the average position of the 2D signal reaches an asymptotic value of $\approx 1.6750 \times 10^4$ cm^{-1}.

In analogy with the analysis of the transient absorption data, we fit the temporal evolution of the $M_1(\widetilde{\nu}_\tau, T)$ at all $\widetilde{\nu}_\tau$ (not just the exemplary ones shown in Fig. 3(f)) with bi-exponential kinetics. The first time constant is allowed to be different for $\widetilde{\nu}_\tau < 1.679 \times 10^4$ cm^{-1}, where an ultrafast (<40 fs) blue-shift is observed. An independent fit of the $M_1(\widetilde{\nu}_\tau, T)$ for different frequencies suggests a small increase of both time constants with increasing $\widetilde{\nu}_\tau$. Such a trend would be expected if the shift originates from the transfer of energy from high- to low-energy exciton states, as relaxation from higher-energy states can proceed through more intermediate steps than from the lower-energy states. However, the signal-to-noise ratio of the data did not allow for an accurate analysis of the $\widetilde{\nu}_\tau$ dependence of the shift rates. Thus, we preferred to describe the evolution of the $M_1(\widetilde{\nu}_\tau, T)$ with the same time constants for all $\widetilde{\nu}_\tau$. The time constants retrieved from this global analysis are 180 ± 30 fs and 4.5 ± 1.1 ps and should be seen as average values over the observed spectral range. These time constants also agree well with the time scales of the band shifts observed in the transient absorption data (Table I).

IV. DISCUSSION

A. Population dynamics

The analysis of the transient absorption data at different excitation energies revealed complex population dynamics. The 2D experiment identified an additional ultrafast (sub-30 fs) component, shorter than our instrumental response function

(see Fig. S9a in the supplementary material[80]). This component accounts for an ultrafast loss of memory in the system, visible as the disappearance of the diagonal elongation in the 2D spectra within the first 100 fs; the non-resonant response of the solvent is also expected to contribute to this signal. An ultrafast (≤25 fs) component was observed with three-pulse photon echo peak shift (3PEPS)[31,56,57] on MEH-PPV at room temperature and ascribed to ultrafast exciton localization. The ultrafast depolarization of the anisotropy, proceeding on a similar time scale, has been explained in terms of several competing molecular processes, including exciton relaxation within a manifold of delocalized states and exciton localization.[14,58] As such processes lead to a loss of the initial memory in the system, we tentatively ascribe the <30 fs component observed in the 2D experiment to the initial exciton relaxation and localization.

Non-exponential kinetics have been repeatedly observed in solutions, films, and isolated molecules of MEH-PPV.[22,24,26,27,30,59,60] It was suggested that photoluminescence decay in isolated chains is mono-exponential with characteristic time scales between 0.4 and 1.2 ns, while non-exponential relaxation was observed in presence of aggregation,[24,27] in films,[17,61,62] and in collapsed MEH-PPV chains.[23,63] All the aforementioned configurations are characterized by a strong reduction in the photoluminescence quantum yield, which is ascribed to the formation of non-emissive interchain species.[16,24,64–66] These species, absorbing above 600 nm, were assigned alternately to excimers, aggregates, polarons, or polaron pairs, which are formed either via direct photoexcitation or via quenching of the singlet excitons.[16,18,58,59,63,67,68]

In none of our experiments on the aggregated phase of MEH-PPV do we detect clear signatures of excited-state absorption signals, neither in the transient spectra nor in the temporal evolution of the signals (Figs. 1(b)-1(c) and Fig. S3 in the supplementary material[80]). This is somewhat surprising, because excited-state absorption to the two-exciton state should appear at energies close to the one-exciton absorption. Deviations from this behavior can be expected in presence of strong electron correlations such as in polyenes. We cannot exclude that some excited-state absorption from the one-exciton states overlaps with the signal at certain wavenumbers (but not with the band B_{01}, see Sec. III A); however, if present, these contributions are not dominant. The 2D signal at $T = 0$ peaks below the diagonal, and this feature could arise from excited-state absorption contributions above the diagonal or from an instantaneous Stokes shift or relaxation process occurring within our time resolution. Although we cannot unambiguously discriminate between the two interpretations, we note that some instantaneous relaxation is expected because of the ultrafast exciton localization process. Two-dimensional double-quantum coherence spectroscopy[69] could provide a direct way to measure the energy position of the two-exciton states in this system, as well as their correlations with the one-exciton states. Instead, we can exclude the presence of long-lived (>1 ns) excited species formed upon direct photoexcitation, which are suggested to relax by repopulation of the emissive singlet exciton state in MEH-PPV films. To the best of our knowledge, such excited species were observed exclusively when the excitation energy was tuned above 2.14 eV,[16,17,24,59,63,67,68] where the coiled phase absorbs. Thus, we suggest that these long-lived species are not generated in significant amounts at the excitation energies of our pulses.

In Sec. III A, we have reported the results of a multi-exponential analysis of the $M_0^{(i)}(T)$ for the three major bands observed in the transient absorption experiments. An alternative model which describes the data as a linear combination of a single exponential and a stretched exponential decay is additionally presented in the supplementary material (Table S1).[80] While our data cannot distinguish unambiguously between the two models, both models result in a similar interpretation for the population dynamics in the aggregated phase of MEH-PPV.

For the following discussion, we distinguish between two kinetic regimes: a "slow regime" comprising processes occurring with characteristic time scales of tens to hundreds of ps and a "fast regime" describing processes faster than 10 ps. The processes occurring in the "slow regime" result in a complete recovery of the transient absorption signal at all detection wavenumbers (i.e., a recovery of the thermalized electronic ground state). As energy transfer between excitonic states occurs on sub-10 ps time scales (see also the detailed discussion in Sec. IV B), we ascribe the population decay in the "slow regime" to the $S_1 \rightarrow S_0$ relaxation of the exciton states at the bottom of the density of states. According to the multi-exponential model, two distributed kinetics account for exciton relaxation in the "slow regime," with average time scales of ≈40 ps and ≈320 ps. Upon 2.10 eV excitation and at 140 K, the ≈40 ps and ≈320 ps components account for a 25% and 43% decay of the excited population, respectively. By lowering the temperature to 120 K, about 38% of the total population decay takes place on 40 ps, while the percentage of excitons relaxing on the long time scale decreases to 32%. The presence of two relaxation processes, with virtually the same time scales as observed here, was previously reported for MEH-PPV aggregates in solution, where interchain interactions are likely to play a role in the photophysics.[70] Motivated by the simultaneous decay of an excited-state absorption and the bleach signal, Rothberg and co-workers[70] ascribed the faster process to the non-radiative decay of polaron pairs, and this interpretation additionally explained the low photoluminescence quantum yield of their sample. In our experiment, the ≈40 ps component appears as a simultaneous decay of the bleach and SE signals. Thus, it cannot be explained by the (non-radiative) decay of non-emissive states like polaron pairs, which would not cause a decay of the SE. It has been suggested that the geminate recombination of polaron pairs may result in a delayed population of the emissive singlet exciton states.[24,61] Such a process has been invoked to explain the long-lived emission tail in MEH-PPV films; however, it can also not explain our experimental observations as it would result in an increase (and not a decrease) of the SE signal and it would not affect the bleach. Instead, we suggest that the 40 ps component might be related to energy transfer proceeding from the lowest-energy exciton states of the aggregated phase to defect sites, while the 320 ps kinetics could map the (radiative and intrinsic non-radiative) relaxation of chromophores that are not in proximity of defect sites, and thus are not quenched by such energy transfer process.

In the same way as when interpreting the data in a multi-exponential way, when describing the dynamics in the "slow regime" as a single stretched exponential, i.e., by assuming that the exciton relaxation has a very broad ($\beta \approx 0.48$) distribution of rates, the slow (>10 ps) kinetics is considered to describe the $S_1 \rightarrow S_0$ relaxation. However, in contrast to the multi-exponential decay, the approximate $\exp\left(-\left(\frac{T}{\tau}\right)^{0.5}\right)$ dependence can be interpreted to indicate dispersive energy transfer, e.g., by dipole-dipole coupling, to lower-energy sites where the excitation is immediately quenched.[8,46,47] The spatial distribution of such defect sites would lead to a concomitant distribution of transfer rates and thus to the stretched-exponential decay observed in the signals from stimulated emission and ground-state bleach. In the structurally closely related alkoxy-PPV-derivative OC1C10-PPV, a density of electron traps with depth 0.7 eV on the order of 1023 m^{-3} was determined. These electron traps have been shown to be omnipresent at about the same density in π-conjugated polymers as they are likely to arise from some kind of water-oxygen complex.[71,72] It has been suggested that they also function as exciton traps and in this way limit the exciton diffusion length.[73]

A significant fraction of the excited population relaxes to the ground electronic state on time scales faster than 10 ps, as shown by the simultaneous decrease of both SE and bleach signals. As shown in Figs. 2(c)-2(d) and Table I, the band-shift evolution, which probes exciton relaxation and transfer (see also the discussion in Sec. IV B), is also limited to the "fast regime." We tentatively ascribe the population decay in the "fast regime" to non-radiative internal conversion processes mediated by the presence of defects in the aggregated phase. According to this interpretation, exciton relaxation and transfer can result in the population of defect states that efficiently quench the excited population.[23] Such interpretation is consistent with the decrease of emission quantum yield reported for MEH-PPV films and aggregates as compared to single solvated chains.[16,24,65,66]

B. Energy transport and relaxation

Turning now to the temporal evolution of the spectral average position of the transient bleach and stimulated emission bands, the analysis of the transient absorption data allowed us to distinguish two processes occurring on ≈200 fs and ≈4 ps time scales. The former appears as a red-shift of only the SE signals, while the latter can be detected in both the ground-state bleach and the SE bands and is absent when exciting at the onset of the absorption (2.03 eV).

Let us consider the slow (≈4 ps) shift first. A spectral shift of the ground-state bleach can arise from spectral diffusion in the electronic ground state or from Förster energy transfer from higher-energy to lower-energy excitons located at different sites in the aggregate (exciton hopping). We now discuss both putative explanations before illustrating how to differentiate them.

Spectral diffusion in the ground state is observed in presence of an inhomogeneous distribution of transition energies. Photoexcitation with spectra narrower than the inhomogeneous spectral width selects a sub-ensemble of chromophores with their electronic transition matching the energy of the excitation pulse. The hole generated in the ground-state distribution by such photoselection is refilled prior to the excited-state relaxation due to environment-induced fluctuations in the transition energy of non-photoexcited chromophores. Depending on whether the excitation pulse selects a sub-ensemble of chromophores in the center of the transition energy distribution (i.e., in the middle of the absorption band) or at one edge of it, this process will appear as a broadening or as a shift of the bleach band, respectively.

As the second possible explanation, (Förster) energy transfer within the exciton density of states also results in a shift of both absorption and emission towards lower energies as the energy flows from higher-energy to lower-energy exciton states located on different segments of the polymer. Förster energy transfer occurs between excitonic states with little or no orbital overlap by dipole-dipole coupling. Since the donor and acceptor excitons do not share a common ground state, relaxation of the excitons absorbing at higher energies results in the recovery of the high-energy tail of the ground-state bleach, while the simultaneous excitation of lower-energy exciton states causes an increase of the low-energy side of the bleach signal.

Coherent 2D spectroscopy can discriminate very clearly between the aforementioned two processes as follows. Spectral diffusion by homogeneous broadening in the ground state appears as a loss of the memory of the initial excitation (i.e., loss of the diagonal elongation), while the 2D signal broadens symmetrically and becomes round. In our data, none of these features is observed on time scales longer than 100 fs. Instead, on a 4 ps time scale, the signal intensity shifts asymmetrically towards the cross-peak below the diagonal, and this signifies excitonic energy transfer. Indeed, a 2D spectrum correlates the initially photoexcited states (along $\tilde{\nu}_\tau$) with the signal arising from the states populated after waiting time T. Thus in 2D spectroscopy, energy transfer appears as a rise of the cross peaks between the initial high-energy states (along $\tilde{\nu}_\tau$) and the final lower-energy states (along $\tilde{\nu}_t$). When, as in the case of MEH-PPV, the high exciton density prevents us to distinguish the single exciton states (and thus the single cross peaks), the energy flow through these states appears as a red-shift of the 2D signal along the detection axis. Consistent with our interpretation, the amplitude of red-shift increases when moving the excitation to higher wavenumbers, because higher-energy excitonic states are accessed (see also Fig. 3(f)).

Two-dimensional spectroscopy further allows us to observe the dynamics of energy transfer as a function of the excitation wavenumber $\tilde{\nu}_\tau$. The amplitude of the ≈4.5 ps red-shift observed in the 2D experiment is obtained from the global analysis of $M_1(\tilde{\nu}_\tau, T)$ and is plotted in Fig. 4 as a function of $\tilde{\nu}_\tau$. Since the bleach and SE components of the signal shift simultaneously and with the same amplitude (as it is well resolved by the analysis of the first moments of the transient absorption bands B_{01} and SE_{01} upon 2.10 eV excitation), the amplitude of the shift at each $\tilde{\nu}_\tau$ reflects the amount of energy relaxation. No shift of the signal is observed, within our signal-to-noise ratio, for $\tilde{\nu}_\tau < 1.6750 \times 10^4$ cm^{-1}, except for a small ultrafast component (<40 fs blue-shift) ascribed to the initial loss of the diagonal elongation. Accordingly,

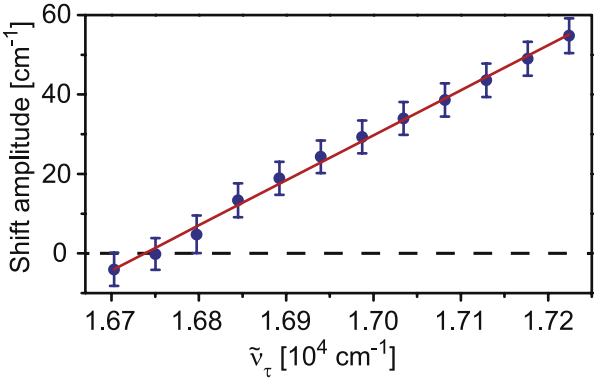

FIG. 4. Amplitude of the ≈4.5 ps red-shift along the detection axis observed in the 2D experiment as a function of the excitation wavenumber $\tilde{\nu}_\tau$, obtained from the bi-exponential global fit of the $M_1(\tilde{\nu}_\tau, T)$. Error bars are $\pm\sigma$. The data are phenomenologically described by a linear fit (red line) with slope of 0.113 ± 0.002.

we conclude that the position of the 0–0 transition for the lowest exciton states in the aggregated phase of MEH-PPV is $\tilde{\nu} = (16750 \pm 50)\,\text{cm}^{-1}$, where the confidence value of 50 cm^{-1} is given by the wavenumber separation between consecutive $\tilde{\nu}_\tau$ points in Fig. 4.

Noteworthy, despite the fact that $M_1(\tilde{\nu}_\tau, T)$ reaches the same asymptotic value for each $\tilde{\nu}_\tau$ (Fig. 3(f)), the ≈4.5 ps red-shift (Fig. 4) accounts only for a small fraction of the energy relaxation (≈55 cm^{-1} at $\tilde{\nu}_\tau = 1.7224 \times 10^4$ cm^{-1} instead of the expected ≈400 cm^{-1}). This indicates that most of the energy relaxation occurs on time scales much faster than 4.5 ps and populates the low-energy exciton states, at most ≈55 cm^{-1} higher in energy than the lowest energy states of the aggregated phase. Thus, Förster energy transfer occurs between states at the bottom of the density of states.

The typical intrachain energy transport in the blue phase of MEH-PPV is on the order of ≈250 ps, while much faster energy transport is observed in films and ascribed to interchain exciton hopping.[12,15,16,74] The short average time scale observed in our work indicates strongly, by comparison, that energy transfer in the aggregated phase has mostly an interchain character. The dominant interchain character of energy hopping in the aggregated phase is not surprising, due to the higher percentage of chromophores with interchain neighbors in the ordered aggregated structure as compared to the solvated molecules at room temperature. Additionally, the average value of ≈4 ps for energy transfer in the aggregated phase of MEH-PPV compares well with the observation by Basché and coworkers,[26] who reported a 3.9 ps average energy transfer time between red-emitting chromophores in packed chain regions of single MEH-PPV molecules. Thus, it is likely that the molecular organization of MEH-PPV in packed chain regions is locally ordered and resembles that of the low-temperature aggregate.

It would be meaningful to compare the average time scale for Förster-like energy transfer in the aggregated phase and in the coiled phase. However, we are not aware of a precise estimation of either the excitation-dependent or the average time constants for interchain exciton energy transfer in the coiled phase of MEH-PPV. Energy transport in both room-temperature and low-temperature films of MEH-PPV is found to occur on a few-ps time scale with a rate that increases with increasing excitation energy;[16,75] however, it is not clear how these value relate with the energy migration between blue and red sites of MEH-PPV, which are believed to co-exist in films.

We noted before that both our transient absorption and 2D experiments show an additional ultrafast (≈200 fs) red-shift of the transient signal, which is observed exclusively in the SE bands and whose amplitude increases at higher excitation energies. The ≈200 fs shift amplitude is plotted in Fig. S10 of the supplementary material[80] as a function of the excitation wavenumber; however, the interpretation of these data is complicated by the presence of overlapping contributions. Several processes can cause a red-shift of the SE, and in general, it is not trivial to distinguish whether such a red-shift arises from exciton relaxation, vibrational relaxation, or conformational dynamics in the excited state. As the ≈200 fs shift is observed exclusively in the SE signal, we can exclude that it originates from Förster electronic energy transfer between states located on different segments of the polymer, which would result also in a red-shift of the bleach signal.

A decay in the transient grating and 3PEPS signals of the room-temperature phase of MEH-PPV on similar time scales (≈200 – 400 fs) was reported[31,56] and ascribed to exciton relaxation. The sub-ps red-shift of the emission observed in several PPV-based polymers at room temperature was also ascribed to exciton relaxation. Indeed, being absent in small oligomers, this red-shift cannot be accounted for exclusively by vibrational relaxation or solvation dynamics.[76,77] A similar argument has also been used to exclude that the aforementioned red-shift is primarily due to conformational dynamics and planarization in the excited state. Conformational dynamics in the excited state are believed to play an important role in the relaxation of photoexcited polymers. In particular, ultrafast structural relaxation on a time scale comparable with the period of high-frequency vibrational modes is believed to

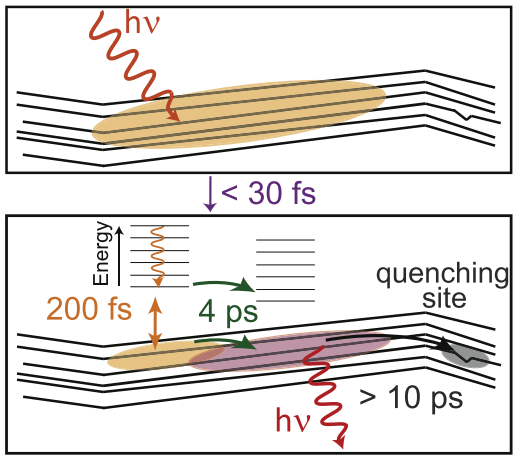

FIG. 5. Schematic view of the photophysics of the aggregated phase of MEH-PPV. The delocalized exciton states initially photoexcited (upper frame) localize on an ultrafast (<30 fs) time scale on smaller domains on the aggregate chains (lower frame). Within the following ≈200 – 250 fs, exciton relaxation within these smaller domains occurs and leads to the population of the exciton states at the bottom of the density of states. On a ≈4 ps time scale, Förster energy transfer leads to migration of the exciton towards the lowest energy states of the aggregated phase, from which energy transfer to defect states and radiative relaxation take place.

be responsible for the ultrafast exciton localization in MEH-PPV.[7,31,57,58] In contrast, torsional relaxation and excited-state planarization are expected to take place on a time scale of a few ps or longer in MEH-PPV at room temperature and in solution.[60,78,79] In an aggregated state and at low temperature, we expect such conformational changes to be even slower.

In agreement with all these observations, we argue that the ≈200 fs shift arises mostly from exciton relaxation within a manifold of electronic states sharing the same ground state (otherwise the bleach would shift as well). This assignment is further supported by the fact that, as discussed above, on a ps time scale, the exciton population is already relaxed to exciton states at the bottom of the density of states, from which Förster energy transfer takes place.

V. SUMMARY AND CONCLUSIONS

Summarizing, the combination of broadband transient absorption and coherent 2D spectroscopy experiments allows us to propose the relaxation pathways shown in Fig. 5 for the aggregated phase of MEH-PPV at low temperatures.

The initially delocalized photoexcited exciton states localize on a sub-30 fs time scale on smaller conjugated domains of the polymer chains (spectroscopic units in the following).[7] Depending on the excitation frequency and owing to the energetic disorder within the aggregate, different spectroscopic units can be accessed. Exciton relaxation within the manifold of states sharing the same ground state occurs on a time scale of ≈200 fs, simultaneous with cooling. This mechanism can be regarded as a relaxation process occurring within each spectroscopic unit and leads to the ultrafast population of the lowest excitonic states belonging to that spectroscopic unit. Our 2D measurements reveal that in the frequency range accessed by our pulses, the average energy of the exciton states populated after the ≈200 fs relaxation is at most ≈55 cm^{-1} higher than the lowest exciton states of the aggregate. It would be interesting to compare this value with the theoretical inhomogeneous width of the lowest-exciton density of states in the aggregated phase that can be accessed by our excitation pulses, as a function of the energetic disorder and the excitonic density of states within the single spectroscopic units.

Diffusion of the relaxed excitons occurs on a longer (≈4 ps) time scale via interchain Förster energy transfer. As no further signatures of energy transfer within the aggregated-phase are detected on longer time scales, we conclude that the ≈4 ps exciton diffusion localizes efficiently the excitons in the energetic states at the bottom of the aggregated-phase density of states. From these states, further exciton transfer towards defect sites, as well as poplation relaxation, occurs with a broad distribution of rates on time scales >10 ps.

Noteworthy, despite chain planarization in the excited state is expected in polymers, we do not see clear signatures of such a process in our data. The MEH-PPV aggregated phase compares better to a bulk polymer than to solvated chains, thus conformational effects are expected on time scales longer than 10 ps. It is possible that due to the already highly planar structure of the aggregated phase, the effects of conformational changes on the emission spectra are too small to be detected in our experiments. Experiments monitoring the aggregated-phase emission with a higher spectral resolution could give an answer to this question.

Coherent 2D spectroscopy is a particularly suited technique to observe the energetic relaxation as a function of the excitation energy in complex systems. By combining coherent 2D spectroscopy and transient absorption, we have characterized the energy relaxation in the aggregated low-temperature phase of MEH-PPV. In particular, we showed that most exciton relaxation is ultrafast with little spatial energy displacement, and that 95% of excitons are localized in the low-energy exciton states within the first ≈12 ps after excitation.

ACKNOWLEDGMENTS

We acknowledge the Free State of Bavaria for financial support through the "Solar Technologies Go Hybrid (Soltech)" program and T.B. acknowledges the European Cooperation in Science and Technology (COST) Action "PERSPECT-H2O" (CM1202). We also thank Professor Patrick Nuernberger, Professor Heinz Bässler, and Dr. Jakub Dostál for helpful discussions.

[1]K. M. Coakley and M. D. McGehee, Chem. Mater. **16**, 4533 (2004).
[2]B. Zhao, Z. He, X. Cheng, D. Qin, M. Yun, M. Wang, X. Huang, J. Wu, H. Wu, and Y. Cao, J. Mater. Chem. C **2**, 5077 (2014).
[3]B. Muhsin, R. Roesch, G. Gobsch, and H. Hoppe, Sol. Energy Mater. Sol. Cells **130**, 551 (2014).
[4]J. You, L. Dou, K. Yoshimura, T. Kato, K. Ohya, T. Moriarty, K. Emery, C.-C. Chen, J. Gao, G. Li, and Y. Yang, Nat. Commun. **4**, 1446 (2013).
[5]I. Hwang and G. D. Scholes, Chem. Mater. **23**, 610 (2011).
[6]S. T. Hoffmann, H. Bässler, and A. Köhler, J. Phys. Chem. B **114**, 17037 (2010).
[7]W. J. D. Beenken and T. Pullerits, J. Phys. Chem. B **108**, 6164 (2004).
[8]L. M. Herz, C. Silva, A. C. Grimsdale, K. Müllen, and R. T. Phillips, Phys. Rev. B **70**, 165207 (2004).
[9]R. Q. Albuquerque, C. C. Hofmann, J. Köhler, and A. Köhler, J. Phys. Chem. B **115**, 8063 (2011).
[10]E. Collini and G. D. Scholes, Science **323**, 369 (2009).
[11]G. Padmanaban and S. Ramakrishnan, J. Am. Chem. Soc. **122**, 2244 (2000).
[12]B. J. Schwartz, T.-Q. Nguyen, J. Wu, and S. H. Tolbert, Synth. Met. **116**, 35 (2001).
[13]E. Hennebicq, G. Pourtois, G. D. Scholes, L. M. Herz, D. M. Russell, C. Silva, S. Setayesh, A. C. Grimsdale, K. Müllen, J. L. Brédas, and D. Beljonne, J. Am. Chem. Soc. **127**, 4744 (2005).
[14]T. E. Dykstra, E. Hennebicq, D. Beljonne, J. Gierschner, G. Claudio, E. R. Bittner, J. Knoester, and G. D. Scholes, J. Phys. Chem. B **113**, 656 (2009).
[15]T.-Q. Nguyen, J. Wu, V. Doan, B. J. Schwartz, and S. H. Tolbert, Science **288**, 652 (2000).
[16]I. Martini, A. Smith, and B. Schwartz, Phys. Rev. B **69**, 035204 (2004).
[17]T.-Q. Nguyen, I. B. Martini, J. Liu, and B. J. Schwartz, J. Phys. Chem. B **104**, 237 (2000).
[18]B. J. Schwartz, Annu. Rev. Phys. Chem. **54**, 141 (2003).
[19]R. J. Kline and M. D. McGehee, J. Macromol. Sci., Part C: Polym. Rev. **46**, 27 (2006).
[20]J. Clark, C. Silva, R. H. Friend, and F. C. Spano, Phys. Rev. Lett. **98**, 206406 (2007).
[21]H. Yamagata, C. M. Pochas, and F. C. Spano, J. Phys. Chem. B **116**, 14494 (2012).
[22]T.-Q. Nguyen, V. Doan, and B. J. Schwartz, J. Chem. Phys. **110**, 4068 (1999).
[23]J. Yu, D. Hu, and P. F. Barbara, Science **289**, 1327 (2000).
[24]C. J. Collison, L. J. Rothberg, V. Treemaneekarn, and Y. Li, Macromolecules **34**, 2346 (2001).
[25]D. Y. Kim, J. K. Grey, and P. F. Barbara, Synth. Met. **156**, 336 (2006).
[26]F. A. Feist, M. F. Zickler, and T. Basché, ChemPhysChem **12**, 1499 (2011).
[27]H. Lin, R. P. Hania, R. Bloem, O. Mirzov, D. Thomsson, and I. G. Scheblykin, Phys. Chem. Chem. Phys. **12**, 11770 (2010).

[28]A. Köhler, S. T. Hoffmann, and H. Bässler, J. Am. Chem. Soc. **134**, 11594 (2012).
[29]P. Wood, I. D. W. Samuel, G. R. Webster, and P. L. Burn, Synth. Met. **119**, 571 (2001).
[30]A. Dogariu, D. Vacar, and A. J. Heeger, Phys. Rev. B **58**, 10218 (1998).
[31]J. Sperling, A. Nemeth, P. Baum, F. Šanda, E. Riedle, H. Kauffmann, S. Mukamel, and F. Milota, Chem. Phys. **349**, 244 (2008).
[32]F. Panzer, H. Bässler, R. Lohwasser, M. Thelakkat, and A. Köhler, J. Phys. Chem. Lett. **5**, 2742 (2014).
[33]J.-L. Brédas, D. Beljonne, V. Coropceanu, and J. Cornil, Chem. Rev. **104**, 4971 (2004).
[34]U. Selig, F. Langhojer, F. Dimler, T. Löhrig, C. Schwarz, B. Gieseking, and T. Brixner, Opt. Lett. **33**, 2851 (2008).
[35]R. Augulis and D. Zigmantas, Opt. Express **19**, 13126 (2011).
[36]T. Brixner, T. Mančal, I. V. Stiopkin, and G. R. Fleming, J. Chem. Phys. **121**, 4221 (2004).
[37]C. Scharsich, R. H. Lohwasser, M. Sommer, U. Asawapirom, U. Scherf, M. Thelakkat, D. Neher, and A. Köhler, J. Polym. Sci., Part B: Polym. Phys. **50**, 442 (2012).
[38]G. Williams, *Electric Phenomena in Polymer Science*, Advances in Polymer Science Vol. 33 (Springer, Berlin, Heidelberg, 1979), pp. 59–92.
[39]J. Klafter and A. Blumen, J. Chem. Phys. **80**, 875 (1984).
[40]R. G. Palmer, D. L. Stein, E. Abrahams, and P. W. Anderson, Phys. Rev. Lett. **53**, 958 (1984).
[41]A. Blumen, G. Zumofen, and J. Klafter, Phys. Rev. B **30**, 5379 (1984).
[42]J. Budimir and J. L. Skinner, J. Chem. Phys. **82**, 5232 (1985).
[43]J. Klafter and A. Blumen, Chem. Phys. Lett. **119**, 377 (1985).
[44]J. Klafter and M. F. Shlesinger, PNAS **83**, 848 (1986).
[45]B. Mollay and H. F. Kauffmann, J. Chem. Phys. **97**, 4380 (1992).
[46]B. Mollay, U. Lemmer, R. Kersting, R. F. Mahrt, H. Kurz, H. F. Kauffmann, and H. Bässler, Phys. Rev. B **50**, 10769 (1994).
[47]K. Brunner, A. Tortschanoff, C. Warmuth, H. Bässler, and H. F. Kauffmann, J. Phys. Chem. B **104**, 3781 (2000).
[48]P. J. Steinbach, R. Ionescu, and C. R. Matthews, Biophys. J. **82**, 2244 (2002).
[49]P. J. Steinbach, Anal. Biochem. **427**, 102 (2012).
[50]S. Mukamel, Annu. Rev. Phys. Chem. **51**, 691 (2000).
[51]T. Brixner, J. Stenger, H. M. Vaswani, M. Cho, R. E. Blankenship, and G. R. Fleming, Nature **434**, 625 (2005).
[52]C. Y.-C. Ginsberg, S. Naomi, and G. R. Fleming, Acc. Chem. Res. **42**, 1352 (2009).
[53]C. Consani, G. Auböck, F. v. Mourik, and M. Chergui, Science **339**, 1586 (2013).
[54]V. I. Prokhorenko, EPA Newsl., issue June 2012, pp. 21–23.
[55]F. Milota, V. I. Prokhorenko, T. Mancal, H. von Berlepsch, O. Bixner, H. F. Kauffmann, and J. Hauer, J. Phys. Chem. A **117**, 6007 (2013).
[56]G. D. Scholes, D. S. Larsen, G. R. Fleming, G. Rumbles, and P. L. Burn, Phys. Rev. B **61**, 13670 (2000).
[57]T. E. Dykstra, V. Kovalevskij, X. Yang, and G. D. Scholes, Chem. Phys. **318**, 21 (2005).
[58]A. Ruseckas, P. Wood, I. Samuel, G. Webster, W. Mitchell, P. Burn, and V. Sundström, Phys. Rev. B **72**, 115214 (2005).
[59]L. J. Rothberg, M. Yan, F. Papadimitrakopoulos, M. E. Galvin, E. W. Kwock, and T. M. Miller, Synth. Met. **80**, 41 (1996).
[60]R. E. Di Paolo, J. Seixas de Melo, J. Pina, H. D. Burrows, J. Morgado, and A. L. Maçanita, ChemPhysChem **8**, 2657 (2007).
[61]M. Yan, L. J. Rothberg, E. W. Kwock, and T. M. Miller, Phys. Rev. Lett. **75**, 1992 (1995).
[62]L. Rothberg, in *Semiconducting Polymers: Chemistry, Physics and Engineering*, 2nd ed. (Wiley, 2006), Chap. Photophysics of Conjugated Polymers, p. 179.
[63]H. Lin, S. R. Tabaei, D. Thomsson, O. Mirzov, P.-O. Larsson, and I. G. Scheblykin, J. Am. Chem. Soc. **130**, 7042 (2008).
[64]H. A. Mizes and E. M. Conwell, Phys. Rev. B **50**, 11243 (1994).
[65]J. W. Blatchford, S. W. Jessen, L.-B. Lin, T. L. Gustafson, D.-K. Fu, H.-L. Wang, T. M. Swager, A. G. MacDiarmid, and A. J. Epstein, Phys. Rev. B **54**, 9180 (1996).
[66]H. Lin, Y. Tian, K. Zapadka, G. Persson, D. Thomsson, O. Mirzov, P.-O. Larsson, J. Widengren, and I. G. Scheblykin, Nano Lett. **9**, 4456 (2009).
[67]R. Jakubiak, C. J. Collison, W. C. Wan, L. J. Rothberg, and B. R. Hsieh, J. Phys. Chem. A **103**, 2394 (1999).
[68]C.-X. Sheng, M. Tong, S. Singh, and Z. Vardeny, Phys. Rev. B **75**, 085206 (2007).
[69]J. Kim, S. Mukamel, and G. D. Scholes, Acc. Chem. Res. **42**, 1375 (2009).
[70]P. Wang, C. J. Collison, and L. J. Rothberg, J. Photochem. Photobiol., A **144**, 63 (2001).
[71]H. T. Nicolai, M. Kuik, G. a. H. Wetzelaer, B. de Boer, C. Campbell, C. Risko, J. L. Brédas, and P. W. M. Blom, Nat. Mater. **11**, 882 (2012).
[72]A. Köhler, Nat. Mater. **11**, 836 (2012).
[73]O. V. Mikhnenko, M. Kuik, J. Lin, N. van der Kaap, T.-Q. Nguyen, and P. W. M. Blom, Adv. Mater. **26**, 1912 (2014).
[74]K. M. Gaab and C. J. Bardeen, J. Phys. Chem. B **108**, 4619 (2004).
[75]J. Sperling, F. Milota, A. Tortschanoff, C. Warmuth, B. Mollay, H. Bässler, and H. F. Kauffmann, J. Chem. Phys. **117**, 10877 (2002).
[76]R. Kresting, U. Lemmer, R. F. Mahrt, K. Leo, H. Kurz, H. Bässler, and E. O. Göbel, Phys. Rev. Lett. **70**, 3820 (1993).
[77]K. S. Wong, H. Wang, and G. Lanzani, Chem. Phys. Lett. **288**, 59 (1998).
[78]S. Westenhoff, W. J. D. Beenken, R. H. Friend, N. C. Greenham, A. Yartsev, and V. Sundström, Phys. Rev. Lett. **97**, 166804 (2006).
[79]P. Parkinson, C. Müller, N. Stingelin, M. B. Johnston, and L. M. Herz, J. Phys. Chem. Lett. **1**, 2788 (2010).
[80]See supplementary material at http://dx.doi.org/10.1063/1.4918645 for information on the linearity of the signal with the photon flux, supplementary figures, two-dimensional decay-associated spectra, and the excitation-dependent amplitude of the fast band-shift.

AIP

Supporting Information for:

Relaxation dynamics and exciton energy transfer in the low-temperature phase of MEH-PPV

Cristina Consani,[1] Federico Koch,[1] Fabian Panzer,[2] Thomas Unger,[2] Anna Köhler,[2] and Tobias Brixner[1, 3, a)]

[1)] *Institut für Physikalische und Theoretische Chemie, Universität Würzburg, Am Hubland, 97074 Würzburg, Germany*

[2)] *Lehrstuhl Experimentalphysik II, Universität Bayreuth, Universitätsstraße 30, 95440 Bayreuth, Germany*

[3)] *Center for Nanosystems Chemistry (CNC), Universität Würzburg, Am Hubland, 97074 Würzburg, Germany*

(Dated: 2 February 2015)

[a)] Electronic mail: brixner@phys-chemie.uni-wuerzburg.de

S1. SUPPLEMENTARY FIGURES AND TABLES

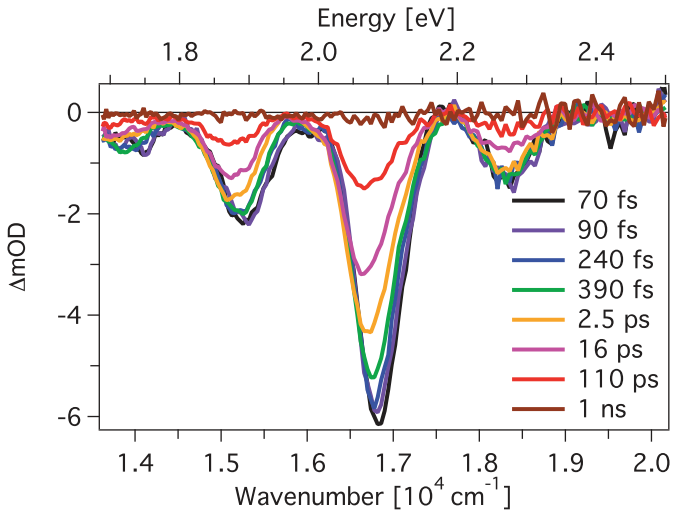

FIG. S1. Selection of transient absorption spectra at different population times for the aggregated phase of MEH-PPV at 120 K and upon excitation at 2.10 eV (1.69×10^4 cm^{-1}).

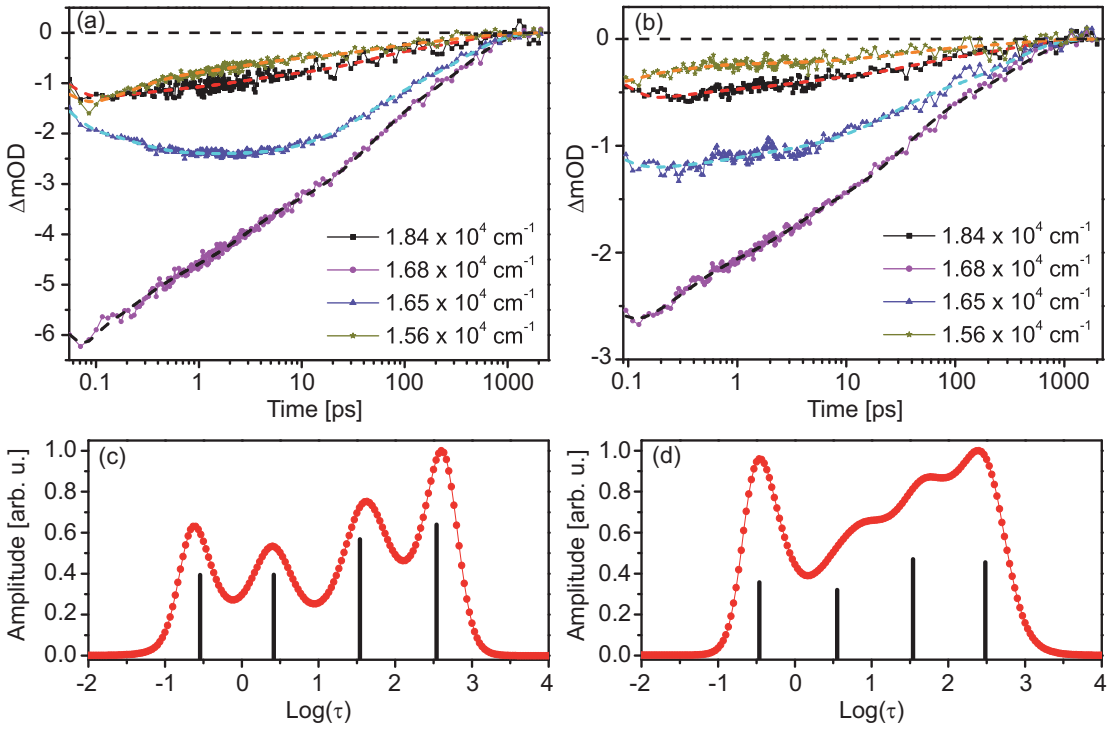

FIG. S2. Temporal evolution of the transient absorption signal at four different probe wavenumbers (symbols) upon (a) 2.10 eV excitation and (b) 2.03 eV excitation. Dashed lines are the best multi-exponential fits to the observed kinetics. The best rate distributions describing the temporal evolution of the signal at 1.68×10^4 cm^{-1} eV are retrieved via the maximum entropy method via the program MemExp and are shown (red) for (c) 2.10 eV excitation and (d) 2.03 eV excitation. Vertical bars (black) indicate the time constants that best describe the data when a multi-exponential model is assumed.

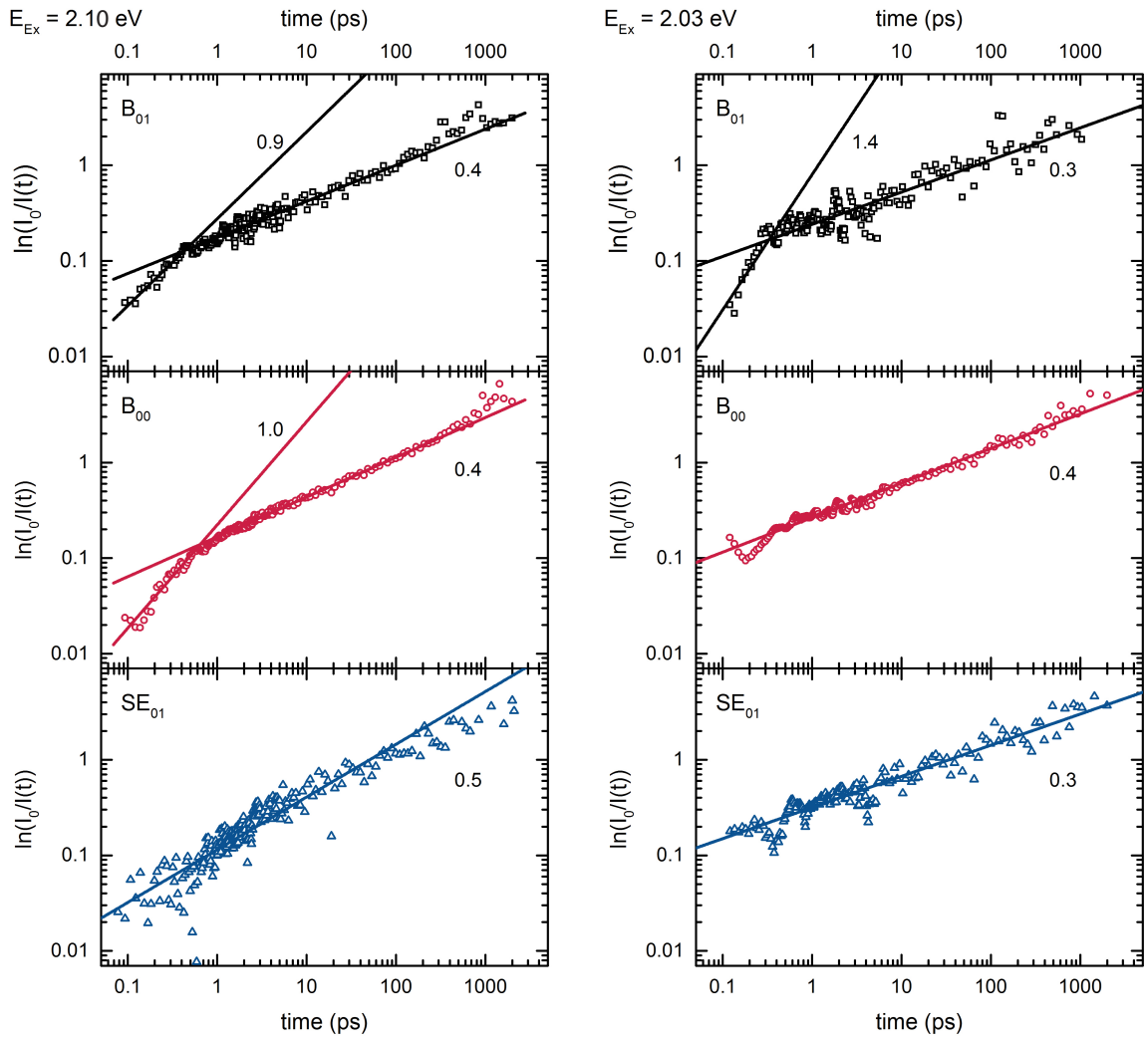

FIG. S3. Kohlrausch-Williams-Watt representation of the $M_0^{(i)}(T)$ decays (symbols) for $i = \mathrm{B}_{01}$, B_{00} and SE_{01} at 140 K upon excitation at 2.10 eV (left panel) and 2.03 eV (right panel). The solid lines indicate different slopes for ease of comparison.

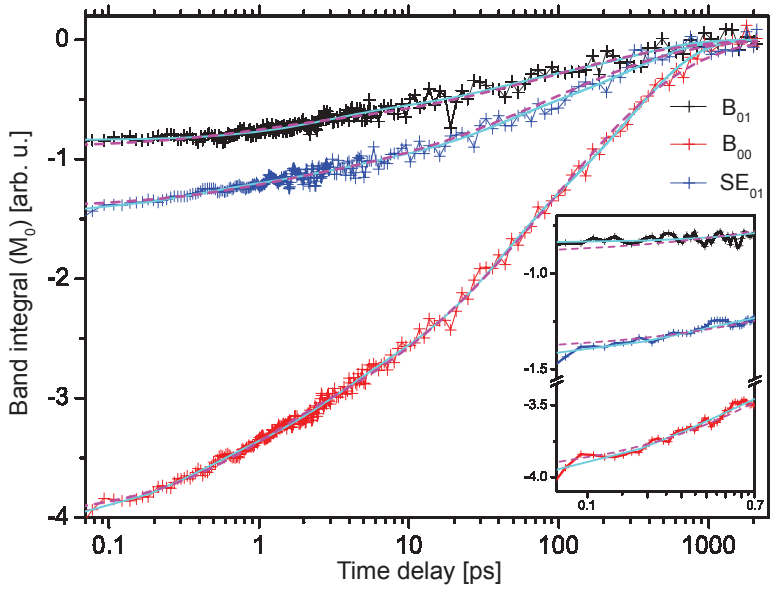

FIG. S4. Comparison between the fit of the $M_0^{(i)}(T)$ with a multi-exponential model (dashed) and with a linear combination of an exponential and stretched exponential decay (solid) upon excitation at 2.10 eV, 140 K.

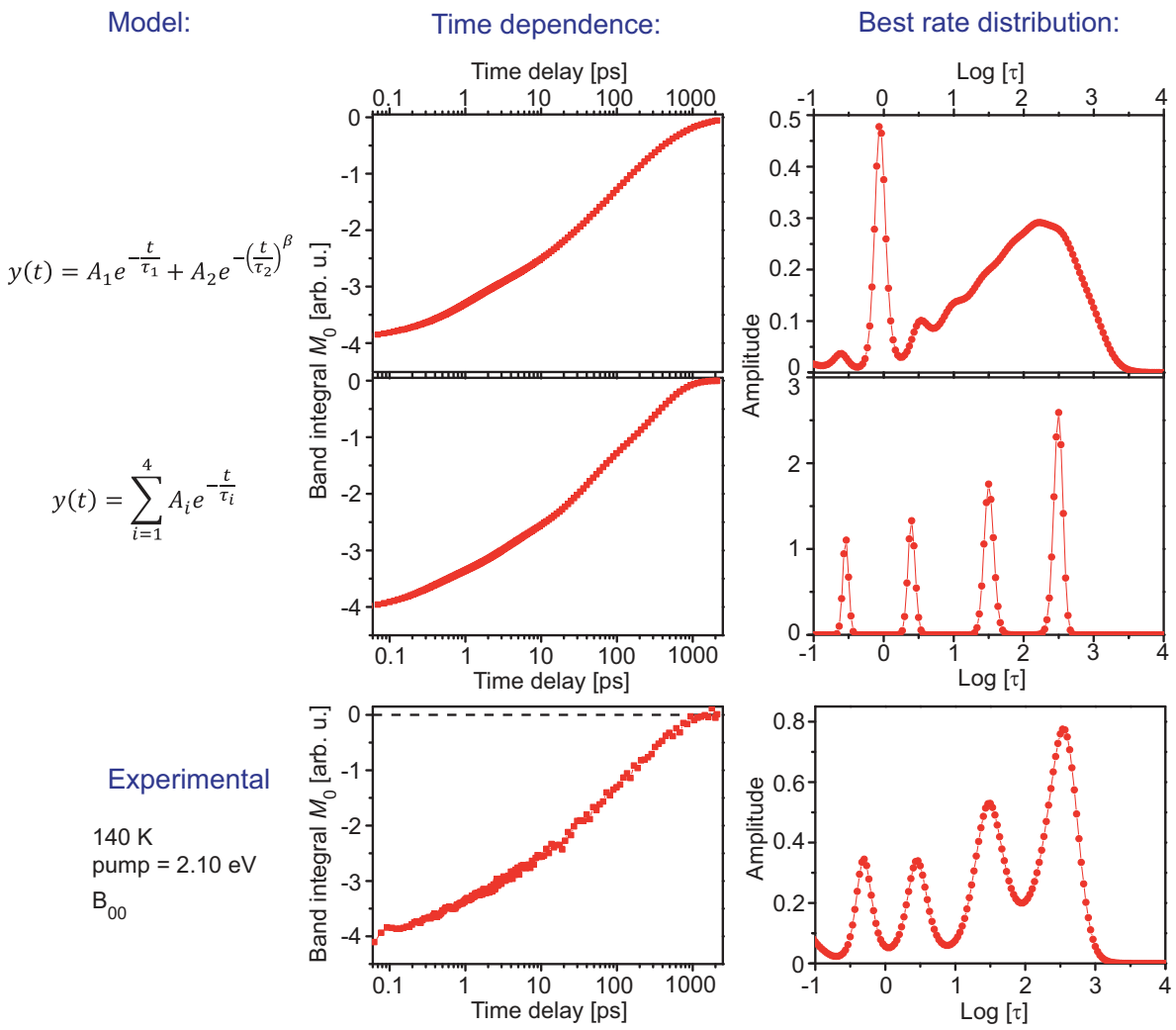

FIG. S5. Comparison between different kinetic models and experimental data. Time dependence and best rate distribution retrieved by the MEM analysis via the program MemExp for the linear combination of an exponential and a stretched exponential decay (first line), a multi-exponential decay with four time constants (second line) and the experimentally measured band integral $M_0^{B_{00}}$ upon excitation at 2.10 eV of the 140 K sample (third line).

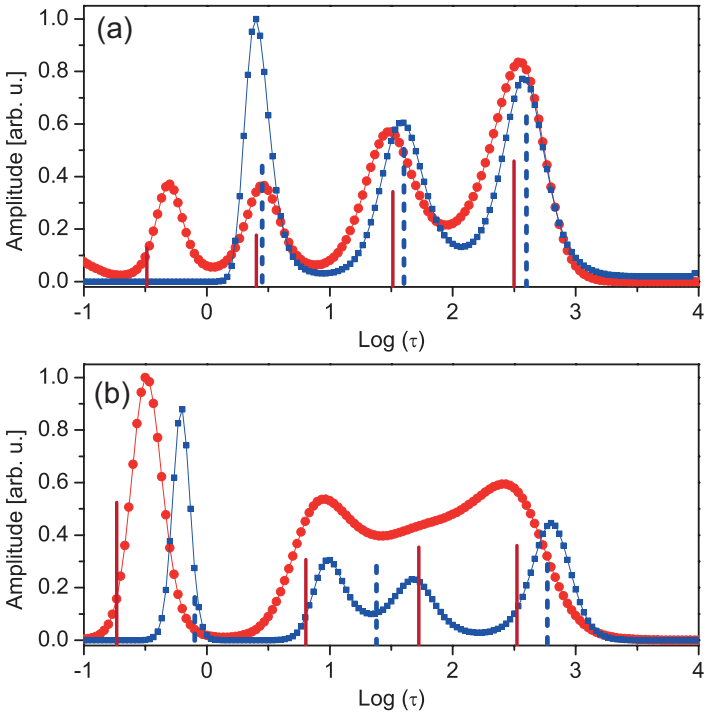

FIG. S6. Best rate distributions describing the temporal evolution of M_0 for the bleach bands B_{01} (blue squares) and B_{00} (red circles), upon excitation at (a) 2.10 eV and (b) 2.03 eV, as retrieved via the maximum entropy method analysis. Vertical blue dashed (red solid) lines show the best rate constants for the multi-exponential fit of the B_{01} (B_{00}) population dynamics.

TABLE S1. Characteristic time constants obtained from a fit of the integrated signals $M_0^{(i)}(T)$ (i = B_{01}, B_{00} and SE_{01}) of the transient absorption data described in Section III.A of the main paper, with the fit function $M^{(i)}(T) = A_1 e^{-\frac{T}{\tau_1}} + A_2 e^{-(\frac{T}{\tau_2})^\beta}$

	Excitation energy	2.10 eV	2.10 eV	2.03 eV
	Temperature	120 K	140 K	140 K
Population decay $M_0(T)$	τ_1 [ps]	1.18 ± 0.12	0.88 ± 0.07	0.26 ± 0.17
	τ_2 [ps]	74 ± 3	94 ± 3	63 ± 3
	β [ps]	0.48 ± 0.01	0.49 ± 0.01	0.45 ± 0.02

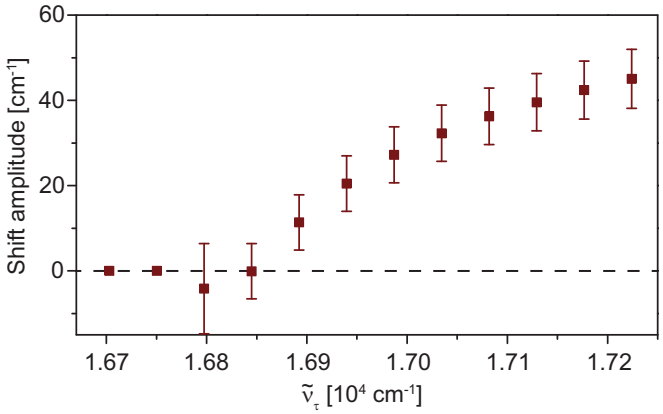

FIG. S7. Amplitude of the ≈ 200 fs red-shift along the detection axis observed in the 2D experiment as a function of the excitation wavenumber $\widetilde{\nu}_\tau$, obtained from the bi-exponential global fit of $M_1(\widetilde{\nu}_\tau, T)$. Error bars are $\pm\sigma$. Note that, in the fit, the amplitude of the ≈ 200 fs component was fixed to 0 for $\widetilde{\nu}_\tau < 1.679 \times 10^4$ cm^{-1}, where no shift on this time constant was observed within our signal-to-noise ratio. Differently from the ≈ 4 ps dynamics, where both the bleach and SE contributions to the signal shift simultaneously towards lower wavenumbers, on a ≈ 200 fs timescale only the SE band red-shifts. Since $M_1(\widetilde{\nu}_\tau, T)$ measures center of mass frequency of a signal composed by overlapping (0-0) bleach and SE bands, the amplitude of the ≈ 200 fs shift is not a direct quantitative measure of the shift of the SE band.

4.6. The Temperature Induced Order-Disorder Transition in Solutions of Conjugated Polymers Probed by Optical Spectroscopy

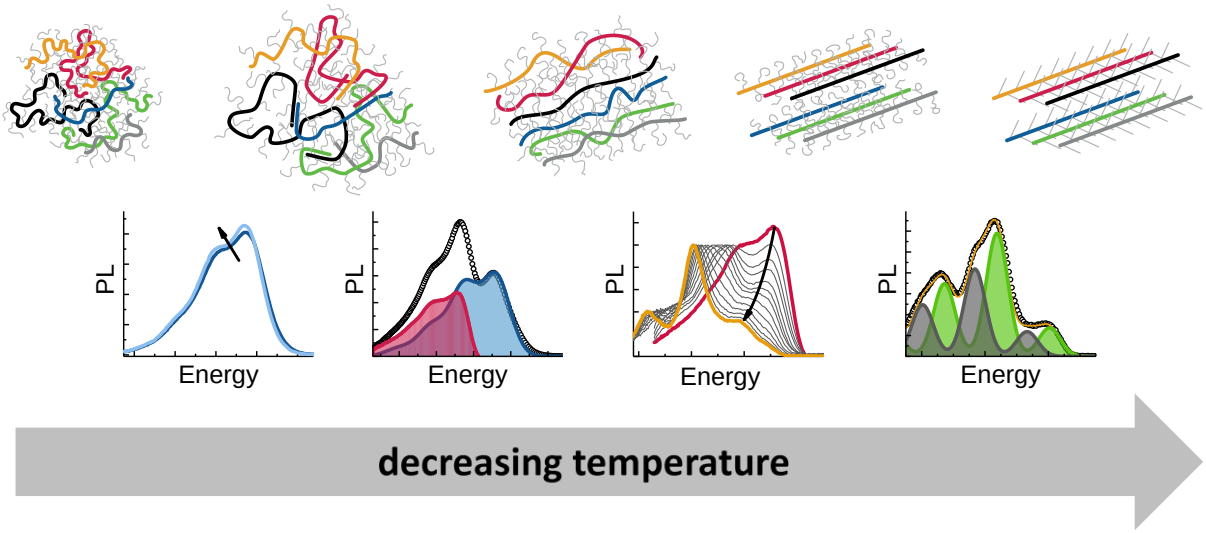

Fabian Panzer, Heinz Bässler and Anna Köhler

Prepared for submission to
The Journal of Physical Chemistry B
As invited Feature Article

The temperature induced order-disorder transition in solutions of conjugated polymers probed by optical spectroscopy

Fabian Panzer[a,b,c], Heinz Bässler[b], Anna Köhler[a,b,*]

[a] Experimental Physics II

University of Bayreuth, 95540 Bayreuth, Germany

[b] Bayreuth Institute of Macromolecular Research (BIMF)

University of Bayreuth, 95440 Bayreuth, Germany

[c] Department of Functional Materials

University of Bayreuth, 95440 Bayreuth, Germany

Corresponding Author

*E-Mail: anna.koehler@uni-bayreuth.de

Keywords: Phase Transition, aggregation, planarization, coil globule, collapse

Abstract

While the aggregation of π-conjugated materials is known to significantly impact on the photophysics of thin films and optoelectronic devices, only little is known about the nature and the mechanisms on how such aggregates form.

In this feature article, we compare and discuss how temperature induced aggregate formation in solution is manifested in a range of conjugated homopolymers, a low-bandgap-type donor-acceptor polymer and in low molecular weight compounds. As aggregation impacts on the electronic structure, (temperature dependent) optical spectroscopy is a simple and powerful tool to analyse aggregate formation. We present how the temperature dependent optical spectra can be analysed and how they are associated to distinct conformational states. We show that aggregate formation proceeds in a similar manner in all the investigated compounds, and that the nature of the order-disorder transition in π-conjugated materials is rather of first order nature. We show that the mechanism of the aggregation process can be understood as a coil-globule process, where the chain expands before it collapses into a highly ordered dense state. We furthermore discuss the important role of side chains and the impact of changes in environmental polarization during aggregate formation. Finally, a summarised picture is derived, where the temperature dependent conformational states are linked to the optical spectra.

Table of Content Graphic

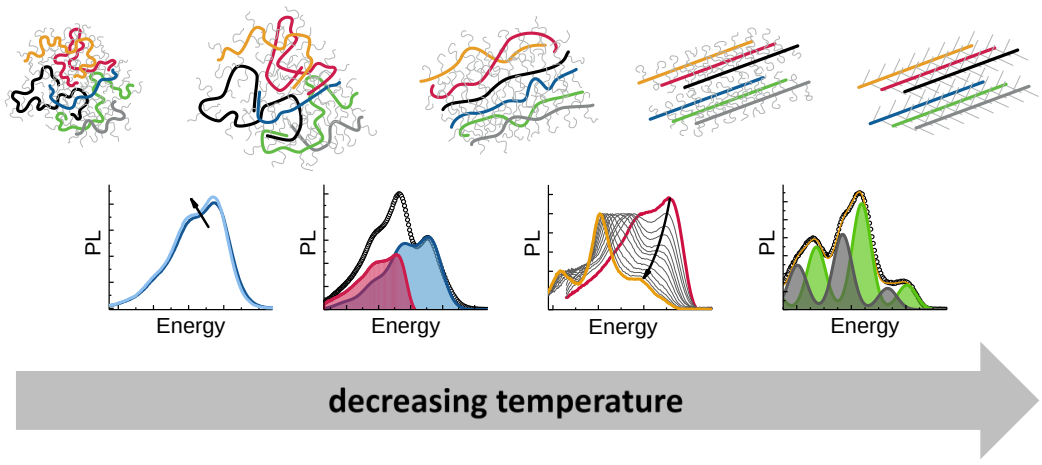

1. Introduction

Thin films of semiconducting polymers are often considered as being amorphous. In many cases, however, intermolecular interactions cause the formation of phases with some degree of short-range, or sometimes even longer-range order. These ordered polymer chains are commonly referred to as "aggregates". By virtue of their mutual interaction, the electronic structure of polymers in such aggregates differs from that of the non-interacting chains in the amorphous matrix surrounding the aggregates. If aggregates are formed, this has a strong impact on the photophysical processes that occur in the polymer films, notably in devices. For example, the field effect mobility μ is higher in films containing aggregates,[1-4] and the dissociation of electron-hole pairs in thin films is enhanced both in films containing only a single-compound,[5-7] as well as in donor-acceptor composites in organic solar cells.[8-12] As a result, there is a need to understand how such aggregates form and how they can be identified by simple spectroscopic means.

The formation of crystalline areas has been studied for several decades with respect to flexible, non-conjugated polymers in the melt.[13] In contrast, investigations on the aggregation of semi-rigid conjugated polymers in solution have emerged only in recent years.[14-19] In consequence, the process of aggregate formation is not yet fully understood. When processing conjugated polymers from solution, e.g. by spin coating onto a substrate, the kinetics of solvent evaporation and associated film formation influences the process of aggregation strongly, and adds complexity to the thermodynamic process.[20] As it is clear that understanding aggregate formation is a prerequisite for controlling the morphology of organic semiconductor films, research focused on assessing the influence of various parameters on the film formation process.

For example, parameters that have been addressed are the role of the boiling point of the solvent (demonstrating that higher boiling point solvents are conducive to aggregate formation),[5,20-22] the role of the solubility parameter of the solvent (showing that a poorer solvent is more likely to induce aggregation),[23] the role of sidechains (long unbranched sidechains often support aggregation while branched sidechains frequently prevent it),[24] and the role of structural regularity (regioregular structure leads to more aggregation in P3HT than regiorandom structure).[25,26] A further parameter that is anecdotally known to

affect aggregation include the "quality" of the batch of polymer – usually it is the polydispersity that is the key parameter here as shall be outlined further below.

So far, investigations concentrated mainly on homopolymers such as polyfluorene with octyl sidechains (PFO),[20,27-30] regioregular poly(3-hexylthiophene) (P3HT),[1,3,31-34] and, to a lesser extent, derivatives of poly(*p*-phenylene vinylene) (PPV),[35-41] and poly(*p*-phenylene ethynylene) (PPE).[17,42-44] In addition to structural methods such as GiSAXS or GiWAXS or GiXRD,[14,45,46] optical spectroscopy has emerged as a powerful tool to identify aggregation. The analysis of the data is greatly facilitated if kinetic effects – such as solvent evaporation rates – are reduced, so that thermodynamic effects are more dominant. A popular approach is therefore to investigate the aggregation processes in solution. For example, by gradually changing the composition of a mixed solvent, the solubility of the polymer may be reduced in a controlled way such as to induce aggregation.[15,18,26,47] .While this approach is systematic, it is laborsome and prone to small errors as every solution needs to be prepared separately in order to keep the overall concentration constant. A simple way to reduce the quality of the solvent in a controlled and continuous way is to reduce the temperature. Many solvents can be classified as a "good" solvent (in the sense that the chains expands in this solvent) at elevated temperatures, and they become "poor" solvents (so that the chain contracts) at lower temperatures. Thus by reducing the temperature, aggregation can be induced to a polymer solution without any other changes to the system. In this feature article, we compare and discuss how aggregate formation is manifested in a range of homopolymers, a low-bandgap-type donor-acceptor polymer and in low molecular weight compounds. These materials have all been investigated by temperature-dependent optical spectroscopy. The focus of this work is to show how aggregation proceeds in a similar manner in all these compounds, and how distinct conformation can be identified by the analysis of the associated spectra.

To achieve this, it is helpful to summarize briefly what is known about the impact of inter-chromophore interaction on the structure of excited states. The changes in the optical spectra due to coupling of different chromophores have been established by Kasha.[48,49] In brief, when two chromophores are adjacent, the electron distribution on one chromophore interacts electrostatically with the electron distribution on the other. In consequence, the energy of an optical transition is modified by two factors. First, the

energies in the ground state and in the excited state of each chromophore are reduced by the polarization energies D and D', respectively, compared to the energies in the isolated chromophores. As D' is typically larger than D, a bathochromic shift ΔD of the transition energy results. This energy shift – sometimes also called "gas-to-crystal shift" is akin to a solvation energy. The mutual van der Waals interaction between the two chromophore alters their charge distribution and thus reduces the overall energies. Second, due to their interaction, the energy levels of the two chromophores split by the resonance energy ß. This is illustrated in Figure 1. The energy of the associated optical transition is given by $\Delta E_{total} = \Delta E + \Delta D \pm \beta$ with ΔE being the excitation energy of a single molecule and $\Delta D = D - D'$ is the difference between D' and D, being negative as usually $|D'| > |D|$.

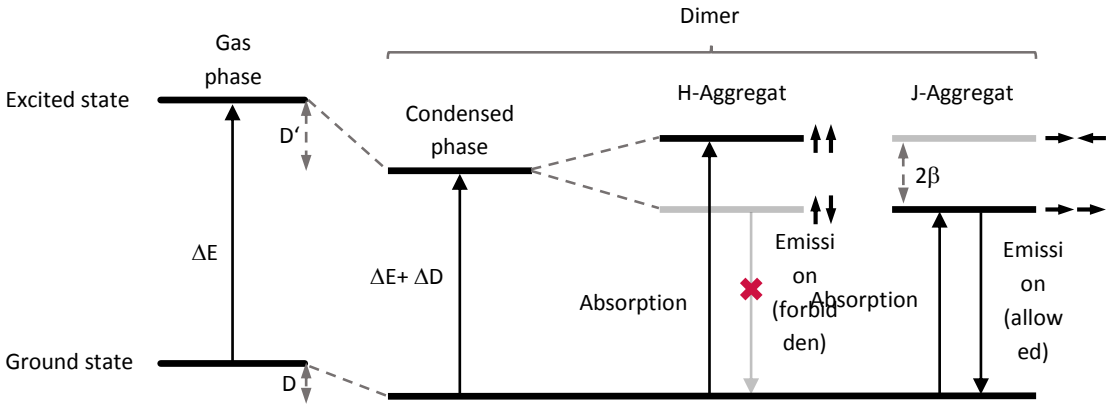

Figure 1: Illustration of the different energetic shifts and splitting of the energy levels occurring for the formation of an ideal dimer. The corresponding relative orientations of the transition dipoles for the two classes of aggregates are indicated as arrows.

If the two chromophores are aligned in a coplanar fashion, the upper of the two energy levels carries all the oscillator strength and the absorption is hypsochromically shifted ("H-aggregate"). Emission and absorption from the lower level carries no oscillator strength in the case of perfectly ordered arrangement. The opposite is the case for a collinear arrangement, called "J-aggregate" or "Scheibe-aggregate" after Jelly,[50] and after Scheibe.[51] Consequently, the radiative decay constant is an important tool to identify whether any emission observed results from an aggregate with a H- or J-type nature. This description has been developed in the case when the coupling between the chromophores is strong, as is often the case for molecules or short oligomers, and in addition to these two limiting cases illustrated, there are other orientations that can

occur. By the way, if the coupling is particularly strong so that the two chromophores change their equilibrium geometry due to the interaction, the resulting excited state is termed an excimer and it is characterized by a particularly broad red-shifted weak emission. A contemporary discussion of H- and J- aggregation for short oligomers has recently been presented by Gierschner and Park,[52] and a review on experimental results in dye molecules is given by Würthner et al.[53] Figure 2 shows how the optical spectra and radiative decay constant are affected as a result of the interaction.

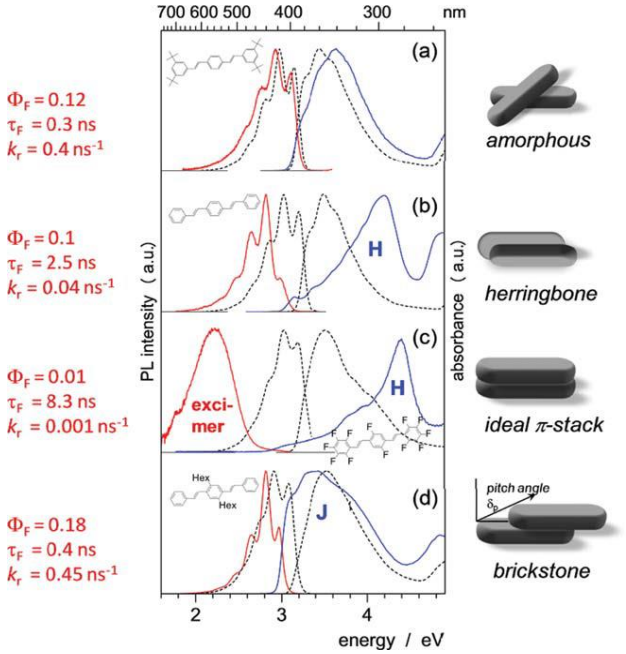

Figure 2: Absorption (blue lines) and emission (red lines) features, and photophysical data (PL quantum yields Φ_F, lifetimes τ_F, and rate constants k_r) of Distyrolbenzene-based materials, as measured on nanoparticle suspensions (solid lines) and in solution (dashed lines). Excimer emission bandshape, and J/H absorption bandshapes are indicated. From Ref [52]

The interaction that occurs between conjugated segments in semiconducting polymers is often weaker than that observed in short oligomers or dye molecules, so that the resulting spectra differ less from the spectra of the non-interacting chromophores. The most noticeable changes are spectral shifts in the range of 100 - 250 meV and changes in the distribution of the vibrational intensities. Spano has addressed these changes in vibrational structure in his theoretical approach.[54-57] He could show that in the case of perfectly ordered weakly interacting H-aggregates at 0 K, the vibrational structure changes so that the 0-0 peak is reduced in absorption yet fully suppressed in emission. Correspondingly opposite changes with enhanced 0-0 peak occur for weakly interacting

J-aggregates. These effects are moderated if the temperature is higher or if the chains are not fully ordered. Importantly, it is possible to extract the intermolecular coupling strength from the relative height of the vibrational peaks in absorption.[54] Spano has successfully applied his theory to the polymers P3HT as an example of a weakly interacting H-aggregate and to MEH-PPV as an example of a disordered, weakly interacting J-aggregate.[57] P3HT nanofibers have also been interpreted as J-type structures. [12,58-60]

In summary, even though it is clear that crystalline areas, resulting from intermolecular interactions, are important for organic solar cells or field effect transistors, the formation of ordered structures in organic semiconductors is not fully understood. In this context, we address two aspects, that are

(i) what causes the formation of ordered structures and how does it happen?

(ii) How does the resulting electronic coupling in ordered structures impact on their electronic structure?

by comparing temperature dependent spectroscopic data on a range of polymers and short oligomers.

2. Results and Discussion

2.1. General phenomenology

We shall first give an overview on the general features that are observed upon aggregation using the polymer P3HT as a model compound. Figure 3 shows temperature dependent absorption spectra of the widely used and intensively studied conjugated polymer P3HT. It is known to undergo an order-disorder transition in solution upon cooling,[61,62] where the occurring spectral changes can be classified into three temperature ranges.

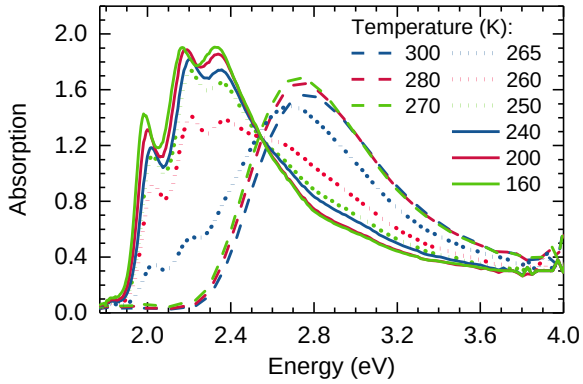

Figure 3: Absorption spectra of P3HT in THF solution for different temperatures. Spectra that belong to the three inherent temperature ranges described in the text are indicated with different lines (dashed, dotted, and straight). From Ref [62]

At the starting temperature at 300 K, the spectrum exhibits a featureless and rather broad spectral shape, which is attributed to a disordered chain conformation. When decreasing the temperature from the starting temperature onwards, the broad absorption spectrum shifts to the red and concomitantly gains intensity until a temperature of 270 K is reached (dashed lines in Figure 3). This red shift and increase in intensity suggests a planarization process of the disordered chains, leading to an increased conjugation length. Upon decreasing the temperature below a certain critical temperature (temperature range 2, dotted lines in Figure 3), the absorption from the higher energy regions decreases while an additional distinct, well structured absorption band appears at lower energy at 2.0 eV - 2.4 eV. In combination with the occurrence of an isosbestic point at 2.53 eV, the spectral changes within this temperature range can be attributed to an order-disorder phase-transition of P3HT. In this framework, the broad

absorption band centered at 2.8 eV is assigned to disordered chains in an amorphous phase whereas the structured absorption band at lower energies is attributed to ordered chains in an aggregated phase. Below this intermediate temperature range, in which the absorption spectrum undergoes the most significant changes, the new spectral features at low energies gain intensity upon further cooling and also shift to the red until the glass transition temperature of the solvent is reached (red lines in Figure 3). Similar to the temperature range 1, the red shift of the absorption feature of the aggregated phase is associated to a further planarization of the aggregated chain segments upon cooling to the lowest temperatures measured. Depending on the solvent, below a certain temperature the solvent forms a glass or crystallizes. In that case, further major conformational changes are prevented and increased light scattering often dominates.

Thus, in summary the order-disorder transition of P3HT occurs in three major steps which are for decreasing temperature: (i) planarization of the disordered phase, (ii) aggregate formation (iii) planarization of the aggregated phase. This sequence of temperature dependent conformational changes is not limited to the case of P3HT but, rather, it appears also in various other conjugated compounds. Figure 4 shows the temperature dependent absorption spectra of a selection of different materials in which we also found aggregation upon cooling a solution. In all these compounds, the above mentioned three step sequence of conformational changes can be observed. In addition to P3HT, the selection of investigated materials also includes the homo-polymers PFO, MEHPPV and MEHPPE (Figure 4a-c).

Furthermore we observed a temperature induced aggregation behaviour for an oligo PPV (Heptamer BEH-PPV, Figure 4e) and also for the more device relevant low bandgap polymer PCPDTBT (Figure 4d).[63] Recently, Reichenberger et al also found that the π-conjugated molecule DTS(FBTTH$_2$)$_2$, used for efficient solar cells, also undergoes a temperature induced order-disorder transition (Figure 4f).[64] Even for this molecule, the same three step sequence of conformational changes upon cooling was observed as for the polymeric compounds. Therefore, the temperature dependent conformational changes appear to be a general phenomenon which not only applies to polymers, but also can be observed in oligomers as well as small molecules.

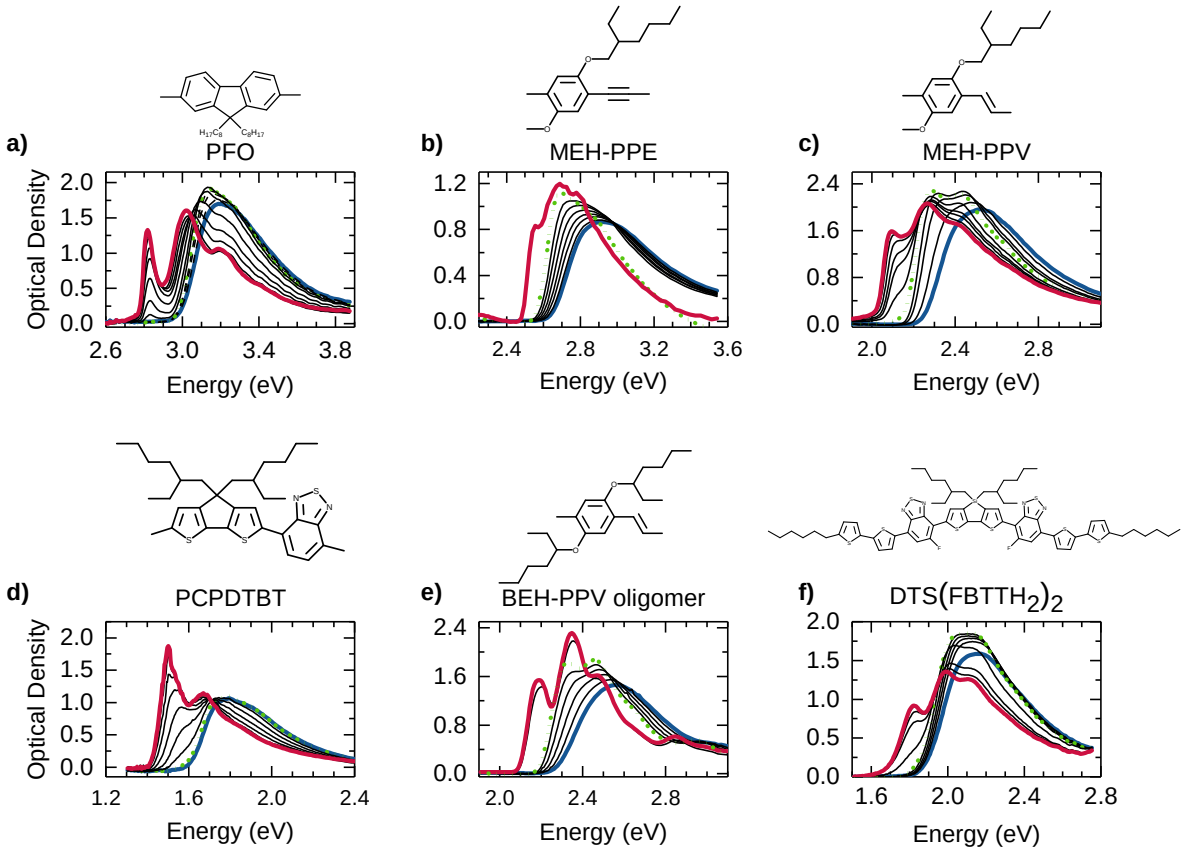

Figure 4: (a) - (f) Temperature dependent absorption spectra of the investigated material systems in MTHF solution showing aggregation behaviour. The chemical structure is indicated on top of each panel. For each compound, the spectrum measured at the highest temperature, at a temperature directly above the phase transition, and at the lowest temperature are indicated in blue, green (dotted) and red respectively.

Nevertheless, when comparing the shape of the absorption spectra, differences between the compounds become evident. This is particularly clear at low temperatures where the aggregated phase dominates (Figure 4, red solid lines).

2.2. Identification of the order-disorder transition by absorption spectroscopy - Approaches to analyse measured absorption spectra

To gain further insights into both, the spectral character of the neat phases and the nature of the phase transition itself, it is necessary to analyze the measured spectra carefully. It is known that, during aggregation, a fraction of the polymer chains are aligned in a well ordered fashion while at the same time the remainder of chains is disordered.[65] This semi-crystalline nature of conjugated polymers also impacts on the

absorption spectra, because the spectra of ordered and disordered domains are superimposed. To identify both phases thus requires a deconvolution of the absorption spectra.[18,19,66-68] This can, for example, be done by suitably normalizing the absorption spectrum of the neat disordered phase (e.g measured at elevated temperature) such that it fits to the high energy side of an absorption spectra taken at a lower temperature where both, disordered and ordered, aggregated chains coexist. The difference between this spectrum and the normalized spectrum of the disordered chains then results from absorption of ordered chains in the neat aggregated phase. In recent studies we applied this method to decompose absorption spectra where features from disordered and ordered chain superimpose, and we found this method to apply to various π-conjugated materials.[41,61,64] We point out that preferably the absorption spectrum measured at a temperature directly above the critical transition temperature of the aggregation process should be used since this takes the planarization processes during the first temperature range into account.

Figure 5a illustrates the result of this approach for the case of MEH-PPV, where the absorption spectrum at 180 K was used for fitting to the high energy side of the 150 K spectrum. The difference between these two spectra is assigned to absorption from aggregated MEH-PPV, thus allowing to determine the fraction of aggregate absorption $f_{absaggr}$ relative to the overall absorption. In order to derive the actual fraction of aggregated chains f_{aggr} from this, on needs to take into count that the oscillator strength may differ for chromophores in the disordered and in the aggregated phase. Following the approach demonstrated by Clark et al for P3HT,[22] we use $f_{absaggr} = F * f_{aggr}$, where F is the relative change of oscillator strength between the disordered and aggregated chain conformation.[22,41,61,63,64] As the oscillator strength ε correlates with the area below the absorption spectra, F can be derived from the temperature dependent absorption spectra by:

$$\frac{\Delta A_{aggregate}}{\Delta A_{disordered}} = \frac{\varepsilon_{aggregate}}{\varepsilon_{disordered}} = F \qquad (1)$$

with the areas $\Delta A_{aggregate}$ and $\Delta A_{disordered}$ taken from the shaded regions as illustrated in Figure 5a. Using this approach, it is possible to calculate the absolute fraction of aggregate for each measured spectrum at a certain temperature below the phase transition.

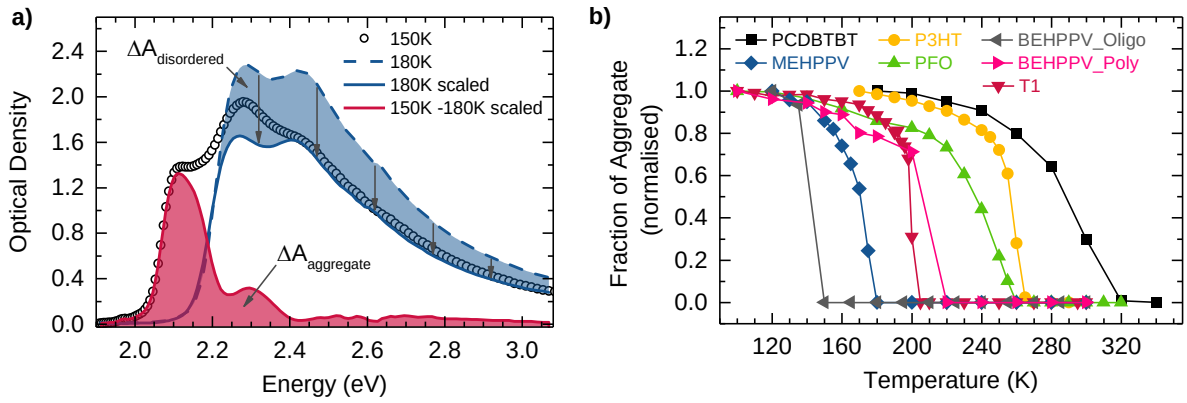

Figure 5: (a) Illustration of the deconvolution approach of the absorption spectrum to obtain the contributions of disordered and aggregate phase (red) for MEHPPV. Areas which are relevant for the determination of the change in oscillator strength between disordered and aggregated phase are also indicated. (b) Temperature dependent fraction of aggregate for the different investigated material systems.

An alternative method to derive the temperature dependent fraction of aggregates is to simply track the 0-0 Peak intensity of the aggregated phase as a function of temperature. While this is a simple, and thus fast approach, it has the disadvantage that only the qualitative character of the fraction of aggregates can be obtained yet absolute values cannot be acquired.

Figure 5b shows the normalised fraction of aggregate as a function of temperature for the different materials investigated. In each case, the fraction of aggregates was obtained by using the above mentioned approach. For every investigated material system the fraction of aggregate is zero above the phase transition, by definition. Below a certain temperature the fraction of aggregate increases steeply and finally saturates at low temperatures. It is obvious that both, the steepness of the transition, $\left(\frac{\partial f}{\partial T}\right)_{T \leq T_c}$ and the transition temperature depends sensitively on the material, while the occurrence of an order-disorder transition is a general property of all compounds investigated. An important parameter toward an understanding of this phenomenon is the critical transition temperature T_c of the order-disorder transition. It is defined as the point of inflection of the fraction of aggregate f_{aggr} and calculated as:

$$\left.\frac{\partial^2 f_{aggr}}{\partial T^2}\right|_{T_c} = 0 \qquad (2)$$

In Table 1 the calculated values of T_c of the investigated compounds are listed from which the variety of critical temperatures that can occur becomes clear again. Furthermore Table 1 also gives further material parameters such as the chain length and polydispersity, whose influences on the phase transition we discuss in the following.

Table 1: Overview of material parameters such as M_w, M_n, resulting Polydispersity Index via PDI=M_w/M_n Number of Repeating units (=Degree of Polymerisation) and relevant parameters that quantify the order-disorder transition; with critical transition temperature T_c, width of the transition ΔT and the factor F which corresponds to the relative change in oscillator strength.

Compound	Type	T_c	ΔT	PDI	Rep unit	M Rep. unit	M_w	M_n	Factor F
		K	K		#	g/mol	kg/mol	kg/mol	-
P3HT	Polymer	266	12	1.2	205	166	39.4	34.2	1.4
		252	35	2.0	113		38.4	18.8	
		258	13	1.2	111		21.6	18.6	
		248	11	1.1	68		12.5	11.3	
		216	24	1.2	30		6.3	5.1	
PFO	Polymer	245	33	2.9	79	391	90.7	30.9	1
MEH-PPE	Polymer	110	n.a.	n.a.	n.a.	n.a.	n.a.	n.a.	n.a.
MEH-PPV	Polymer	175	13	3.8	210	276	218.8	58.1	1
PCPDTBT	Polymer	295	50	1.7	25	535	23	13.5	1.4
BEH-PPV	Polymer	210	33	n.a.	n.a.	359	n.a.	n.a.	1
	Oligomer	155	22	n.a.	7		n.a.	n.a.	1.1
p-DTS-(FBTTH$_2$)$_2$	Molecule	200	6	1	1	1220	-	-	0.6

When the spectrum of the aggregated chains is identified, it can be analysed with respect to the intensities of the different vibrational peaks in the framework of the theories developed by Spano or Gierschner.[66,67]

In the Spano-model, the free exciton bandwidth W can be inferred from the ratio of the 0-0 and 0-1 vibrational peaks, A_{0-0} and A_{0-1}, according to

$$\frac{A_{0-0}}{A_{0-1}} \approx \left(\frac{1-0.24W/E_p}{1+0.073W/E_p}\right)^2 \quad (3)$$

With E_p being the main vibrational energy, which is often assumed to be dominated by the symmetric C=C stretch at 0.18 eV. When doing this, it is a good idea to actually analyse the spectra in terms of a Franck-Condon progression so that the intensities of the two vibrational peaks can be identified clearly (without contributions due to their overlap). Typical values for the bandwidth are in the range of 80 - 100 meV for P3HT, [22,34] and for MEHPPV and PFO in the range of 30 meV.[57 69]

2.3. The nature of the phase transition

When the fraction of aggregates is recorded as a function of temperature in a commercially available sample such as MEH-PPV, the resulting curve (see Figure 5b) increases only gradually. It turns out that the shape of the curve empirically fits to a function of the form $f(T) = \left(\frac{T_c - T}{T_c}\right)^{1/3}$, which is characteristic for a 2nd order phase transition, suggesting that this might apply to the order-disorder transition in MEH-PPV.[35] In subsequent work, we addressed the issue of resolving the nature of the phase transition in a systematic manner by comparing the temperature dependence of the transition in a range of P3HTs with different molecular weights. These samples had been synthesized using a Grignard metathesis reaction method that ensured that all batches had not only a high degree of regioregularity but also, in particular, a small polydispersity as detailed in Table 1.[61] Figure 6a shows the normalized fraction of aggregate as a function of temperature for P3HTs with molecular weights of 5, 11, 19 and 34 kDa. Except for the lowest molecular weight, one can see that the transition is steep, i.e. it occurs in a narrow temperature range. Moreover, the transition temperature T_c, inferred from the the inflection point, reduces with reducing chain length. This is illustrated further in the bottom panel, where the critical transition temperature is displayed as a function of repeat units in the chain. The same dependence had also been observed for PFO.[19,70] In the case of PFO, Vanden Bout and co-workers used a model by Sanchez et al. to fit the chain lengths dependence. The model is based on a mean field theory of a polymer chain

with excluded volume and attractive interactions and describes the thermodynamic behaviour of polymer chains that undergo a coil globule transition.[71] In the framework of the Sanchez-model, the critical transition temperature T_c depends on the number of repeat units N according to

$$\frac{\theta - T_c}{T_c} = \frac{\varphi}{\sqrt{N}} \quad (4)$$

where φ is a constant that depends on the chain stiffness and the theta temperature θ, which is the critical temperature of an infinite chain. For an infinite chain, this is a second-order transition in the Landau sense, yet it becomes pseudo-second order for finite chain lengths. Figure 6a shows that the Sanchez-model of the coil-globule transition is suitable to describe the chain lengths dependence of the transition temperature also for P3HT. Due to the low polydispersity of the P3HT samples, the agreement is even improved compared to the PFO samples investigated by Vanden Bout et al.[19] From Figure 6 it also becomes clear that, for short chains, T_c can be lower than the glass temperature or crystallization temperature of the solvent used, so that the phase transition cannot be observed in the temperature range in which the solvent is liquid. This is manifested, for example, for oligomers of PFO and of PPV-derivatives. We observed the order-disorder transition of the polymers PFO in MTHF solution at a temperature of 245 K, and of BEH-PPV at 210 K. In contrast, we could not observe any transition for analogous oligo-fluorenes with 7 repeat units, consistent with a report by Cone et al.[19] Using the Sanchez-model would predict the T_c to be below 140 K for the PFO heptamer, i.e. at or below the glass temperature of MTHF which is about 130-140 K.[72] Similarly, for a heptamer for a BEH-PPVs, the transition can still be observed at T_c = 155 K, yet it is not measurable for the pentamer.

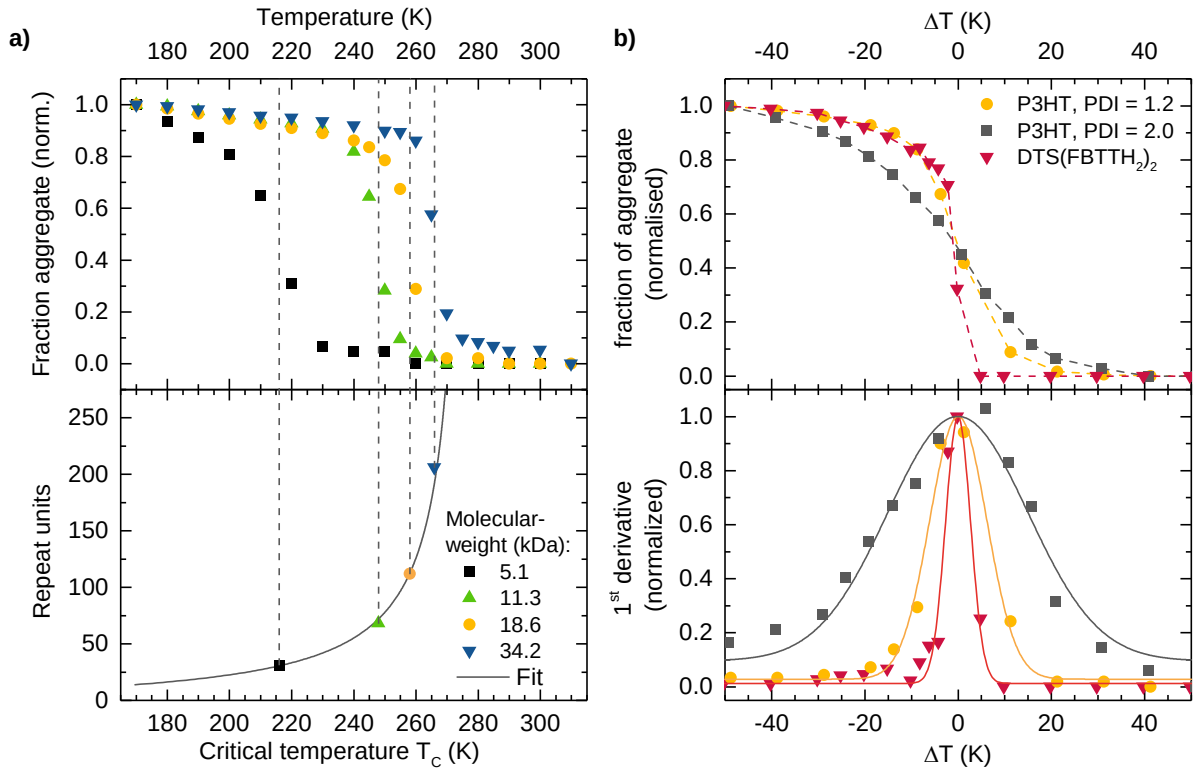

Figure 6: (a) Normalised fraction of aggregate as a function of temperature four batches of P3HT with different molecular weights (top) and the corresponding critical transition temperatures (bottom), together with a fit of equation 4 (grey line, see text). (b) Normalised fraction of aggregate as a function of relative temperature (top) and corresponding normalised first derivative of the for the small molecule p-DTS(FBTTH$_2$)$_2$ and two P3HT samples with similar molecular weight and regioregularity yet different polydispersity (data from Refs [61] and [64]).

When considering the dependence of T_c on molecular weight for P3HT, we noticed that the samples with low polydispersity showed a significantly more narrow transition range than commercial samples with higher polydispersity yet the same molecular weight. This is displayed in Figure 6b. A measure for this is the width of the peak in the first derivative taken from the temperature dependent fraction of aggregate. This is shown in Figure 6b as a function of temperature difference to T_c. Two samples of P3HT with same molecular weight (~19 kDa) yet PDIs of 1.2 and 2.0, respectively, show a width (FWHM) of the transition of ΔT=13 K and ΔT=35 K, respectively. For comparison, we also include data for the molecule p-DTS(FBTTH$_2$)$_2$ which has a PDI of 1.0 and shows a width of ΔT=6 K. This evolution can easily be understood in the framework of the Sanchez-model. If the transition temperature depends on chain length, then in more polydisperse samples different transition temperatures for the different chain lengths co-exist. Upon lowering the temperature, the longest chains collapse first, followed by the shorter chains at a

lower temperature, and as a result the transition appears to broaden out. This smearing out masks the actual temperature dependence of the transition. Figure 7a shows the temperature dependent fraction of aggregates for the two P3HT samples with different polydispersity plotted versus $\left(\frac{T_c-T}{T_c}\right)^{1/3}$ on a double-logarithmic scale.

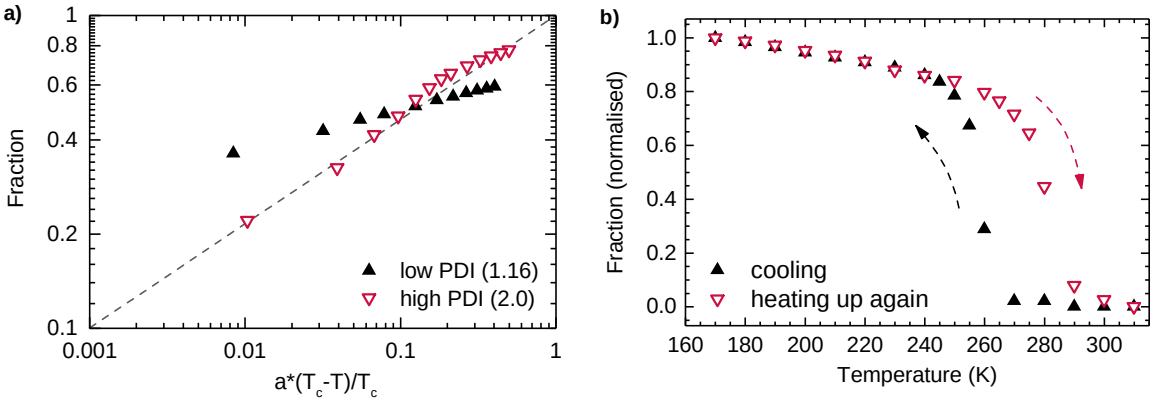

Figure 7: (a) The fraction of aggregated as a function of $(T_c-T)/T_c$ in a double logarithmic presentation for the two P3HT samples with low and high PDI as indicated. The dashed line indicates a slope of 1/3. (b) Normalized fraction of aggregate of P3HT as a function of temperature upon cooling and subsequent heating. From Ref [61]

The solid line indicates a slope of 1/3, indicative of the second order phase transition. One can see that the more polydisperse sample appears to follow this relationship and only for the less polydisperse sample does the deviation from the slope of 1/3 become manifest and evident. This suggests that the transition is rather of first order nature, yet that it may appear as second order due to the superposition of different transition temperatures. Further support for the identification as first order is given by the fact that the transition temperature observed upon cooling and upon heating differ, e.g. by 20 K in the case of P3HT (Figure 7b). This can be attributed to the latent heat of crystallization and is often said to be a defining feature of a first-order phase transition.[73]

So far, we focussed on the phenomenological description of the order-disorder transition and its manifestation in the absorption spectra. In summary, we found that (i) the transition proceeds in a three-step fashion, with the first step being a planarization and concomitantly often a swelling of the chain, the second step being the actual collapse into an ordered, electronically interacting structure, and the third step being the further elongation and perfection of order in the aggregated structure. (ii) We showed that the transition temperature depends on the chain length and can be described in the

framework of a mean-field model developed by Sanchez for coil-globule transitions. Finally, (iii), we demonstrated that in polydisperse samples, the temperature dependence of the transition can be smeared out due the distribution of molecular weights and associated transition temperatures. Moreover, we established that these phenomena are not limited to any particular semiconducting polymer but, rather, that they occur for a wide range of compounds encompassing homopolymers, copolymers, short oligomers and a molecule. We now discuss which general insight be inferred from these observations on the mechanism of the transition.

2.4. The mechanism of the aggregation process

A particular unusual feature in the order-disorder transition is the initial swelling of the polymer chain, caused by its planarization when the temperature of the solution is lowered within the first stage. The commonplace understanding of a coil-globule transition is that a chain is swollen in a "good" solvent yet collapses into a globule in a "poor" solvent.[74] Thus, as the quality of a solvent is reduced upon reducing the temperature, one would expect a (continuously) reduced radius of gyration of the polymer. The associated increased number of twists and turns in the polymer chain would reduce the mean conjugation length so that one would expect a hypsochromic shift in the absorption spectra. However, the opposite effect is observed, i.e. the absorption spectra shift to the red spectral range upon cooling. A bathochromic shift usually suggests an *increased* conjugation length. The increase of conjugation length is confirmed by the fact that the oscillator strength of the transition also increases (see Figure 3, dashed lines and Figure 4). For a given non-interacting polymer chain or π-conjugated molecule, an increased conjugation length suggests that conjugated segments have become more planar and, in the case of a polymer, more elongated. Due to the overall rigidity of semiconducting polymer chains, it is thus reasonable to infer a more swollen, expanded chain conformation at the lower temperature limit of the first stage, immediately prior to the collapse. This scenario may, at first, appear unusual since it is not observed for the well-investigated range of flexible polymer chains such as polystyrene.[75] However, our scenario is corroborated by Kolinski et. al.[76] who investigated how the stiffness of a polymer chain impacts on the temperature-dependence of the radius of gyration using Monte-Carlo (MC) simulations. This is shown in Figure 8a.

Kolinski and co-workers consider the ratio between chain stiffness, parametrized by ϵ_g, and attractive interaction, expressed by ϵ_a. If the chain is flexible relative to ϵ_a, the radius of gyration indeed decreases continuously as shown in Figure 8. However, when the stiffness parameter exceeds twice the interaction parameter, the chain expands prior to a sudden collapse that becomes discontinuous for very rigid chains. Regarding the nature of the transition, Kolinski notes: "Sanchez's mean field theory prediction that the polymer collapse transition is second order does not contradict our findings since he assumes a priori a highly flexible chain. Our MC results also show a smooth gradual collapse transition for flexible polymers". Figure 8b shows typical calculated chain conformations that pertain to the two limiting cases. The top row shows how a flexible chain (ϵ_g/ϵ_a=1) in the random coil, high temperature state collapses in the dense random coil. For a stiffer chain (ϵ_g/ϵ_a=4), the collapse into a highly ordered dense state is shown in the lower row of Figure 8b. This highly ordered dense state that is predicted by the MC calculation is also evident in the absorption spectra in form of the structured, red-shifted lower energy absorption that is established in the third stage of the phase transition (c.f. Figure 3, dotted lines). The ordered arrangement can be inferred from the high degree of structure in the aggregate absorption as well as from the analysis of the spectral shape in the framework of Spano's model of weakly interacting H- or J-aggregates (*vide supra*).

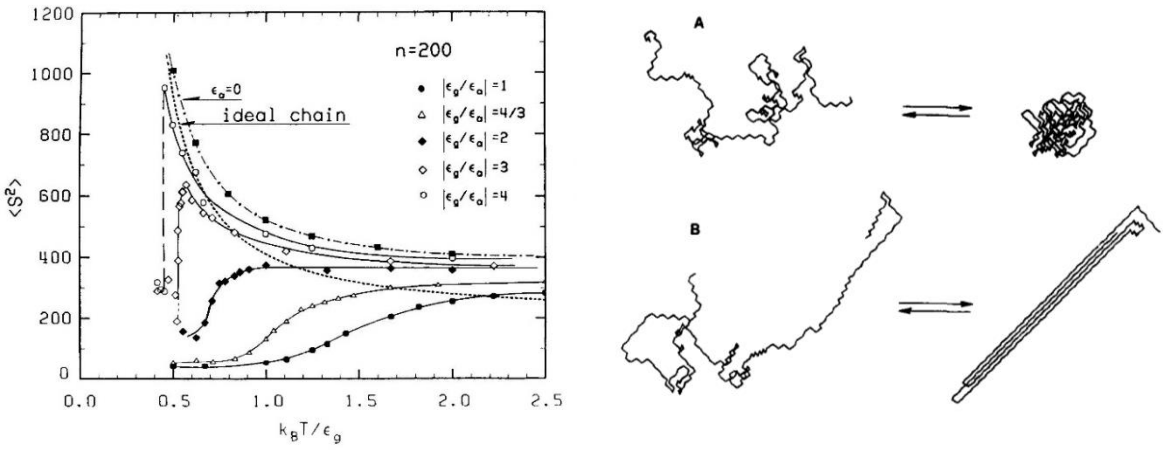

Figure 8: Understanding the temperature dependent order-disorder transition as a collapse process. (a) Calculated radius of gyration as a function of temperature for polymer chains with different stiffness. (b) Illustration of two different cases: The collapse process of a flexible chains leads to a dense random coil state (top), whereas for a stiff polymer, the collapsed state can show an inner structure/order (bottom).

Thus, the conclusions that can be drawn from the absorption spectra on the mechanism of aggregation are (i) that the chain expands before collapsing, and (ii) that the collapsed chain adopts a highly ordered arrangement. Further, we conclude that (iii) the transition can be described in the frameworks developed by Sanchez et al. and Kolinski et al. for coil-globule transitions.[71,76] We note in particular that the first two points mark a difference in the aggregation mechanism to the order-disorder transition that is commonly described for flexible polymer chains such as polystyrenes.

2.5. The role of side chains in the aggregation process

From the preceding discussion, the misleading impression may arise that polymer chains always collapse into a dense ordered form provided the solvent can be cooled to sufficiently low temperatures and remains liquid. This is, of course, not the case. A key parameter that controls whether or not a chain collapses into an ordered arrangement are the sidechains. If sidechains induce structural disorder, e.g. by occurring in a regiorandom arrangement or by being branched, the tendency to aggregate is reduced compared to polymers with regioregular sidechain arrangement or linear sidechains. Classical examples are regioregular P3HT versus regiorandom P3HT,[25] polyfluorene or polyindenofluorene with octyl side chains (PFO, PIFTO) compared to the polymers with ethyl-hexoxy sidechains (PF2/6, PIFTO).[7,27,77]

Sidechains can also promote aggregation when they induce a planar backbone conformation. This is the case of PPV-derivatives, with heptoxy-substituted PPV aggregates while heptyl-substituted PPV does not.[78] The reason is that the heptoxy-substituted PPVs adopt a fully planar conformation in contrast to the heptyl-substituted ones. This is likely to be associated with the lesser steric demand of the oxygen compared to a CH_2 at the same place. The dominant role of sidechains is also evident when considering MeLPPP. The ladder-type polymer is rigid and planar, yet the sidechains have been synthesized with the aim of preventing aggregation by being sterically demanding. LPPP-derivatives with less elaborate sidechains were prone to the formation of excimers which is undesired for OLED applications.[79]

Even though the theories on order-disorder transitions mentioned above consider only the interaction of polymer segments of the main chain, they are able to capture

essential elements of the transition such as the dependence of T_c on chain length,[71] and the change in polymer conformation upon cooling.[76] This suggests that for these polymers, i.e. P3HT, PFO and MEH-PPV, the role of the sidechains in the transitions is a secondary one. Clearly, more theoretical development that includes the effects of sidechains, e.g. as in hairy rod models, would be desirable.[80] This is even more the needed as in some cases, the crystallization of long alkyl side chains can precede and even drive the crystallization of the polymer backbone.[81]

As an example for the role of sidechains in the aggregation process we discuss the changes observed in P3HT upon cooling in solution, shown in Figure 9. The same batch of P3HT had also been investigated by small-angle and wide-angle X-ray scattering (SAXS and WAXS) when cooling from the melt, so that the structural data and the spectroscopic data could be correlated.[62,82] Whereas so far, we always considered the *absorption* spectra, Figure 9 display the *emission* spectra, that, for several reasons, are more sensitive to changes in the associated polymer conformations. In Figure 9a, the evolution of the spectra from 300 K and 160 K is shown for ease of comparison. The associated absorption is given by Figure 3, and the transition temperature is about 260 K. We can attribute the two spectra at 300 K and 280 K to the random coil conformation of the amorphous polymer phase. At 265 K, some aggregate formation has already occurred. Analogous to the absorption spectra, we can decompose the 265 K spectrum into spectral contributions from the disordered chains (blue shaded area in Figure 9b) and to contributions from the aggregated chains (red shaded area in Figure 9b). The X-ray data suggest that at this stage, there is some phase separation between the polymer backbones and the polymer sidechains, so that the polymer backbones are already on top of each other, though are not yet fully planar. In Figure 9c, only the spectra of the aggregated chains are displayed for different temperatures. Upon cooling, strong spectral changes occur that indicate further planarization and an increase of electronic interaction.[62] This correlates with the structural signatures of backbone planarization observed in the SAXS and WAXS data. Few spectral changes occur from 160 K to 5 K, except that the spectra shift slightly to the red and they become better resolved. As a consequence of the better resolved vibrational structure, it becomes evident that the 5 K spectrum cannot be described in terms of a Franck-Condon vibrational progression of *one* emitting state. Rather, it results from the superposition of emission from *two* states. This was further confirmed by site selective PL spectroscopy as well as by time-resolved PL spectroscopy. The SAXS and WAXS data

indicate that there are, in fact, indeed *two* crystal structures.[82,83] In both structures, the P3HT backbone is planarized and aggregated. However, in one structure, associated with the higher energy state, the sidechains are still disordered.

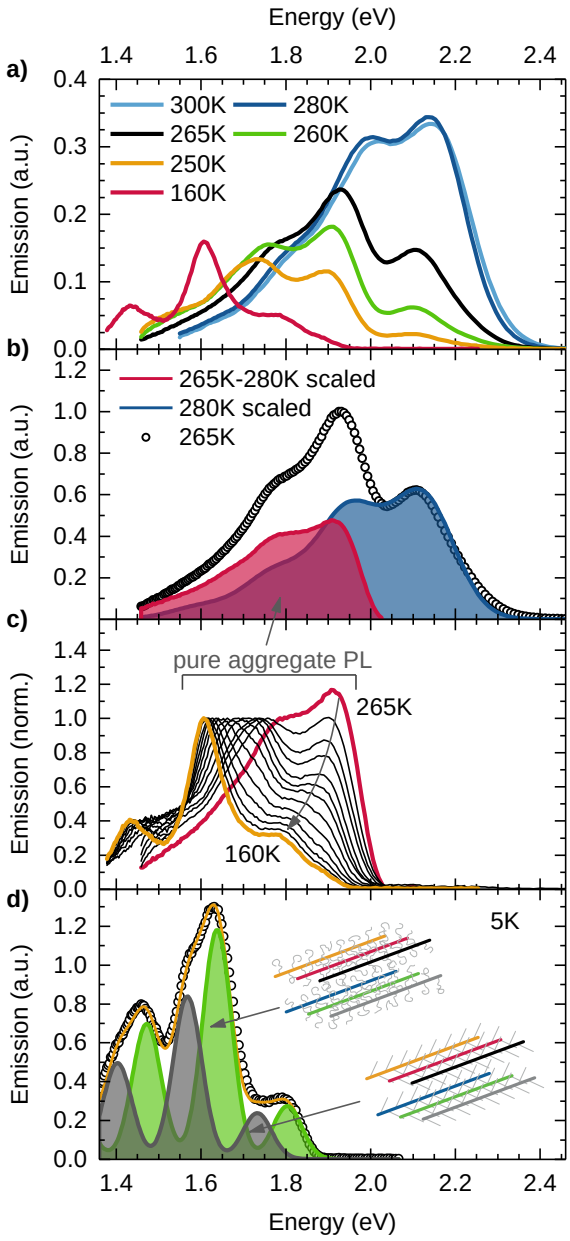

Figure 9: (a) PL-spectra of P3HT (19 kD) in THF solution for different temperatures. (b) Illustration of decomposing the PL spectrum at 265 K, to obtain the contributions from PL from disordered and aggregated phase. The 280 K emission of the disordered phase (blue) is scaled to the high energy tail of the 265 K emission spectra (black dots). The difference between the two spectra is assigned to PL from the aggregated phase (red). (c) PL spectra of the pure aggregated phase in the range between 265 K and 160 K, normalized to the intensity of the $S_1 \rightarrow S_0$ 0-1 feature. (d) PL spectrum of P3HT at 5 K (black dots). The two vibronic progressions that are needed to model the spectrum are shown as grey and green areas. Illustrations of the different morphologies that are correlated to the two aggregate species are also indicated.

This implies that the stacks of P3HT backbones are not well defined with respect to the position of the neighboring stack. In the other structure, associated with the lower energy state, both, backbone and sidechain are crystalline. In consequence, there is long-range order as the position of adjacent stacks is better defined. We stress that for both structures, the planarity and order in the backbone arrangement is very similar, as is also evident from the similar ratios in the vibrational peaks. Even though they only differ in the degree of side chain order, the 0-0 transition energies of the two structures varies by about 80 meV.

2.6. Role of environmental polarization

The difference in energies between the two structures, i.e. the one where both backbone and sidechain are crystallized ("low energy progression", LEP) and the one where only the backbones are crystallized ("high energy progression", HEP) is intriguing. It cannot be accounted for by the electronic resonance interaction between the chromophores, e.g. as described in Spano's theory, since this only encompasses the interaction of the π-systems within a one-dimensional stack of backbones. This is also manifested by the similar ratios of the vibrational peaks for both progressions.

What can give rise to this energy difference? We have already mentioned that upon the transition from isolated chains to condensed chains, the energy levels of the chromophores shift by the polarization energy ΔD, which contains the van der Waals interactions of one chromophore with its environment. In a simplified treatment, this is often worked out in terms of point dipoles, yet for a more detailed analysis, one may need to consider extended charge distributions. The key difference between the phases pertaining to the HEP and the LEP is the degree of long-range order. In the case of, presumably, the LEP, the position of the adjacent π-stacks is well-defined and ordered with respect to a particular conjugated segment of a chain, whereas this is not the case for the HEP, where stacks still have some degree of translational variation between adjacent stacks. As a result, there is a higher degree of long-range order for the LEP than for the HEP. We conjecture, that this affects the electrostatic van der Waals type interaction between chromophores, so that these differences in structural order translate

into differences in the polarization energies ΔD. Sophisticated electrostatic calculations would be required to probe this hypothesis.

With this in mind, we reconsider the PL spectrum of P3HT at 265 K (Figure 9b). It is remarkable that the shape of the aggregate spectrum closely resembles the spectrum of the disordered chain in the amorphous phase. Recall that the structural data indicate a stack of still disordered P3HT backbones. On the one hand, it may be possible to describe the spectral shape in terms of a highly disordered so-called HJ-aggregate,[55] where the usual suppression of the 0-0 peak in emission is alleviated by the prevailing disorder. One the other hand, it may worthwhile to consider whether this feature could alternatively still be described in terms of a disordered polymer chain (without noticeable resonance interaction with adjacent backbones) whose energy levels are reduced by the increased polarization energy ΔD in the stack environment. As the polarization energy depends on the polarizability of the molecules in the environment, it is evident that the mean local polarization energy is higher if the backbone is surrounded in its immediate vicinity only by the alkyl sidechains of neighbouring chains than if it is sandwiched in a stack, wedged between two backbones with extended π-systems that are far more polarizable than alkyl chains. Clearly, there is a need for theoretical investigations into the effect of environmental polarization on the transition energies in order to accurately describe the spectral changes that occur in an order-disorder transition.

2.7. Concluding summary and outlook

We have shown that for π-conjugated polymers and molecules, the formation of aggregates can be understood in terms of an order-disorder transition. The mechanism of aggregation differs from flexible polymers insofar that the chains planarize and may even swell up prior to collapsing into an ordered aggregate. This feature is common for a range of materials and is not particular to a specific compound. We demonstrated that, by analysing the absorption and emission spectra, detailed information can be obtained on the fraction of aggregates in the sample as well as on the degree of order and interaction that prevails in the aggregates and on the conjugation length. The nature of the phase transition has been identified as first order, though the superposition of different transition temperatures for different chain lengths in polydisperse samples can

give the impression of a second-order transition. The role of the sidechains has been highlighted.

Figure 10 summarizes the changes that occur in morphology and spectra upon cooling a solution such as to induce an order-disorder transition. Future work should consider how the effect of sidechain interactions as well as of environmental polarization may be included in a theoretical treatment.

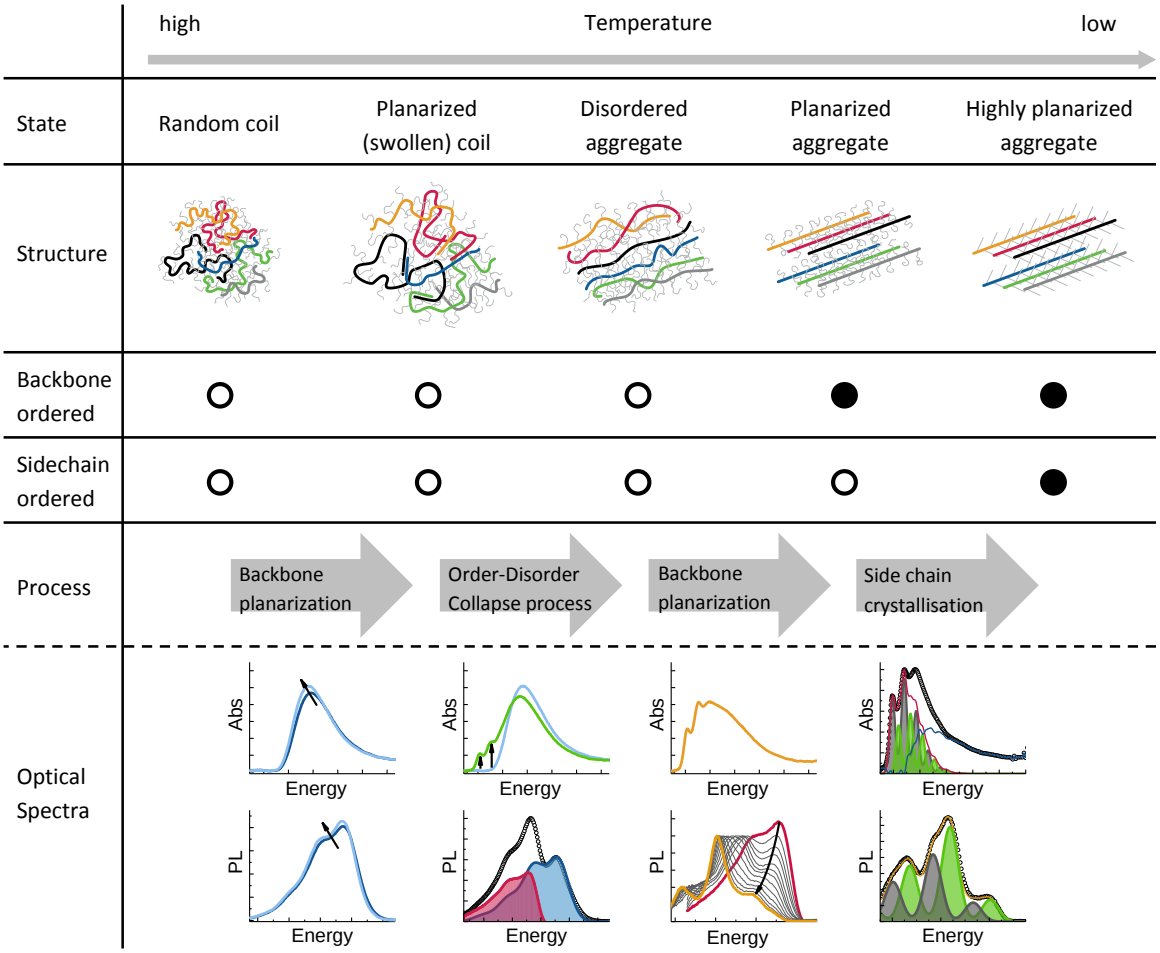

Figure 10: Summary of the changes that can occur in morphology and optical spectra upon cooling a solution of conjugated polymers.

Acknowledgements:

We acknowledge financial support by the Bavarian State Ministry of Science, Research, and the Arts through the Collaborative Research Network 'Solar Technologies go Hybrid' and by the German Science Foundation DFG through the research training group GRK1640. We thank Natalie Stingelin and Markus Reichenberger for stimulating discussions and Konstantin Schötz for the help with the setups.

Acronyms:

P3HT: Poly(3-hexylthiophene-2,5-diyl)

PFO: Poly(9,9-di-n-octylfluorenyl-2,7-diyl)

PCPDTBT: Poly[2,6-(4,4-bis-(2-ethylhexyl)-4H-cyclopenta [2,1-b;3,4-b′]dithiophene)-alt-4,7(2,1,3-benzothiadiazole)]

MEH-PPE: Poly[2-methoxy-5-(2-ethylhexyloxy)-1,4-phenyleneethynylene]

BEH-PPV: Poly[2,5-bis(2′-ethylhexyloxy)-1,4-phenylenevinylene]

MEH-PPV: Poly[2-methoxy-5-(2-ethylhexyloxy)-1,4-phenylenevinylene]

DTS(FBTTH$_2$)$_2$: 7,7′-[4,4-Bis(2-ethylhexyl)-4H-silolo[3,2-b:4,5-b′]dithiophene-2,6-diyl]bis[6-fluoro-4-(5′-hexyl-[2,2′-bithiophen]-5-yl)benzo[c][1,2,5]thiadiazole]

References:

(1) Pingel, P.; Zen, A.; Abellón, R. D.; Grozema, F. C.; Siebbeles, L. D. A.; Neher, D. Temperature-Resolved Local and Macroscopic Charge Carrier Transport in Thin P3HT Layers. *Advanced Functional Materials* **2010**, *20*, 2286.

(2) Chang, J.-F.; Sun, B.; Breiby, D. W.; Nielsen, M. M.; Sölling, T. I.; Giles, M.; McCulloch, I.; Sirringhaus, H. Enhanced Mobility of Poly(3-hexylthiophene) Transistors by Spin-Coating from High-Boiling-Point Solvents. *Chemistry of Materials* **2004**, *16*, 4772.

(3) Sirringhaus, H.; Brown, P. J.; Friend, R. H.; Nielsen, M. M.; Bechgaard, K.; Langeveld-Voss, B. M. W.; Spiering, A. J. H.; Janssen, R. A. J.; Meijer, E. W.; Herwig, P.; de Leeuw, D. M. Two-dimensional charge transport in self-organized, high-mobility conjugated polymers. *Nature* **1999**, *401*, 685.

(4) Kline, R. J.; McGehee, M. D.; Kadnikova, E. N.; Liu, J.; Fréchet, J. M. J. Controlling the Field-Effect Mobility of Regioregular Polythiophene by Changing the Molecular Weight. *Advanced Materials* **2003**, *15*, 1519.

(5) Khan, A. L. T.; Sreearunothai, P.; Herz, L. M.; Banach, M. J.; Köhler, A. Morphology-dependent energy transfer within polyfluorene thin films. *Physical Review B* **2004**, *69*, 085201.

(6) Hayer, A.; Khan, A. L. T.; Friend, R. H.; Köhler, A. Morphology dependence of the triplet excited state formation and absorption in polyfluorene. *Physical Review B* **2005**, *71*, 241302.

(7) Carlos, S.; David, M. R.; Anoop, S. D.; Laura, M. H.; Clément, D.; Neil, C. G.; Ana, C. A.; Sepas, S.; Klaus, M.; Richard, H. F. Exciton and polaron dynamics in a step-ladder polymeric semiconductor: the influence of interchain order. *Journal of Physics: Condensed Matter* **2002**, *14*, 9803.

(8) Gruber, M.; Wagner, J.; Klein, K.; Hörmann, U.; Opitz, A.; Stutzmann, M.; Brütting, W. Thermodynamic Efficiency Limit of Molecular Donor-Acceptor Solar Cells and its Application to Diindenoperylene/C60-Based Planar Heterojunction Devices. *Advanced Energy Materials* **2012**, *2*, 1100.

(9) Liu, Y.; Zhao, J.; Li, Z.; Mu, C.; Ma, W.; Hu, H.; Jiang, K.; Lin, H.; Ade, H.; Yan, H. Aggregation and morphology control enables multiple cases of high-efficiency polymer solar cells. *Nature Communications* **2014**, *5*.

(10) Dou, F.; Buchaca-Domingo, E.; Sakowicz, M.; Rezasoltani, E.; McCarthy-Ward, T.; Heeney, M.; Zhang, X.; Stingelin, N.; Silva, C. The effect of phase morphology on the nature of long-lived charges in semiconductor polymer:fullerene systems. *Journal of Materials Chemistry C* **2015**, *3*, 3722.

(11) Scarongella, M.; De Jonghe-Risse, J.; Buchaca-Domingo, E.; Causa', M.; Fei, Z.; Heeney, M.; Moser, J.-E.; Stingelin, N.; Banerji, N. A Close Look at Charge Generation in Polymer:Fullerene Blends with Microstructure Control. *Journal of the American Chemical Society* **2015**, *137*, 2908.

(12) Scarongella, M.; Paraecattil, A. A.; Buchaca-Domingo, E.; Douglas, J. D.; Beaupre, S.; McCarthy-Ward, T.; Heeney, M.; Moser, J. E.; Leclerc, M.; Frechet, J. M. J.; Stingelin, N.; Banerji, N. The influence of microstructure on charge separation dynamics in organic bulk heterojunction materials for solar cell applications. *Journal of Materials Chemistry A* **2014**, *2*, 6218.

(13) Waheed, N.; Ko, M. J.; Rutledge, G. C.: Atomistic Simulation of Polymer Melt Crystallization by Molecular Dynamics. In *Progress in Understanding of Polymer Crystallization*; Reiter, G., Strobl, G. R., Eds.; Springer Berlin Heidelberg: Berlin, Heidelberg, 2007; pp 457-480.

(14) Steyrleuthner, R.; Schubert, M.; Howard, I.; Klaumünzer, B.; Schilling, K.; Chen, Z.; Saalfrank, P.; Laquai, F.; Facchetti, A.; Neher, D. Aggregation in a High-Mobility n-Type Low-Bandgap Copolymer with Implications on Semicrystalline Morphology. *Journal of the American Chemical Society* **2012**, *134*, 18303.

(15) Li, T.; Huang, L.; Bai, Z.; Li, X.; Liu, B.; Lu, D. Study on the forming condition and mechanism of the β conformation in poly (9,9-dioctylfluorene) solution. *Polymer* **2016**, *88*, 71.

(16) Bencheikh, F.; Duché, D.; Ruiz, C. M.; Simon, J.-J.; Escoubas, L. Study of Optical Properties and Molecular Aggregation of Conjugated Low Band Gap Copolymers: PTB7 and PTB7-Th. *The Journal of Physical Chemistry C* **2015**, *119*, 24643.

(17) Prince, R. B.; Saven, J. G.; Wolynes, P. G.; Moore, J. S. Cooperative Conformational Transitions in Phenylene Ethynylene Oligomers: Chain-Length Dependence. *Journal of the American Chemical Society* **1999**, *121*, 3114.

(18) Scharsich, C.; Lohwasser, R. H.; Sommer, M.; Asawapirom, U.; Scherf, U.; Thelakkat, M.; Neher, D.; Köhler, A. Control of aggregate formation in poly(3-hexylthiophene) by solvent, molecular weight, and synthetic method. *Journal of Polymer Science Part B: Polymer Physics* **2012**, *50*, 442.

(19) Cone, C. W.; Cheng, R. R.; Makarov, D. E.; Vanden Bout, D. A. Molecular Weight Effect on the formation of β Phase Poly(9,9′-dioctylfluorene) in Dilute Solutions. *The Journal of Physical Chemistry B* **2011**, *115*, 12380.

(20) Peet, J.; Brocker, E.; Xu, Y.; Bazan, G. C. Controlled β-Phase Formation in Poly(9,9-di-n-octylfluorene) by Processing with Alkyl Additives. *Advanced Materials* **2008**, *20*, 1882.

(21) Lee, J. K.; Ma, W. L.; Brabec, C. J.; Yuen, J.; Moon, J. S.; Kim, J. Y.; Lee, K.; Bazan, G. C.; Heeger, A. J. Processing additives for improved efficiency from bulk heterojunction solar cells. *Journal of the American Chemical Society* **2008**, *130*, 3619.

(22) Clark, J.; Chang, J.-F.; Spano, F. C.; Friend, R. H.; Silva, C. Determining exciton bandwidth and film microstructure in polythiophene films using linear absorption spectroscopy. *Applied Physics Letters* **2009**, *94*, 163306.

(23) Khan, A. L. T.; Banach, M. J.; Köhler, A. Control of β-phase formation in polyfluorene thin films via Franck–Condon analysis. *Synthetic Metals* **2003**, *139*, 905.

(24) Bright, D. W.; Dias, F. B.; Galbrecht, F.; Scherf, U.; Monkman, A. P. The Influence of Alkyl-Chain Length on Beta-Phase Formation in Polyfluorenes. *Advanced Functional Materials* **2009**, *19*, 67.

(25) Herrmann, D.; Niesar, S.; Scharsich, C.; Köhler, A.; Stutzmann, M.; Riedle, E. Role of Structural Order and Excess Energy on Ultrafast Free Charge Generation in Hybrid Polythiophene/Si Photovoltaics Probed in Real Time by Near-Infrared Broadband Transient Absorption. *Journal of the American Chemical Society* **2011**, *133*, 18220.

(26) Huang, L.; Huang, X.; Sun, G.; Gu, C.; Lu, D.; Ma, Y. Study of β phase and Chains Aggregation Degrees in Poly(9,9-dioctylfluorene) (PFO) Solution. *The Journal of Physical Chemistry C* **2012**, *116*, 7993.

(27) Knaapila, M.; Monkman, A. P. Methods for Controlling Structure and Photophysical Properties in Polyfluorene Solutions and Gels. *Advanced Materials* **2013**, *25*, 1090.

(28) Knaapila, M.; Torkkeli, M.; Galbrecht, F.; Scherf, U. Crystalline and Noncrystalline Forms of Poly(9,9-diheptylfluorene). *Macromolecules* **2013**, *46*, 836.

(29) Scherf, U.; List, E. J. W. Semiconducting Polyfluorenes—Towards Reliable Structure–Property Relationships. *Advanced Materials* **2002**, *14*, 477.

(30) Neher, D. Polyfluorene Homopolymers: Conjugated Liquid-Crystalline Polymers for Bright Blue Emission and Polarized Electroluminescence. *Macromolecular Rapid Communications* **2001**, *22*, 1365.

(31) Koch, F. P. V.; Rivnay, J.; Foster, S.; Müller, C.; Downing, J. M.; Buchaca-Domingo, E.; Westacott, P.; Yu, L.; Yuan, M.; Baklar, M.; Fei, Z.; Luscombe, C.; McLachlan, M. A.; Heeney, M.; Rumbles, G.; Silva, C.; Salleo, A.; Nelson, J.; Smith, P.; Stingelin, N. The impact of molecular weight on microstructure and charge transport in semicrystalline polymer semiconductors–poly(3-hexylthiophene), a model study. *Progress in Polymer Science* **2013**, *38*, 1978.

(32) Kline, R. J.; McGehee, M. D. Morphology and Charge Transport in Conjugated Polymers. *Journal of Macromolecular Science, Part C* **2006**, *46*, 27.

(33) Brown, P. J.; Sirringhaus, H.; Harrison, M.; Shkunov, M.; Friend, R. H. Optical spectroscopy of field-induced charge in self-organized high mobility poly(3-hexylthiophene). *Physical Review B* **2001**, *63*, 125204.

(34) Clark, J.; Silva, C.; Friend, R. H.; Spano, F. C. Role of Intermolecular Coupling in the Photophysics of Disordered Organic Semiconductors: Aggregate Emission in Regioregular Polythiophene. *Physical Review Letters* **2007**, *98*, 206406.

(35) Köhler, A.; Hoffmann, S. T.; Bässler, H. An Order–Disorder Transition in the Conjugated Polymer MEH-PPV. *Journal of the American Chemical Society* **2012**, *134*, 11594.

(36) Collison, C. J.; Rothberg, L. J.; Treemaneekarn, V.; Li, Y. Conformational Effects on the Photophysics of Conjugated Polymers: A Two Species Model for MEH–PPV Spectroscopy and Dynamics. *Macromolecules* **2001**, *34*, 2346.

(37) So, W. Y.; Hong, J.; Kim, J. J.; Sherwood, G. A.; Chacon-Madrid, K.; Werner, J. H.; Shreve, A. P.; Peteanu, L. A.; Wildeman, J. Effects of Solvent Properties on the Spectroscopy and Dynamics of Alkoxy-Substituted PPV Oligomer Aggregates. *The Journal of Physical Chemistry B* **2012**, *116*, 10504.

(38) Resta, C.; Di Pietro, S.; Majerić Elenkov, M.; Hameršak, Z.; Pescitelli, G.; Di Bari, L. Consequences of Chirality on the Aggregation Behavior of Poly[2-methoxy-5-(2′-ethylhexyloxy)-p-phenylenevinylene] (MEH-PPV). *Macromolecules* **2014**, *47*, 4847.

(39) Traiphol, R.; Charoenthai, N.; Srikhirin, T.; Kerdcharoen, T.; Osotchan, T.; Maturos, T. Chain organization and photophysics of conjugated polymer in poor solvents: Aggregates, agglomerates and collapsed coils. *Polymer* **2007**, *48*, 813.

(40) Mirzov, O.; Scheblykin, I. G. Photoluminescence spectra of a conjugated polymer: from films and solutions to single molecules. *Physical Chemistry Chemical Physics* **2006**, *8*, 5569.

(41) Unger, T.; Panzer, F.; Consani, C.; Koch, F.; Brixner, T.; Bässler, H.; Köhler, A. Ultrafast Energy Transfer between Disordered and Highly Planarized Chains of Poly[2-methoxy-5-(2-ethylhexyloxy)-1,4-phenylenevinylene] (MEH-PPV). *ACS Macro Letters* **2015**, *4*, 412.

(42) Bunz, U. H. F.; Imhof, J. M.; Bly, R. K.; Bangcuyo, C. G.; Rozanski, L.; Vanden Bout, D. A. Photophysics of Poly[p-(2,5-didodecylphenylene)ethynylene] in Thin Films. *Macromolecules* **2005**, *38*, 5892.

(43) Halkyard, C. E.; Rampey, M. E.; Kloppenburg, L.; Studer-Martinez, S. L.; Bunz, U. H. F. Evidence of Aggregate Formation for 2,5-Dialkylpoly(p-phenyleneethynylenes) in Solution and Thin Films. *Macromolecules* **1998**, *31*, 8655.

(44) Stangl, T.; Wilhelm, P.; Remmerssen, K.; Höger, S.; Vogelsang, J.; Lupton, J. M. Mesoscopic quantum emitters from deterministic aggregates of conjugated polymers. *Proceedings of the National Academy of Sciences* **2015**, *112*, E5560.

(45) Brinkmann, M. Structure and morphology control in thin films of regioregular poly(3-hexylthiophene). *Journal of Polymer Science Part B: Polymer Physics* **2011**, *49*, 1218.

(46) Pröller, S.; Liu, F.; Zhu, C.; Wang, C.; Russell, T. P.; Hexemer, A.; Müller-Buschbaum, P.; Herzig, E. M. Following the Morphology Formation In Situ in Printed Active Layers for Organic Solar Cells. *Advanced Energy Materials* **2016**, *6*, n/a.

(47) Kitts, C. C.; Vanden Bout, D. A. The effect of solvent quality on the chain morphology in solutions of poly(9,9′-dioctylfluorene). *Polymer* **2007**, *48*, 2322.

(48) Kasha, M. Energy Transfer Mechanisms and the Molecular Exciton Model for Molecular Aggregates. *Radiation Research* **1963**, *20*, 55.

(49) Kasha, M.; Rawls, H.; Ashraf El-Bayoumi, M. The exciton model in molecular spectroscopy. *Pure and Applied Chemistry* **1965**, *11*, 371.

(50) Jelley, E. E. Spectral Absorption and Fluorescence of Dyes in the Molecular State. *Nature* **1936**, *138*, 1009.

(51) Scheibe, G. Über die Veränderlichkeit der Absorptionsspektren in Lösungen und die Nebenvalenzen als ihre Ursache. *Angewandte Chemie* **1937**, *50*, 212.

(52) Gierschner, J.; Park, S. Y. Luminescent distyrylbenzenes: tailoring molecular structure and crystalline morphology. *Journal of Materials Chemistry C* **2013**, *1*, 5818.

(53) Würthner, F.; Kaiser, T. E.; Saha-Möller, C. R. J-Aggregates: From Serendipitous Discovery to Supramolecular Engineering of Functional Dye Materials. *Angewandte Chemie International Edition* **2011**, *50*, 3376.

(54) Spano, F. C. Modeling disorder in polymer aggregates: The optical spectroscopy of regioregular poly(3-hexylthiophene) thin films. *The Journal of Chemical Physics* **2005**, *122*, 234701.

(55) Yamagata, H.; Spano, F. C. Interplay between intrachain and interchain interactions in semiconducting polymer assemblies: The HJ-aggregate model. *The Journal of Chemical Physics* **2012**, *136*, 184901.

(56) Spano, F. C. The Spectral Signatures of Frenkel Polarons in H- and J-Aggregates. *Accounts of Chemical Research* **2010**, *43*, 429.

(57) Spano, F. C.; Silva, C. H- and J-Aggregate Behavior in Polymeric Semiconductors. *Annual Review of Physical Chemistry* **2014**, *65*, 477.

(58) Martin, T. P.; Wise, A. J.; Busby, E.; Gao, J.; Roehling, J. D.; Ford, M. J.; Larsen, D. S.; Moulé, A. J.; Grey, J. K. Packing Dependent Electronic Coupling in Single Poly(3-hexylthiophene) H- and J-Aggregate Nanofibers. *The Journal of Physical Chemistry B* **2013**, *117*, 4478.

(59) Baghgar, M.; Labastide, J. A.; Bokel, F.; Hayward, R. C.; Barnes, M. D. Effect of Polymer Chain Folding on the Transition from H- to J-Aggregate Behavior in P3HT Nanofibers. *The Journal of Physical Chemistry C* **2014**, *118*, 2229.

(60) Baghgar, M.; Labastide, J.; Bokel, F.; Dujovne, I.; McKenna, A.; Barnes, A. M.; Pentzer, E.; Emrick, T.; Hayward, R.; Barnes, M. D. Probing Inter- and Intrachain Exciton Coupling in Isolated Poly(3-hexylthiophene) Nanofibers: Effect of Solvation and Regioregularity. *The Journal of Physical Chemistry Letters* **2012**, *3*, 1674.

(61) Panzer, F.; Bässler, H.; Lohwasser, R.; Thelakkat, M.; Köhler, A. The Impact of Polydispersity and Molecular Weight on the Order–Disorder Transition in Poly(3-hexylthiophene). *The Journal of Physical Chemistry Letters* **2014**, *5*, 2742.

(62) Panzer, F.; Sommer, M.; Bässler, H.; Thelakkat, M.; Köhler, A. Spectroscopic Signature of Two Distinct H-Aggregate Species in Poly(3-hexylthiophene). *Macromolecules* **2015**, *48*, 1543.

(63) Scharsich, C.; Fischer, F. S. U.; Wilma, K.; Hildner, R.; Ludwigs, S.; Köhler, A. Revealing structure formation in PCPDTBT by optical spectroscopy. *Journal of Polymer Science Part B: Polymer Physics* **2015**, *53*, 1416.

(64) Reichenberger, M.; Love, J. A.; Rudnick, A.; Bagnich, S.; Panzer, F.; Stradomska, A.; Bazan, G. C.; Nguyen, T.-Q.; Köhler, A. The effect of intermolecular interaction on excited states in p – DTS(FBTTH2)2. *The Journal of Chemical Physics* **2016**, *144*, 074904.

(65) Noriega, R.; Rivnay, J.; Vandewal, K.; Koch, F. P. V.; Stingelin, N.; Smith, P.; Toney, M. F.; Salleo, A. A general relationship between disorder, aggregation and charge transport in conjugated polymers. *Nature Materials* **2013**, *12*, 1038.

(66) Spano, F. C. Modeling disorder in polymer aggregates: the optical spectroscopy of regioregular poly(3-hexylthiophene) thin films. *The Journal of Chemical Physics* **2005**, *122*, 234701.

(67) Clark, J.; Silva, C.; Friend, R. H.; Spano, F. C. Role of intermolecular coupling in the photophysics of disordered organic semiconductors: aggregate emission in regioregular polythiophene. *Physical Review Letters* **2007**, *98*, 206406.

(68) Rahimi, K.; Botiz, I.; Stingelin, N.; Kayunkid, N.; Sommer, M.; Koch, F. P. V.; Nguyen, H.; Coulembier, O.; Dubois, P.; Brinkmann, M.; Reiter, G. Controllable Processes for Generating Large Single Crystals of Poly(3-hexylthiophene). *Angewandte Chemie International Edition* **2012**, *51*, 11131.

(69) Yamagata, H.; Hestand, N. J.; Spano, F. C.; Köhler, A.; Scharsich, C.; Hoffmann, S. T.; Bässler, H. The red-phase of poly[2-methoxy-5-(2-ethylhexyloxy)-1,4-phenylenevinylene] (MEH-PPV): A disordered HJ-aggregate. *The Journal of Chemical Physics* **2013**, *139*, 114903.

(70) Shiraki, T.; Shindome, S.; Toshimitsu, F.; Fujigaya, T.; Nakashima, N. Strong main-chain length-dependence for the [small beta]-phase formation of oligofluorenes. *Polymer Chemistry* **2015**, *6*, 5103.

(71) Sanchez, I. C. Phase Transition Behavior of the Isolated Polymer Chain. *Macromolecules* **1979**, *12*, 980.

(72) Tan, R.-R.; Shen, X.; Hu, L.; Zhang, F.-S. Liquid-to-glass transition of tetrahydrofuran and 2-methyltetrahydrofuran. *Chinese Physics B* **2012**, *21*, 086402.

(73) Jaeger, G. The Ehrenfest Classification of Phase Transitions: Introduction and Evolution. *Archive for History of Exact Sciences* **1998**, *53*, 51.

(74) Jones, R. A. L.: *Soft Condensed Matter*; OUP Oxford, 2002.

(75) Swislow, G.; Sun, S.-T.; Nishio, I.; Tanaka, T. Coil-Globule Phase Transition in a Single Polystyrene Chain in Cyclohexane. *Physical Review Letters* **1980**, *44*, 796.

(76) Kolinski, A.; Skolnick, J.; Yaris, R. The collapse transition of semiflexible polymers. A Monte Carlo simulation of a model system. *The Journal of Chemical Physics* **1986**, *85*, 3585.

(77) Knaapila, M.; Bright, D. W.; Nehls, B. S.; Garamus, V. M.; Almásy, L.; Schweins, R.; Scherf, U.; Monkman, A. P. Development of Intermolecular Structure and Beta-phase of Random Poly[9,9-bis(2-ethylhexyl)fluorene]-co-(9,9-dioctylfluorene) in Methylcyclohexane. *Macromolecules* **2011**, *44*, 6453.

(78) Hoffmann, S. T.; Bässler, H.; Köhler, A. What Determines Inhomogeneous Broadening of Electronic Transitions in Conjugated Polymers? *The Journal of Physical Chemistry B* **2010**, *114*, 17037.

(79) Scherf, U.; Müllen, K. Polyarylenes and poly(arylenevinylenes), 7. A soluble ladder polymer via bridging of functionalized poly(p-phenylene)-precursors. *Die Makromolekulare Chemie, Rapid Communications* **1991**, *12*, 489.

(80) Knaapila, M.; Stepanyan, R.; Torkkeli, M.; Haase, D.; Fröhlich, N.; Helfer, A.; Forster, M.; Scherf, U. Effect of side-chain asymmetry on the intermolecular structure and order-disorder transition in alkyl-substituted polyfluorenes. *Physical Review E* **2016**, *93*, 042504.

(81) Kline, R. J.; DeLongchamp, D. M.; Fischer, D. A.; Lin, E. K.; Richter, L. J.; Chabinyc, M. L.; Toney, M. F.; Heeney, M.; McCulloch, I. Critical Role of Side-Chain Attachment Density on the Order and Device Performance of Polythiophenes. *Macromolecules* **2007**, *40*, 7960.

(82) Wu, Z.; Petzold, A.; Henze, T.; Thurn-Albrecht, T.; Lohwasser, R. H.; Sommer, M.; Thelakkat, M. Temperature and Molecular Weight Dependent Hierarchical Equilibrium Structures in Semiconducting Poly(3-hexylthiophene). *Macromolecules* **2010**, *43*, 4646.

(83) Martín, J.; Nogales, A.; Martín-González, M. The Smectic–Isotropic Transition of P3HT Determines the Formation of Nanowires or Nanotubes into Porous Templates. *Macromolecules* **2013**, *46*, 1477.

4.7. Reversible Laser Induced Amplified Spontaneous Emission from Coexisting Tetragonal and Orthorhombic Phases in Hybrid Lead Halide Perovskites

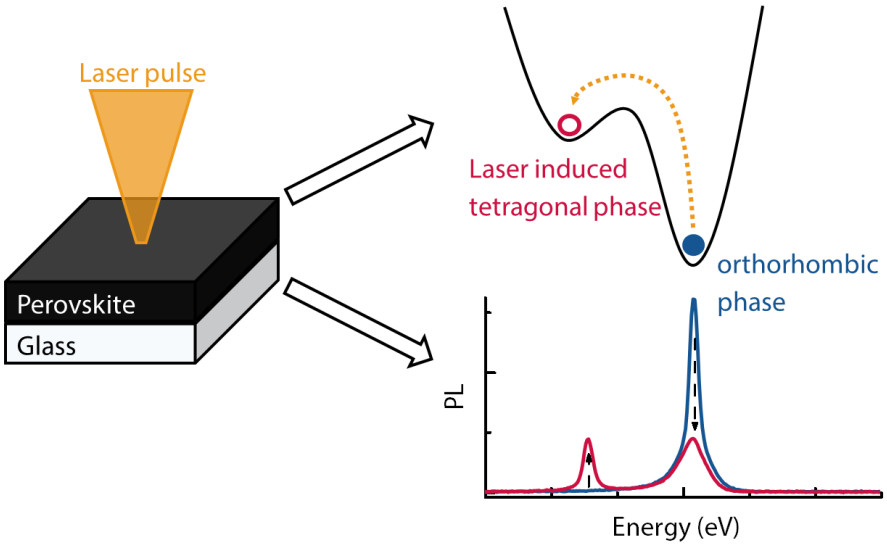

Fabian Panzer, Sebastian Baderschneider, Tanaji P. Gujar, Thomas Unger, Marius Jakoby, Sergey Bagnich, Heinz Bässler, Jürgen Köhler, Ralf Moos, Mukundan Thelakkat, Richard Hildner and Anna Köhler

Published in
Advanced Optical Materials
DOI: 10.1002/adom.201500765

ADVANCED OPTICAL MATERIALS
www.advopticalmat.de

Reversible Laser Induced Amplified Spontaneous Emission from Coexisting Tetragonal and Orthorhombic Phases in Hybrid Lead Halide Perovskites

*Fabian Panzer, Sebastian Baderschneider, Tanaji P. Gujar, Thomas Unger, Sergey Bagnich, Marius Jakoby, Heinz Bässler, Sven Hüttner, Jürgen Köhler, Ralf Moos, Mukundan Thelakkat, Richard Hildner, and Anna Köhler**

The photoluminescence in a lead halide perovskite is measured for different temperatures (5–300 K) and excitation fluences (21–1615 μJ cm^{-2}). It is found that amplified spontaneous emission (ASE) is observed for an excitation density larger than about 1×10^{18} cm^{-3} for both the tetragonal phase above 163 K and the orthorhombic phase below about 163 K. The fluence that is required to obtain this excitation density depends on temperature and phase since the nonradiative decay of excitations is temperature activated with different activation energies of 85 ± 20 and 24 ± 5 meV for the tetragonal and orthorhombic phase, respectively. The ASE from the tetragonal phase—usually prevailing at temperatures above about 163 K—can also be observed at 5 K, in addition to the ASE from the orthorhombic phase, when the sample is previously exposed to a fluence exceeding 630 μJ cm^{-2} at a photon energy of 3.68 eV. This additional ASE can be removed by mild heating to 35 K or optically, by exposing the sample by typically a few seconds with a fluence around 630 μJ cm^{-2}. The physical mechanism underlying this optically induced phase transition process is discussed. It is demonstrated that this phase change can, in principle, be used for an all-optical "write–read–erase" memory device.

1. Introduction

Organic–inorganic mixed halide perovskites received enormous attention over the last few years. They allow for the production of crystalline films with a high structural stability[1,2] and with low trap-state densities.[3] This enabled the fabrication of perovskites solar cells that convinced the solar cell community with high performances such as power conversion efficiencies of over 20%,[4,5] while offering the possibility for low cost production, e.g., by solution-processing.[6] Meanwhile, further device applications for organic–inorganic mixed halide perovskites have been discovered. For example, in 2014, low threshold levels for amplified spontaneous emission showed that mixed halide perovskites can also be used for the facile fabrication of lasers with high quality factors.[7–10] Furthermore, it is known that most halide perovskite materials can exist in different crystal structures, depending on environmental conditions such as temperature.[11–13] Here, we show that a coexistence of tetragonal and orthorhombic phases within apparently the same crystalline grain can be optically induced into the halide perovskite $CH_3NH_3PbI_3$ at low temperatures, leading to amplified spontaneous emission (ASE) simultaneously at two distinct wavelengths. The ASE feature associated with the (high temperature) tetragonal phase can be reproducibly written, read-out, and erased at 5 K by choosing appropriate

F. Panzer, T. Unger, Dr. S. Bagnich, M. Jakoby, Prof. A. Köhler
Experimental Physics II
University of Bayreuth
95440 Bayreuth, Germany
E-mail: anna.koehler@uni-bayreuth.de
F. Panzer, S. Baderschneider, T. Unger, Prof. H. Bässler, Prof. J. Köhler, Dr. R. Hildner, Prof. A. Köhler
Bayreuth Institute of Macromolecular Research (BIMF)
University of Bayreuth
95440 Bayreuth, Germany
F. Panzer, Prof. R. Moos
Department of Functional Materials
University of Bayreuth
95440 Bayreuth, Germany
S. Baderschneider, Prof. J. Köhler, Prof. R. Hildner
Experimental Physics IV
University of Bayreuth
95440 Bayreuth, Germany
Dr. T. P. Gujar, Prof. M. Thelakkat
Applied Functional Polymers
Macromolecular Chemistry I
University of Bayreuth
95440 Bayreuth, Germany
Prof. S. Hüttner
Organic and Hybrid Electronics
Macromolecular Chemistry I
University of Bayreuth
95440 Bayreuth, Germany

DOI: 10.1002/adom.201500765

laser fluences or raising the temperature. Finally, we show to which extend our findings can be exploited for use as an all optical data storage device.

The paper is structured as follows. Section 2 briefly introduces the spectral features observed in the photoluminescence spectra for excitation at low and at high fluence as a function of temperature. In Section 3 we show that ASE of the tetragonal phase—usually prevailing at temperatures above 163 K—can be observed at 5 K provided the sample was previously exposed to high intensity illumination, and this feature can be removed by mild heating or illumination at moderate intensity. We discuss the underlying physical mechanism. Section 4 demonstrates that this phenomenon could, in principle, be used toward an all-optical 2D "write–read–erase" random access memory device, though its technological exploitation is limited by the associated low (<35 K) operational temperature. Our findings are summarized in Section 5, and experimental details are detailed in Section 6.

2. Spectroscopic Characterization of the Emission

2.1. Results

We synthesized a pore free and compact crystalline $CH_3NH_3PbI_3$ layer consisting of micrometer sized grains by slightly modifying a published procedure.[14] To characterize the emission from this film, we carried out temperature dependent steady state photoluminescence (PL) measurements at different excitation fluences. Using a *low* excitation fluence of 0.75 μJ cm^{-2}, we observe the broad and featureless emission centered at about 1.60 eV at 300 K that is associated with the radiative decay of excited states in the tetragonal crystal structure (**Figure 1**a).[15,16] On cooling the sample to 140 K, a higher energy emission appears around 1.68 eV along with the existing emission at 1.57 eV. On further cooling to 40 K, the emission shifts to 1.64 eV and it dominates the spectrum. Upon excitation with a *higher* fluence of 85 μJ cm^{-2} we observe the same behavior of the broad and featureless emission bands upon cooling. However, in addition to these bands, sharp peaks emerge, and strongly grow in intensity, upon cooling (Figure 1b). Like the broad emission bands, the narrow peaks also show a red shift with decreasing temperature down to 1.61 eV at 5 K. For ease of reference, characteristic emissions obtained for low and high fluences are displayed on a linear scale in Figure 1c for a temperature of 170 and 40 K, respectively. The fluence dependence of the integrated photoluminescence intensity and of the full width at half maximum (FWHM) of the emission are displayed in **Figure 2**a,b for three different temperatures. The associated spectra are detailed in the Supporting Information (Figure S1). These data show a characteristic threshold behavior, and we find that *the lower the temperature, the lower the value of the threshold fluence*. Vice versa, for the fluence of 85 μJ cm^{-2} chosen here, the threshold temperature for the narrow peak at 1.56 eV to appear is ≈210 K in case of the "high-temperature" regime, and for the "low-temperature" range the narrow peak at 1.65 eV appears below 135 K (see Figure 2c,d).

2.2. Discussion

The hybrid perovskite $CH_3NH_3PbI_3$ is well known to undergo a transition from the tetragonal to the orthorhombic structure at about 160 K.[12,13,17] Using X-ray diffraction (XRD), we confirmed that this transition also takes place in our sample (see Figure S2, Supporting Information). At low fluence such as 0.75 μJ cm^{-2}, we thus attribute the broad emission above 160 K centered at 1.60 to 1.75 eV to emission from the tetragonal crystal structure, while the broad emission centered at 1.64–1.68 eV at temperatures below 160 K is attributed to the orthorhombic phase. The narrow, intense peaks that appear in addition upon cooling when exciting at high fluence such as 85 μJ cm^{-2} are attributed ASE.[8,18,19] We base our assignment on the observation that, at a given temperature, these peaks show a characteristic line narrowing with simultaneous increase in emission intensity as a function of excitation fluence. This is summarized in Figure 2a,b and further detailed in the Supporting Information (Figure S1). For both the tetragonal and the orthorhombic phases, the emission shows a roughly linear bathochromic shift, consistent with earlier work,[13,20] and an increasing intensity upon cooling from 300 to 150 K (tetragonal) and from 140 to 5 K (orthorhombic).

To account for the intensity dependence of the emission at low fluence, we recall that the intensity of emission is given by $I(T) = \frac{k_r}{k_r + k_{nr}} I_0$, where I_0 is the emission intensity in the absence of nonradiative decay processes, k_r and k_{nr} denote the radiative and nonradiative decay rates. We measured the temperature-dependence of the absorption at the excitation wavelength and found it to be independent of temperature (Figure S3a, Supporting Information). The Einstein coefficients then require the radiative decay rate k_r also to be temperature-independent. Thus, any temperature dependence of the emission must be attributed to k_{nr}. This applies to both the tetragonal and the orthorhombic phase. If we consider a simple thermally activated nonradiative decay process and write $k_{nr} = k_{nr}^0 e^{-\frac{E_B}{kT}}$, the temperature-dependent emission intensity becomes $I(T) = [1 + \frac{k_{nr}^0}{k_r} \exp(-\frac{E_B}{kT})]^{-1} I_0$. Fitting the experimentally obtained temperature dependent PL intensity we find activation energies E_B of 85 ± 20 and 24 ± 5 meV for the temperature-dependent nonradiative decay rate in the tetragonal and orthorhombic phase, respectively. The temperature dependence of the absorption and of the emission as well as the associated fits is shown in Figure S3 of the Supporting Information. The straight lines that are obtained in an Arrhenius-like representation, where $\ln[\frac{I(0)}{I(T)} - 1]$ is displayed as a function of inverse temperature, confirm that a thermally activated nonradiative decay process is a valid approach.

A thermally activated nonradiative decay process is also the mechanism that can account for the temperature-dependent ASE. The evolution of ASE in both phases as a function of temperature at constant higher laser fluence is remarkable, and it is consistent with the observation that the minimum fluence required to induce the ASE reduces with temperature. A prerequisite for amplified spontaneous emission is that the

Adv. Optical Mater. 2016,
DOI: 10.1002/adom.201500765

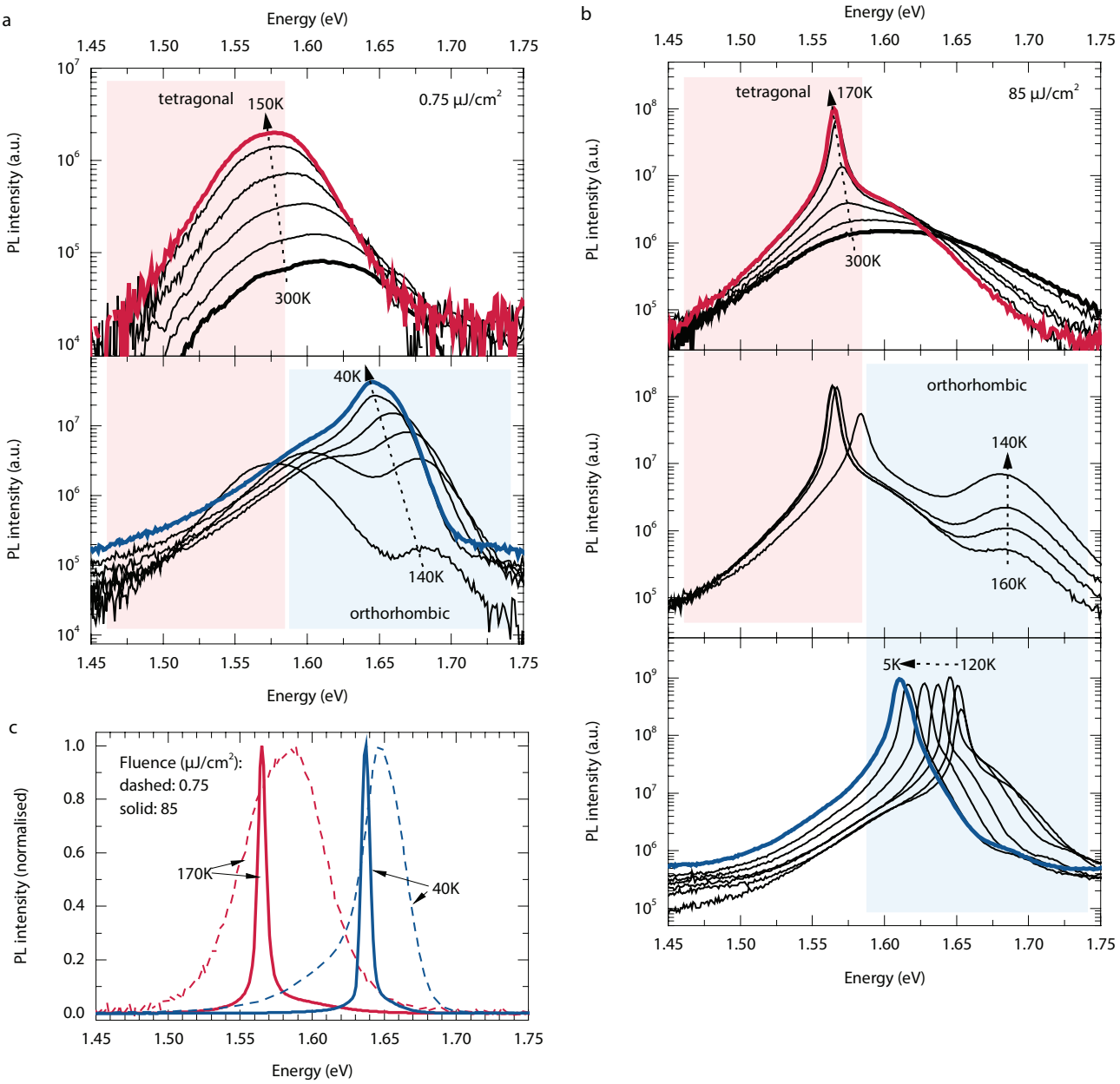

Figure 1. Temperature dependent photoluminescence (PL) spectra recorded with a) fluences of 0.75 μJ cm^{-2} and b) of 85 μJ cm^{-2}. The characteristic spectral ranges of tetragonal and orthorhombic PL are indicated by the red and blue areas, respectively. c) The characteristic PL spectra in the tetragonal phase at 170 K (red line) and in the orthorhombic phase at 40 K (blue line) for both high fluence (solid line) and low fluence (dashed line) on a linear scale.

optical gain exceeds the radiative and nonradiative losses in the medium. Thus it can only occur at a sufficiently high density of excitations. Such a density n builds up if the generation rate G, controlled by the fluence, exceeds the rates of radiative and nonradiative decay, i.e., $0 < \frac{dn}{dt} = G - (k_r + k_{nr}(T))n$. From the above-mentioned temperature-dependent absorption and photoluminescence measurements we found k_r and G to be temperature independent while k_{nr} shows a simple temperature-activated behavior with activation energies of 85 ± 20 and 24 ± 5 meV for the tetragonal and orthorhombic phases, respectively. By combining the fluence dependence and temperature dependence with the activation energy, we can *estimate the threshold exciton density n that is required for ASE* to take place in our sample. We obtain $n_{threshold}^{tetragonal} = (1.02 \pm 0.2)\ 10^{18}$ cm^{-3} for the tetragonal phase from 200 to 280 K and $n_{threshold}^{orthorhombic} = (1.4 \pm 0.2)\ 10^{18}$ cm^{-3} for the orthorhombic phase at 135 K. The fact that for both phases the threshold exciton density required for ASE is found within the same range and essentially independent of temperature is a gratifying confirmation of our approach (Figure 2e). The estimate is based on the notion that, at a certain temperature, the density of excitations, n, contributing to ASE is given by $n = n_{generated}\ \Phi = n_{generated}\ \frac{I(T)}{I_0}$, where Φ is the photoluminescence

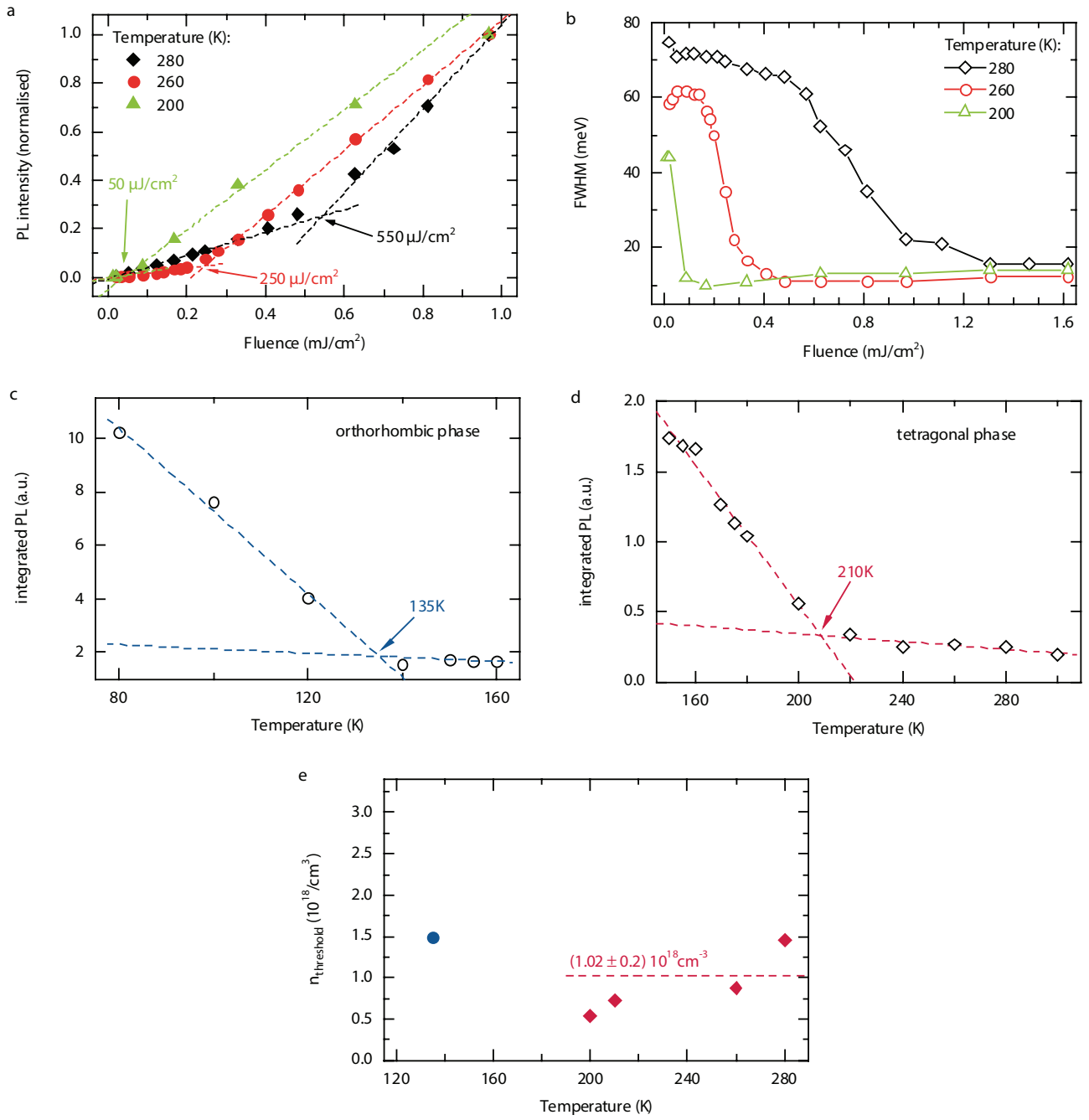

Figure 2. a) The integrated photoluminescence (PL) intensity and b) the full width at half maximum (FWHM) for excitation at 3.68 eV as a function of laser fluence from 21 to 1615 µJ cm^{-2} at 280, 260, and 200 K. c) The integrated PL intensity as a function of temperature, recorded with a laser fluence of 85 µJ cm^{-2} for the temperature range between 80 and 160 K, and d) for the temperature range between 160 and 300 K. e) The calculated values of $n_{threshold}$ as a function of temperature. The average value of $n_{threshold}$ between 280 and 200 K is indicated as dashed line. The blue circle indicates the data point obtained for the orthorhombic phase, the red diamonds pertain to data points in the tetragonal phase.

quantum yield and $n_{generated}$ is the number of excitons generated at the excitation intensity in the excitation volume. $\frac{I(T)}{I_0}$ is given by $[1+\frac{k_{nr}^0}{k_r}\exp(-\frac{E_B}{kT})]^{-1}$. $n_{generated}$ is given by the excitation energy divided by the photon energy and excitation volume. When the threshold energy for ASE is used for the excitation energy, this delivers the threshold density of excitations required for ASE. Full details of the calculation are given in the Supporting Information (Figure S4).

An essential notion in our discussion is the experimental finding that the nonradiative decay rate is thermally activated. From our data, we cannot unambiguously determine the origin of this thermally activated nonradiative decay process and its identification is not required for the analysis of our results.

Adv. Optical Mater. **2016**,
DOI: 10.1002/adom.201500765

Following the approach by Wu et al.,[15] Chen et at.,[21] and Savenije et al.,[22] one might attribute the nonradiative decay channel mainly to thermally activated dissociation of excitons and associate the activation energies with exciton binding energies. The values of 85 ± 20 and 24 ± 5 meV that we obtained for the tetragonal and orthorhombic phase are consistent with exciton binding energies reported earlier on the basis of temperature-dependent photoluminescence measurements.[15,22] We note, however, that exciton binding energies are known to vary within a rather broad range between few meV up to 70 meV,[13,15,22–27] and depend on the method chosen for investigation as well as on the particular crystal structure and composition of the hybrid perovskite.[27]

3. Reversible Induced Amplified Spontaneous Emission

3.1. Results

We observe that the emission recorded under low fluence excitation is different when the sample had previously been exposed to high fluence excitation. **Figure 3**a shows the photoluminescence taken from the sample at 5 K upon low fluence excitation at 21 μJ cm^{-2} before and after a previous exposure to 100 pulses at 15 Hz at a high fluence of 1615 μJ cm^{-2}. Even though the excitation fluence is as low as 21 μJ cm^{-2}, the emission centered at 1.61 eV at 5 K is narrow with a FWHM of 9 meV, implying that it is due to ASE from the orthorhombic phase. When the sample had previously been exposed to high fluence excitation, a second narrow low energy peak at 1.53 eV appears (FWHM of 9 meV) at the expense of intensity from the peak at 1.61 eV. The relative intensity of the two peaks can be controlled by tuning the preceding fluence. Figure 3b illustrates, on a logarithmic intensity scale, that the narrow low energy peak does not appear when previously exposing the sample to 100 pulses at 15 Hz with fluences of 168 or 329 μJ cm^{-2} and then recording the spectrum with excitation at 21 μJ cm^{-2}. When the sample is exposed to a previous pulse train with a fluence of 627 μJ cm^{-2}, the spectrum recorded under excitation at 21 μJ cm^{-2} shows a weak shoulder to appear at about 1.54 eV. For previous exposure to a pulse train with a fluence of 968, 1304 or 1615 μJ cm^{-2}, the spectra obtained with excitation at 21 μJ cm^{-2} clearly show a narrow low energy peak, centered at 1.530, 1.523, and 1.522 eV, respectively. While the intensity of the 1.61 eV peak is not affected by previous exposure at fluences of 168 or 329 μJ cm^{-2}, it reduces for previous exposure to fluences from 627 μJ cm^{-2} onward, whereas the intensity of the low energy shoulder or peak increases.

This narrow low energy peak that can be induced by previous exposure to fluences above 627 μJ cm^{-2} appears to be

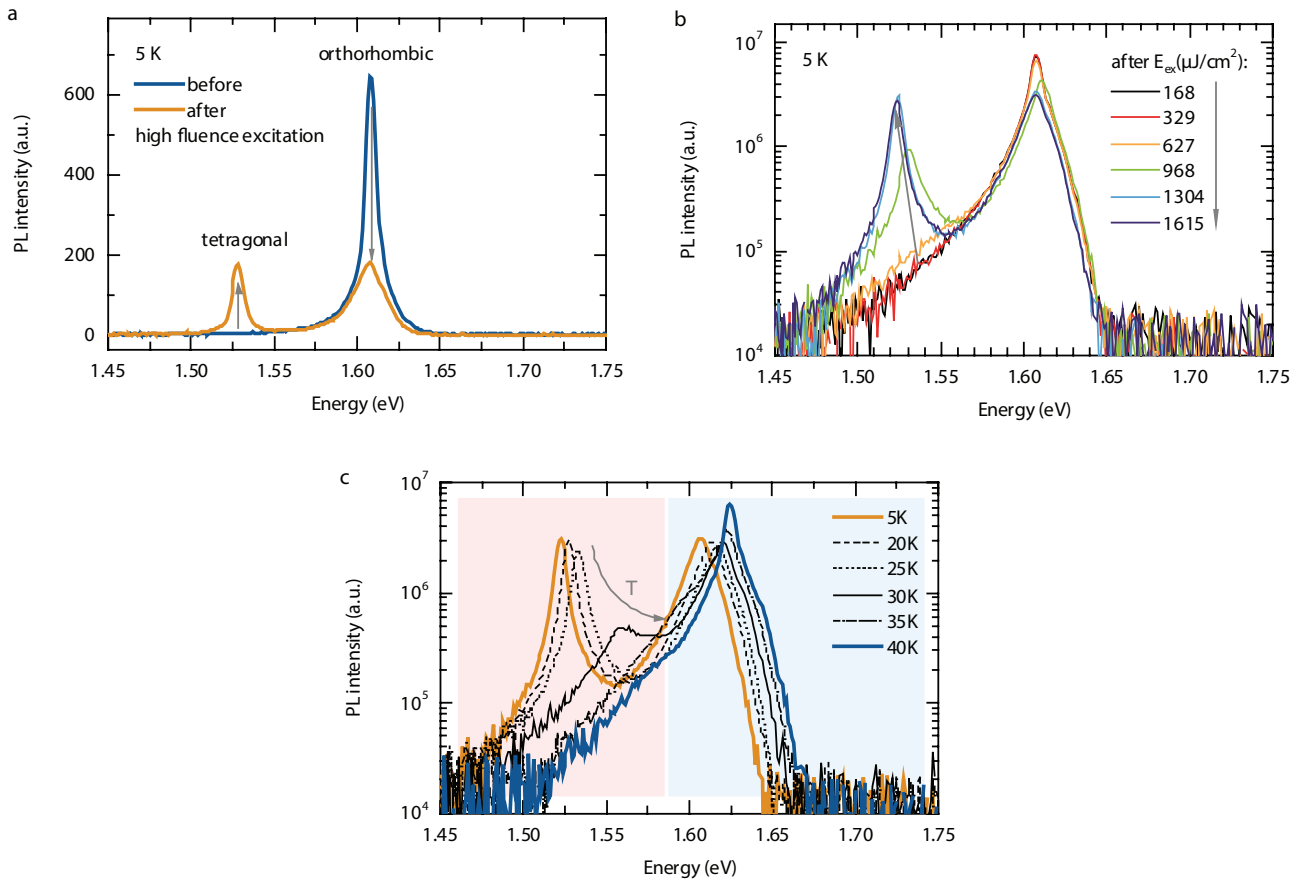

Figure 3. a) The emission spectrum of perovskite film at 5 K before (blue line) and after (orange line) high fluence (1615 μJ cm^{-2}) excitation, recorded with a fluence of 21 μJ cm^{-2}. b) Emission spectra recorded at low-excitation fluence (21 μJ cm^{-2}) after exposure to different high-fluence excitation. c) PL spectra for increasing temperatures, recorded with a fluence of 21 μJ cm^{-2} after previous exposure to 1615 μJ cm^{-2}.

stable with time when recorded using an excitation fluence of 21 μJ cm^{-2}. We observed no change in intensity in the course of our measurements. This is displayed in Figure S5 of the Supporting Information for a time scale of 30 min. Although the induced peak is stable with respect to time when recorded under low fluence, it is not stable with respect to temperature. Figure 3c shows that upon heating the sample from 5 K onward, the narrow low energy peak reduces in intensity and, concomitantly, shifts to higher energies. For temperatures above 35 K it disappears. Modeling the reduction in the low energy peak as a thermally activated process, using $\frac{\Delta I}{I_0} = e^{\frac{-\Delta E}{k_B T}}$, with ΔI being the change of emission intensity of the tetragonal phase relative to its maximum intensity I_0 at 5 K, yields a thermal activation energy of $\Delta E = 3$ meV for the removal of the narrow low energy peak.

In order to understand how exposure to high fluence may induce a remaining narrow low energy peak, it is instructive to consider the PL spectra recorded *during* exposure to high fluence. **Figure 4**a shows the emission spectra recorded for, first, exposure to a pulse train of 100 pulses at 15 Hz at a fluence of 329 μJ cm^{-2} (dashed line) and then recorded for exposure to the same pulse train at a fluence of 1615 μJ cm^{-2} (solid line). For reference, a Gaussian peak centered on 1.53 eV with a FWHM of 9 meV is also shown. Note that the spectra are displayed on a logarithmic intensity scale. In addition to the emission centered on 1.61 eV that is attributed to ASE from the orthorhombic phase, the spectrum recorded under a fluence of 1615 μJ cm^{-2} shows an emission band of unusual shape that ranges from about 1.58 to 1.53 eV, where its emission intensity falls off drastically. This low energy edge of the band perfectly matches the Gaussian peak centered on 1.53 eV with a FWHM of 9 meV. Figure 4b displays the spectra that result when the sample was *first* exposed to a pulse train of 100 pulses at 15 Hz at a fluence of 1615 μJ cm^{-2} and *then* recorded using a *single pulse* of increasing fluences from 168 μJ cm^{-2} onward. It is evident that the low energy edge of the additional band remains identical in all spectra, whereas the high energy edge of the band increases in energy with increasing fluence. The position of the maximum intensity in the band, close to the high energy edge, is displayed in Figure 4c as a function of fluence.

Further insight into the origin of the low energy band observed *during* high fluence excitation, and, concomitantly, the low energy peak seen *after* high fluence excitation can be

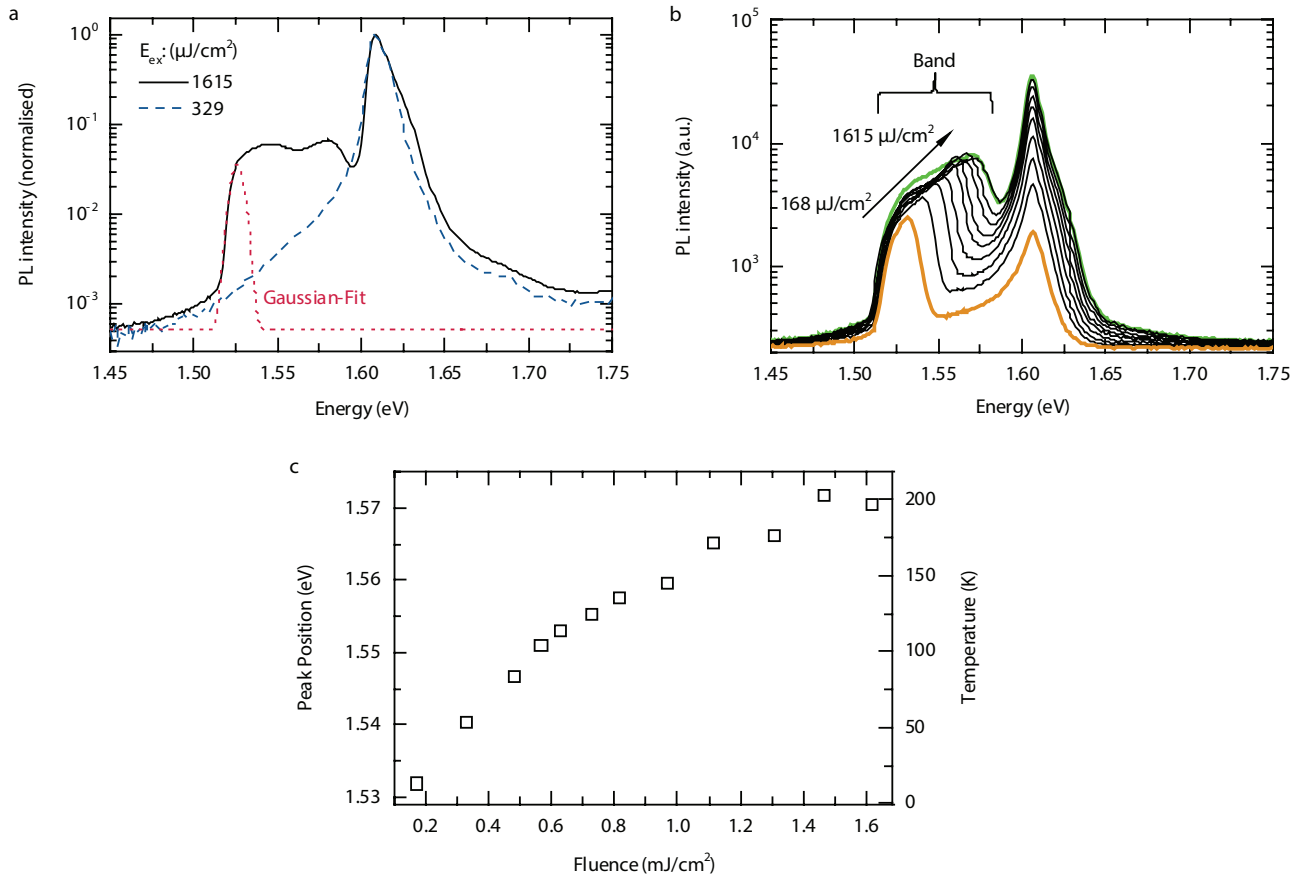

Figure 4. a) Emission spectra at 5 K recorded first using a low excitation fluence of 329 μJ cm^{-2} (dashed blue line) and then using a high excitation fluence of 1615 μJ cm^{-2} (solid black line). The red dotted line indicates a Gaussian peak with a full width at half maximum of 9 meV, corresponding to the value for the 5 K ASE of the tetragonal peak. b) Emission recorded with different high fluence excitation as indicated in the figure, after the sample was previously excited by a pulse train with fluences of 1615 μJ cm^{-2}. c) Energetic peak position of the peak in the lower energy band of (b), as a function of fluence. For ease of reference, the right axis shows the temperature associated with the peak position, taken from the dashed black line in Figure 6b below.

Adv. Optical Mater. **2016**,
DOI: 10.1002/adom.201500765

gained from time-resolved PL spectra (**Figure 5**). In Figure 5a, a film at 5 K had first been exposed to an excitation fluence of 1615 μJ cm^{-2}. After that, its emission was recorded at 5 K as a function of time for excitation at a fluence of 630 μJ cm^{-2} with 15 Hz. The top panel shows the resulting emission spectra on a linear scale at 0.1, 1.0, and 3.5 s after excitation. For all three spectra, the ASE peak of the orthorhombic phase at 1.61 eV is clearly visible. In addition, there is a low energy emission band with a peak that shifts from 1.55 eV to higher energies with increasing time. From about 1.0 s onward, it reduces in intensity while the 1.61 eV peak increases. This is displayed more clearly in the right panel. Similar spectra have been taken for a range of recording fluences, in each case after a previous exposure to a pulse train at 1615 μJ cm^{-2}. The peak position of the low energy band as a function of time is shown in Figure 5b for the different recording fluences. We observe two trends. First, the initial position of the low energy peak is at higher energies for higher fluences. Second, with increasing recording fluence the blue shift in peak position with time increases. While the low energy peak remains essentially constant at about 1.532 eV upon recording at 168 μJ cm^{-2}, it shifts by about 20 meV to higher energies within less than a second when recording the spectra at 810 μJ cm^{-2}.

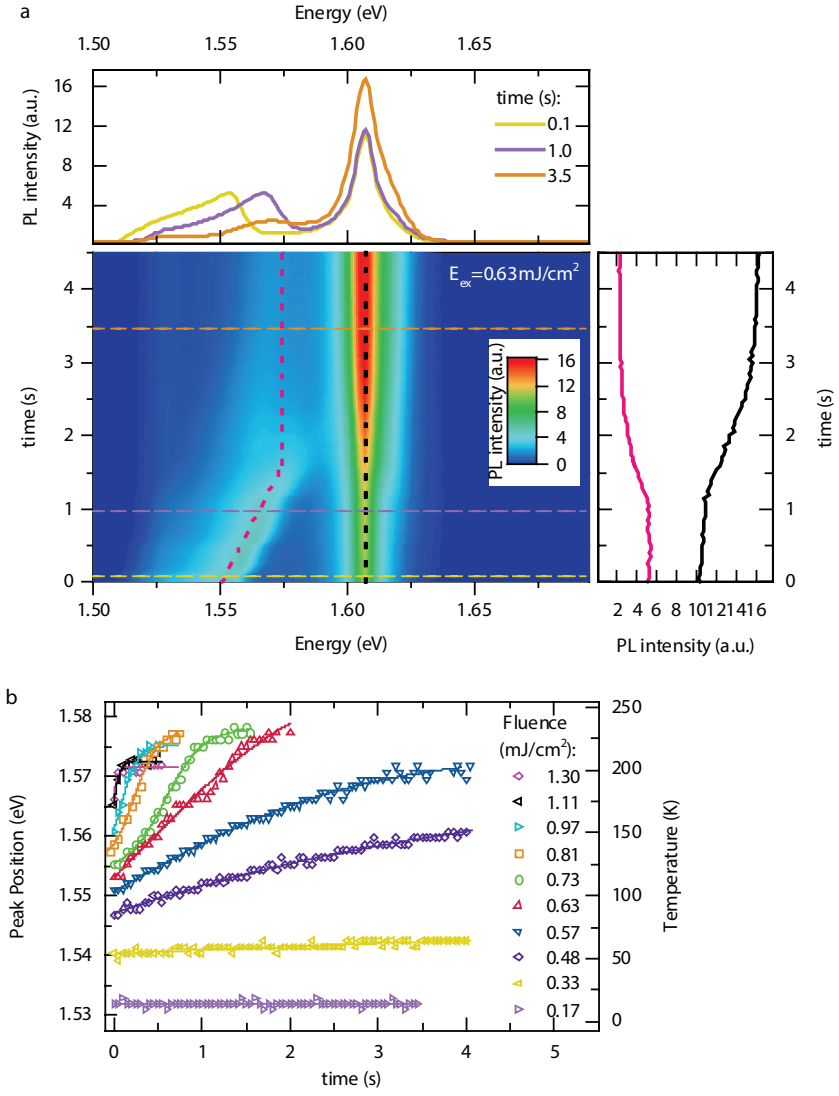

Figure 5. a) Emission spectra taken during illumination with a fluence of 630 μJ cm^{-2} as a function of time. The spectra are recorded immediately after the start of excitation. The film had previously been illuminated with high fluence of 1615 μJ cm^{-2}. The color indicates the photoluminescence intensity. The top panel shows the spectra on a linear scale, obtained after a time of 0.1 s (yellow line), 1.0 s (purple line), and 3.5 s (orange line). The right panel shows the PL intensity of the peak at 1.61 eV (black line), attributed to the orthorhombic phase, and of the peak in the low energy band (pink line), attributed to the tetragonal phase, as a function of time. Dashed lines in the central panel indicate these positions. b) The time-dependent evolution of the ASE peak in the tetragonal phase taken during illumination with a fluence as indicated in the figure. The sample had previously been illuminated with a high fluence of 1615 μJ cm^{-2}.

3.2. Discussion

The observation that a narrow low energy peak can be induced in a hybrid lead iodide perovskite by previous illumination at sufficiently high fluences, and that it can be removed by raising the temperature of the sample in a moderate way (Figure 3) raises some questions. First, it needs to be clarified what the narrow low energy emission is due to. Second, the process of how it forms and disappears for various experimental conditions (Figures 4 and 5) should be illuminated.

Various works have shown that the emission spectra of hybrid lead iodide perovskites can consist of different spectral features at low temperatures.[8,15,16,28,29] Xing et al.,[8] Fang et al.,[16] and Kong et al.[28] attribute the additional emission features they found in addition to the free exciton emission of the orthorhombic phase to the transition of bound excitons. Their feature is typically at about 40 meV below the energy of the free exciton transition and it has a spectral width in the range of 50 meV with PL lifetimes in the μs range.[16] In contrast to this, the low energy peak we observe, for example, in Figure 3a at 1.53 eV, is separated by about 80 meV from the emission feature of the orthorhombic phase and shows a FWHM of 9 meV. Time resolved PL measurements at low temperature using a STREAK Camera Setup further reveals, that the induced emission feature decays on a ns timescale (see Figure S6, Supporting Information). Due to these differences in spectral signature and dynamics we dismiss emission from the bound excitons as a possible explanation for the low energy peak. In a similar way, we also discard emission from trap states as a possible origin. Trap states were found to show a broadly distributed emission over a spectral range between approximately 1.3 and 1.5 eV, in contrast to the narrow emission we observe.[30] As will be shown in Section 4 further below, the narrow low energy

peak is highly reproducible and reversible, so that any permanent damage to the sample such as a decomposition of the organic cation can be excluded. An indication to the origin of the low energy peak is its narrow spectral width, e.g., of 9 meV at 1.53 eV (Figure 3a). This is in good agreement with the linewidth of about 10–15 meV that we found for the ASE peak from the tetragonal phase as shown in Figures 2b. In fact, the energies at which the laser-induced narrow low energy peak is observed matches with the energies where ASE from excitations in the tetragonal phase could be expected at low temperatures, provided that a linear extrapolation of the temperature dependence of the ASE peaks is valid as a first rough approximation. **Figure 6**b shows the temperature evolution of the ASE peaks in the orthorhombic and tetragonal phases, taken from Figure 1, along with the energies of the laser induced narrow low energy peak taken from Figure 3. Based on the narrow linewidth and energetic position we attribute the low energy emission to ASE from the tetragonal phase.

This assignment raises further questions. First of all, it is unexpected to observe a coexistence of peaks from the orthogonal and tetragonal phase below 40 K. Naively, one would expect energy transfer from the higher-energy peak to the induced lower-energy peak to suppress any emission from the orthorhombic phase. Evidently, the experimental data suggest that complete energy transfer does not occur, implying a somewhat localized character of the fast decaying excitations. Second, it is equally unexpected to observe emission from a *tetragonal* phase at temperatures as low as 5 K, since this phase is known to be the stable phase only above 160 K.

To account for the laser-induced existence of a tetragonal phase at low temperatures such as 5 K, we propose the following: *Local heating during excitation with high fluence induces a partial modification of the crystal structure toward the tetragonal phase.* This structure is then kinetically frozen in when the high intensity laser is turned off, thus leading to tetragonal inclusions in an orthorhombic matrix. Indeed, a simple estimate of the local heating effects during excitation indicates that a temperature above 163 K is reached for laser fluences above approximately 600 µJ cm^{-2}. This is in good agreement with the observation that a threshold fluence above about 630 µJ cm^{-2} is required to induce the 1.53 eV peak (see Figure 3b). Furthermore, based on the heat capacities and thermal conductivities of the lead halide perovskite and the supporting quartz substrate,[31] a fast drop of temperature back to 5 K can be expected on a timescale of a few 100 ns. The estimates for laser-induced heating and thermal dissipation of heat are detailed in the Supporting Information. Thus, the scenario of a remaining, kinetically frozen out tetragonal phase within an orthorhombic matrix is consistent with the material parameters. This hypothesis is illustrated in Figure 6a. Since the orthorhombic phase prevails at 5 K while the tetragonal phase is observed from 163 K onward, we consider that the two phases, pertaining to different configuration coordinates, are separated by an associated thermal activation energy of 163 K*k_B = 14 meV for the orthorhombic-to-tetragonal phase transition. From the analysis of Figure 3b we learned that a small activation energy of 3 meV is sufficient to convert the tetragonal phase back to the orthorhombic phase. This small activation energy for overcoming the barrier to the energetically more stable orthorhombic phase is reasonable given that the structural difference between the tetragonal and orthorhombic phase are only minor (lattice parameters: $a = c = 8.65$ Å, $b = 12.45$ Å at 155 K – tetragonal; $a = 8.90$ Å, $b = 12.67$ Å, $c = 8.65$ Å at 150 K – orthorhombic).[11] This picture also explains why coexisting emission from the tetragonal and orthorhombic phase has so far been reported only close to the temperature of the phase transition (≈160 K).[28]

Our hypothesis of local laser-induced heating is also consistent with the peculiar photoluminescence spectrum that is obtained *during* the high fluence (1615 µJ cm^{-2}) illumination, shown in Figure 4a. In this framework, we attribute the broad emission band to a superposition of ASEs from the tetragonal phase. Since the overall sample is held at 5 K, yet illumination with 1615 µJ cm^{-2} induces a local temperature well above 163 K, we expect a temperature gradient across the Gaussian excitation profile, resulting in ASEs from tetragonal phases with a temperature distribution. From the already obtained correlation

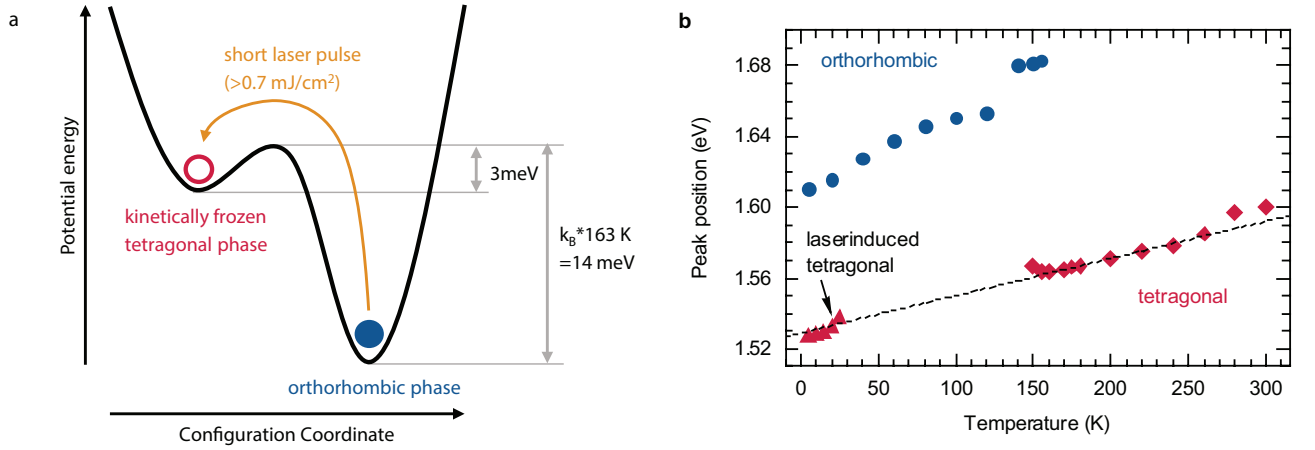

Figure 6. a) Schematic illustrating how illumination by an intense laser pulse can induce the formation of a metastable trapped tetragonal phase. b) The positions of the ASE peaks in the orthorhombic (blue dots) and in the tetragonal phase (red diamonds) as a function of temperature, recorded with a fluence of 85 µJ cm^{-2}. The dashed line indicates a linear interpolation of the peak position for the tetragonal phase. Red triangles indicate peak positions of ASE due to the tetragonal phase below 35 K that has been induced using previous illumination with a high fluence of 1615 µJ cm^{-2}.

Adv. Optical Mater. **2016**,
DOI: 10.1002/adom.201500765

between temperature and peak position of the ASE from the tetragonal phase (Figure 6b), the spectral positions can directly be transferred to corresponding temperatures. It is a gratifying consistency that the range of the band from 1.52 to 1.58 eV matches with a temperature range from 5 to 210 K.

This is further supported by Figure 4b. We consider that the preceding pulse train with 1615 μJ cm^{-2} induces the transition to the tetragonal phase that is then kinetically frozen in. For subsequent illumination with a low fluence pulse of 21 μJ cm^{-2}, we obtain the spectrum of ASE in the tetragonal phase at 5 K, i.e., a peak at 1.53 eV. Upon raising the fluence of the recording pulse from 168 μJ cm^{-2} onward, the center of the excitation spot raises in temperature, implying a temperature gradient to the border of the excitation spot. Consequently, the high energy tail of the band shifts to increasingly higher energies with temperature, while the low energy edge at 1.53 eV remains.

The energetic position of the high energy edge of the band in Figure 4b is displayed at the time $t = 0$ in Figure 5b. The shift that is observed in Figure 5 in the course of time when the spectrum is recorded during continuous illumination with 15 Hz at different fluences can easily be accounted for in our interpretation in a framework of local heating. It seems that for illumination with a low fluence, such as 168 μJ cm^{-2}, the heat deposited into the excitation spot with each pulse is dissipated sufficiently rapid so that both the temperature of the excited spot as well as that of the surrounding material at 5 K remain unaltered. For a higher fluence, e.g., 630 μJ cm^{-2}, the blue-shift of high-energy edge of the band within the first second indicates ASE from a tetragonal phase with an increasingly hot center, while the temperature surrounding the excitation spot is still sufficiently cold, i.e., below 35 K, to prevent an annealing of kinetically trapped tetragonal phase. This is also confirmed by the unaltered intensity of the ASE peak of the orthogonal phase at 1.61 eV. After about one second, a stationary position of the high energy edge in the ASE band from the tetragonal phase indicates a stationary equilibrium between the heat deposited into the excitation spot and the heat dissipated into the surrounding material, i.e., perovskite and substrate. Ultimately, this also raises the temperature of the material around the excitation spot beyond the 35 K limit, thus allowing for detrapping of the kinetically trapped tetragonal-to-orthorhombic phase transition. Accordingly, this is accompanied by an increase in the intensity of the ASE from the orthogonal phase at 1.61 eV.

The fact that the phase transitions between tetragonal and orthorhombic phase can be induced and removed by suitable adjusting the fluence of the laser illumination implies that lead halide perovskites could, in principle, be used to build an all-optical "random-access memory device."

4. All Optical Write–Read–Erase Cycles

4.1. Results

Figure 7 shows a simple proof-of-principle demonstration for such an all-optical memory device. As indicated in the top panel, the sample was illuminated with consecutive trains of 100 pulses at 15 Hz at, first, 1615 μJ cm^{-2} (the "write" process), then 21 μJ cm^{-2} (the "read" process), then 811 μJ cm^{-2} (the "erase" process) and finally again 21 μJ cm^{-2} (the "write" process). The intensities of the ASE peaks from the orthorhombic phase at 1.61 eV and of the tetragonal phase at 1.53 eV, recorded during the "read" process, are displayed in the bottom panel of Figure 7. The reproducibility of the process is clearly evident (see also Figure S5b, Supporting Information). After each "write" process, the intensities of the two ASE peaks are comparable, and after each "erase" process, the orthorhombic ASE peak takes a maximum value while the tetragonal ASE peak almost disappears. Due to the apparently localized character of the excitations associated with the ASE peaks, data writing and reading (i.e., a strong tetragonal ASE peak) can be implemented in a two-dimensional fashion.

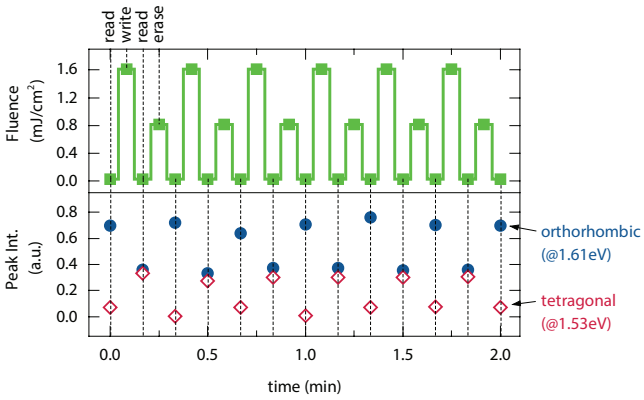

Figure 7. (Lower panel) Peak intensities at 5 K of the ASE at 1.61 eV (blue dots) in the orthorhombic phase and of the ASE at 1.53 eV (red diamonds), attributed to the tetragonal phase. The peak intensities were recorded using a fluence of 21 μJ cm^{-2} (= "read" mode) after previous illumination with pulses at a fluence of 1615 μJ cm^{-2} (= "write" mode) or at 811 μJ cm^{-2} (= "erase" mode) as illustrated in the upper panel.

The reproducibility of the "write" and "erase" processes is also manifested on a microscopic scale. **Figure 8** shows 2D intensity maps of the emission spectra for a 5 μm × 5 μm area of the film that was acquired at 1.5 K using a home-built confocal microscope with a spatial resolution of about 500 nm. The color scale decodes overall emission intensity that is spectrally integrated from 1.3 to 1.7 eV. The PL spectra, averaged over the entire 5 μm × 5 μm area for Figure 8a,c, and averaged over two smaller, 0.3 μm × 0.3 μm areas for Figure 8b, are shown in the bottom panels. In a pristine sample, only the 1.61 eV peak for the ASE of the orthorhombic phase is observed, though its intensity strongly varies across this area, as also observed by de Quilettes et al.[32] The size of the bright and darker regions in the film matches well with the grain size distribution found by transmission electron microscopy (0.2–1.2 μm), see Figure S7 in the Supporting Information.

After a "write" process, we observe first a change in intensity distribution across the sample area. Second, we observe that the additional 1.53 eV peak, indicative of a tetragonal crystal structure, has been induced everywhere across the investigated area (Figure 8b), albeit to different degrees. This observation suggests that both phases coexist within the same crystalline grain. Sample areas which have lower overall emission intensity have a higher relative contribution from the 1.53 eV peak. After an "erase" process, the original intensity distribution recovers and

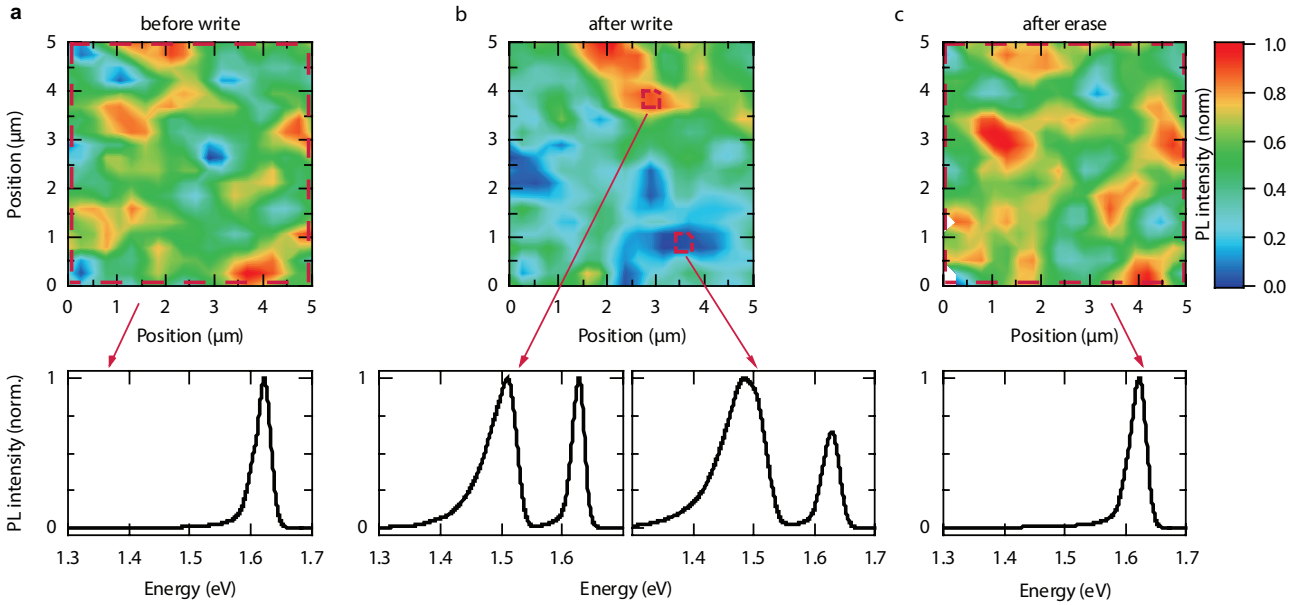

Figure 8. Spatially resolved emission map of the perovskite film at 1.5 K. a) 5×5 μm² area of the film before writing. The spectrally integrated PL intensity is color-coded (top panel). The PL spectrum averaged over the entire 5×5 μm² area demonstrates the presence of only the orthorhombic phase (bottom panel). b) The same 5×5 μm² area as in (a) after exposure to a high-fluence writing pulse (top panel). Two representative spectra acquired in the red boxed regions are depicted in the two bottom panels, indicating the presence of both the tetragonal as well as the orthorhombic phase all over the film. c) Same area after applying an erase pulse train (top panel) together with the PL spectrum integrated over the entire area (bottom panel), which shows that only the orthorhombic phase prevails.

we again observe merely emission at 1.61 eV across the entire sample area.

4.2. Discussion

The write–read–erase cycles shown in Figure 7 clearly demonstrate that, in principle, the phase transition in the lead halide perovskite could be used for "all optical random-access-memory" applications, using the induced tetragonal ASE peak as information carrier. The fluences used in Figure 7 for the "read" and for the "erase" process were chosen such as to ensure that the sample is not affected by the laser fluence during the "read" process, and to allow for a reasonably fast "erase" process. The "write" and the "read" process can be carried out in single shot mode, so that the time required for these processes is only limited by the pulse width of the laser and its repetition rate (see Figure S8, Supporting Information). The "erase" process, in contrast, requires sample heating above 35 K in an area surrounding the spot size. In the present mode of operation, this is achieved by controlling the balance of dose accumulation and heat dissipation. The initial laser energy is deposited in the excitation area through optical absorption followed by subsequent vibrational cooling, and the resulting heat flow into the surrounding material generates a temperature gradient. The "erase" process, i.e., the tetragonal-to-orthorhombic transition occurs for the sample area where the temperature is above 35 K yet below 160 K. An "erase" process with high fluence generates a strong temperature gradient across the excitation spot, so that the relevant temperature range is reached after a short accumulation time, yet only for a small circumference around the hotter center, leading to only partial "erase" of the 1.53 eV peak. A more complete "erase" process, requiring a shallower temperature gradient, can be obtained by using a moderate fluence over a longer period of time. This trade-off explains why, in this mode of optical excitation with visible light, a single-shot "erase" process is not possible. The situation may be different for excitation with light in the infra-red spectral range. An interesting feature is the option to "write" and "read" in a 2D fashion. The entire area could, in principle, be "written in" in parallel by using patterning and be "read out" by full size illumination combined with a charge-coupled device (CCD) camera, thus allowing for fast data access.

5. Concluding Summary

We have shown that for this lead halide perovskite amplified spontaneous emission occurs for an excitation density exceeding 1×10^{18} cm^{-3}. Whether this excitation density can be sustained depends on the balance between excitation fluence and sample temperature. At temperatures below the tetragonal-to-orthorhombic phase transition temperature of 163 K, high intensity laser pulses can locally heat the excitation spot thus resulting in a local orthorhombic-to-tetragonal phase transition that can get trapped kinetically if the surrounding material is at a temperature below 35 K. Detrapping is possible by mild heating above 35 K. This temperature can also be reached in the material surrounding the excitation spot by suitably adjusting the illumination fluence and time. In principle, this phase change could be employed to make an all optical

Adv. Optical Mater. **2016**,
DOI: 10.1002/adom.201500765

write–read–erase memory device, yet in practice the low temperature associated with the phase change limits its potential.

6. Experimental Section

Materials: All materials were purchased from Sigma-Aldrich and used as received.

CH_3NH_3I Synthesis: Methylammonium iodide (MAI) was synthesized as discussed elsewhere.[33] In short, MAI was synthesized by reacting 24 mL of methylamine (33 wt% in absolute ethanol) and 10 mL of hydroiodic acid (57 wt% in water) in a round-bottom flask at 0 °C for 2 h with stirring. The precipitate was recovered by putting the solution on a rotary evaporator and carefully removing the solvents at 50 °C. The white raw product MAI was redissolved in 80 mL absolute ethanol and precipitated with the addition diethyl ether. After filtration, the step was repeated two times and white solid was collected and dried at 60 °C in a vacuum oven for 24 h.

$CH_3NH_3PbI_3$ Film Preparation: The quartz substrates were cleaned with detergent diluted in deionized water, rinsed with deionized water, acetone, and ethanol, and dried with clean dry air. After cleaning, the substrates were transferred in a glovebox under nitrogen atmosphere. For perovskite formation, PbI_2 (1 M) was dissolved in *N*,*N*-dimethyl formamide overnight under stirring conditions at 100 °C and 80 µL solution was spin coated on the quartz substrates at 2000 rpm for 50 s, and dried at 100 °C for 5 min. Powder of MAI (100 mg) was spread out around the PbI_2 coated substrates with a petri dish covering on the top and heated at 165 °C for 13 h. To avoid that the samples were affected by air and humidity, 40 mg mL^{-1} poly(methylmethacrylate) (PMMA; Aldrich) in butyl acetate was spin-coated on top of the perovskite at 2000 rpm for 30 s. All steps were carried out under a nitrogen atmosphere in a glove box. See Figure S7 of the Supporting Information for morphology of the perovskite film showing the micrometer sized crystalline grains.

Temperature Dependent Emission Measurements: Emission spectra were recorded with a home-built setup. For cooling, the sample was put into a continuous flow cryostat (Oxford Instruments, Optistat CF) and excited by a Nitrogen Laser (LTB, MNL 100) with 337 nm pulses and a repetition rate of 15 Hz. Changes in the laser output energy were achieved by a controllable polarization attenuator, which led to available fluences in the range between 0.75 and 1615 µL cm^{-2}. The generated laser pulses were coupled into an optical fibre and directed toward the sample while being refocused by a lens. Emission from the sample was collected by another lens, focused to a spectrograph (Andor Shamrock 303i, spectral resolution ≈2 nm) which was coupled with a cooled CCD camera (Andor iDus), acting as the detection unit. Measured spectra were corrected for CCD and grating responsivity.

Spatially Resolved Emission Measurements: For the spatially resolved PL spectroscopy, we used a home-built low-temperature confocal microscope. The sample is mounted in a liquid-helium bath cryostat at 1.5 K. To read out the ASE from the perovskite films, we used a diode laser (BCL-020-405, CrystaLaser) operating at 405 nm. This laser light was directed to the cryostat, and focused by a microscope objective (NA = 0.85, Microthek) that was immersed in liquid helium. The combination of a motorized scan mirror and a telecentric lens system in front of the objective allowed to move the focal spot laterally across the sample in well-defined steps. The PL was collected by the same objective and passed the beam splitter and dielectric long pass filters to suppress residual laser light. Finally, it was focussed onto the entrance slit of a spectrograph (SpectraPro-150, Acton Research Corporation), spectrally dispersed by a grating (150 lines mm^{-1}), and imaged onto a CCD-camera (Pixelfly, PCO).

Supporting Information

The Supporting Information is available from the Wiley Online Library or from the author.

Acknowledgements

The authors acknowledge financial support by the Bavarian State Ministry of Science, Research, and the Arts through the Collaborative Research Network "Solar Technologies go Hybrid" and by the German Science Foundation DFG through the research training group GRK1640 and SFB 840. R.H. and S.B. acknowledge additional funding from DFG within project HI1508/2. The authors thank Cheng Li for stimulating discussions and Konstantin Schötz and Anna Gräser for the help with the setups.

Received: December 20, 2015
Revised: February 1, 2016
Published online:

[1] H. S. Kim, C. R. Lee, J. H. Im, K. B. Lee, T. Moehl, A. Marchioro, S. J. Moon, R. Humphry-Baker, J. H. Yum, J. E. Moser, M. Grätzel, N. G. Park, *Sci. Rep.* **2012**, *2*, 591.
[2] J. Burschka, N. Pellet, S. J. Moon, R. Humphry-Baker, P. Gao, M. K. Nazeeruddin, M. Grätzel, *Nature* **2013**, *499*, 316.
[3] D. Shi, V. Adinolfi, R. Comin, M. Yuan, E. Alarousu, A. Buin, Y. Chen, S. Hoogland, A. Rothenberger, K. Katsiev, Y. Losovyj, X. Zhang, P. A. Dowben, O. F. Mohammed, E. H. Sargent, O. M. Bakr, *Science* **2015**, *347*, 519.
[4] NREL Solar efficiency chart, http://www.nrel.gov/ncpv/images/efficiency_chart.jpg (accessed: September **2015**).
[5] W. S. Yang, J. H. Noh, N. J. Jeon, Y. C. Kim, S. Ryu, J. Seo, S. I. Seok, *Science* **2015**, *348*, 1234.
[6] W. Nie, H. Tsai, R. Asadpour, J.-C. Blancon, A. J. Neukirch, G. Gupta, J. J. Crochet, M. Chhowalla, S. Tretiak, M. A. Alam, H.-L. Wang, A. D. Mohite, *Science* **2015**, *347*, 522.
[7] H. Zhu, Y. Fu, F. Meng, X. Wu, Z. Gong, Q. Ding, M. V. Gustafsson, M. T. Trinh, S. Jin, X. Y. Zhu, *Nat. Mater.* **2015**, *14*, 636.
[8] G. Xing, N. Mathews, S. S. Lim, N. Yantara, X. Liu, D. Sabba, M. Gratzel, S. Mhaisalkar, T. C. Sum, *Nat. Mater.* **2014**, *13*, 476.
[9] F. Deschler, M. Price, S. Pathak, L. E. Klintberg, D.-D. Jarausch, R. Higler, S. Hüttner, T. Leijtens, S. D. Stranks, H. J. Snaith, M. Atatüre, R. T. Phillips, R. H. Friend, *J. Phys. Chem. Lett.* **2014**, *5*, 1421.
[10] F. Laquai, *Nat. Mater.* **2014**, *13*, 429.
[11] T. Baikie, Y. Fang, J. M. Kadro, M. Schreyer, F. Wei, S. G. Mhaisalkar, M. Graetzel, T. J. White, *J. Mater. Chem. A* **2013**, *1*, 5628.
[12] C. C. Stoumpos, C. D. Malliakas, M. G. Kanatzidis, *Inorg. Chem.* **2013**, *52*, 9019.
[13] V. D'Innocenzo, G. Grancini, M. J. Alcocer, A. R. Kandada, S. D. Stranks, M. M. Lee, G. Lanzani, H. J. Snaith, A. Petrozza, *Nat. Commun.* **2014**, *5*, 3586.
[14] H. Zhou, Q. Chen, G. Li, S. Luo, T. B. Song, H. Duan, Z. Hong, J. You, Y. Liu, Y. Yang, *Science* **2014**, *345*, 542.
[15] K. Wu, A. Bera, C. Ma, Y. Du, Y. Yang, L. Li, T. Wu, *Phys. Chem. Chem. Phys.* **2014**, *16*, 22476.
[16] H.-H. Fang, R. Raissa, M. Abdu-Aguye, S. Adjokatse, G. R. Blake, J. Even, M. A. Loi, *Adv. Funct.Mater.* **2015**, *25*, 2378.
[17] J. Even, L. Pedesseau, C. Katan, M. Kepenekian, J.-S. Lauret, D. Sapori, E. Deleporte, *J. Phys. Chem. C* **2015**, *119*, 10161.
[18] B. R. Sutherland, S. Hoogland, M. M. Adachi, C. T. Wong, E. H. Sargent, *ACS Nano* **2014**, *8*, 10947.
[19] S. D. Stranks, S. M. Wood, K. Wojciechowski, F. Deschler, M. Saliba, H. Khandelwal, J. B. Patel, S. J. Elston, L. M. Herz, M. B. Johnston, A. P. Schenning, M. G. Debije, M. K. Riede, S. M. Morris, H. J. Snaith, *Nano Lett.* **2015**, *15*, 4935.
[20] R. Pässler, *Phys. Status Solidi B* **1997**, *200*, 155.
[21] K. Chen, A. J. Barker, F. L. C. Morgan, J. E. Halpert, J. M. Hodgkiss, *J. Phys. Chem. Lett.* **2015**, *6*, 153.

[22] T. J. Savenije, C. S. Ponseca, L. Kunneman, M. Abdellah, K. Zheng, Y. Tian, Q. Zhu, S. E. Canton, I. G. Scheblykin, T. Pullerits, A. Yartsev, V. Sundström, *J. Phys. Chem. Lett.* **2014**, *5*, 2189.
[23] K. Tanaka, T. Takahashi, T. Ban, T. Kondo, K. Uchida, N. Miura, *Solid State Commun.* **2003**, *127*, 619.
[24] Y. Yang, D. P. Ostrowski, R. M. France, K. Zhu, J. van de Lagemaat, J. M. Luther, M. C. Beard, *Nat. Photonics* **2015**, *10*, 53.
[25] A. Miyata, A. Mitioglu, P. Plochocka, O. Portugall, J. T.-W. Wang, S. D. Stranks, H. J. Snaith, R. J. Nicholas, *Nat. Phys.* **2015**, *11*, 582.
[26] Q. Lin, A. Armin, R. C. R. Nagiri, P. L. Burn, P. Meredith, *Nat. Photonics* **2014**, *9*, 106.
[27] K. Zheng, Q. Zhu, M. Abdellah, M. E. Messing, W. Zhang, A. Generalov, Y. Niu, L. Ribaud, S. E. Canton, T. Pullerits, *J. Phys. Chem. Lett.* **2015**, *6*, 2969.
[28] W. Kong, Z. Ye, Z. Qi, B. Zhang, M. Wang, A. Rahimi-Iman, H. Wu, *Phys. Chem. Chem. Phys.* **2015**, *17*, 16405.
[29] C. Wehrenfennig, M. Liu, H. J. Snaith, M. B. Johnston, L. M. Herz, *APL Mater.* **2014**, *2*, 081513.
[30] X. Wu, M. T. Trinh, D. Niesner, H. Zhu, Z. Norman, J. S. Owen, O. Yaffe, B. J. Kudisch, X. Y. Zhu, *J. Am. Chem. Soc.* **2015**, *137*, 2089.
[31] A. Pisoni, J. Jaćimović, O. S. Barišić, M. Spina, R. Gaál, L. Forró, E. Horváth, *J. Phys. Chem. Lett.* **2014**, *5*, 2488.
[32] D. W. de Quilettes, S. M. Vorpahl, S. D. Stranks, H. Nagaoka, G. E. Eperon, M. E. Ziffer, H. J. Snaith, D. S. Ginger, *Science* **2015**, *348*, 683.
[33] M. M. Lee, J. Teuscher, T. Miyasaka, T. N. Murakami, H. J. Snaith, *Science* **2012**, *338*, 643.

Adv. Optical Mater. **2016**,
DOI: 10.1002/adom.201500765

Supporting Information

Reversible Laser Induced Amplified Spontaneous Emission from Coexisting Tetragonal and Orthorhombic Phases in Hybrid Lead Halide Perovskites.

Fabian Panzer[a,b,c], Sebastian Baderschneider[b,d], Tanaji Gujar[e], Thomas Unger[a,b], Sergey Bagnich[a], Marius Jakoby[a], Heinz Bässler[b], Sven Hüttner[f], Jürgen Köhler[b,d], Ralf Moos[c], Mukundan Thelakkat[e], Richard Hildner[b,d], Anna Köhler[a,b,*]

[a] Experimental Physics II

[b] Bayreuth Institute of Macromolecular Research (BIMF)

[c] Department of Functional Materials

[d] Experimental Physics IV

[e] Applied Functional Polymers, Macromolecular Chemistry I

[f] Organic and Hybrid Electronics, Macromolecular Chemistry I

University of Bayreuth, 95440 Bayreuth, Germany

1. Transition from spontaneous emission to amplified spontaneous emission (ASE)

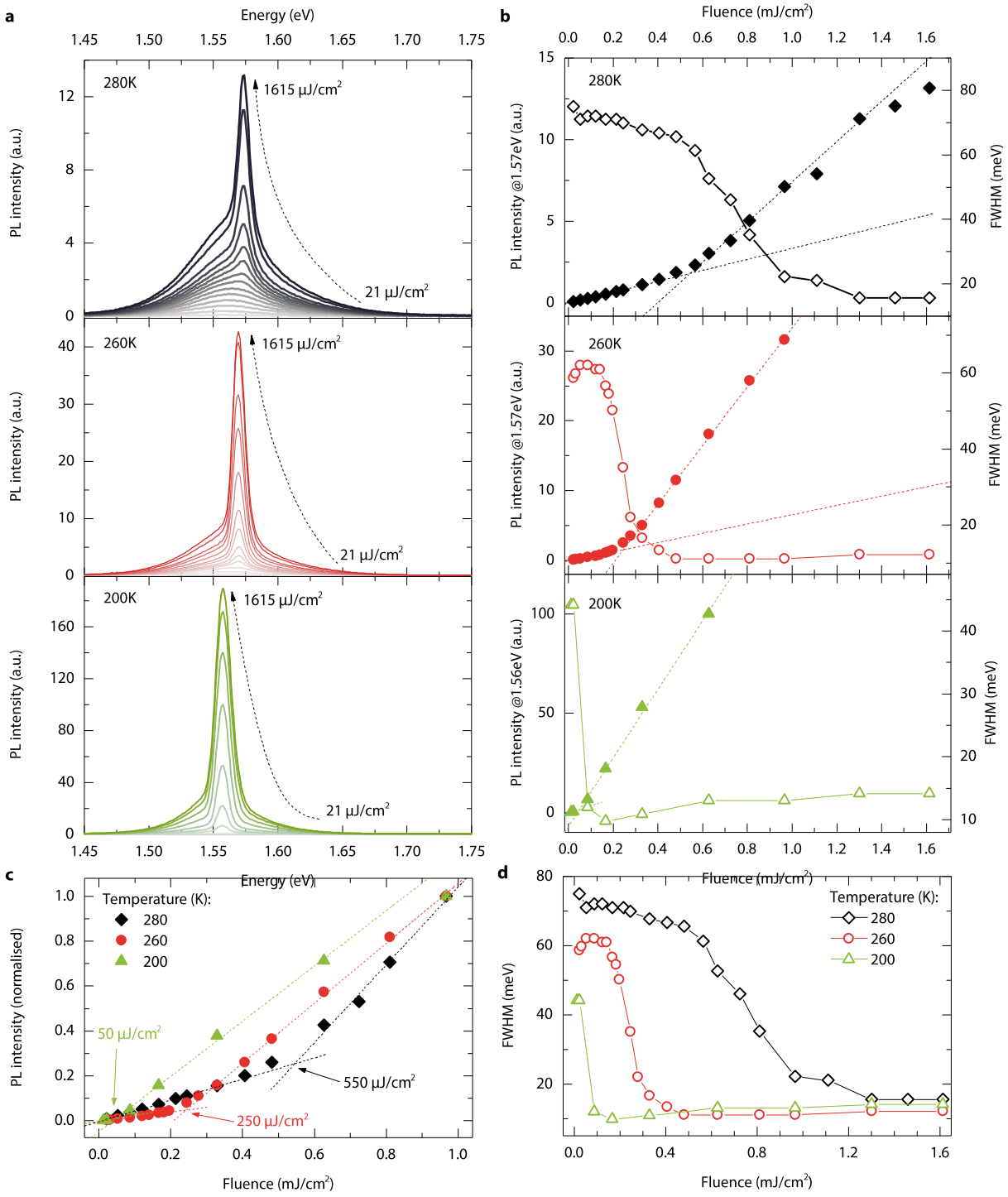

Figure S1: (a) The photoluminescence (PL) spectra for excitation at 3.68 eV with increasing laser fluence from 21 to 1615 μJ/cm² at 280, 260 and 200 K. (b) The PL intensity (solid symbols) and FWHM (open symbols) as a function of laser fluence at 280, 260 and 200 K. Solid and dotted lines are guides to the eye. (c,d) Summary of the results on the PL intensity (c) and FWHM (d) as a function of laser fluence for 280 (black), 260 (red) and 200 K (green). In (c), threshold fluences for ASE are determined by the points of intersections from corresponding linear fits.

2. Temperature dependent XRD measurements

This research was undertaken on the SAXS beamline at the Australian Synchrotron, Victoria, Australia.

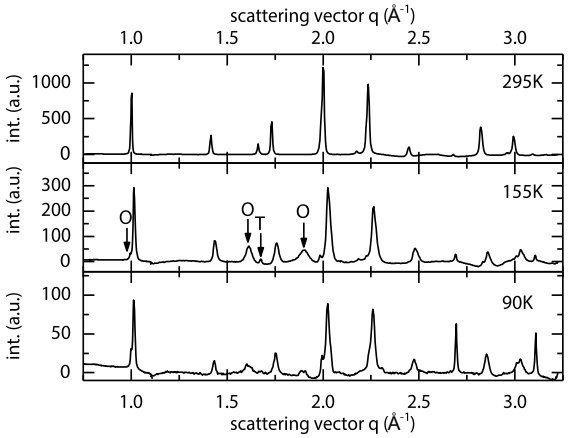

Figure S2: XRD patterns of the investigated sample at 295 K, 155 K and 90 K. The marks identify the existence of tetragonal (T) and orthorhombic (O) phases at 155 K.

3. Calculation of exciton binding energy

The intensity of emission is given by

$$I(T) = \frac{k_r}{k_r + k_{nr}} I_0 \qquad \text{eq. S1}$$

where $I(T)$ is the temperature dependent emission intensity and I_0 is the emission intensity in the absence of non-radiative decay processes, thus corresponding to the number of photogenerated excitons. k_r and k_{nr} denote the radiative and non-radiative decay rates. Since the absorption is independent of temperature, the Einstein coefficients require the radiative decay also to be temperature-independent (Figure S3a). On the other hand, Figure 1a in the manuscript shows that the photoluminescence quantum yield, Φ, increases strongly upon cooling. From $\Phi = k_r/(k_r + k_{nr})$ it follows that the non-radiative decay rate in this lead halide perovskite reduces upon cooling. This applies to both the tetragonal and the orthorhombic phase. We conclude that the non-radiative decay channel is mainly due to a thermally activated process such as exciton dissociation. Hence, the temperature dependent non-radiative decay rate can be written as $k_{nr} = k_{nr}^0 e^{-\frac{E_B}{kT}}$, where E_B is the exciton binding energy. Eq. S1 therefore becomes

$$I(T) = \left[1 + \frac{k_{nr}^0}{k_r} \exp\left(-\frac{E_B}{kT}\right)\right]^{-1} I_0. \qquad \text{eq. S2}$$

The activation energy can be thus determined from fitting the experimentally obtained temperature dependent PL intensity analogous to recent reports in literature.[1, 2] We find activation energies of $85 \pm 20\ meV$ and $24 \pm 5\ meV$ for tetragonal and orthorhombic phase respectively. The prefactor $\frac{k_{nr}^0}{k_r}$ is $(2.4 \pm 1.0)10^3$ and 70 ± 20 for the two phases, respectively. The agreement between experimental data and fit is shown in Figures S3b on a linear temperature scale and on Figure S3c in an Arrhenius fashion.

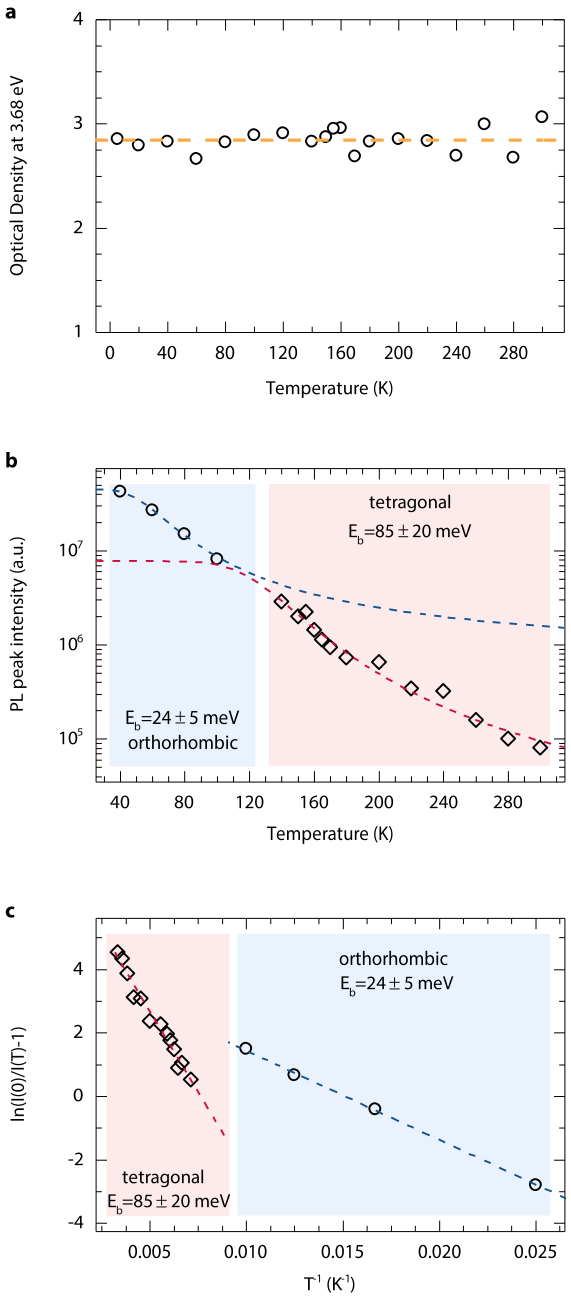

Figure S3: (a) Optical Density at 3.68 eV, which corresponds to the wavelength of the excitation laser, as a function of temperature. The dashed line indicates the constant average value. (b) PL peak intensity as a function of temperature for excitation fluence of 0.75 μJ/cm^2. (c) $\ln\left[\frac{I(0)}{I(T)}-1\right]$ as a function of inverse temperature. For both, (b) and (c) symbols indicate experimental data and dashed lines correspond to fits. The temperature ranges pertaining to the orthorhombic and tetragonal phase are indicated by blue and red shading, respectively.

4. Estimation of critical exciton density for ASE

The critical density of excitons for ASE decreases with temperature. From the discussion in section 3, we attributed non-radiative decay of excitations to a thermally activated process, while the radiative decay is independent of temperature. Thus, the density of excitations that contribute to ASE at a certain temperature is given by

$$n_{threshold} = n_{generated}\Phi = n_{generated}\frac{I(T)}{I_0}\ , \qquad \text{eq. S3}$$

where Φ is the photoluminescence quantum yield and $n_{generated}$ is the number of excitations generated at the ASE threshold intensity in the excitation volume. $\frac{I(T)}{I_0}$ is given by $\left[1+\frac{k_{nr}^0}{k_r}\exp\left(-\frac{E_B}{kT}\right)\right]^{-1}$, with $E_B = 85\ \text{meV}$ and $\frac{k_{nr}^0}{k_r} = (2.4 \pm 1.0)10^3$ for the tetragonal phase. $n_{generated}$ is given by,

$$n_{generated} = \frac{ASE\ threshold\ fluence * excitation\ area}{excitation\ volume * photon\ energy}. \qquad \text{eq. S4}$$

We assume illumination within the full layer thickness of 100 nm, and a radius of the laser spot of 0.091 cm, implying an excitation area of 0.026 cm^2. This yields an excitation volume of V = 0.026 cm^2 * 100 nm= 2.6*10^{-6} m^2 * 10^{-7} m=2.6*10^{-13} m^3 = 2.6*10^5 μm^3 = 2.6*10^{-7} cm^3. The photon energy of the laser excitation is 3.68 eV. The ASE threshold excitation fluence in the tetragonal phase is taken from Figures S1c. With this, we get densities of $9.3\ 10^{19} cm^{-3}$, $8.5\ 10^{19} cm^{-3}$ and $4.2\ 10^{19}\ cm^{-3}$ for 280, 260 and 200 K respectively. Furthermore from Figure 2, we identified the ASE threshold for the tetragonal phase at 210 K when using a fluence of 85 μJ/cm^2, which then corresponds to a generated excitation density of $1.4\ 10^{19}\ cm^{-3}$.

Figure S4 shows the values of $n_{generated}$ (black colour), $\frac{I(T)}{I_0}$ (red colour) and the resulting n_{ASE} (blue colour), all as a function of temperature for the tetragonal phase. We find a temperature independent density of $n_{threshold}^{tetragonal} = (1.02 \pm 0.2)\ 10^{18} cm^{-3}$ for the tetragonal phase.

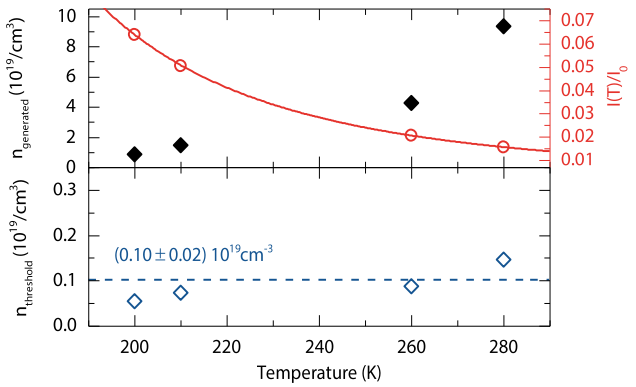

Figure S4: The values of $n_{generated}$ (black diamonds), $\frac{I(T)}{I_0}$ (red circles) and the resulting $n_{threshold}$ (blue open diamonds), all as a function of temperature for the tetragonal phase.

For the orthorhombic phase, we calculate the ASE threshold density at 135 K using the same approach as for the tetragonal phase yet using an activation energy of 24 meV and a prefactor $\frac{k_{nr}^0}{k_r} = 70 \pm 20$.

This leads to a value of $n_{threshold}^{orthorhombic} = (1.4 \pm 0.2)10^{18} cm^{-3}$, which is similar to the corresponding density of the tetragonal phase.

5. Stability and Reproducibility

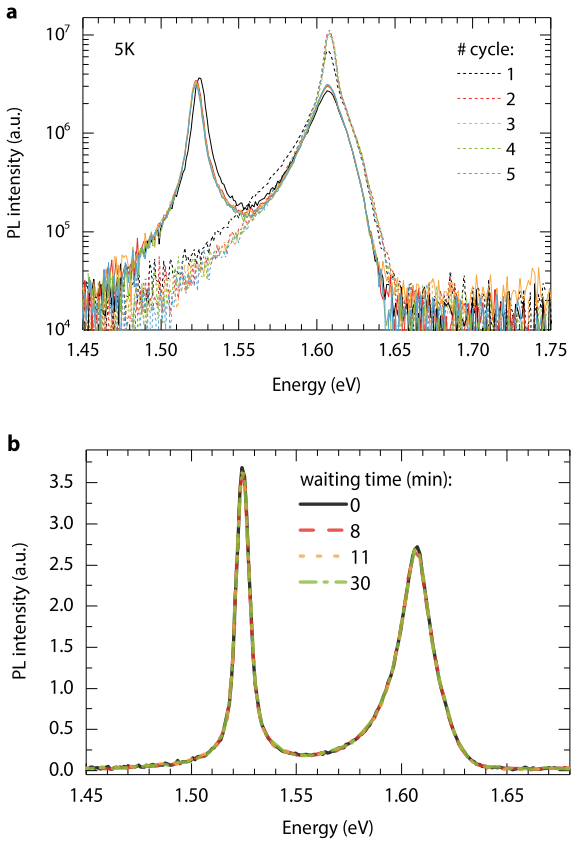

Figure S5: (a) 5 K emission spectra taken with 21 μJ/cm^2 first after illumination with a high fluence 1615 μJ/cm^2 pulse train (solid lines) and then after heating to 100 K (erase) and decreasing the temperature back to 5 K (dashed lines) for 5 consecutive cycles. (b) 5 K emission spectra taken with 21 μJ/cm^2 at different times after initial illumination with a high fluence 1615 μJ/cm^2 pulse train.

6. Time resolved emission spectra before and after writing process

The time-dependent photoluminescence spectra were recorded using an Optronis SC-10 streak camera with a TSU12-10 deflection unit, operated in single acquisition mode with analogue accumulation. The integration time of the SRU-BA readout unit was set to 40 ms and 300 frames have been added within each measurement. The excitation source was an 80 MHz pulsed Coherent Chameleon Ultra laser with a pulse width of 140 fs. An APE pulse select divided the 80 MHz by a factor of 162, before the light was frequency doubled by an APE second-harmonic generator. The excitation energy hitting the sample, which was held in an Oxford Instrument cryostat, was set to 3.4 eV. Prior to the detection in the streak camera the photoluminescence spectra was diffracted by an Acton SP- 2300i spectrograph. The instrumental response function had a FWHM of 2 ns. All spectra were recorded with an excitation fluence of 20 $\mu J/cm^2$.

For high fluence excitation we used the same Nitrogen Laser as for the steady state emission measurements with an excitation fluence of 1615 $\mu J/cm^2$. The sample was exposed to the high fluence by a pulse train of 100 pulses. Prior to high fluence excitation, the PL decay of the peak centred at 1.61 eV can be fitted using a biexponential decay with lifetimes of 4.5 (76%) and 30 ns (24%). After high fluence excitation, an additional new emission feature at 1.53 eV appears, similar to the scenario described in section 3 in the main text. Fitting the PL decay of the new emission feature using a biexponential function gives values of 1.5 ns (52%) and 6.3 ns (48%). In the same manner, the PL decay of the Peak at 1.61 eV gives values of 3.1 ns (54%) and 12.5 ns (46%). Overall, the PL-Signals before and after high fluence excitation decay within tens of nanoseconds. No µs lifetimes were detected within the entire spectral range investigated.

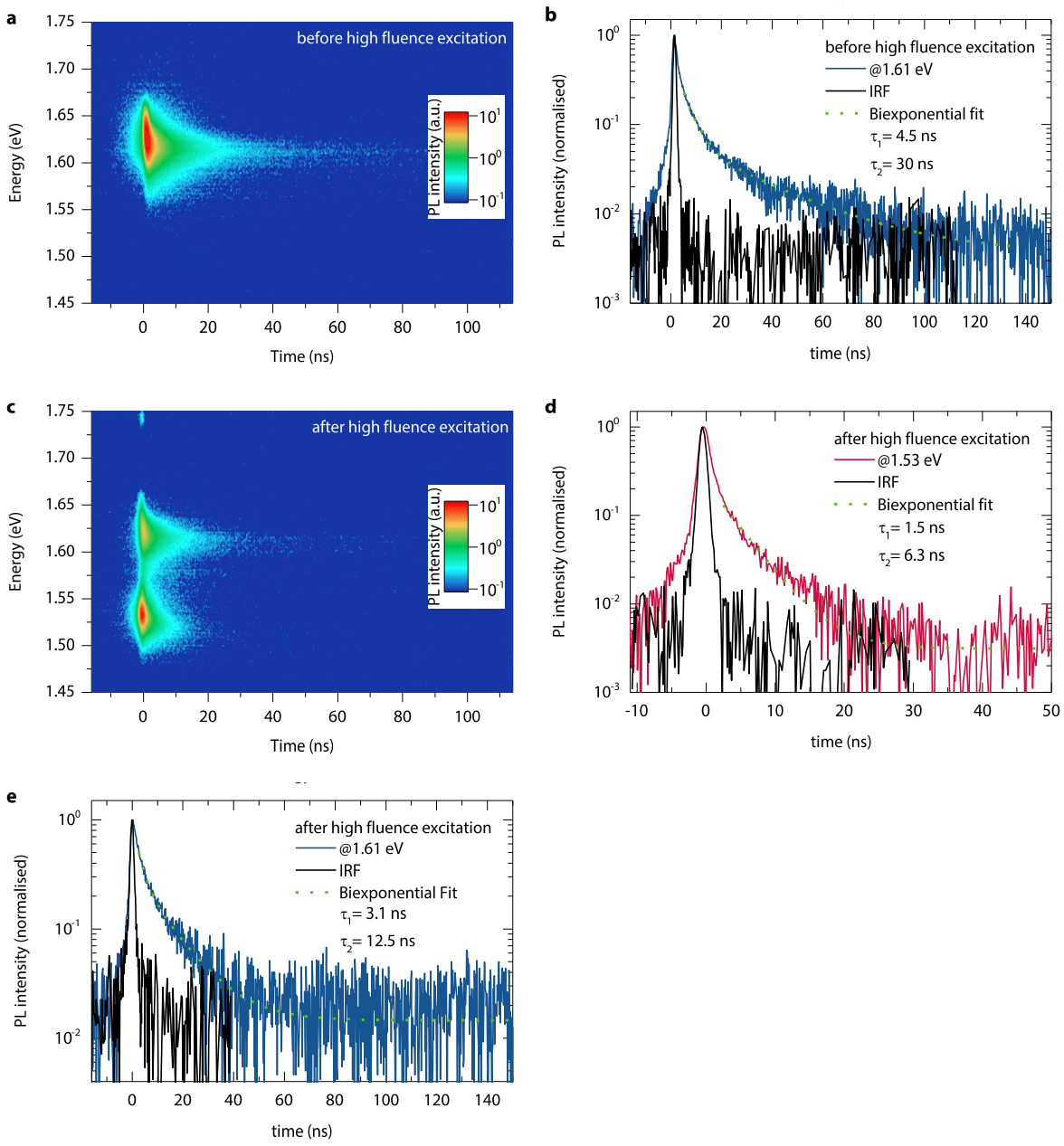

Figure S6: Time resolved photoluminescence spectra at 20 K taken with an excitation fluence of 20 µJ/cm^2, before (a,b) and after (c-e) high fluence excitation. The two streak images of the time resolved PL spectra (a) before and (c) after high fluence excitation are accompanied by corresponding PL decays at 1.61 eV (blue line) and at 1.53 eV (red line). In (b,d,e) the corresponding instrumental response function (black line) and a biexponential fit (green dashed line), together with obtained values of the lifetimes are shown.

7. Estimate of local heating and temperature dissipation effects

The change of temperature upon heating is given by the amount of heat delivered, Q, divided by the heat capacity C of the perovskite, ie.e $\Delta T = Q / C$.

The heat capacity of lead-halide perovskites is $C < 200$ J/(K*mol).[3] We need the heat capacity per absorber, which is the unit cell. As shown in section 4, the excitation volume is $2.6*10^{-7}$ cm^3. In the orthorhombic phase, the unit cell has lattice parameter of a=0.88 nm, b=0.87 nm, c=1.28 nm,[4-6] which implies a volume of 0.98 nm^3 = $0{,}98*10^{-9}$ µm^3 for the unit cell. Hence, there are approximately $2.7*10^{14}$ orthorhombic unit cells within our excitation volume, which corresponds to $4.5*10^{-10}$ mol of unit cells. Therefore, the specific heat capacity c for the excitation volume is

c= 200 JK^{-1}mol^{-1}*$4.5*10^{-10}$ mol = $9*10^{-2}$ µJ/K.

In order to estimate the energy per pulse which can be used to heat up the material (=heat amount per pulse), we consider the difference between excitation pulse energy (3.68 eV) and the energetic level from which emission takes place at 5 K (1.61 eV). This yields 3.68 eV-1.61 eV=2.07 eV = $3.3165*10^{-19}$J/Photon. Since the absorption is constant with temperature, no correction is needed. Further, we neglect reflection and scattering and assume that the entire laser pulse is absorbed. To obtain the number of photons per laser pulse we divide the energy of the laser (= fluence * excitation spot size) by the energy of a photon.

Table T1 summarizes the temperature changes obtained per pulse for the different fluences.

Fluence (µJ/cm^2)	ΔT (K)
21	5
168	36
329	71
482	104
627	136
811	176
968	210
1111	241
1304	283
1461	317
1615	350

Excitation with a fluence of 1615 µJ/cm^2 raises the temperature of the sample by 350 K. Due to the flat geometry of our excitation volume (cylinder with 100 nm height and 0.18 cm diameter), the associated heat is mainly dissipated into the quartz substrate underneath the excitation spot. Let us assume that the heat dissipation raises the temperature of the bath, i.e. the quartz substrate, only insignificantly, e.g. by 1K from 5K to 6K. This leads to a temperature difference of $\Delta T = 344K$ between the heated sample and the bath (=quartz substrate). Using a heat capacity of $c_{perovskite}$= 200 JK^{-1}mol^{-1} implies that a value of 31 µJ of heat needs to be dissipated. Quartz has a typical heat capacity of $C_{quartz} \approx 700J/(kg\ K)$. Thus, 31 µJ of heat can be dissipated while raising the temperature of the quartz by only 1K when using a mass of 44*10^{-9} kg of quartz. Since the density of quartz is $\rho_{quartz} = 2.2\ g/cm^3$, this implies a volume of roughly 20 10^{-12} m^3 is required. As the excitation spot is circular with an area of 0.026cm^2, this implies that a height of 6.3 µm of our quartz substrate is needed to dissipate the laser induced heat. This is easily fulfilled as the height of the substrates used in this study is approx. 3 mm.

The timescale at which the induced high temperature due to laser excitation dissipates in the manner described above can be estimated using the heat equation:

$$\frac{\Delta Q}{\Delta t} = \lambda \frac{\Delta T}{l} A \qquad \text{eq.S5}$$

Where ΔQ is the heat to be dissipated, Δt the time that is needed for disspation, λ the thermal conductivity, ΔT is the temperature difference, A is the area normal to heat flow, l the length over which the dissipation takes place. Rearranging equation S5 gives: $\Delta t = \frac{l}{\lambda\, \Delta T} \frac{\Delta Q}{A}$.

Using values of $\Delta Q = 31 \mu J$, A = π*10^{-6} cm^2 , l = 6 µm , ΔT=344 K and the thermal conductivity of lead halide perovskites which is $\lambda = 0.5\ \frac{W}{K\ m}$,[7] leads to a value of Δt= 132 ns.

9. SEM Images of the used Perovskite Film

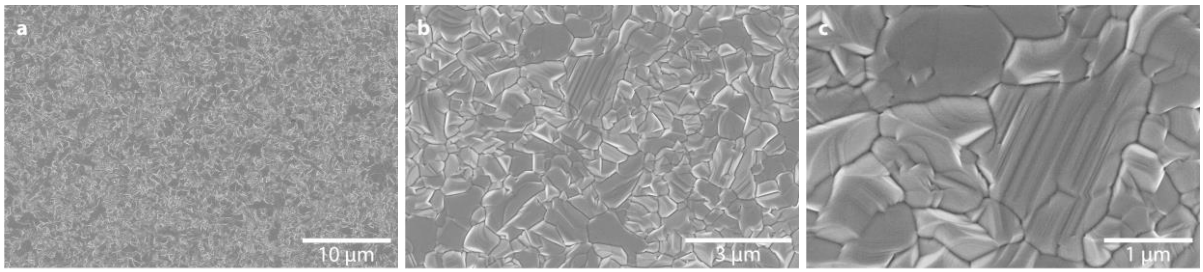

Figure S7: Top View SEM image of the used perovskite thin film at low (a), mid (b) and high (c) magnification.

10. Single shot writing

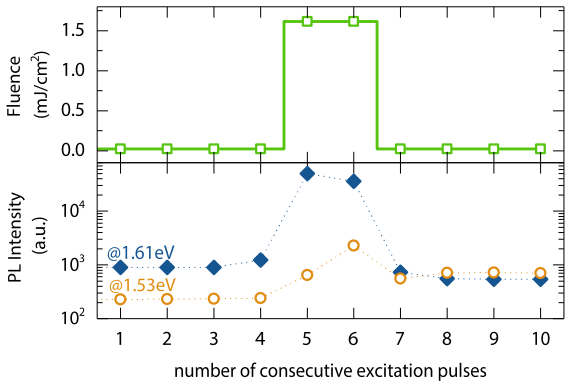

Figure S8: (a) Intensity of the ASE peaks at 1.53 eV (orange circles) and 1.61 eV (filled blue diamonds) measured for ten consecutive laser excitation shots with low fluence (21 µJ/cm^2) and with high fluence (1615 µJ/cm^2) as indicated in the top panel. We note that the low energy ASE peak already appears with the first high fluence shot.

References:

[1] K. Wu, A. Bera, C. Ma, Y. Du, Y. Yang, L. Li, T. Wu, Physical chemistry chemical physics : PCCP 2014, 16, 22476.

[2] T. J. Savenije, C. S. Ponseca, L. Kunneman, M. Abdellah, K. Zheng, Y. Tian, Q. Zhu, S. E. Canton, I. G. Scheblykin, T. Pullerits, A. Yartsev, V. Sundström, The Journal of Physical Chemistry Letters 2014, 5, 2189.

[3] O. Knop, R. E. Wasylishen, M. A. White, T. S. Cameron, M. J. M. V. Oort, Canadian Journal of Chemistry 1990, 68, 412.

[4] W. J. Yin, Y. F. Yan, S. H. Wei, J Phys Chem Lett 2014, 5, 3625.

[5] T. Baikie, Y. Fang, J. M. Kadro, M. Schreyer, F. Wei, S. G. Mhaisalkar, M. Graetzel, T. J. White, Journal of Materials Chemistry A 2013, 1, 5628.

[6] G. Grancini, S. Marras, M. Prato, C. Giannini, C. Quarti, F. De Angelis, M. De Bastiani, G. E. Eperon, H. J. Snaith, L. Manna, A. Petrozza, The Journal of Physical Chemistry Letters 2014, 5, 3836.

[7] A. Pisoni, J. Jaćimović, O. S. Barišić, M. Spina, R. Gaál, L. Forró, E. Horváth, The Journal of Physical Chemistry Letters 2014, 5, 2488.

4.8. Effect of Thermal and Structural disorder on Electronic Structure of Hybrid Perovskite Semiconductor $CH_3NH_3PbI_3$

Shivam Singh, Cheng Li, Fabian Panzer, K. L. Narasimhan, Anna Gräser, Tanaji P. Gujar, Anna Köhler, Mukundan Thelakkat, Sven Hüttner and Dinesh Kabra

Submitted

Effect of Thermal and Structural Disorder on Electronic Structure of Hybrid Perovskite Semiconductor $CH_3NH_3PbI_3$

Shivam Singh[1#], Cheng Li[2#], Fabian Panzer[3,4,5] K. L. Narasimhan[6], Anna Graeser[2],Tanaji P. Gujar[7],Anna Köhler[3,4], Mukundan Thelakkat[7], Sven Hüttner[2]*, and Dinesh Kabra[1*]

Department of Physics[1] and Electrical Engineering[6], Indian Institute of Technology Bombay, Powai, Mumbai (India) – 400076.

Organic and Hybrid Electronics Group - Macromolecular Chemistry I [2], Experimental Physics II[3], Bayreuth Institute of Macromolecular Research (BIMF)[4], Department of Functional Materials[5], Applied Functional Polymers - Macromolecular Chemistry I[7], University of Bayreuth, 95440 Bayreuth, Germany

# Authors contributed equally

Abstract

In this paper, we investigate the temperature dependence of the optical properties of methylammonium lead iodide ($MAPbI_3$ = $CH_3NH_3PbI_3$) from room temperature to 6K. In both, the tetragonal (T> 163K) and the orthorhombic (T<163K) phase of $MAPbI_3$, the band gap (from both absorption and photoluminescence (PL) measurements) decreases with decrease in temperature - in contrast to what is normally seen for many inorganic semiconductors, like; Si, GaAs, GaN etc. We show that in the perovskites reported here, the temperature co-efficient of thermal expansion is large and accounts for the positive temperature coefficient of the band gap. A detailed analysis of the exciton linewidth allows to distinguish between static and dynamic disorder. The low energy tail of the exciton absorption is reminiscent of Urbach absorption. The Urbach energy is a measure of the disorder, which is modelled using thermal and static disorder for both the phases separately. The static disorder component, manifested in the exciton linewidth at low temperature is small. Above 60 K, thermal disorder increases the linewidth. Both these features are a measure of the high crystal quality and low disorder of the perovskite films even though they are produced from solution.

Introduction

In recent times lead based hybrid perovskite materials found a lot of attention, exhibiting solar cell efficiencies >20%[1,2,3,4], high efficiency light emitting diodes[5,6,7] and other optoelectronic applications[8,9]. The band gap of these materials can be tuned from NIR to UV by changing the halide ion. In a recent study, it has been shown that the temperature dependence of the band gap is anomalous – i.e. the band gap increases with temperature[10]. However, a clear understanding on the origin of this temperature dependence has not been established so far. In this paper we present a detailed study on the temperature dependence of the optical absorption and emission of high quality $CH_3NH_3PbI_3$ films prepared on quartz substrate. First we study and explain the temperature dependence of the optical band gap, the exciton Γ_{EX} and the sub-band gap absorption in these samples. Since the material undergoes a structural transition at low temperature, our studies encompass the room and low temperature phases of the material[11].

Results and discussion

Structure and Lattice expansion:

Hybrid perovskite $MAPbI_3$ is known to have temperature dependent structural phase transitions. As depicted in Figure 1a, for temperatures T < 163 K it is in the orthorhombic phase ($a \neq b \neq c$; $\alpha=\beta=\gamma=90^0$) and for temperatures 163 K <T< 327.3K it remains in the tetragonal phase $a=b\neq c$; $\alpha=\beta=\gamma=90^0$. Beyond 3-27.3 K, $MAPbI_3$ forms a cubic phase ($a=b=c$; $\alpha=\beta=\gamma=90^0$). As shown in the supporting information, these crystalline structures can be clearly identified by X-ray scattering. With these temperature dependent X-ray measurements, we are able to determine the lattice expansion coefficient $\left(\frac{dln(V)}{dT}\right)_P$. In particular, we have estimated this coefficient for the tetragonal and orthorhombic phase using temperature dependent X-ray scattering to be in the order of 10^{-4} K^{-1} which is in agreement with previously reported data by Kawamuraet.al.[12] who found $\left(\frac{dln(V)}{dT}\right)_P$

= (1.35±0.014) x 10^{-4} K^{-1}. Using this value, we estimate $\left(\frac{dE_g}{dln(V)}\right)_T$ to be 1.26 eV which is in good agreement with theoretical values estimated for the perovskite for example by Frost et al.[13]. V corresponds to the volume of the unit cell calculated as depicted in Figure 2a. In the next section we will show the direct relation of the lattice expansion on the optical properties.

Absorption

Figure 1c and Figure 1d (See also in Figure 1S and Figure 2S in the Supporting Information) show the optical absorption spectra of a $MAPbI_3$ film on quartz substrate in its orthorhombic and tetragonal phase at different temperatures. The onset of the optical absorption moves to higher energies with increase in temperature for both phases. Strong excitonic absorption features dominate the optical absorption edge[10] and become even more pronounced at lower temperatures. In order to separate the band-to-band absorption from the UV-Vis spectra we use Elliot theory (described in detail in the supporting information, Equation S1 and Fig.S1)[6,14,15] to find the contribution of excitonic and interband absorption, i.e., $\alpha_{UV-Vis}(\varepsilon) = \alpha_{excitonic} + \alpha_{band-to-band}$.

Fitting the optical absorption using this model provides the exciton binding energy (E_x), FWHM (Γ_{EX}) of the exciton peak and the electronic bandgap (E_g)[6]. Table 1 shows the respective fitting parameters and Figure 2b the variation of the band gap with temperature. The band gap increases with temperature in contrast to what is normally observed in crystalline semiconductors where it decreases.[16,17] In the vicinity of 160K the band gap exhibits a discontinuity, due to the structural phase transition from the orthogonal to the tetragonal phase.[11] The respective temperature coefficient of bandgap (dE_g / dT) is larger in the orthorhombic phase and in general the temperature dependence of the band gap E_g, can be expressed as [17-19]

$$\left(\frac{dE_g}{dT}\right)_P = \left(\frac{dE_g}{dT}\right)_V + \left(\frac{dE_g}{dln(V)}\right)_T \times \left(\frac{dln(V)}{dT}\right)_P \quad (1)$$

The first term explicitly represents the electron phonon coupling through the deformation potential which results in a decrease of the band gap with temperature. The second term implicitly represents the lattice dilatation term which causes the band gap to increase with temperature.

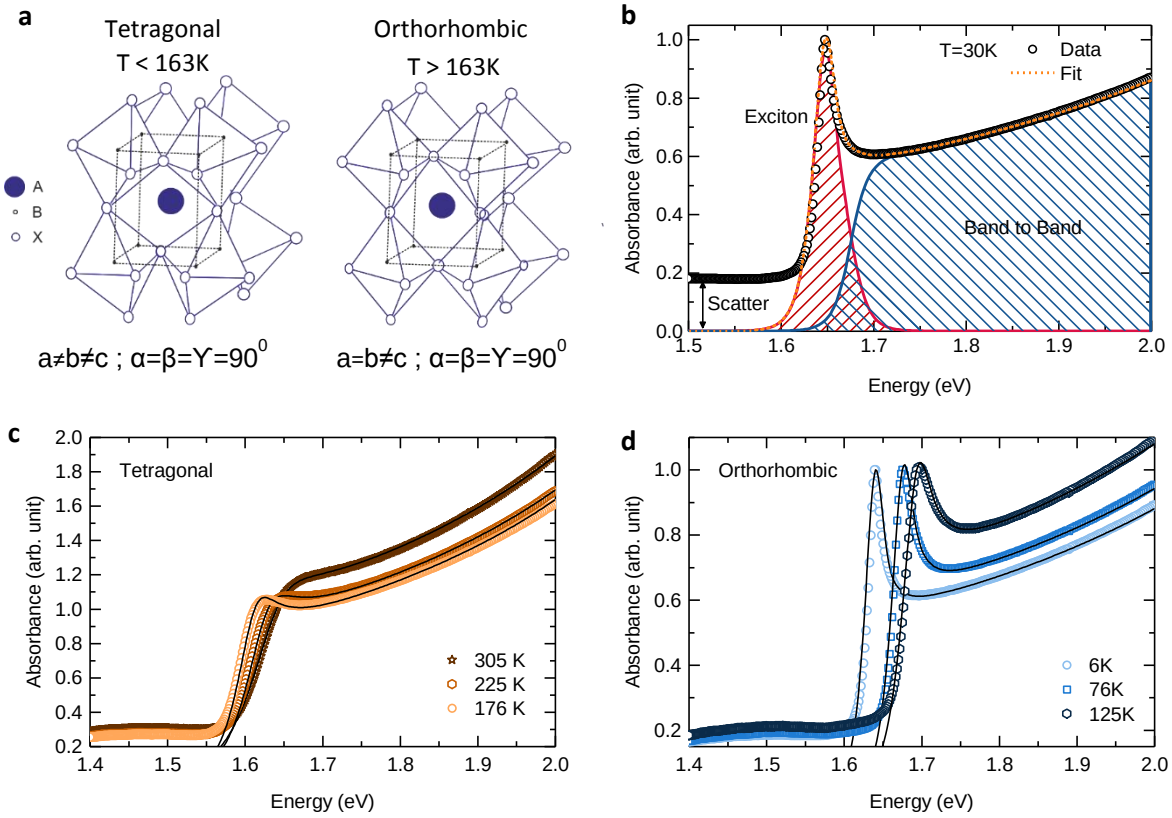

Figure 1. (a) Crystal structure of $MAPbI_3$ in orthorhombic and tetragonal phase, respectively. (b) Illustration of the fitting of the absorption spectra using Elliots theory with the excitonic and band-to-band contribution.UV-Vis absorption spectra of $MAPbI_3$ thin film at different temperatures in (c) the orthorhombic and (d) the tetragonal phase respectively. Black solid line is the fit to the experimental absorption spectra (Scatter points).

For most inorganic semiconductors the lattice dilatation term is much smaller than the electron phonon interaction term. Hence the band gap decreases with temperature for many inorganic semiconductors.[18] This, however, is different in organometal halide perovskites such as $MAPbI_3$, which can be seen when we express our experimental data using eq. 1. The second term, i.e. the lattice dilatation term, dominates the temperature dependence of the band gap for the lead perovskite reported here. From Fig. 2b we estimate $\left(\frac{dE_g}{dT}\right)_P$ to be (2.50 ± 0.11) x 10^{-4} eV/K for the tetragonal phase and (4.85 ± 0.28) x 10^{-4}eV/K for the orthorhombic phase. We estimate the volume expansion coefficient (vide supra) for the tetragonal phase to be $\left(\frac{dln(V)}{dT}\right)_P$ = (3.829±0.014) x 10^{-4} K^{-1}. Using this value, we estimate $\left(\frac{dE_g}{dln(V)}\right)_T$ to be 1.26 eV which is in good agreement with theoretical values estimated for the perovskite[13]. We would like to point out that this value is a lower

limit as we have ignored the (negative) contribution to $\left(\frac{dE_g}{dT}\right)_P$ from the electron phonon term in eq.1. The thermal expansion coefficient of the perovskite samples is almost 50 times larger than similar data for Si (3 x 10^{-6} K^{-1}).[19] We mention in passing that other lead compounds- like lead chalcogenides also have a positive temperature coefficient of the band gap, where volume expansion coefficient is higher than $MAPbI_3$ resulting in an even higher $\left(\frac{dE_g}{dT}\right)_P$ than $MAPbI_3$.[20]

After having discussed the temperature dependence of the electronic band gap we will now discuss the temperature dependence of this excitonic absorption term. The exciton binding energy E_x accounts for the energy difference between the electronic band gap and the excitonic peak position. The line width of the excitonic peak is a signature of the disorder present in the semiconductor. The disorder can be of static (structural) and/or dynamic (thermal) nature - both will broaden the excitonic line width.[21,26] Figure 2a shows the FWHM line width Γ_{EX} as a function of temperature. Γ_{EX} decreases linearly with temperature till about 60K and begins to flatten out at lower temperature and decreases continuously through the phase transition. At very low temperature, broadening due to static disorder dominates Γ_{EX} and is about 11.5 meV, which can be seen as a lower-bound of the inherent disorder in the film.

For all higher temperatures the Γ_{EX} is influenced by dynamic disorder (which will be analysed in more detail further below). The instrument broadened line width with about 3 meV is much smaller than measured Γ_{EX} at 60K.[21]

A very typical approach well-known for inorganic solids attributes the dynamic disorder to the interaction with phonons. Then, the broadening Γ_{EX}, can be fitted using a Bose-Einstein type expression.[22, 23]

$$\Gamma_{EX}(T) = \Gamma_0 + \frac{\Gamma_{ep}}{\exp\left(\frac{E_P}{k_B T}\right)-1} \qquad (2)$$

where, Γ_0= intrinsic Γ_{EX} width at T=0K, Γ_{ep}= coupling constant and E_P = phonon energy. Figure 2b shows the fit for two phases separately over the whole temperature range. The respective fitting parameters are summarized in Table 1. We note that Γ_0= 11.64 meV (orthorhombic) and Γ_0= 15.05 meV (tetragonal) is small for both phases, which is an indicative of high crystal quality of the film. Γ_0 is marginally smaller for the orthorhombic

phase than tetragonal phase, which suggests that the orthorhombic phase is relatively more ordered than tetragonal phase in agreement with literature.[24]

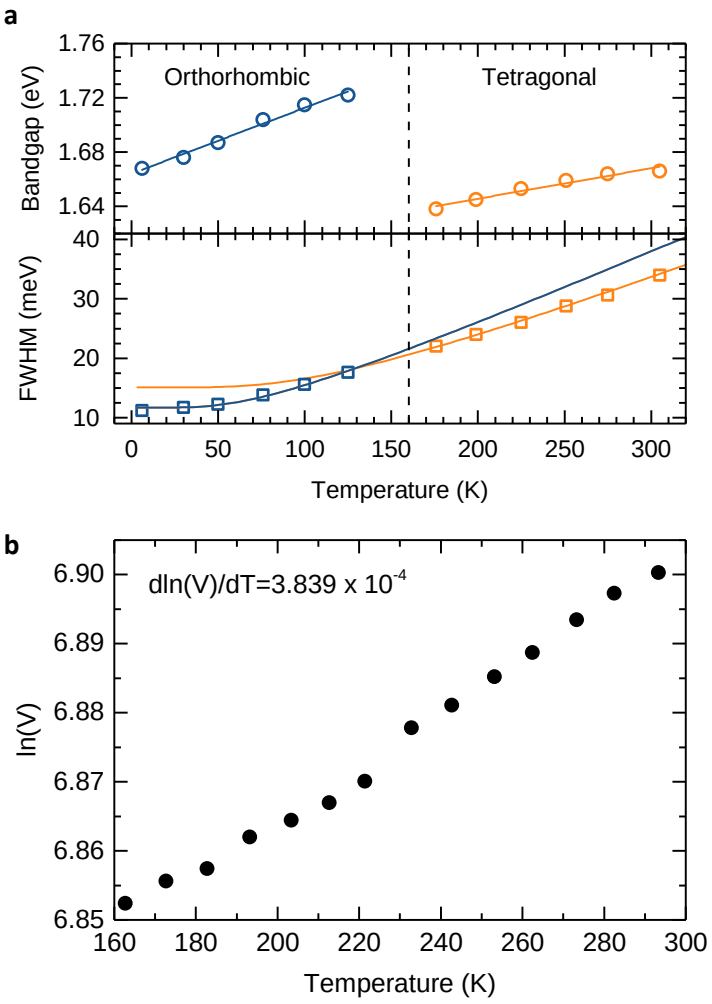

Figure 2. (a) Log of Volume of $MAPbI_3$ in tetragonal phase as a function of temperature and solid line is a linear fit. (b) Variation of bandgap and FWHM of excitonic peak with temperature in orthorhombic and tetragonal phase of $MAPbI_3$. Blue open circles (○) and red open squares (□) represents the bandgap at different temperature in orthorhombic and tetragonal phase. Blue solid circles (●) and red solid squares (■) represents the FWHM exciton in orthorhombic and tetragonal phase respectively. Blue and red solid lines are fits to the experimental data in the orthorhombic and tetragonal phase respectively.

Considering that E_p (using equation 2) is ~ 210 cm^{-1} first principle calculations have shown that such low energy phonon modes relate to the coupled phonon mode between the inorganic cage and the MAI^+ motion.[24],[25] In $MAPbI_3$, the orthorhombic phase restricts the molecular ion motion relatively more compared to the tetragonal phase resulting in a lower dynamic disorder. Figure 3a and 3b show the plots of log α vs $h\nu$ at different

temperatures for the low energy side of the absorption of exciton peak for the two phases.

The low energy edge of the exciton peak satisfies the following empirical relation[26]

$$\alpha = \alpha_0 \exp[\frac{\sigma(h\nu - E_0)}{kT}] \quad (3)$$

Where α is the absorption coefficient, σ the steepness parameter (vide infra) and k the Boltzmann constant. This empirical relation is valid for many semiconductor materials and is known as the Urbach rule.[26] The exponential absorption is indicative of tail states which are a consequence of disorder.[18, 26, 28, 29]. In a logarithmic plot the fitting of the band edge at different temperatures results in a common focus E_0.

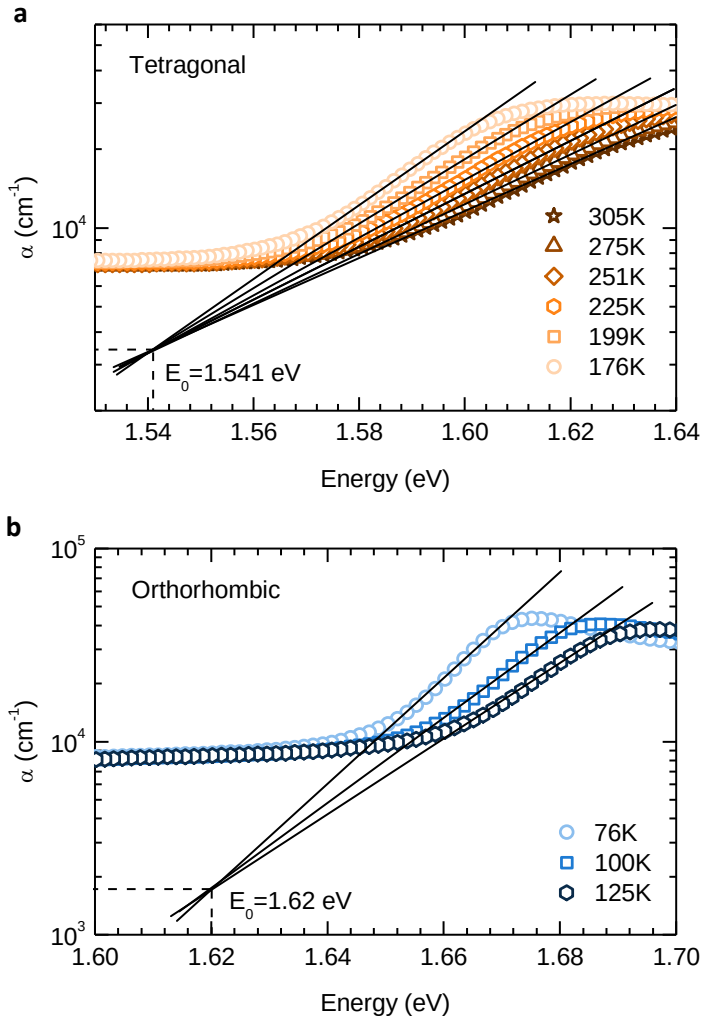

Figure 3. Logarithmic variation of absorption coefficient (α) with photon energy at different temperatures in (a) orthorhombic and (b) tetragonal phase of $MAPbI_3$.

This Urbach focus is one of the characteristic features of Urbach absorption. As shown in Figure 3, the lines come to a separate common focus (E_0) for each of the phases. A single E_0 cannot fit both phases, reflecting the prevalence of different disorder of each of the phases. In most semiconductors the Urbach focus E_0 is located at energies which are greater than the optical band gap providing theoretical maximum bandgap estimation.[18, 26, 28] In the present case however, as T decreases, the bandgap decreases and the slope of optical absorption becomes steeper. Since the temperature dependence of the band gap is positive, the Urbach focus (E_0) now takes place at energies less than the band gap. The applicability of the Urbach rule in this case provides an elegant way in describing the minimum possible bandgap which can be achieved in $MAPbI_3$ at zero disorder.

We note, that due to the high absorption cross section and due to the primary relevance of higher tail states a fit accounting of even less than one order of optical density suffices this formalism. In particular, the excellent convergence substantiate the applicability of the Urbach rule within this rather small optical density range. As can be seen from photothermal deflection measurements[27] the exponential tail may extend another 2-3 magnitudes yet this is partially obscured here by scattering effects.

Furthermore, the prevalence of the common focus shows that the Urbach rule is compatible with the above explained band gap shift due to lattice dilatation. The temperature dependence is accounted by the steepness factor σ which is described in the following section. Figure 4a shows the steepness parameter σ as a function of temperature obtained by using equation 4. The steepness parameter is temperature dependent and, following the Urbach formalism, is approximated by[26]

$$\sigma = \sigma_0\left(2kT/h\nu_p\right)tanh(h\nu_p/2kT) \qquad (4)$$

σ_0 is a constant which is characteristic of the excitation and $h\nu_p$ quantifies the energy of involved phonons. Table 1 summarises the values of σ_0 and $h\nu_p$ obtained for the two phases. Using the values of σ_0 we calculate the Urbach energy. The energy $kT/\sigma = E_u$ is known as the Urbach energy and is related to the degree of disorder.

Following Cody, the total disorder can be thought of as the sum of two terms - thermal disorder and static disorder.[18] The thermal disorder arises from excitations of phonon modes and the static disorder is due to inherent structural disorder. Figure 4b shows the Urbach energy as a function of temperature.

Table 1: Slope of E_g vs. T, E_g vs. E_u, volume vs. T, and extracted parameters Γ_0, Γ_{ep}, E_{LO}, Θ, P, E_u (T=0) in orthorhombic and tetragonal phase of $MAPbI_3$ film.

$MAPbI_3$	Orthorhombic	Tetragonal
$dE_g/.dT(10^{-4}$ eV/K)	4.85±0.28	2.50±0.11
Γ_0(meV)	11.64±0.17	15.05±0.51
Γ_{ep} (meV)	26.11±1.47	36.35±1.42
E_{LO} (meV)	17.81	27.98
Θ (K)	197±25 K	324±33 K
P	$8.92X10^{-4}$	0.002
σ_0	0.403±0.017	0.464±0.005
$h\nu_p$(meV)	17.81±1.4	27.98±1.19
E_u (at T=0K) (meV)	21.47	32.37
d(lnV)/ dT (K^{-1})	9.91×10^{-5}	1.35×10^{-4}
dE_g/dE_u	4.91±0.49	1.57±0.11

This can be written quantitatively as a sum of thermal and structural disorder:[18]

E_u (T, X) =K ($\langle U^2\rangle_T + \langle U^2\rangle_x$).

Here,$\langle U^2\rangle_T$ is related to the mean square displacement of atoms (similar to the Debye Waller factor) and $\langle U^2\rangle_x$ is the quenched in inherent structural disorder. The temperature dependence of E_u can be estimated by describing the phonon spectrum to be an assembly of Einstein oscillators[18].

Following the procedure of Cody et al we write[28]

$$E_u(T,P) = K\left(\frac{\Theta}{\sigma_0}\right)\left[\frac{1+P}{2} + \{\exp\left(\frac{\Theta}{T}\right) - 1\}^{-1}\right] \quad (5)$$

where, Θ is the Einstein characteristic temperature which corresponds to the mean frequency of lattice phonon excitation; P is the structural disorder and is defined as $P = \langle U^2\rangle_x / \langle U^2\rangle_0$ - the suffix 0 denotes the zero point vibrational mode. In a perfectly ordered semiconductor film P =0. Equation 5 is used to fit the data of E_u vs T for the two phases and the results are summarized in Table 1.

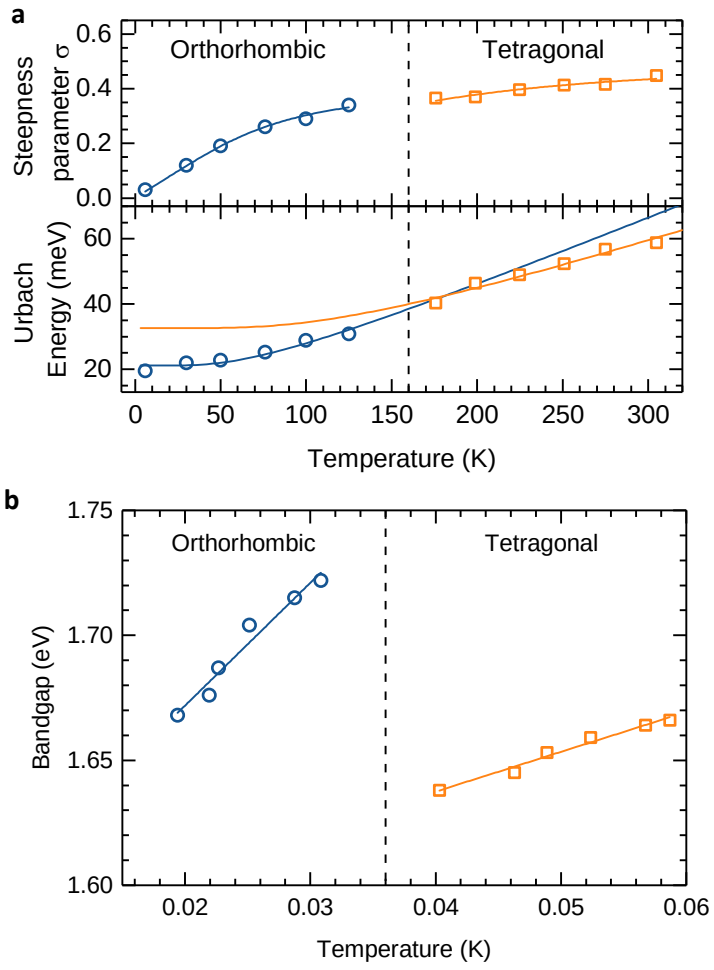

Figure 4. (a) Steepness parameter as a function of temperature for $MAPbI_3$together with corresponding fit (solid lines) of the experimental data using equation 4. (b) Urbach's energy as a function of temperature for $MAPbI_3$ in orthorhombic and tetragonal phase. (c) Bandgap as a function of Urbach energy. Blue circles (○) and red squares (□) represents the steepness parameter and corresponding solid colour lines represents the fit to the experimental data in orthorhombic and tetragonal phase respectively.

The small value of *P* reflects again the high crystal quality in these films and we again note that *P* is larger for tetragonal phase than orthorhombic phase confirming that the orthorhombic phase is more ordered. For comparison, structural disorder value *P* is found to be approximately 2.2 for a:Si.[18] It is worth mentioning that the phonon modes, responsible for thermal disorder in the two phases match the ones responsible for exciton Γ_{EX} broadening (see Table 1).The Einstein characteristic temperature Θ is lower for the orthorhombic phase confirming that the orthorhombic phase is more ordered than the tetragonal phase.

In order to discuss how much the extrinsic disorder ($E_u(T, P = 0)$, which can be thermal or structural due to different processing conditions)[29] of the material affects the band gap with respect to the intrinsic disorder ($E_u(T = 0, P)$), we analyse the change in bandgap and E_u at a particular temperature. Figure 4 shows E_g vs E_u for the $MAPbI_3$ film for both phases. As E_u increases, E_g also increases in both phases. The slope of E_g vs E_u is almost three times higher for the orthorhombic phase (dE_g/dE_u = 4.91±0.49) than for the tetragonal phase (dE_g/dE_u = 1.57± 0.11).

This analysis establishes a relationship between the bandgap and the width of the absorption tail, i.e., E_u for each phase, which suggests that the bandgap of this material is determined by the degree of the thermal disorder in the film at given T. Since the orthorhombic phase is the relatively more ordered phase, a small change in E_u results in a larger change in E_g as compared to the tetragonal phase of $MAPbI_3$.

Photoluminescence

Of course, the temperature dependency also affects the emission of the sample. In the following we will limit our discussion to two peculiarities which nicely confirm our results on disorder. Temperature dependent photoluminescence (PL) studies are carried out on $MAPbI_3$ films. Figure 5a show the normalized PL spectra at different temperatures for the orthorhombic, (T< 167K) and tetragonal (T>167K) phase, respectively. The PL peak moves towards lower energy as temperature decreases in agreement with the band gap shift as seen in absorption measurements (Figure 5b).

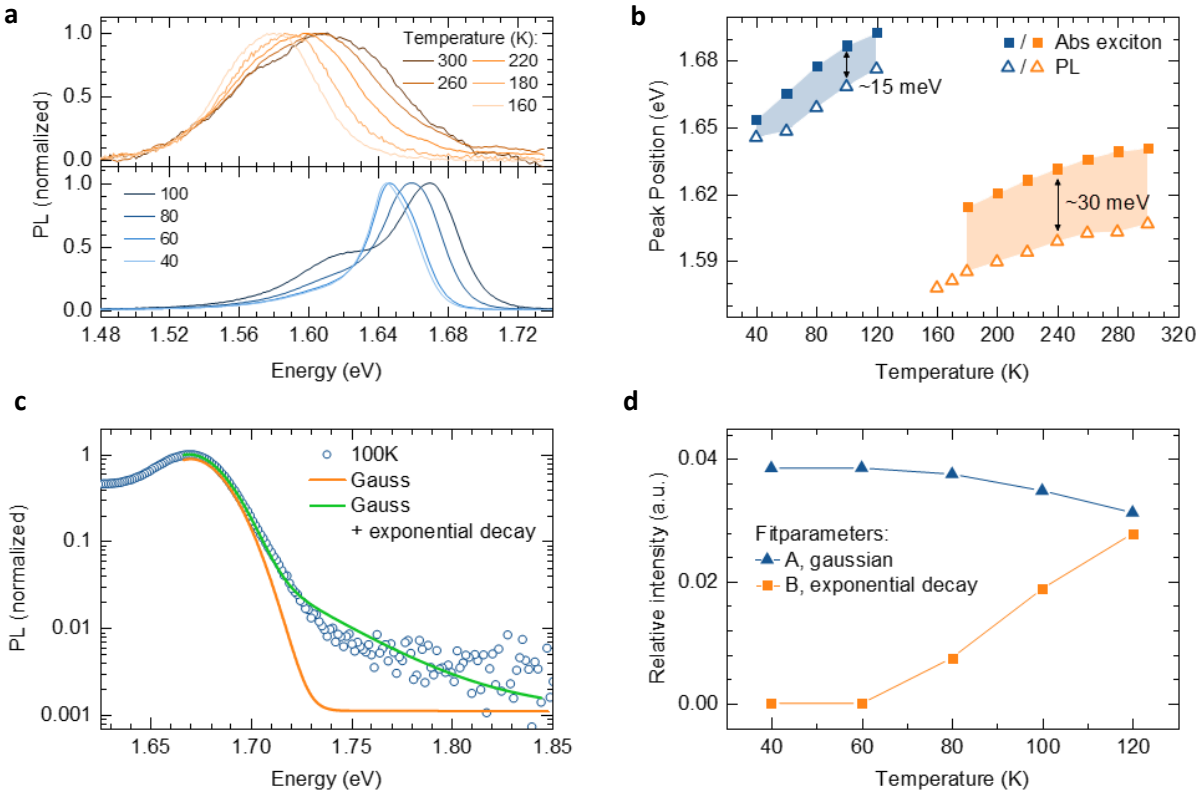

Figure 5. (a) Photoluminescence of $MAPbI_3$ film on glass substrate at T< 167K, i.e., in orthorhombic phase and at T >167K,i.e, in tetragonal phase of $MAPbI_3$. (b) Plot of PL and excitonic peak positions at different temperatures (see also S6 of SI). (c) Example for fit of higher energy PL edge using a Gaussian and exponential function (d) Respective contributions of Gaussian and exponential function to the fit.

For the PL spectra of the orthorhombic phase, we observe a remaining PL feature from the tetragonal phase around 1.6 eV in the vicinity of the transition temperature.[30,35] The temperature dependent energetic positions of the PL peak and the already determined excitonic peak from the absorption data is shown in Figure 5b. The energy difference between absorption and emission is about twice as large for the tetragonal phase than for the orthorhombic phase. We consider this difference arises from the broadening of the density of states induced by thermal disorder and is beautifully consistent with the results obtained from the absorption spectra analysis.

This conclusion can be further substantiated by considering the evolution of the photoluminescence spectra with temperature.

For the analysis of the photoluminescence spectra we focus on the high energy edge where the spectrum is not affected by lower energy emission features such as remaining tetragonal incorporations or possible bound exctions.[30,31,35,8] We fit the blue edge by a

superposition of a Gaussian peak – attributed to the inhomogeneously broadened DOS due to static disorder – and exponential tails that reflect the additional broadening caused by thermal disorder (Figure 5c and supporting information).[26] Considering the relative contributions of the Gaussian part (A) and the exponential contribution (B), we find that a Gaussian peak is fully sufficient to describe the emission below 60 K, yet from 60 K onwards there is an increasing exponential contribution (Figure 5d). This is nicely consistent with the increase in FWHM observed in the absorption spectra (Figure 2b) and thus further supports our overall approach.

Conclusion

In conclusion, we have studied the temperature dependence of the optical properties of $MAPbI_3$ perovskite films. The onset of optical absorption is dominated by exciton absorption. The band gap increases with temperature which is in strong contrast with the decrease in band gap with temperature seen in most crystalline inorganic semiconductors. This is confirmed from both absorption and photoluminescence measurements. We show that the positive temperature coefficient of the bandgap relates to the large temperature coefficient of lattice expansion in these materials. Lattice dilatation plays a much more significant role than electron–phonon interactions. The volume coefficient of $MAPbI_3$ is $(1.35 \pm 0.014) \times 10^{-4}$ K^{-1}, which is ~ 50 times larger than that for crystalline Si. A model, using Einstein oscillators fits to the exciton linewidth Γ_{EX} indicates that the orthorhombic phase is slightly more ordered than the tetragonal phase. The low energy dependence of the exciton absorption is given by an exponential absorption tail reminiscent and consistent of classical Urbach absorption. From the temperature dependence of the Urbach energy, we estimate the disorder and show that it is surprisingly small in these samples - remarkable for solution processed semiconductors. The analysis on temperature dependent PL data consistently supports this picture. It allows to analyse the impact of static and dynamic disorder on the spectra by differentiating between Gaussian and exponential contributions to the shape of the PL. Overall, our study establishes a methodology using optical techniques for the concise characterisation of disorder in new perovskite materials. It correlates fundamental

aspects such as lattice dilatation, static and dynamic disorder to the optical properties of perovskite semiconductors. This provides important insights to the electronic and structural properties of $MAPbI_3$ based perovskites which can be transferred to many related organic metal-halide perovskites.

Experimental Methods

CH_3NH_3I Synthesis

All materials were purchased from Sigma-Aldrich and used as received. Methylammonium iodide (MAI) was synthesized as discussed elsewhere[32,33] MAI was synthesized by reacting 24 mL of methylamine (33 wt. % in absolute ethanol) and 10 mL of hydroiodic acid (57 wt% in water) in a round-bottom flask at 0 °C for 2 h under Ar with stirring. The raw precipitate was recovered by removing the solvent in a rotary evaporator at 50 °C. The raw product was washed with dry ether, dried in vacuum at 60 °C and redissolved in minimum possible boiling absolute ethanol. The pure MAI recrystallized on cooling is filtered and dried at 60 °C in a vacuum oven for 24 h.

$CH_3NH_3PbI_3$ Film Preparation

For perovskite film formation, we adapted a published procedure.[33,34]The quartz substrates (spectrosil B) were cleaned with detergent diluted in deionized water, rinsed with deionized water, acetone and ethanol, and dried with clean dry air. After cleaning, the substrates were transferred in a glovebox under nitrogen atmosphere. For perovskite formation, PbI_2 (1M) was dissolved in N,N-dimethyl formamide overnight under stirring conditions at 100 °C and 80 µl solution was spin coated on the quartz substrates at 2000 rpm for 50 s, and dried at 100 °C for 5 min. Powder of MAI (100 mg) was spread out around the PbI_2 coated substrates with a petridish covering on the top and heated at 165 °C for 13 h. To protect the samples from air and humidity, 40 mg/ml poly(methylmethacrylate) (PMMA; Aldrich) in butyl acetate was spin-coated on top of

the perovskite at 2000 rpm for 30 sec. All steps were carried out under a nitrogen atmosphere in a glove box.

Optical characterisation

The films were measured in a quartz windows fitted helium flow cryostat unit. The absorption spectra were recorded using an Ocean Optics DS3000 Halogen-Deuterium light source and an Ocean Optics QE Pro spectrometer coupled with fiberoptics and lenses to the cryostat system. A temperature-step profile was applied to obtain the UV-Vis spectra at the respective temperatures, allowing 10min equilibration time.

For temperature dependent emission spectra we used a home built setup that was described in more detail recently.[35] In Brief, the sample was put into a continuous flow cryostat (Oxford Instruments, Optistat CF) and was excited by a Nitrogen Laser (LTB, MNL 100) with 337 nm pulses, at a fluence of 0.75 μJ/cm^2 and a repetition rate of 15 Hz. The emitted light was detected by a CCD camera (AndoriDus) coupled to a spectrograph (Andor Shamrock 303i). Measured spectra were corrected for CCD and grating responsivity.

XRD characterisation

Perovskite films were prepared as described, but then scratched off in the glovebox and transferred into a Kapton sample holder (Aluminium discs sealed with Kapton tape, serving as windows). The samples were transported in inert atmosphere to the Australian Synchrotron, where they were measured at the SAXS beamline in a liquid nitrogen cooled temperature stage (Linkam) which was purged with nitrogen. The X-ray energy was at 10keV using a 4k Pilatus detector for the WAXS signal collection.

Acknowledgement:

Financial support by the Bavarian State Ministry of Science, Research, and the Arts for the Collaborative Research Network ''Solar Technologies go Hybrid'' and Federal Ministry of Education and Research BMBF (03SF0484C) are gratefully acknowledged. DK and SS

acknowledge financial support from Department of Science and Technology, India and IRCC -IITB. FP acknowledges financial support by the German Science Foundation DFG through the research training group GRK1640 and thanks Prof. Heinz Bässler, Thomas Unger and Tobias Meier for stimulating discussions.Part of this research was undertaken on the SAXS beamline at the Australian Synchrotron, Victoria, Australia. We acknowledge the experimental support by Kyra Schwartz and Valerie Mitchel.

Author contributions

T.G. and M.T. processed the MAPI films, C.L., S.H., F.P. and A.K. carried out the spectroscopic experiments, A.G and S.H. conducted the X-ray experiments, K.L.N. and D.K. provided the theory, S.S. and D.K. analysed the absorption data. D.K., S.H., F.P., C.L., M.T. and A.K. wrote the manuscript.

References:

[1] Liu, M., Johnston. M. B. & Snaith, H. J. Efficient planar heterojunction perovskite solar cells by vapour deposition. *Nature* **501,** 395-398 (2013).

[2] Wu, C. G., Chaing, C. H., Tseng, Z. L., Nazeeruddin, M. K., Hagfeldt, A. & Graetzel, M. High efficiency stable inverted perovskite solar cells without current hysteresis. *Energy Enviorn. Sci.* **8,** 2725-2733 (2015).

[3] Jeon, N. J., Noh, J. H., Kim, Y. C., Yang, W. S., Ryu, S. & Seok, S. Solvent engineering for high performance inorganic-organic hybrid perovskite solar cell. *Nat. Mater.* **13,** 897-903 (2014).

[4] Zhou, H. *et al.* Interface engineering of highly efficient perovskite solar cell. *Science* **345**, 542-546 (2014).

[5] Tan, Z. K. *et al.* Bright Light emitting diodes based on organometal halide perovskite. *Nat. Nanotechnol.* **9,** 687-692 (2014).

[6] Kumawat, N.K., Dey, A., Kumar, A., Gopinathan, S.P., Narasimhan, K.L. & Kabra, D. Bandgap tuning of $CH_3NH_3Pb(Br_{1-x}Cl_x)_3$ hybrid perovskite for blue electroluminescence. *ACS Appl. Mater. Interfaces* **7**, 13119-13124 (2015).

[7] Yu, J. C., Kim, D. B., Baek, G., Jung, E. D., Cho, S. & Song, M. H. High performance planar perovskite optoelectronic devices: A morphological and interfacial control by polar solvent Treatment. *Adv. Mater.* **27,** 3492-3500 (2015).

[8] Xing, G. *et al.* Low Temperature solution-processed wavelength tunable perovskites for lasing. *Nat. Mater.* **13,** 476-480 (2014).

[9] Dou, L. *et al.* Solution-processed hybrid perovskite photodetectors with high detectivity. *Nat. Commun.* **5,** 5404 (2014).

[10] D'Innocenzo, V. *et al.* Excitons versus free charges in organo-Lead tri-halide perovskites. *Nat. Commun.* **5,** 3586 (2014).

[11] Miyata, A. *et al.* Direct measurement of the exciton binding energy and effective masses for charge carriers in organic-inorganic tri-halide perovskites. *Nat. Phys.* **11**, 582-587 (2015).

[12] Kawamura, Y., Mashiyama, H. & Hasebe, K., Structural study on cubical-tetragonal transition of $CH_3NH_3PbI_3$. *J Phy. Soc. Jpn.* **71**, 1694 (2002).

[13] Frost, J. M., Butler, K.T., Brivio, F., Hendon, C. H. & Schilfgaarde, M. V. Atomistic origin of high performance in hybrid halide perovskite Solar cells. *Nano Lett.* **14**, 2584-2590 (2014).

[14] Kumar, A., Kumawat, N.K., Maheshwari, P. & Kabra. D. Role of halide anion on exciton binding energy and disorder in hybrid perovskite semiconductors. *IEEE PVSC.* DOI: 10.1109/PVSC.2015.7355732.

[15] Elliott, R. J. Intensity of optical absorption by excitons. *Phys. Rev.***108**, 1384 (1957).

[16] Olguı´n, D., Cardona, M. & Cantarero, A. Electron–phonon effects on the direct band gap in semiconductors: LCAO calculations. *Solid State Commun.* **122**, 575–589 (2002).

[17] Varshni, Y.P. Temperature dependence of the energy gap in semiconductor. *Physica*, **34**, 149-154 (1967).

[18] Cody, G. D., Tiedje, T., Abeles, B., Brooks, B. & Goldstein, Y. Disorder and optical-absorption edge of hydrogenated amorphous Silicon. *Phys. Rev. Lett.* **47**, 1480 (1981).

[19] Wantanabe, H., Yamada, N. & Okaji, M. Linear thermal coefficient of silicon from 293K to 1000K. *Int. J. Thermo Phys.* **25,** 221 (2004).

[20] (i) Lin, P. J. & Kleinman, L. Energy bands of PbTe, PbSe, and PbS. *Phys. Rev.* **142**, 478 (1966) (ii) Martinez, G., Schlüter, M. & Cohen, M. L. Electronic structure of PbSe and PbTe. I. Band structures, densities of states, and effective masses. *Phys. Rev. B* **11**, 651 (1975).

[21] Wasim, S. M., Marin, G., Rincon, C. & Sanchez perez, G. Urbach–Martienssen's tail in the absorption spectra of the ordered vacancy compound CuIn3Se5. *J. Appl. Phys.* **84**, 5823 (1998).

[22] Chen, Y., Kothiyal, G. P., Singh, J. & Bhattacharya, P. K. Absorption and photoluminescence studies of the temperature dependence of exciton life time in lattice-matched and strained quantum well systems. *Superlattice. Microst.* **3**, 657 (1987).

[23] Qiang, H. & Pollaka, F.H. Size dependence of the thermal broadening of the exciton linewidth in GaAs/$Ga_{0.7}Al_{0.3}As$ Single quantum wells. *Appl. Phys. Lett.* **61**, 1411 (1992).

[24] Brivio, F*. et al.* Lattice dynamics and vibrational spectra of orthorhombic, tetragonal and cubic phases of methylammonium lead Iodide. *Phys. Rev. B* **92**, 144308 (2015)

[25] Pérez-Osorio, M. A. *et al.* Vibrational properties of the organic–Inorganic halide perovskite $CH_3NH_3PbI_3$ from theory and experiment: factor group analysis, First-Principles calculations, and low-temperature infrared spectra. *J. Phys. Chem. C* **119**, 25703 (2015)

[26] a) Kurik, M. V. Urbach rule. *Phys. Stat. Sol.* (a) **8**, 9 (1971). b) Studenyak, I., Kranjcec, M. & Kurik, M. Urbach rule in solid state physics. *Int. J. Opt. Appl.* **4**, 76 (2014)

[27] Pathak, S. *et al.* Atmospheric influence upon crystallization and electronic disorder and its impact on the photophysical properties of organic–inorganic perovskite solar cells. *ACS Nano* **9**, 2311-2320 (2015)

[28] Wasim, S. M., Marín, G., Rincón, C. & Pérez, G. S. Urbach–Martienssen's tail in the absorption spectra of the ordered vacancy compound $CuIn_3Se_5$. *J. Appl. Phys.* **84,** 5823 (1998).

[29] Wasim, S.M., Marín, G., Rincón, C., Bocaranda, P. & Pérez, G. S. Urbach's tail in the absorption spectra of the ordered vacancy compound $CuGa_3Se_5$. *J. Phys. Chem. Solids* **61**, 669–673 (2000).

[30]a) Kong, W. *et al.* Characterization of an abnormal photoluminescence behavior upon crystal-phase transition of perovskite $CH_3NH_3PbI_3$. *Phys. Chem. Chem. Phys.* **17**, 16405 (2015) b) Fang, H.-H. *et al.* Photophysics of organic–inorganic hybrid lead iodide perovskite single crystals, *Adv. Funct. Mater.* **25**, 2378 (2015).

[31] Wehrenfennig, C., Liu, M., Snaith, H. J., Johnston, M. B. & Herz, L. M. Charge carrier recombination channels in the low-temperature phase of organic-inorganic lead halide perovskite thin films. *APL Mater.* **2**, 081513 (2014).

[32] Lee, M. M., Teuscher, J., Miyasaka, T., Murakami, T. N. & Snaith, H. J. Efficient hybrid solar cells based on meso-superstructured organometal halide perovskites. *Science* **338**, 643-647 (2012).

[33] Gujar, T. P. & Thelakkat, M. Highly reproducible and efficient perovskite solar cells with extraordinary stability from robust $CH_3NH_3PbI_3$: towards large area devices. *Energy Technol.* **4**, 449 (2016).

[34] Chen, Q. *et al.* Planar heterojunction perovskite solar cells via vapor-assisted solution process. *J. Am. Chem. Soc.* **136**, 622−625 (2014).

[35] Panzer, F. *et al.* Reversible laser induced amplified spontaneous emission from coexisting tetragonal and orthorhombic phases in hybrid lead halide perovskites. *Adv. Opt. Mater*. DOI: 10.1002/adom.201500765.

Supporting Information:

Effect of Thermal and Structural Disorder on Electronic Structure of Hybrid Perovskite Semiconductor $CH_3NH_3PbI_3$

Shivam Singh[1#], Cheng Li[2#], Fabian Panzer[3,4,5] K. L. Narasimhan[6], Anna Graeser[2],Tanaji Gujar[7],Anna Köhler[3,4], Mukundan Thelakkat[7], Sven Huettner[2]*, and Dinesh Kabra[1*]

Department of Physics[1] and Electrical Engineering[6], Indian Institute of Technology Bombay, Powai, Mumbai (India) – 400076.

Organic and Hybrid Electronics Group - Macromolecular Chemistry I [2], Experimental Physics II[3], Bayreuth Institute of Macromolecular Research (BIMF)[4], Department of Functional Materials[5], Applied Functional Polymers - Macromolecular Chemistry I[7], University of Bayreuth, 95440 Bayreuth, Germany

# Authors contributed equally

UV-Vis Spectrum analysis:

In order to determine the electronic bandgap and excitonic properties of these materials we model our experimental results using Elliot's theory of Wannier exciton in 3D semiconductors. The following equation is used to fit measured UV-Vis spectrums of $CH_3NH_3PbI_3$ films:

$$\alpha(E) \propto \frac{\mu^2}{E}\left[\sum_n \frac{2E_x}{n^3} sech\left(\frac{E-E_n^x}{\Gamma}\right) + \int_{E_g}^{\infty} sech\left(\frac{E-E_n^x}{\Gamma}\right) \frac{1}{1-e^{-2\pi\sqrt{E_x/E_1-E_g}}} \frac{1}{1-\frac{128\pi\mu b}{\hbar}\left(E_1-E_g\right)} dE_1\right]$$

Where E_x, μ, Γ, E and b are exciton binding energy, transition dipole moment, FWHM of excitonic peak, photon energy and non-parabolic contribution, respectively. This equation is valid for bulk semiconductors with E_x much smaller than the E_g (Wannier excitons) and was used to describe optical transitions to bound and/or ionized excitonic states in model inorganic semiconductors. In above equation there are two terms, first term represents excitonic levels below the conduction band of various perovskite semiconductors and second terms represents the continuum of states beyond the energy of E_g as band-to-band transition contribution in the overall optical absorption. The absorption in the continuum spectrum does not simply resemble a square root dependence of the density of states on energy $\alpha(h\ )^2 = A(E-E_g)$ as expected for bare band-to-band transitions between uncorrelated electrons and holes. The excitonic enhancement of the optical density of states at band-edge depends on the strength of the Coulomb interaction, through the exciton binding energy and reflects the strength of their correlation.[36]

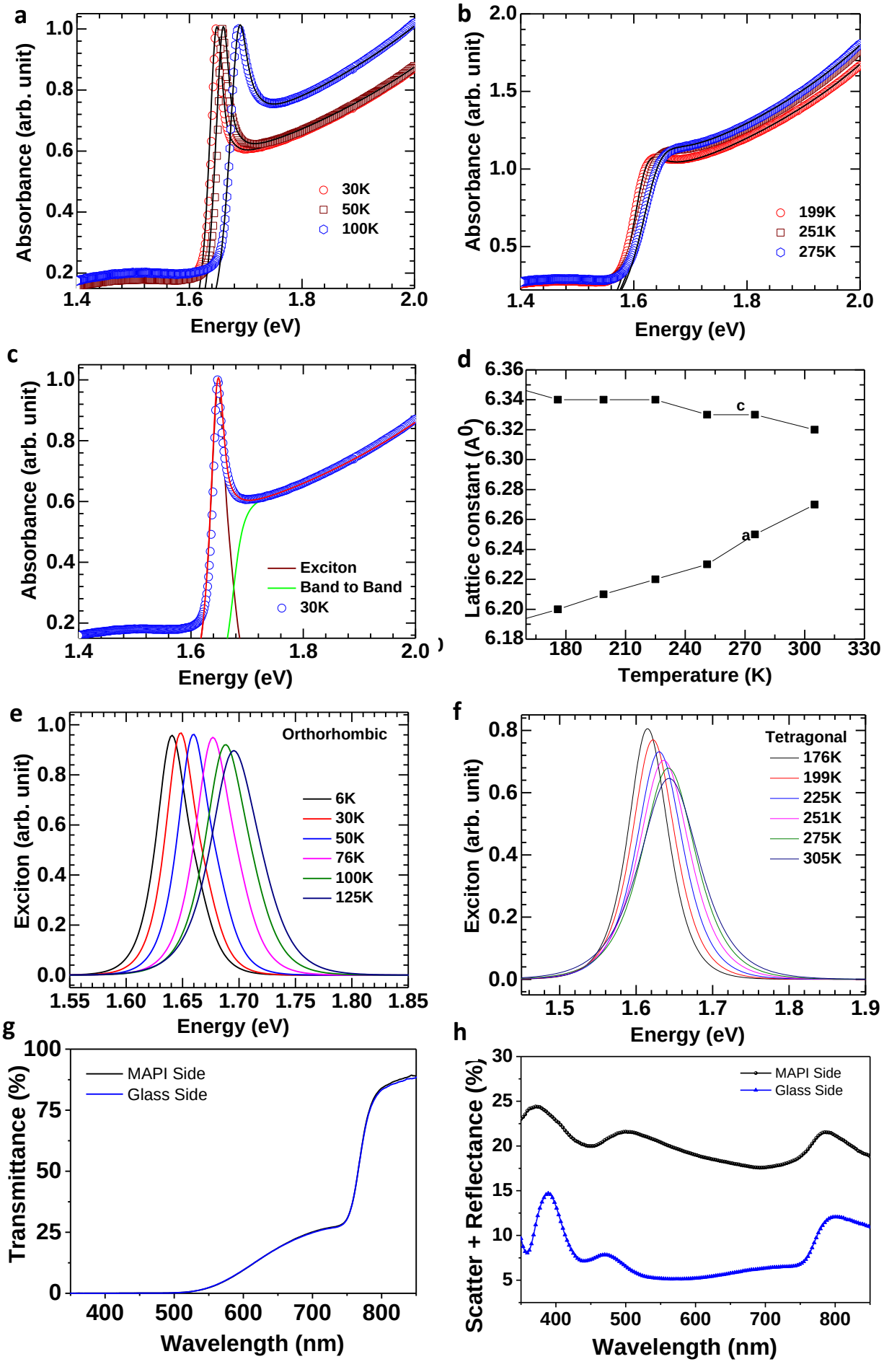
a
Absorbance (arb. unit)
Energy (eV)
30K
50K
100K
b
Absorbance (arb. unit)
Energy (eV)
199K
251K
275K
c
Absorbance (arb. unit)
Energy (eV)
Exciton
Band to Band
30K
d
Lattice constant (A0)
Temperature (K)
c
a
e
Exciton (arb. unit)
Energy (eV)
Orthorhombic
6K
30K
50K
76K
100K
125K
f
Exciton (arb. unit)
Energy (eV)
Tetragonal
176K
199K
225K
251K
275K
305K
g
Transmittance (%)
Wavelength (nm)
MAPI Side
Glass Side
h
Scatter + Reflectance (%)
Wavelength (nm)
MAPI Side
Glass Side

Figure S1: UV-Vis absorption spectra of $CH_3NH_3PbI_3$ thin film at different temperatures: (a) Orthorhombic (b) Tetragonal phase of ABI_3. Black solid line is fit to the experimental absorption spectra (Scatter points). (c) UV-Vis absorption spectra of $CH_3NH_3PbI_3$ at 30K. Red line is fit to the experimental absorption spectra (blue scatter points), where wine and olive line represents the exciton and band to band contributions respectively. (d) Variation of lattice constant with temperature (adapted from[37]). (e) Excitonic contribution in orthorhombic phase and (f) in tetragonal phase, visualizing the broadening with higher temperature. (g,h) transmittance, scatter and reflectance measured with an integrating sphere showing that a certain amount of scattering is involved with these samples.

Fitting of Variation of exciton FWHM with temperature [Fig S2(a)]

$$\Gamma(T) = \Gamma_0 + \frac{\Gamma_{ep}}{exp\left(\frac{E_P}{K_B T}\right) - 1}$$

Where, Γ_0= intrinsic linewidth at T=0K = (11.45±0.21) meV

Γ_{ep} = coupling constant =(14.55±1.67)meV

E_P = LO phonon energy = (13.14±1.21) meV

Here, K_B= 8.61X 10^{-2} meV/K

Results from the fitting of Fig S2 (b)

σ_0 = (0.433±0.009) ; $h\nu_p$ = (20.58±1.13) meV

Results from fitting of Fig S2 (c)

Θ = Einstein Characteristic Temperature = (223±19) K

P = Structural Disorder = (0.017±0.0.05)

N = Thermal Phonon Interaction Term = 1 (Fixed)

E_u (T=0K) = 21.47 meV E_u(T=305K)= 58.72 meV

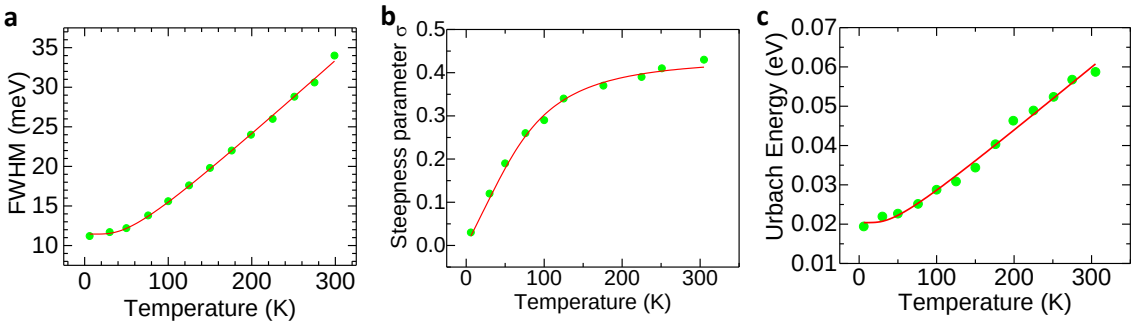

Figure S2: (a) Variation of FWHM of excitonic peak with temperature in $CH_3NH_3PbI_3$. (b) Steepness parameter as a function of temperature for $CH_3NH_3PbI_3$. (c) Urbach energy as a function of temperature for $CH_3NH_3PbI_3$. Red solid line is fit to the experimental data. Fittings are done without separating phases of $CH_3NH_3PbI_3$.

Volume expansion coefficient of $MAPbI_3$

The volume expansion coefficient was determined by plotting ln(V) against T(K) and using the slope of the linear fit (Figure S3). The volume for the tetragonal cell was calculated after: V= a_c * c

For comparison Kawamura et al.[38] calculated the volume after the same equation where **a** was calculated from $\tilde{a}$ = a / $\sqrt{2}$ and **c** from $\tilde{c} = c/2$.

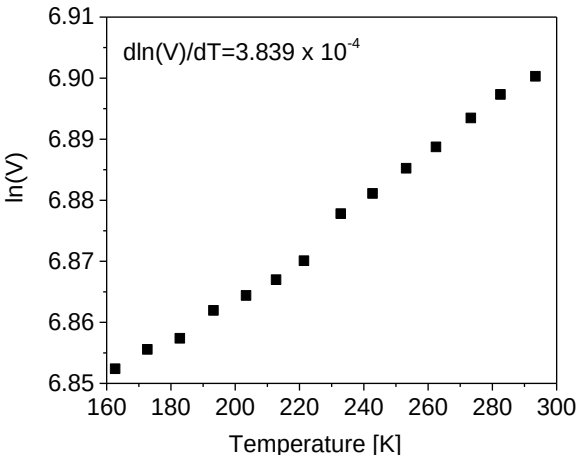

Figure S3: Thermal expansion within the tetragonal phase during cooling (approx. 10K/min).

For the orthorhombic cell the volume was calculated after V=a*b*c (Figure S4).

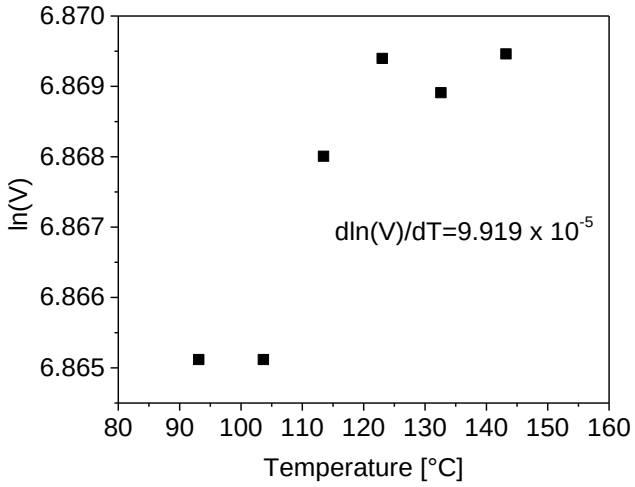

Figure S4: Thermal expansion within the orthorhombic phase within the heating cycle (approx. 10K/min)

Photoluminescence:

High energy side of the PL of the orthorhombic phase was fitted for temperatures <120K using a superposition of an exponential decay and a Gaussian:

$$y = y_0 + A * e^{-\frac{x-x_0}{t_1}} + \left(\frac{B}{w\sqrt{\pi/2}}\right) e^{-2\left(\frac{x-x_C}{w}\right)^2}$$

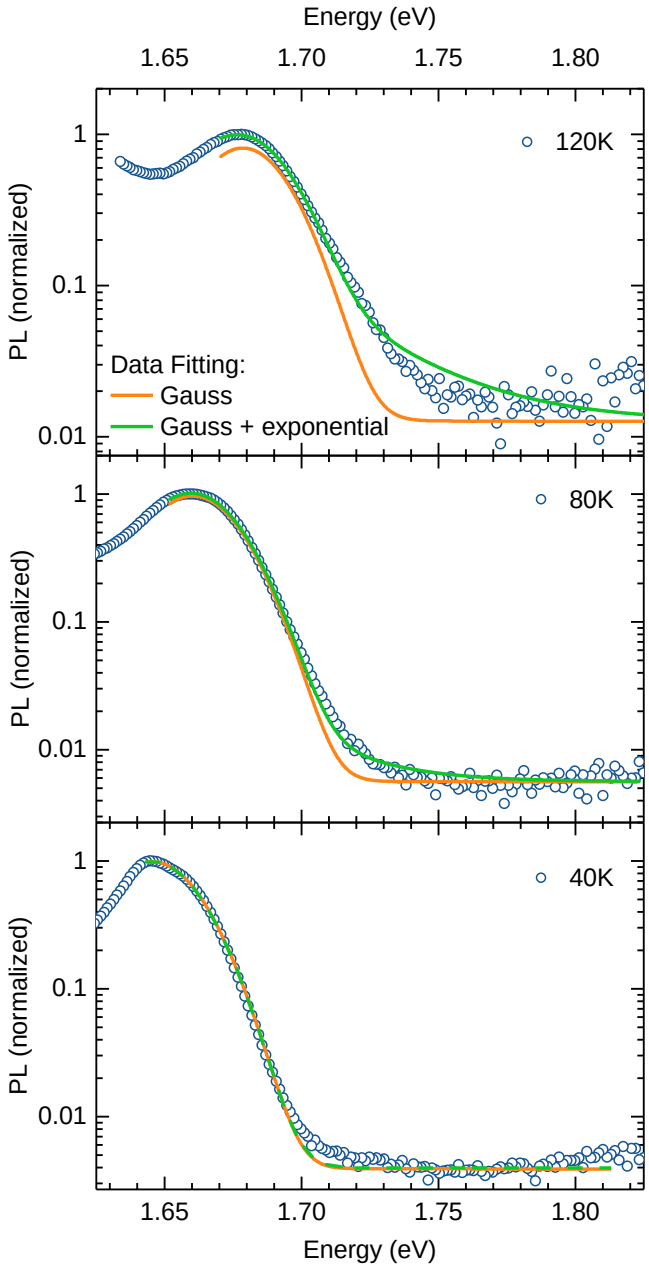

Figure S5: PL spectra at 120K (top), 80K (middle) and 40K (bottom) together with best fits of the high energy side of the spectra using either a superposition of a Gaussian and an exponential (green line) or only a Gaussian (orange line).

Stokes Shift approach:

By calculating the difference between the temperature dependent energetic positions of the PL peak and the already determined excitonic peak from the absorption data (Figure 2), we obtain the temperature dependent Stokes shift (Figure S6).

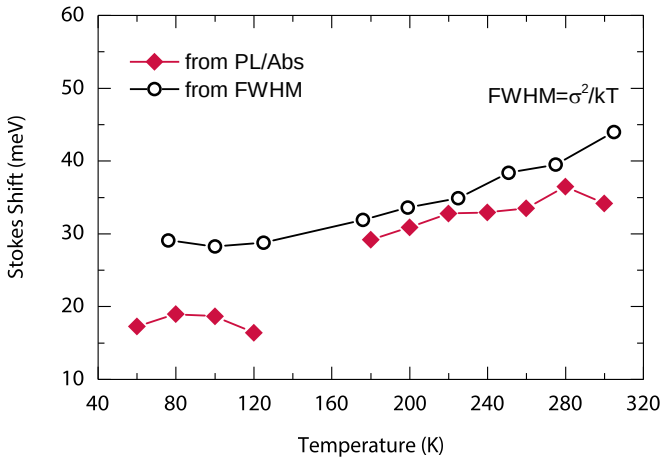

Figure S6: Calculated stokes shift form peak positions of the excitonic absorption peak and the photoluminescence peak (red symbols). The spectral diffusion calculation is given by the black open symbols.

Within the tetragonal phase (300 K – 160 K) values are in the range of 30 - 35 meV and in the orthorhombic phase (< 160 K) in the range between 15-20 meV.

It is known that, besides other parameters, the Stokes shift correlates with the degree of disorder in the material. As already established above, the structural disorder is small in both phases, which leads only to a small Stokes shift that we observe in our data in the entire temperature range investigated. To further investigate to which extend the observed Stokes shift can be attributed toward the small amount of disorder in the material, we fit the data set with a spectral diffusion term. Spectral diffusion is the diffusion of excited states through various energy sites at a given temperature. Assuming a Gaussian distribution of energy levels of the excitons with the width Γ_{EX}, the difference between the PL and exciton absorption peak (Stokes shift) at given T is given by[2]:

$$\Delta\epsilon = \frac{\sigma\,{\Gamma_{EX}}^2}{kT}$$

The slope as well as the absolute values of the Stokes shift match well within the temperature range of the tetragonal phase, we therefore attribute the Stokes shift in

the tetragonal phase to be a consequence of the disorder in the material, which possibly can stem from a distribution of trap states and/or a distribution of excitonic active areas with different sizes within single grains. In contrast to the tetragonal phase, for temperatures below the phase transition the values $\Delta\epsilon$ which were calculated based on the FWHM of the PL Peaks seem to overestimate the Stokes shift by about 10-15 meV. While the detailed explanation and analysis on this difference is beyond the scope of this work, it nevertheless shows the higher order in the orthorhombic phase due to the experimentally obtained small Stokes shift at temperatures below the phase transition.

[36] Saba, M. *et al.* Correlated electron–hole plasma in organometal perovskites. Nature Communications **5**, 5049, (2014)
[37] Kawamura, Y., Mashiyama, H. & Hasebe, K. Structural study on cubical-tetragonal transition of $CH_3NH_3PbI_3$. *J Phy. Soc. Jpn.* **71**, 1694 (2002)
[2] Hoffmann, S. T. *et al.* Spectral diffusion in poly(para-phenylene)-type polymers with different energetic disorder. *Phys. Rev. B* **81**, 11510 (2010)

4.9. Compact Layers of Hybrid Halide Perovskites Fabricated via the Aerosol Deposition Process – Uncoupling Material Synthesis and Layer Formation

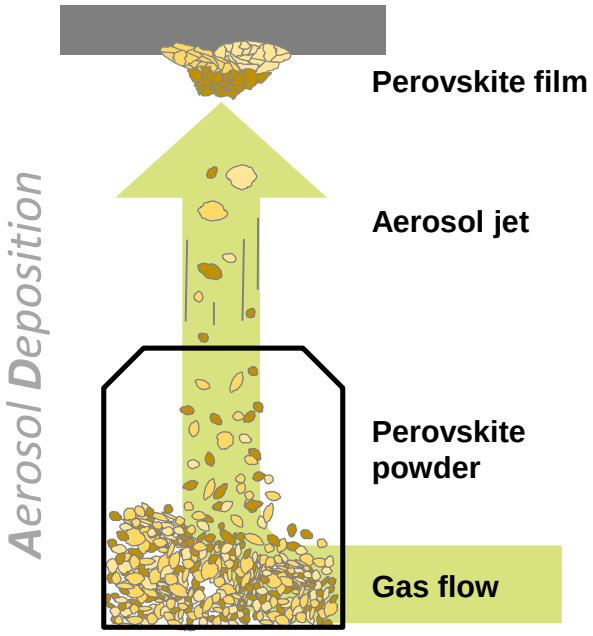

Fabian Panzer, Dominik Hanft, Tanaji Gujar, Frank-Julian Kahle, Mukundan Thelakkat, Anna Köhler, Ralf Moos

Published in
Materials
DOI: 10.3390/ma9040277

Reproduced from Materials, 9, (**2016**), 277.

materials

MDPI

Communication

Compact Layers of Hybrid Halide Perovskites Fabricated via the Aerosol Deposition Process—Uncoupling Material Synthesis and Layer Formation

Fabian Panzer [1,2,3], Dominik Hanft [1], Tanaji P. Gujar [4], Frank-Julian Kahle [2,3], Mukundan Thelakkat [4], Anna Köhler [2,3] and Ralf Moos [1,*]

1 Department of Functional Materials, University of Bayreuth, Bayreuth 95440, Germany; fabian.panzer@uni-bayreuth.de (F.P.); functional.materials@uni-bayreuth.de (D.H.)
2 Experimental Physics II, University of Bayreuth, Bayreuth 95440, Germany; julian.kahle@uni-bayreuth.de (F.-J.K.); anna.koehler@uni-bayreuth.de (A.K.)
3 Bayreuth Institute of Macromolecular Research (BIMF), University of Bayreuth, Bayreuth 95440, Germany
4 Applied Functional Polymers, Macromolecular Chemistry I, University of Bayreuth, Bayreuth 95440, Germany; tanaji.gujar@uni-bayreuth.de (T.P.G.); mukundan.thelakkat@uni-bayreuth.de (M.T.)
* Correspondence: functional.materials@uni-bayreuth.de; Tel.: +49-(0)921-55-7401

Academic Editor: Anke Weidenkaff
Received: 1 March 2016; Accepted: 1 April 2016; Published: 8 April 2016

Abstract: We present the successful fabrication of $CH_3NH_3PbI_3$ perovskite layers by the aerosol deposition method (ADM). The layers show high structural purity and compactness, thus making them suitable for application in perovskite-based optoelectronic devices. By using the aerosol deposition method we are able to decouple material synthesis from layer processing. Our results therefore allow for enhanced and easy control over the fabrication of perovskite-based devices, further paving the way for their commercialization.

Keywords: AD; room temperature impact consolidation (RTIC); methylammonium lead trihalide; $MAPI_3$; $CH_3NH_3PbI_3$; perovskite solar cell; X-ray diffraction; optical spectroscopy; scanning electron microscopy (SEM)

1. Introduction

Hybrid lead-halide perovskites are attracting increasing attention among various research communities due to their remarkable optoelectronic properties, which render them suitable for use as highly efficient active semiconductors in different types of devices. Up to now, their most prominent application is in perovskite-based solar cells, where efficiencies have grown from 9% in 2012 up to a remarkable and commercially interesting 21% in 2015 [1,2]. Meanwhile, applications in the field of lighting technology have also been developed. Here, different types of perovskite-based laser devices have been reported within the past two years [3–6]. Further, by embedding the perovskite material in a host matrix, perovskite-based white light light-emitting diodes were fabricated [7]. Since perovskites also absorb in higher-energy spectral regions, a successful use as UV- or X-ray detectors was demonstrated recently [8–12]. Additionally, hybrid halide perovskites were found to work as memory devices [13,14] and transistors [15], thus further extending the number of possible fields of application for this material class. In general, all these different types of applications impressively demonstrate the high potential of this class of materials.

Obtaining good control over the formation of the perovskite layer is a key requirement to enable the exploitation of the perovskite's optoelectronic properties in any of these applications. As a

consequence, a variety of different methods for the formation of thin films of perovskite were presented within the last years [16,17]. Most of the methods are based on the same principle. Two different compounds, where at least one of them is a halide, are combined to result in a perovskite structure. Usually, this is done in solution and the perovskite formation occurs during the drying process which leads to the film [16]. This approach has the disadvantage that synthesis of the perovskite is interconnected with the formation of the film, so that changes in the processing of the film imply concomitant changes in the optoelectronic properties of the perovskites. Furthermore, it is difficult to obtain layers with thicknesses significantly above 1 µm, which are needed, for instance, when the perovskite is used in X-ray detectors. The development of an alternative approach, where the perovskite synthesis is decoupled from the formation of the film and where films with a wide range of thicknesses can be made easily and without altering the material's properties, is therefore highly desired. This would allow for more control over the processing of the various kinds of perovskite-based devices, further paving the way for commercialization.

A novel processing method that may satisfy the aforementioned requirements is the so-called aerosol deposition (AD) process or method. As we showed in several previous studies [18–22], this method, emerging from the field of ceramics engineering, has proved to be applicable to various material systems and applications. As a result, it attracted much attention over the past decade [23]. Moreover, AD was already used for the controlled formation of TiO_2 layers in dye-sensitized solar cells (DSSCs) [24,25]. In general, it is a method that is used to produce dense ceramic coatings fully at room temperature conditions directly from a bulk powder. The powder is transferred into an aerosol and then spray-coated onto a substrate where dense films are formed. Reported film thicknesses range from a single micron up to several hundreds of micrometers, while reaching film porosities in the single percent range without an additional sintering step [23]. This makes AD superior to other manufacturing methods, especially for materials with low decomposition/degrading temperatures, as is the case in organic-inorganic hybrid perovskites.

The dry nature of the AD process is in contrast to the already-used spray-coating methods that have been applied to hybrid perovskites so far [26–30]. These methods have in common that the perovskite is synthesized *in situ* after *wet* deposition of the reactants, which can render control over the reaction difficult. For example, a perovskite precursor containing methylammonium iodide and lead chloride is deposited by spray-coating and the perovskite forms after annealing [7,26], or PbI_2 and Ch_3NH_3I are subsequently deposited on a substrate by aerosol-assisted chemical vapor deposition and an annealing step results in perovskite formation [28,30,31]. The dry deposition of perovskite powder that we employ, however, implies that the synthesis of the perovskite and the formation of the film are, finally, detached from each other and can be optimized independently. This is a major advancement on the way to the commercialization of this class of semiconductor.

In this proof-of-principle study, we present the successful use of AD to form $CH_3NH_3PbI_3$ perovskite layers, which show high crystalline quality, compactness and optoelectronic activity, thus making this compound suitable for use as active elements in various perovskite-based devices.

2. Results and Discussion

A schematic illustration of the AD system that was used in this study is presented in Figure 1. It consists of three main components, a deposition chamber, a vacuum pump, and an aerosol generation unit. In the aerosol generation unit, a carrier gas flow (*i.e.*, N_2) is directed at the perovskite powder filling which creates aerosolized particles within the aerosol chamber. Due to the pressure difference compared to the deposition chamber, which is evacuated by a vacuum pump (*ca.* 10 mbar), the perovskite particle gas flow is accelerated and dragged through a connecting pipe into the deposition chamber. A slit nozzle is mounted to the exit of the pipe for additional acceleration of the aerosol flow to form a high velocity jet. This jet is then focused toward a movable substrate, where it forms a film when the particles impact on the substrate and consolidate (Figure 1) [23,32]. Here, various parameters such as particle size, hardness of the material or velocity of the particle jet are known to

affect the formation of a film processed by AD. For a detailed overview of the AD with parameters influencing film formation, materials investigated so far (*i.e.*, TiO_2) and possible applications, we refer to the reviews [20,23]. In contrast to the related method of organic vapor-phase deposition, which has been used successfully for the fabrication of organic light-emitting diodes yet requires heating of the equipment and the carrier gas to temperatures in the range of 200–300 °C, the aerosol formation and deposition occurs at room temperature [33,34]. Thus, the principle of film formation is also called Room Temperature Impact Consolidation (RTIC) [23].

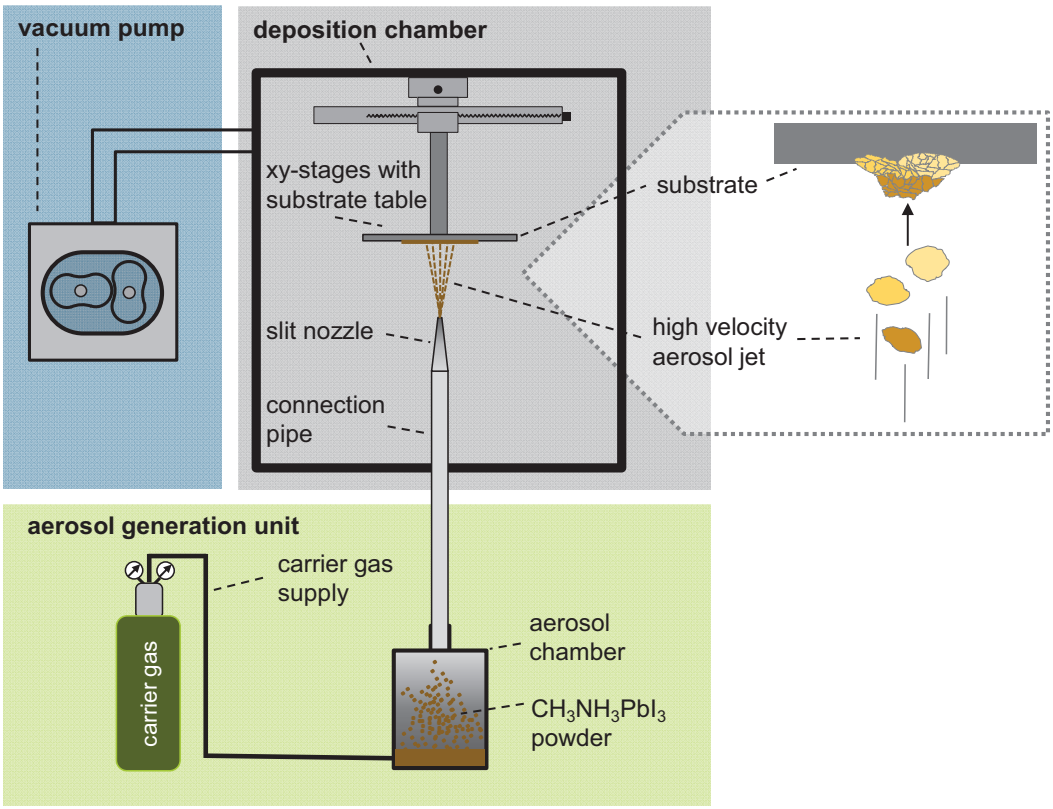

Figure 1. Schematic representation of an aerosol deposition setup with its typical components. The zoomed area at the right-hand side illustrates the film formation process in more detail.

We prepared perovskite powder following a synthesis method as described in more detail in the Experimental Section. Here, the perovskite material was pestled to a powder as the last preparation step before spraying. Figure 2 shows an SEM top-view image of the synthesized powder. From this, a broad distribution of particle sizes in the range of submicrons up to 30 µm becomes obvious. In principle, such a wide distribution as well as the strong agglomeration of the powder particles is disadvantageous for the AD process, where a rather narrow particle size distribution in the single-micron range is usually desired [20,23]. When having a detailed view of the particles (Figure 2b), it can be seen that they consist of smaller constituents, which reveals the partially agglomerated character of the powder, which is also not advantageous for ADM. As will be explained in more detail below, it nevertheless was possible to transform the perovskite powder into a film using AD.

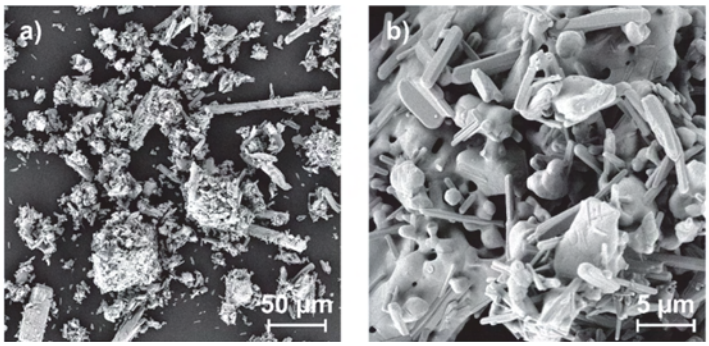

Figure 2. Top-view SEM images of the synthesized perovskite powder before spraying at (**a**) lower; and (**b**) higher magnification.

To prove that film formation is possible on relevant interfaces, the perovskite powder was then processed in terms of the above-described AD onto a glass substrate that was covered with a TiO_2 layer. The latter is frequently used as a transport layer in perovskite solar cells (Figure 3a) [35]. Figure 3b shows the room temperature absorption spectrum of the thus-prepared perovskite film, along with the corresponding normalized photoluminescence spectrum of the sample. The spectra exhibit the typical optical features of $CH_3NH_3PbI_3$ [36], which is a broad absorption within the entire visible range with an absorption onset in the spectral range of about 770 nm. In emission, the samples show the typical near–band edge emission feature at about 780 nm with a FWHM of 46 nm, in accordance with reported literature values [36,37].

To further address the question on the structural quality of the processed layer, we performed XRD measurements. Figure 3c shows the XRD pattern of one of the prepared samples processed via AD, together with the XRD results of a perovskite film which was fabricated via an optimized vapor-assisted crystallization approach for comparison. The latter approach was developed recently in our group and was proven to result in highly stable, uniform and compact layers [38]. When comparing the XRD spectra, both methods lead to diffraction patterns with main features at 14.1°, 28.4°, 31.8° and 43.2° which are assigned to the 110, 220, 114 and 330 peaks of the $CH_3NH_3PbI_3$ perovskite structure, respectively [38–40]. From this, a perovskite-type structure of the AD-processed layer is evident. Notably, no feature in the range of 12.6° is observed. Such a feature is commonly attributed to PbI_2 incorporations, indicative of a non-completed perovskite formation during material synthesis or a degradation process of the perovskite [39]. Thus, the absence of such characteristic features of PbI_2 in our spectra is formidable proof of the nondestructive character of the AD when processing lead-halide perovskite powders. In contrast to the X-ray diffraction spectrum of the layer produced by vapor-assisted crystallization, the X-ray diffraction features of the AD-processed sample generally show less intensity and, simultaneously, a broader width of the peaks. From both of these observations a smaller average grain size can be concluded [41].

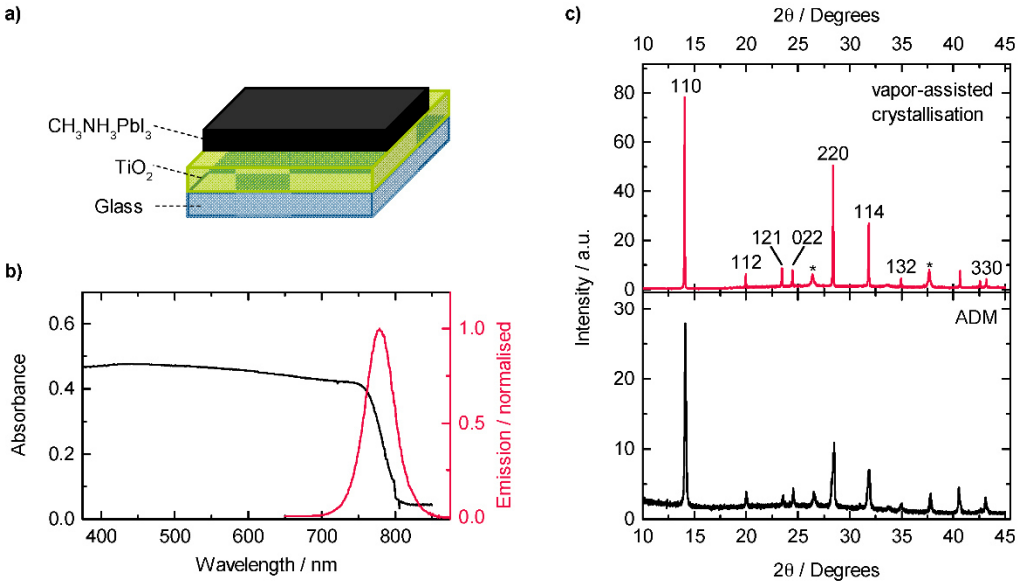

Figure 3. (**a**) Schematic of the sample with an AD-processed perovskite layer; (**b**) Absorption (black solid line) and normalized photoluminescence spectrum (red solid line) of the AD-processed perovskite film; (**c**) XRD patterns of a reference film produced by a vapor-assisted crystallization approach (top) and the AD-processed film (bottom).

This becomes further evident when considering top-view SEM images (Figure 4). Here we find a wide distribution of grain sizes ranging from below 100 nm up to 1000 nm in the AD-processed film (Figure 4a). This is smaller than the reported grain sizes for the optimized vapor-assisted crystallization method, which are in the range between 500 nm and 2000 nm. We assume the rather wide distribution of grain sizes in the case of the AD-processed layers to be due to the distribution of particle sizes of the perovskite powder on the one hand, as no classifying or filtering treatments were applied to the source material. On the other hand, the crystallite size in the 20 to 50 nm range, as can be seen in Figure 4b, can be attributed to the RTIC film formation mechanism that typically governs the AD process. Here, the high kinetic energy of impacting particles results in their fracturing and in a consolidation of previously deposited particles by hammering.

Figure 4b shows that the processed layer exhibits a compact character within the investigated area which is an important layer property for highly efficient optoelectronic applications. For the latter, another important requirement is an intimate contact between the perovskite and TiO_2. From a fracture cross-sectional SEM image of the AD-processed layer (Figure 4c), such a direct contact between the two components can also be seen in our case. Therefore, from the data in Figures 3 and 4 we conclude that AD can transfer the source material to a layer without destroying the crystal structure. From Figure 4c, the layer structure can be characterized as primarily dense with an occasionally distributed number of flaws. We attribute the latter to result from the completely untreated and thus not-for-AD-optimized nature of the initial powder (see Figure 2). Thus, an optimization of the initial powder is an apparent starting point to improve the overall process. This may be achieved by powder preparation methods as they are typical for ceramics, *i.e.*, ball-milling or attritor milling.

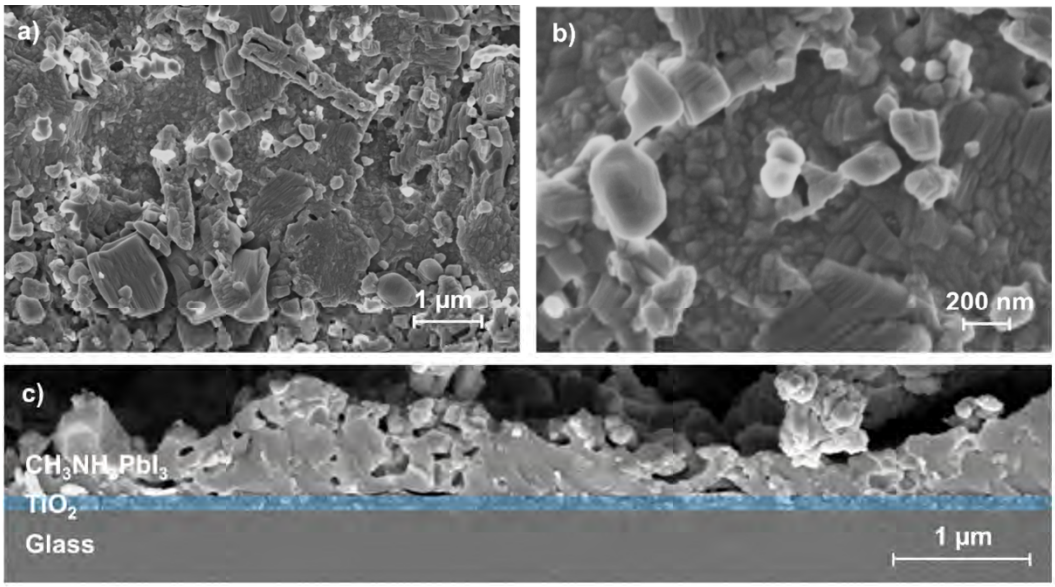

Figure 4. (**a**) Top-view SEM images of the AD-processed perovskite layer with a lower; and (**b**) higher magnification; and (**c**) fracture cross-section of the AD-processed substrate with the TiO_2 layer highlighted in blue.

In summary, we have shown the successful and nondestructive deposition of lead-halide perovskite $CH_3NH_3PbI_3$ powders leading to a compact layer with high chemical purity. The aerosol deposition method employed decouples the synthesis of the perovskite from the layer formation process. It is well established that aerosol deposition allows for the fabrication of a wide range of layer thicknesses [20], that it can also be employed to deposit Al_2O_3 [18] and TiO_2 [25], which are frequently used as transport layers in perovskite solar cells, and that it lends itself to the deposition of mixtures of different source materials [22,42–44]. Thus, this method has potential for a range of different perovskite-based solar cell device architectures. Moreover, this method is scalable and thus is suited for rapid, high-throughput deposition and patterning, as required in an industrial context.

3. Materials and Methods

Materials: All materials were purchased from Sigma-Aldrich and used as received.

CH_3NH_3I Synthesis: Methylammonium iodide (MAI) was synthesized as discussed elsewhere [38]. In short, MAI was synthesized by reacting 24 mL of methylamine (33 wt. % in absolute ethanol) and 10 mL of hydroiodic acid (57 wt. % in water) in a round-bottom flask at 0 °C for 2 h with stirring. The precipitate was recovered by putting the solution on a rotary evaporator and carefully removing the solvents at 50 °C. The white raw product MAI was re-dissolved in 80 mL absolute ethanol and precipitate with the addition diethyl ether. After filtration, the step was repeated two times and white solid was collected and dried at 60 °C in a vacuum oven for 24 h.

Preparation of $CH_3NH_3PbI_3$ powder: The MAI and Lead(II) iodide (PbI_2) were mixed together with 1:1 ratio in 2 mL N, N-dimethyl formamide (DMF) in round-bottom flask. The mixture was stirred for 30 min and degassed under N_2 gas for 30 min followed by drying under N_2 atmosphere at 100 °C. Finally, the dried powder was collected and ground using mortar.

Film Deposition: For deposition we used a custom-made AD apparatus. We used a 10 mm slit nozzle to prepare films of 10 × 15 mm² area on the TiO_2-coated glass substrate.

Layer characterization: Absorption spectrum at room temperature was measured in an integrating sphere using a Cary 5000 UV/Vis spectrometer from Varian (Santa Clara, CA, USA). For emission measurement, we used a FP-8600 spectral photometer from JASCO where the sample was excited

at a wavelength of 405 nm. The film was examined by X-ray diffraction (XRD), using a Bruker D8 Advance, with Cu Kα (λ = 1.5406) X-Ray source. The scanning was conducted in the range of $2\theta = 10^{\circ}$–45°, with a step size of 0.008° and at a rotation speed of 15 min^{-1}. The generator voltage and current were set to 40 kV and 40 mA, respectively. The surface morphology was characterized by field emission scanning electron microscopy (FE-SEM) using a Zeiss 1530 instrument (Zeiss, Oberkochen, Germany).with an accelerating voltage of 3.0 kV.

Acknowledgments: Financial support by the Bavarian State Ministry of Science, Research, and the Arts for the Collaborative Research Network "Solar Technologies go Hybrid", Federal Ministry of Education and Research BMBF (Project: 03SF0484C) and DFG (SFB 840) and through the research training group GRK1640 are gratefully acknowledged. We thank Martina Fried for the synthesis of MAI, Steffen Tscheuschner and Chetan Raj Singh for the help with measurements, the Department of Metal and Alloys for XRD measurements and A. Mergner (Department for Functional Materials) and M. Heider (BIMF) for help with SEM sample preparation and characterization. This publication was funded by the German Research Foundation (DFG) and the University of Bayreuth in the funding program—Open Access Publishing.

Author Contributions: Ralf Moos conceived the idea and designed the AD experiment. Dominik Hanft performed the AD experiments with the help of Fabian Panzer supervised by Ralf Moos. Fabian Panzer performed all optical measurements. Tanaji P. Gujar synthesized the perovskite powder, prepared the sample substrate and carried out the SEM measurements, all under the supervision of Mukundan Thelakkat. Frank-Julian Kahle contributed to analysis and interpretation of all data. Fabian Panzer, Anna Köhler, and Ralf Moos wrote the manuscript. All authors discussed the results, interpreted the findings, and reviewed and revised the manuscript.

Conflicts of Interest: The authors declare no conflict of interest.

References

1. NREL Solar Efficiency Chart. Available online: http://www.nrel.gov/ncpv/images/efficiency_chart.jpg (accessed on 20 February 2015).
2. Luo, S.; Daoud, W. Crystal Structure Formation of $CH_3NH_3PbI_{3-x}Cl_x$ Perovskite. *Materials* **2016**, *9*, 123. [CrossRef]
3. Deschler, F.; Price, M.; Pathak, S.; Klintberg, L.E.; Jarausch, D.D.; Higler, R.; Hüttner, S.; Leijtens, T.; Stranks, S.D.; Snaith, H.J.; *et al*. High photoluminescence efficiency and optically pumped lasing in solution-processed mixed halide perovskite semiconductors. *J. Phys. Chem. Lett.* **2014**, *5*, 1421–1426. [CrossRef] [PubMed]
4. Zhu, H.; Fu, Y.; Meng, F.; Wu, X.; Gong, Z.; Ding, Q.; Gustafsson, M.V.; Trinh, M.T.; Jin, S.; Zhu, X.Y. Lead halide perovskite nanowire lasers with low lasing thresholds and high quality factors. *Nat. Mater.* **2015**, *14*, 636–642. [CrossRef] [PubMed]
5. Stranks, S.D.; Wood, S.M.; Wojciechowski, K.; Deschler, F.; Saliba, M.; Khandelwal, H.; Patel, J.B.; Elston, S.J.; Herz, L.M.; Johnston, M.B.; *et al*. Enhanced amplified spontaneous emission in perovskites using a flexible cholesteric liquid crystal reflector. *Nano Lett.* **2015**, *15*, 4935–4941. [CrossRef] [PubMed]
6. Saliba, M.; Wood, S.M.; Patel, J.B.; Nayak, P.K.; Huang, J.; Alexander-Webber, J.A.; Wenger, B.; Stranks, S.D.; Horantner, M.T.; Wang, J.T.; *et al*. Structured organic-inorganic perovskite toward a distributed feedback laser. *Adv. Mater.* **2016**, *28*, 923–929. [CrossRef] [PubMed]
7. Pathak, S.; Sakai, N.; Wisnivesky Rocca Rivarola, F.; Stranks, S.D.; Liu, J.; Eperon, G.E.; Ducati, C.; Wojciechowski, K.; Griffiths, J.T.; Haghighirad, A.A.; *et al*. Perovskite Crystals for tunable white light emission. *Chem. Mater.* **2015**, *27*, 8066–8075. [CrossRef]
8. Náfrádi, B.; Náfrádi, G.; Forró, L.; Horváth, E. Methylammonium lead iodide for efficient X-ray energy conversion. *J. Phys. Chem. C* **2015**, *119*, 25204–25208. [CrossRef]
9. Maculan, G.; Sheikh, A.D.; Abdelhady, A.L.; Saidaminov, M.I.; Haque, M.A.; Murali, B.; Alarousu, E.; Mohammed, O.F.; Wu, T.; Bakr, O.M. $CH_3NH_3PbCl_3$ Single Crystals: Inverse Temperature Crystallization and Visible-Blind UV-Photodetector. *J. Phys. Chem. Lett.* **2015**, *6*, 3781–3786. [CrossRef] [PubMed]
10. Yakunin, S.; Sytnyk, M.; Kriegner, D.; Shrestha, S.; Richter, M.; Matt, G.J.; Azimi, H.; Brabec, C.J.; Stangl, J.; Kovalenko, M.V.; *et al.* Detection of X-ray photons by solution-processed lead halide perovskites. *Nat. Photonics* **2015**, *9*, 444–449. [CrossRef]
11. Wang, F.; Mei, J.; Wang, Y.; Zhang, L.; Zhao, H.; Zhao, D. Fast photoconductive responses in organometal halide perovskite photodetectors. *ACS Appl. Mater. Interfaces* **2016**, *8*, 2840–2846. [CrossRef] [PubMed]

12. Ramasamy, P.; Lim, D.H.; Kim, B.; Lee, S.H.; Lee, M.S.; Lee, J.S. All-inorganic cesium lead halide perovskite nanocrystals for photodetector applications. *Chem. Commun.* **2016**, *52*, 2067–2070. [CrossRef] [PubMed]
13. Yoo, E.J.; Lyu, M.; Yun, J.H.; Kang, C.J.; Choi, Y.J.; Wang, L. Resistive switching behavior in organic-inorganic hybrid $CH_3NH_3PbI_{3-x}Cl_x$ perovskite for resistive random access memory devices. *Adv. Mater.* **2015**, *27*, 6170–6175. [CrossRef] [PubMed]
14. Panzer, F.; Baderschneider, S.; Gujar, T.P.; Unger, T.; Bagnich, S.; Jakoby, M.; Bässler, H.; Hüttner, S.; Köhler, J.; Moos, R.; *et al*. Reversible laser induced amplified spontaneous emission from coexisting tetragonal and orthorhombic phases in hybrid lead halide perovskites. *Adv. Opt. Mater.* **2016**. [CrossRef]
15. Chin, X.Y.; Cortecchia, D.; Yin, J.; Bruno, A.; Soci, C. Lead iodide perovskite light-emitting field-effect transistor. *Nat. Commun.* **2015**, *6*, 7383. [CrossRef] [PubMed]
16. Stranks, S.D.; Nayak, P.K.; Zhang, W.; Stergiopoulos, T.; Snaith, H.J. Formation of thin films of organic-inorganic perovskites for high-efficiency solar cells. *Angew. Chem. Int. Ed.* **2015**, *54*, 3240–3248. [CrossRef] [PubMed]
17. Ono, L.K.; Leyden, M.R.; Wang, S.; Qi, Y. Organometal halide perovskite thin films and solar cells by vapor deposition. *J. Mater. Chem. A* **2016**. [CrossRef]
18. Schubert, M.; Exner, J.; Moos, R. Influence of carrier gas composition on the stress of Al_2O_3 coatings prepared by the aerosol deposition method. *Materials* **2014**, *7*, 5633–5642. [CrossRef]
19. Sahner, K.; Kaspar, M.; Moos, R. Assessment of the novel aerosol deposition method for room temperature preparation of metal oxide gas sensor films. *Sens. Actuators B Chem.* **2009**, *139*, 394–399. [CrossRef]
20. Hanft, D.; Exner, J.; Schubert, M.; Stöcker, T.; Fuierer, P.; Moos, R. An overview of the aerosol deposition method: Process fundamentals and new trends in materials applications. *J. Ceram. Sci. Technol.* **2015**, *6*, 147–182.
21. Exner, J.; Hahn, M.; Schubert, M.; Hanft, D.; Fuierer, P.; Moos, R. Powder requirements for aerosol deposition of alumina films. *Adv. Powder Technol.* **2015**, *26*, 1143–1151. [CrossRef]
22. Exner, J.; Fuierer, P.; Moos, R. Aerosol deposition of (Cu,Ti) substituted bismuth vanadate films. *Thin Solid Films* **2014**, *573*, 185–190. [CrossRef]
23. Akedo, J. Room temperature impact consolidation (RTIC) of fine ceramic powder by aerosol deposition method and applications to microdevices. *J. Therm. Spray Technol.* **2008**, *17*, 181–198. [CrossRef]
24. Yang, S.; Kim, H.; Ahn, S.-H.; Lee, C.S. The effect of the agglomerated microstructure of dry-deposited TiO_2 electrodes on the performance of dye-sensitized solar cells. *Electrochim. Acta* **2015**, *166*, 117–123. [CrossRef]
25. Cho, S.H.; Yoon, Y.J. Multi-layer TiO_2 films prepared by aerosol deposition method for dye-sensitized solar cells. *Thin Solid Films* **2013**, *547*, 91–94. [CrossRef]
26. Bhachu, D.S.; Scanlon, D.O.; Saban, E.J.; Bronstein, H.; Parkin, I.P.; Carmalt, C.J.; Palgrave, R.G. Scalable route to $CH_3NH_3PbI_3$ perovskite thin films by aerosol assisted chemical vapour deposition. *J. Mater. Chem. A* **2015**, *3*, 9071–9073. [CrossRef]
27. Barrows, A.T.; Pearson, A.J.; Kwak, C.K.; Dunbar, A.D.F.; Buckley, A.R.; Lidzey, D.G. Efficient planar heterojunction mixed-halide perovskite solar cells deposited via spray-deposition. *Energy Environ. Sci.* **2014**, *7*, 2944–2950. [CrossRef]
28. Chen, S.; Briscoe, J.; Shi, Y.; Chen, K.; Wilson, R.M.; Dunn, S.; Binions, R. A simple, low-cost CVD route to high-quality $CH_3NH_3PbI_3$ perovskite thin films. *Cryst. Eng. Comm.* **2015**, *17*, 7486–7489. [CrossRef]
29. Ishihara, H.; Sarang, S.; Chen, Y.C.; Lin, O.; Phummirat, P.; Thung, L.; Hernandez, J.; Ghosh, S.; Tung, V. Nature inspiring processing route toward high throughput production of perovskite photovoltaics. *J. Mater. Chem. A* **2016**. [CrossRef]
30. Lewis, D.J.; O'Brien, P. Ambient pressure aerosol-assisted chemical vapour deposition of $(CH_3NH_3)PbBr_3$, an inorganic-organic perovskite important in photovoltaics. *Chem. Commun.* **2014**, *50*, 6319–6321. [CrossRef] [PubMed]
31. Leyden, M.R.; Ono, L.K.; Raga, S.R.; Kato, Y.; Wang, S.; Qi, Y. High performance perovskite solar cells by hybrid chemical vapor deposition. *J. Mater. Chem. A* **2014**, *2*, 18742–18745. [CrossRef]
32. Lee, D.W.; Kim, H.J.; Kim, Y.H.; Yun, Y.H.; Nam, S.M. Growth process of α-Al_2O_3 ceramic films on metal substrates fabricated at room temperature by aerosol deposition. *J. Am. Ceram. Soc.* **2011**, *94*, 3131–3138. [CrossRef]
33. Arnold, M.S.; McGraw, G.J.; Forrest, S.R.; Lunt, R.R. Direct vapor jet printing of three color segment organic light emitting devices for white light illumination. *Appl. Phys. Lett.* **2008**, *92*, 053301. [CrossRef]

34. McGraw, G.J.; Forrest, S.R. Vapor-Phase Microprinting of Multicolor Phosphorescent Organic Light Emitting Device Arrays. *Adv. Mater.* **2013**, *25*, 1583–1588. [CrossRef] [PubMed]
35. Shi, S.W.; Li, Y.F.; Li, X.Y.; Wang, H.Q. Advancements in all-solid-state hybrid solar cells based on organometal halide perovskites. *Mater. Horiz.* **2015**, *2*, 378–405. [CrossRef]
36. Galisteo-Lopez, J.F.; Anaya, M.; Calvo, M.E.; Miguez, H. Environmental effects on the photophysics of organic-inorganic halide perovskites. *J. Phys. Chem. Lett.* **2015**, *6*, 2200–2205. [CrossRef] [PubMed]
37. Stranks, S.D.; Eperon, G.E.; Grancini, G.; Menelaou, C.; Alcocer, M.J.; Leijtens, T.; Herz, L.M.; Petrozza, A.; Snaith, H.J. Electron-hole diffusion lengths exceeding 1 micrometer in an organometal trihalide perovskite absorber. *Science* **2013**, *342*, 341–344. [CrossRef] [PubMed]
38. Gujar, T.P.; Thelakkat, M. Highly reproducible and efficient perovskite solar cells with extraordinary stability from robust $CH_3NH_3PbI_3$: Towards large-area devices. *Energy Technol.* **2016**, *4*, 449–457. [CrossRef]
39. Liu, M.; Johnston, M.B.; Snaith, H.J. Efficient planar heterojunction perovskite solar cells by vapour deposition. *Nature* **2013**, *501*, 395–398. [CrossRef] [PubMed]
40. Chen, Q.; Zhou, H.; Hong, Z.; Luo, S.; Duan, H.S.; Wang, H.H.; Liu, Y.; Li, G.; Yang, Y. Planar heterojunction perovskite solar cells via vapor-assisted solution process. *J. Am. Chem. Soc.* **2014**, *136*, 622–625. [CrossRef] [PubMed]
41. Bellet, D.; Bellet-Amalric, E. Physical Characterisation of Photovoltaic Materials. In *Solar Cell Materials*; John Wiley & Sons: New York, NY, USA, 2014; pp. 35–63.
42. Exner, J.; Fuierer, P.; Moos, R. Aerosol codeposition of ceramics: Mixtures of Bi_2O_3-TiO_2 and Bi_2O_3-V_2O_5. *J. Am. Ceram. Soc.* **2014**, *98*, 717–723. [CrossRef]
43. Park, J.H.; Akedo, J.; Nakada, M. Surface plasmon resonance in novel nanocomposite gold/lead zirconate titanate films prepared by aerosol deposition method. *Jpn. J. Appl. Phys.* **2006**, *45*, 7512–7515. [CrossRef]
44. Ryu, J.; Hahn, B.D.; Choi, J.J.; Yoon, W.H.; Lee, B.K.; Choi, J.H.; Park, D.S. Porous photocatalytic TiO_2 thin films by aerosol deposition. *J. Am. Ceram. Soc.* **2010**, *93*, 55–58. [CrossRef]

List of Publications

Peer-reviewed publications:

1. Fabian Panzer, Heinz Bässler, Ruth Lohwasser, Mukundan Thelakkat and Anna Köhler,
   The Impact of Polydispersity and Molecular Weight on the Order– Disorder Transition in Poly(3-hexylthiophene),
   Journal Physical Chemistry Letters 5 (**2014**), 2742–2747

2. Fabian Panzer, Michael Sommer, Heinz Bässler, Mukundan Thelakkat and Anna Köhler,
   Spectroscopic Signature of Two Distinct H-Aggregate Species in Poly(3-hexylthiophene),
   Macromolecules 48 (**2015**), 1543–1553

3. Thomas Unger, Fabian Panzer, Cristina Consani, Federico Koch, Tobias Brixner, Heinz Bässler and Anna Köhler,
   Ultrafast Energy Transfer between Disordered and Highly Planarized Chains of Poly[2-methoxy-5-(2-ethylhexyloxy)-1,4-phenylenevinylene] (MEH-PPV),
   ACS Macro Letters 4 (**2015**), 412-416

4. Cristina Consani, Federico Koch, Fabian Panzer, Thomas Unger, Anna Köhler and Tobias Brixner,
   Relaxation dynamics and exciton energy transfer in the low-temperature phase of MEH-PPV,
   The Journal of Chemical Physics 142 (**2015**), 212429

5. Markus Reichenberger, John A. Love, Alexander Rudnick, Sergey Bagnich, Fabian Panzer, Anna Stradomska, Guillermo C. Bazan, Thuc-Quyen Nguyen and Anna Köhler,
   The effect of intermolecular interaction on excited states in p-DTS(FBTTH$_2$)$_2$,
   The Journal of Chemical Physics 144 (**2016**), 074904

6. Fabian Panzer, Heinz Bässler and Anna Köhler,
   The Temperature Induced Order-Disorder Transition in Solutions of Conjugated Polymers Probed by Optical Spectroscopy,
   Journal Physical Chemistry B. (**2016**), invited Feature Article (prepared for submission)

7. Fabian Panzer, Sebastian Baderschneider, Tanaji P. Gujar, Thomas Unger, Marius Jakoby, Sergey Bagnich, Heinz Bässler, Jürgen Köhler, Ralf Moos, Mukundan Thelakkat, Richard Hildner and Anna Köhler,
   Reversible Laser Induced Amplified Spontaneous Emission from Coexisting Tetragonal and Orthorhombic Phases in Hybrid Lead Halide Perovskites,
   Advanced Optical Materials (**2016**), DOI: 10.1002/adom.201500765

8. Shivam Singh, Cheng Li, Fabian Panzer, K. L. Narasimhan, Anna Gräser, Tanaji P. Gujar, Anna Köhler, Mukundan Thelakkat, Sven Hüttner, and Dinesh Kabra,
   Effect of Thermal and Structural Disorder on Electronic Structure of Hybrid Perovskite Semiconductor $CH_3NH_3PbI_3$,
   (**2016**), submitted

9. Fabian Panzer, Dominik Hanft, Tanaji P. Gujar, Frank-Julian Kahle, Mukundan Thelakkat, Anna Köhler and Ralf Moos,
   Compact Layers of Hybrid Halide Perovskites Fabricated via the Aerosol Deposition Process – Uncoupling Material Synthesis and Layer Formation,
   Materials 9 (**2016**), 277

Patents:

Maximilian Fleischer, Tanaji P. Gujar, Dominik Hanft; Ralf Moos, Fabian Panzer, Mukundan Thelakkat:
Aerosolbasierte Kaltabscheidung von Perowskitischen Schichten für Röntgendetektoren, Siemens AG, Germany

Selected Talks and Presentations:

1. **Understanding How the Order-Disorder Transition in P3HT Impacts on its Optical Properties**
   Fabian Panzer, Heinz Bässler, Mukundan Thelakkat, Anna Köhler
   Talk at the Material Research Society spring meeting, San Francisco, USA, April 2015.

2. **Understanding temperature induced order-disorder transitions in solutions of organic materials**
   Fabian Panzer
   Talk at the Rank Prize Funds: Symposium of Exciton Processes in Molecular Materials, Grasmere, England, September 2015.
   For this talk I was awarded as Best Junior Speaker

3. **Reversible Laser Induced Amplified Spontaneous Emission from Coexisting Tetragonal and Orthorhombic Phases in Hybrid Lead Halide Perovskites**
   Fabian Panzer, Sebastian Baderschneider, Tanaji Gujar, Thomas Unger, Heinz Bässler, Ralf Moos, Mukundan Thelakkat, Richard Hildner and Anna Köhler
   Talk at the DPG Spring Meeting, Regensburg, Germany, March 2016.

4. **Temperature induced conformational changes in P3HT**
   Fabian Panzer, Ruth Lohwasser, Mukundan Thelakkat, and Anna Köhler
   Poster Presentation at the Gordon Research Conference on Electronic Processes in Organic Materials, Barga, Italy, April 2014.

5. **Evidence for two distinct H-Aggregate species in P3HT**
   Fabian Panzer, Heinz Bässler, Ruth Lohwasser, Mukundan Thelakkat, Anna Köhler,
   Poster Presentation at the 3rd SolarTech – International Conference, Wildbad Kreuth, Germany, April 2014.

6. **Temperature induced Order-Disorder transition and Spectroscopic Evidence for different H-type Aggregates in P3HT**
   Fabian Panzer, Heinz Bässler, Mukundan Thelakkat, Anna Köhler
   Poster Presentation at the Light-Harvesting Processes Conference, Banz, Germany, March 2015.

Danksagung

Zunächst möchte ich mich herzlichst bei Prof. Anna Köhler und Prof. Ralf Moos für die hervorragende Betreuung meiner Arbeit in den letzten Jahren bedanken. Beide schafften es in den Richtigen Momenten die nötigten Impulse, sowohl in wissenschaftlicher als auch in menschlicher Hinsicht zu geben, was maßgeblich zum Gelingen dieser Arbeit beigetragen hat. Ich möchte mich für das viele Vertrauen und die Freiheiten bedanken die ich im Hinblick auf die Entwicklung meiner wissenschaftlichen Arbeiten und Projekte genießen durfte. Auch das Ermöglichen der vielseitigen Kooperationen, und die Möglichkeit meine Arbeit auf diversen internationalen Tagungen vorzustellen, waren für mich große Bereicherungen.

Prof. Heinz Bässler gilt mein besonderer Dank. Bei unseren Diskussionen schaffte er es immer wieder mir neue Blickwinkel auf Fragestellungen und Probleme zu eröffnen, auch abseits der Wissenschaft. Von Dir habe ich viel gelernt und kann auch noch viel lernen. Vielen Dank dafür!

Des Weiteren möchte ich mich bei allen Kooperationspartnern bedanken. Hier gilt mein Dank insbesondere Prof. Mukundan Thelakkat, der mir als Mentor stets mit einem offenen Ohr als wertvoller Ansprechpartner zur Seite stand. Tanaji Gujar danke ich für die wissenschaftlich und menschlich bereichernden Diskussionen und für das Bereitstellen sämtlicher Perowskit-Proben.

Ein spezieller Dank geht an die Studenten Steffen Grauf, Konstantin Schötz, Tobias Meier und Marius Jakoby die ich während meiner Promotion betreuen durfte. Danke für eure Unterstützung und euren steten Einsatz, auch wenn ich euch ab und zu mit meinen Ideen viel gefordert habe. Durch euch ist der Lehrstuhl gewachsen und ich habe durch eure Arbeiten vieles Neues lernen können und wertvolle positive Erfahrungen gesammelt.

Ich danke Thomas Vogtmann für die schnellen Hilfen bei Problemen mit den Messgeräten, Irene Bauer für die Hilfe bei chemischen Fragestellungen, Michaela Fischer die bei organisatorischen Themen stets weiterhelfen konnte und insbesondere Frank Schirmer für seinen unermüdlichen Einsatz am Lehrstuhl. Er war bei technischen Problemen und Fragestellungen immer zur Stelle, was sicherlich dazu beigetragen hat, dass ich meine Messungen in den letzten Jahren so reibungsfrei durchführen konnte.

Ein großer Dank geht an alle meine Kollegen in den Arbeitsgruppen Köhler und Moos für die gute Arbeitsatmosphäre, die vielen Hilfestellungen, den geselligen Zusammenkünften, den produktiven Gesprächen und den Kicker-Runden. Ohne euch hätte die Promotion nicht halb so viel Spaß gemacht, dafür danke ich jeden Einzelnen!

Ein herzlicher Dank gilt meinen Eltern, Geschwistern und Großeltern, für ihre Unterstützung während des Studiums und während der Promotion.

Zu guter Letzt gilt mein größter Dank meiner Familie - meiner Frau Marie-Luis und meiner Tochter Johanna. Ich danke meiner Frau von ganzem Herzen für die unermüdliche und liebevolle Unterstützung in allen Lebenslagen, das offene Ohr und dafür, dass sie mir in den stressigen Zeiten während der Promotion immer den Rücken freigehalten hat. Ich danke meiner Tochter Johanna für die unendliche positive Energie die sie mir seit (und auch schon vor) ihrer Geburt gibt und gegeben hat – Diddsdü Bebbl Beberer! Ich danke euch für die Liebe die ihr mir täglich schenkt und dass ihr mir immer wieder klar werden lasst, dass es neben dem Beruf noch mehr auf dieser Welt gibt. Ich liebe euch dafür!

Erklärung

Hiermit erkläre ich mich einverstanden, dass die elektronische Fassung meiner Dissertation unter Wahrung meiner Urheberrechte und des Datenschutzes einer gesonderten Überprüfung hinsichtlich der eigenständigen Anfertigung der Dissertation unterzogen werden kann. (§ 8 S. 2 Nr. 6 PromO)

Hiermit versichere ich eidesstattlich, dass ich die Dissertation selbständig verfasst und keine anderen als die von mir angegebenen Quellen und Hilfsmittel benutzt habe. (§ 8 S. 2 Nr. 8 PromO)

Hiermit erkläre ich, dass ich nicht bereits versucht habe eine Dissertation einzureichen oder mich einer Doktorprüfung zu unterziehen. (§ 8 S. 2 Nr. 9 PromO)

Hiermit erkläre ich, dass ich bisher keine Hilfe von gewerblichen Promotionsberatern bzw. Promotionsvermittlern in Anspruch genommen habe und diese auch künftig nicht in Anspruch nehmen werde. (§ 8 S. 2 Nr. 10 PromO)

Bayreuth, den 02.06.2016